

DOE/NASA/0017/1
NASA CR-159865
DDA EDR 10156

N81-19118

CERAMIC APPLICATIONS IN TURBINE ENGINES

Progress Report for 1 July 1979 to 31 December 1979

S. Michael Hudson
Michael A. Janovicz
Franklin A. Rockwood

Detroit Diesel Allison Division
General Motors Corporation

(NASA-CR-159865) CERAMIC APPLICATIONS IN
TURBINE ENGINES Semianual Progress Report,
1 Jul. 1979 - 3 Dec. 1979 (Detroit Diesel
Allison, Indianapolis, Ind.) 157 p

May 1980 HC A08/MF A01

N81-19118

Unclassified
CSCL 21E H2/07 17802

Prepared for
NATIONAL AERONAUTICS AND SPACE ADMINISTRATION
Lewis Research Center
Under Contract DEN 3-17

for

U.S. DEPARTMENT OF ENERGY
Assistant Secretary for Conservation & Solar Applications
Office of Transportation Programs

REPRODUCED BY
NATIONAL TECHNICAL
INFORMATION SERVICE
U.S. DEPARTMENT OF COMMERCE
SPRINGFIELD, VA. 22161

NOTICE

This report was prepared to document work sponsored by the United States Government. Neither the United States nor its agent, the United States Department of Energy, nor any Federal employees, nor any of their contractors, subcontractors or their employees, makes any warranty, express or implied, or assumes any legal liability or responsibility for the accuracy, completeness, or usefulness of any information, apparatus, product or process disclosed, or represents that its use would not infringe privately owned rights.

NOTICE

THIS DOCUMENT HAS BEEN REPRODUCED
FROM THE BEST COPY FURNISHED US BY
THE SPONSORING AGENCY. ALTHOUGH IT
IS RECOGNIZED THAT CERTAIN PORTIONS
ARE ILLEGIBLE, IT IS BEING RELEASED
IN THE INTEREST OF MAKING AVAILABLE
AS MUCH INFORMATION AS POSSIBLE.

1. Report No. NASA CR-159865	2. Government Accession No.	3. Recipient's Catalog No.	
4. Title and Subtitle CERAMIC APPLICATIONS IN TURBINE ENGINES Progress Report for 1 July 1979 to 31 December 1979		5. Report Date May 1980	
		6. Performing Organization Code	
7. Author(s) S. Michael Hudson, Michael A. Janovicz, Franklin A. Rockwood		8. Performing Organization Report No. EDR 10156	
9. Performing Organization Name and Address Detroit Diesel Allison Division, General Motors Corporation Post Office Box 894 Indianapolis, Indiana 46206		10. Work Unit No.	
		11. Contract or Grant No. DEN 3-17	
		13. Type of Report and Period Covered Contractor Report	
12. Sponsoring Agency Name and Address U. S. Department of Energy Office of Transportation Programs Washington, D.C. 20545		14. Sponsoring Agency Code DOE/NASA/0017/1	
15. Supplementary Notes Semianual Report. Prepared under Interagency Agreement EC-77-A-31-1040. Project Manager, T. Miller, Transportation Propulsion Division, NASA Lewis Research Center, Cleveland, Ohio 44135.			
16. Abstract This report describes Detroit Diesel Allison's continued activities in ceramic material characterization and testing of ceramic nozzle vanes, turbine tip shrouds, and regenerator disks at 36°C (65°F) above the base-line engine TIT and the design, analysis, fabrication and development activities taking place between July 1 and December 31, 1979. The design of ceramic components for the next-generation engine to be operated at 2070°F was completed. Fabrication of 2070°F configuration ceramic parts continued with preparations for initial component rig testing of the all-ceramic vane nozzle assembly scheduled for the first quarter of CY 80. Concurrently, ceramics from new sources and alternate materials were being utilized in 1900°F configuration parts for rig and engine testing, broadening the ceramic technology base of the project. Coupons simulating the critical 2070°F rotor blade have been hot spin tested to failure with sufficient margin to qualify sintered silicon nitride and sintered silicon carbide, validating both the attachment design and the finite element model strength. Ceramic suppliers are making progress in increasing demonstrated strength, minimizing variability, and developing nondestructive evaluation techniques but realization of full properties capability in fabricated shapes will require continuing effort throughout the duration of the project.			
17. Key Words (Suggested by Author(s)) Fuel economy Ceramic components Component efficiencies		18. Distribution Statement Unclassified - unlimited STAR Category 85 DOE Category UC-96	
19. Security Classif. (of this report) Unclassified	20. Security Classif. (of this page) Unclassified	21. No. of Pages 155	22. Price*

DOE/NASA/0017/1
NASA CR-159865
DDA EDR 10156

CERAMIC APPLICATIONS IN TURBINE ENGINES

Progress Report for 1 July 1979 to 31 December 1979

S. Michael Hudson
Michael A. Janovicz
Franklin A. Rockwood

Detroit Diesel Allison
Division of General Motors Corporation

P.O.Box 894 Indianapolis, Indiana 46206

May 1980

Prepared for
NATIONAL AERONAUTICS AND SPACE ADMINISTRATION
Lewis Research Center
Cleveland, Ohio 44135
Under Contract DEN 3-17

for

U.S. DEPARTMENT OF ENERGY
Assistant Secretary for Conservation & Solar Applications
Office of Transportation Programs
Washington, D.C. 20545
Under Interagency Agreement EC-77-A-31-1040

Preceding page blank

TABLE OF CONTENTS

<u>Section</u>	<u>Title</u>	<u>Page</u>
I	Introduction and Summary.	1
II	Engine Assembly and Test.	7
	Assembly and Laboratory Test Activity	7
	Component Rig Status.	16
III	Materials Behavior and Characterization	19
	Introduction.	19
	Characterization of Pure Carbon SiC	19
	Characterization of Regenerator Matrix Materials.	24
	Ceramic Abradable Seal Materials.	36
	DDA Ceramic Turbine Tip Shroud.	41
	Nondestructive Evaluation	49
	NDE Development	51
	Component Nondestructive Characterization	62
	Shroud Abradability	66
	Ceramic Machining Development	70
IV	Ceramic Turbine Components.	73
	Introduction.	73
	Gasifier Turbine Nozzle	73
	Gasifier Turbine Blade.	95
	Gasifier Turbine Inlet Plenum	116
V	Ceramic Regenerator Development	117
	Introduction and Summary.	117
	Regenerator Disk.	117
	Regenerator Seals	126
	Hot Performance Rig Testing	130
	High-Temperature Regenerator Rig.	138
	Leaf Rig Testing.	139
VI	General Engine Design and Development	141
	Introduction.	141
	Engine Design Modifications	141
	2070°F Combustor.	144
	Controls.	147
VII	Associated Activities--Papers and Exhibits.	149
	Acknowledgements	151

Preceding page blank

LIST OF ILLUSTRATIONS

<u>Figure</u>	<u>Title</u>	<u>Page</u>
1	Engine test hour summary.	8
2	Gasifier turbine ceramic nozzle vane engine hours	8
3	Gasifier turbine ceramic tip shroud engine hours.	9
4	Ceramic regenerator engine hours.	9
5	Failed silicon carbide vane	12
6	Gasifier turbine nozzle with ceramic turbine tip shroud and ceramic rope packing.	15
7	Microstructure of Pure Carbon reaction-bonded silicon carbide .	20
8	Photomicrograph of extruded Pure Carbon reaction-bonded silicon carbide	21
9	Surface structure of as-fired, slip-cast, Pure Carbon reaction- bonded silicon carbide.	21
10	Fracture surface of extruded, reaction-bonded silicon carbide .	23
11	Surface structure of as-fired, slip-cast, reaction-bonded silicon carbide after exposure at 1250°C (2282°F)	25
12	Surface structure of slip-cast and ground Pure Carbon RB SiC after exposure at 1250°C (2282°F)	26
13	Surface structure of extruded, Pure Carbon RB SiC after exposure at 1250°C (2282°F)	27
14	Fracture surface of slip-cast, oxidized Pure Carbon RB SiC. . .	28
15	Photomicrograph of fracture surface of slip-cast, oxidized Pure Carbon RB SiC.	29
16	Correlation of wall width and modulus of rupture.	31
17	Correlation of mean separator wall thickness and disk radius. .	33
18	Fracture comparison in typical test bars.	34
19	Comparison of phase transformation rate of alumina-silicate matrix materials.	35
20	8H1 cordierite vs Mar-M246.	37
21	Mar-M246 blade tip after rub against 8H1 cordierite	38
22	8H1 erosion	38
23	8H2 cordierite.	39
24	Mar-M246 blade tip after rub against 8H2 cordierite	39
25	8H2 erosion	40
26	GTE silicon nitride	40
27	GTE silicon nitride erosion	41
28	Pure Carbon RB SiC sample I-2	42
29	Pure Carbon RB SiC sample II-1.	42
30	Pure Carbon RB SiC sample I-3	43
31	Pure Carbon RB SiC sample II-2.	43
32	Pure Carbon RB SiC sample III-3.	44
33	Pure Carbon RB SiC sample I-2 erosion	44
34	Pure Carbon RB SiC sample II-1 erosion.	45
35	Pure Carbon RB SiC sample I-3 erosion	45
36	Pure Carbon RB SiC sample II-2 erosion.	46
37	Pure Carbon RB SiC sample II-3 erosion.	46
38	Alumina silicate coating bonded to silicon carbide coupon . .	47
39	Zirconium silicate coating bonded to silicon carbide coupon .	47
40	Plasma-sprayed zircon coating on silicon carbide coupon C-3 .	48
41	Dual-density zirconia coating on silicon carbide coupon C-7 .	48

<u>Figure</u>	<u>Title</u>	<u>Page</u>
42	High-frequency ultrasonic C-scan system for flaw detection in structural ceramics	52
43	Schematic layout of the seeded defects in NC-132 billets	52
44	Photomicrographs showing surface roughness of NC-132 seeded billets	53
45	X-ray radiograph of machined, seeded billet of NC-132	54
46	X-ray radiograph of unmachined, seeded billet of NC-132	55
47	Ultrasonic C-scan of machined billet of NC-132	57
48	Photoacoustic signals from successive scans of a microhardness indentation in alpha silicon carbide.	58
49	Photoacoustic signals from successive scans of a microhardness indentation in reaction-bonded silicon nitride.	59
50	Reverberations in water film between stage and specimen	60
51	Water film between stage and specimen	61
52	Schematic diagram of acoustic interference associated with "edge effect"	62
53	Interferogram of specimens scanned along two edges in the midspan	63
54	Interferogram of alpha silicon carbide specimen with 1-mm (0.04 in.) thick water stage.	64
55	Low-speed abradability test rig	66
56	LAS shroud FX 23081	67
57	LAS shroud FX 23083	67
58	Shroud FX 23082	68
59	LAS shroud FX 23082 erosion test.	69
60	Carborundum shroud FX 23782	69
61	Carborundum shroud FX 23781	70
62	2070°F ceramic vane assembly.	74
63	Inner vane support ring	74
64	Finite element model of ceramic inner vane support ring	75
65	CATE 2070°F engine thermal transients for heat transfer analysis.	75
66	Ceramic vane inner support ring environment	76
67	Ceramic vane inner support ring steady-state temperatures	77
68	Inner vane support ring transient temperatures.	77
69	Inner vane support ring temperature distribution at 8 sec into heat-up thermal transient	78
70	Inner vane support ring maximum principal stress distribution at 8 sec into heat-up thermal transient	79
71	Secondary gas flow over 2070°F ceramic vane and outer support ring.	80
72	Outer vane support ring	81
73	Thixotropic cast inner vane support ring showing numerous air bubbles and voids	87
74	Thixotropic cast inner vane support ring after siliconizing	88
75	Outer view of green inner ring, ultrasonic machined holes	89
76	Outer ring after ultrasonic machining, siliconizing, and sandblasting.	90
77	Finish-machined vane outer support ring	91
78	2070°F ceramic blade geometry	96
79	2070°F blade computer model simplification.	100

<u>Figure</u>	<u>Title</u>	<u>Page</u>
80	Spin coupon No. 22.	102
81	Spin coupon No. 23.	103
82	Spin coupon No. 25.	104
83	Hot cyclic spin evaluation of compliant layers.	105
84	Hot cyclic spin test of IN-600 compliant layers	106
85	Hot cyclic spin test of 347 SS compliant layers	107
86	Spin coupon No. 20.	108
87	Multicrack at peak stress area in spin coupon No. 20.	109
88	2500-cycle hot spin test of L605 compliant layer.	110
89	Partially machined 2070°F silicon carbide blade	116
90	Changes introduced into ring gear mounting adapter to protect edge of ceramic matrix.	118
91	Regenerator disk hub failure encountered during hot rig running	119
92	Close-up of hub showing unusual passage slant	120
93	Failed ceramic regenerator disk	121
94	Cracked ceramic regenerator disk.	122
95	HRD-AB disk 4	123
96	Failed NGK regenerator disk	124
97	Cross section of regenerator disk rim, drive gear, and face seal rims	127
98	Regenerator inboard seal.	128
99	Leakage of inboard seals with 85% NiO/15% CaF ₂ crossarms sprayed by DDA.	131
100	Retest of crossarm seal	131
101	Leaf side of inboard seal	132
102	Effectiveness and pressure drop vs airflow.	134
103	Disk rim coating and face fill process.	134
104	Hot rig performance of inboard regenerator seals with crossarms of NiO/CaF ₂ plasma sprayed over Metnet.	135
105	Hot rig performance of thick-platform inboard regenerator seals with 70% NiO/30% CaF ₂ crossarm wearface	136
106	Crossarm inboard seal	137
107	Leakage performance of seal with resprayed crossarm	138
108	982°C (1800°F) regenerator test rig ducting arrangement	138
109	Leaf rig test of effect of simulated block crossarm distortion at three leaf heights	140
110	Block crossarm and rear bulkhead with 0.018 kg/s (0.04 lb/sec) ambient air cooling at 982°C (1800°F) T ₆	142
111	Block crossarm and rear bulkhead with 0.009 kg/s (0.02 lb/sec) ambient air cooling at 982°C (1800°F) T ₆	143
112	Combustor pressure loss	145
113	Lean burn limit	145
114	Low-speed combustion efficiency	146
115	Combustor exit temperature traverse	146
116	Thermal paint results at 1132°C (2070°F) BOT.	147
117	T ₆ microprocessor engine control.	148
118	Exhibit of various GT 404 projects that utilize ceramic components.	149

LIST OF TABLES

<u>Table</u>	<u>Title</u>	<u>Page</u>
I	Engine durability time of ceramic components	7
II	Summary of test hours for silicon carbide vanes (C-1, Test 1)	10
III	Summary of test hours for regenerator components (C-1, Test 1)	11
IV	Projected seal life.	11
V	Summary of test hours for silicon carbide vanes (C-1, Test 3)	13
VI	Summary of test hours for regenerator components (C-1, Test 3)	13
VII	Summary of test hours for regenerator components (C-2, Test 1)	14
VIII	Summary of test hours for shrouds and regenerators (C-2, Tests 2 & 3)	17
IX	Ceramic component rig test summary	18
X	Strength of Pure Carbon RB SiC material.	22
XI	Oxidation effect on strength of Pure Carbon RB SiC materials	24
XII	1000°C (1832°F) AS material matrix variability	30
XIII	X-ray evaluation of seeded billets of NC-132	56
XIV	Nondestructive characterization of gasifier vanes.	62
XV	Nondestructive characterization of gasifier blades	64
XVI	Nondestructive characterization of hot flow path components.	65
XVII	Nondestructive characterization of strut shells.	65
XVIII	Nondestructive characterization of silicon nitride blade coupons.	66
XIX	Summary of gasifier turbine nozzle ceramic component analysis.	78
XX	Carborundum transfer-molded, reaction-sintered silicon carbide strength characterization.	83
XXI	Carborundum compression-molded, reaction-sintered silicon carbide strength characterization.	85
XXII	Dimensional changes in plastic-molded vane support rings	87
XXIII	Dimensional changes in thixotropic cast inner support ring	88
XXIV	Average strength results of warm-compression-molded, reaction-sintered silicon carbide billets	92
XXV	4-point bend test summary, combined results of nonporous materials.	93
XXVI	Redefined material variation matrix.	94
XXVII	Nondestructive characterization of gasifier vanes.	94
XXVIII	Effects of proof test speed on blade reliability	97
XXIX	Effect of dynamic stress on blade reliability.	98
XXX	Effect of spin proof and dynamic stress on blade reliability	99
XXXI	Spin test summary.	101
XXXII	Ceramic blade injection molding optimization experiments	113
XXXIII	Free-shafting rig test conditions.	124
XXXIV	Leakage of 85/15 inboard regenerator seals	130
XXXV	Effectiveness and pressure drop of recently tested disks	133

I. INTRODUCTION AND SUMMARY

This report relates progress made from 1 July 1979 to 31 December 1979 on the National Aeronautics and Space Administration (NASA) Contract DEN3-17, funded by the Department of Energy (DOE). This contract, to apply ceramic materials to an existing Detroit Diesel Allison (DDA) 404 industrial gas turbine engine, has continued to show excellent progress in building a ceramic materials design data base, establishing design approaches for ceramic components in turbine engines, involving the ceramics industry in fabrication of high technology ceramic components, and defining the true structural, thermal, and chemical environment of ceramic components in turbine engines by rig and engine testing of selected ceramic components. These elements are essential to the highway vehicles. The development of the high-temperature ceramic materials allows increased (relative to metal components) engine-operating temperatures in gas turbine engines. This increased temperature capability yields a more efficient engine that has the potential of reduced fuel usage per mile (by more than 20%). Furthermore, the ceramic components can potentially reduce the cost from that of metal parts and help make feasible a production vehicular (truck, bus, or passenger car) gas turbine.

DDA with its 404/505/605 series industrial gas turbine (IGT) engines presented a unique opportunity to explore specific fuel consumption (SFC) improvement since it is a highly developed gas turbine engine with near term production potential for introduction into truck, bus and generator set markets. These markets use approximately 21% of the transportation petroleum products. Consequently, using this engine as a test bed for ceramic application is a logical first step to the broad automotive marketplace. Technology developed in this program is readily transferred to the passenger car gas turbine engines.

Contract activities were initiated in 1976 to demonstrate ceramic components in a DDA 404-4 industrial gas turbine. Initial work provided studies and analyses of the 404-4 engine defining the parametric sensitivities and identifying the candidate components for ceramic application and efficiency improvement. The initial activity also included fabrication and test of selected ceramic components, ceramic material characterization and qualification, and conversion of two contractor-owned engines to an initial ceramic configuration capable of operation at 1038°C (1900°F).

The analyses and studies explored operating turbine inlet temperatures of 1002°C (1835°F) (base-line IGT) to 1371°C (2500°F). These studies concluded that a configuration at 1241°C (2265°F) with component efficiency improvements would be the optimum approach. Ceramics would be introduced to the gasifier turbine nozzle vanes, gasifier turbine tip shroud, gasifier turbine blades, power turbine nozzle vanes, inlet plenum, combustor, and regenerator disks. Component efficiency improvements would be made in compressor, plenum flow uniformity, power turbine (two stage), gasifier turbine nozzle and tip shroud, and gasifier turbine tip and wall losses. These components would be introduced at three discrete TIT steps -- the 1038°C (1900°F), 1132°C (2070°F), and 1241°C (2265°F) configurations. The project plan that included ceramic material test and characterization, rig testing, engine performance and durability, and vehicle demonstration at each

of the temperature levels was published as DOE/NASA Report CONS0064-1 in May of 1977. Subsequently, this plan became the basis for the project now in progress at DDA.

Previously issued semiannual reports cover the ceramic materials characterization, component design, rig test, and engine test activities of the project from January 1978 through June 1979. Through that period, DDA engaged in 4600 hours of engine operation to truck and bus operating cycles with the initial ceramic parts at a turbine inlet temperature of 1038°C (1900°F)--some 36°C (65°F) above that of the all-metal base-line engine. These initial tests of ceramic parts indicated the chemical and structural stability of silicon carbide nozzle vanes, sintered silicon nitride and silicon carbide turbine tip shrouds and alumina silicate regenerator disks. In addition, reaction bonded silicon carbide nozzle vanes and alumina silicate regenerator disks have successfully withstood 7660 km (4760 miles) of over-the-road engine use, including exposure to rigorous road hazard test courses, in a turbine powered truck. This truck experience has served as a demonstration of the utility and durability of ceramic parts operating in a turbine engine under actual vehicle application operating conditions. During this time, activities were conducted to characterize ceramic material candidates, improve realized strength of ceramics in part configurations, define ceramic design methodology, explore nondestructive evaluation (NDE) techniques applicable to ceramic materials, qualify parts with rigs simulating critical engine conditions, and design a configuration to operate at 1132°C (2070°F) utilizing the data, experience, and methodology being obtained to effectively apply ceramics in a turbine engine configuration.

Activities over this report period are marked by the completion of testing of the initial 1038°C (1900°F) ceramic components, fabrication and accompanying process development leading to the first set of 2070°F ceramic components, development of the component and subsystem technologies to support ceramic applications at 1132°C (2070°F), evaluation of alternative ceramic materials and sources, and development of NDE techniques specifically aimed at identifying of critical-sized flaws in ceramic materials.

Engine testing continued, combining durability evaluation of second-generation and alternative ceramic parts with data and development tests for secondary systems required to support the future 2070°F configuration. Over the period, 1675 additional hours of engine operating time with ceramic parts installed were accumulated, bringing the total ceramic experience in the project to 6270 hours. Utilizing the two project engines, overall ceramic part experience stands as follows: reaction-bonded silicon carbide nozzle vanes - 2596 hours; reaction-bonded silicon nitride nozzle vanes - 81 hours; Purebide REFL silicon carbide nozzle vanes - 293 hours; reaction-bonded silicon carbide abradable turbine tip shrouds - 1546 hours; sintered silicon nitride turbine tip shroud - 113 hours; lithium alumina silicate with glass filler abradable coated turbine tip shroud - 11 hours; and alumina silicate regenerator disks - 6270 hours. No silicon nitride components were tested during the period because parts with suitable properties for the applications were not available. On the other hand, the successful introduction of two alternative materials has been encouraging. One alumina silicate regenerator disk has now been retired after 3050 hours of operation, and the high-time reaction-bonded silicon carbide nozzle vanes and tip shrouds have accrued 1499 and 985 hours, respec-

tively. These accumulations attest to the durability of the material. Special tests have been introduced for each of the project engines to pave the way for operation at 1132°C (2070°F) next year. Engine C-1 has been modified to accept power turbine exhaust area (T_6) thermocouples. Initially the engine was operated with gasifier turbine inlet thermocouples (T_4) and T_6 temperatures were recorded to serve as a data base for the design of a T_6 control for the 2070°F configuration because current thermocouples cannot withstand the anticipated T_4 temperatures reliably for any significant length of time. A prototype T_6 control was subsequently tested successfully with the engine. The control is based upon microprocessor technology rather than the current analog design. This initial testing success is particularly gratifying in that both the completely new microprocessor approach and the more difficult T_6 temperature sensing were integrated simultaneously. The second project engine (C-2) has been used for evaluating the improved block insulation and block crossarm air cooling. These tests, which are continuing, provide the necessary technology to design a cooling scheme which will both protect the cast iron block and control block thermal distortion upon exposure to the higher heat loads applied at the 1132°C (2070°F) operating temperature.

Ceramic source participation has grown from four to eleven who are or have been suppliers of ceramic parts. Except for regenerator disks which are alumina silicate, silicon carbide materials predominate. However, the fabrication of silicon nitride blades and vanes as an alternative material for the 2070°F configuration has been started. Experience with sintered silicon nitride from the initial-configuration turbine tip shroud is the basis for an alternative for the ring-type structures of the 2070°F nozzle assembly. Process development activities with the reaction-bonded and sintered alpha silicon carbide are nearing completion; only the fabrication of a complement of parts to the final process remains. Process development has led to significant improvement in realizable part strength as in the case of reaction-bonded silicon carbide, whose strength has increased some 35% over the past two years, as four generations of vanes were produced. Machining experiments have been extended to the ceramic parts being incorporated in the two project engine configurations. Surface grinding, ring grinding, and jig grinding with diamond wheels are well established, and ultrasonic machining is showing exceptional promise for economical production of holes, slots, and pockets. Plasticizing has eliminated edge chipping of fully hardened ceramic parts.

All metal and ceramic parts for the first 2070°F configuration gasifier nozzle and tip shroud assembly have been fabricated and assembled for initial rig thermal shock testing early in the next report period. Twenty-eight unmachined sintered alpha silicon carbide vanes are retained by pockets and slots in warm compression-molded, reaction-bonded silicon carbide support rings. A retaining ring of Purebide REFEL silicon carbide closes the slots in the outer support ring, capturing the vanes. The turbine tip shroud is warm compression-molded, reaction-bonded silicon carbide with the inside diameter leached for abradability. Metal inner and outer support rings capture the shroud and support rings connecting the nozzle to the block and inner structure of the base-line engines. Loads and centering of the inner and outer supports are established by four air-cooled metal struts shielded from the gas stream by slip

cast REFEL silicon carbide shells. A combustor of high-flow Lamilloy®* sheet, to withstand the temperature of the 2070°F engine, has successfully completed performance development tests. The plenum to direct the hot combustion gas to the gasifier nozzle is of sheet metal; its gas side is plasma coated with NASA Lewis Research Center-developed yttria-stabilized zirconia to form a thermal barrier. This coating has been quite successful in protecting the plenum metal structure during operation at 1038°C (1900°F). Initial ceramic plenums of slip or drain cast sintered alpha silicon carbide and NC-430 have been successfully fired. Process development to meet the interface dimensional requirements is continuing.

The gasifier turbine consists of 40 individual ceramic blades attached through a dovetail to a Waspaloy rotor. Sintered alpha silicon carbide injection-molded blades are now being fabricated following process development which has led to structurally sound pieces with the airfoil dimensionally consistent enough for use without machining. Spin test coupons simulating blade mass and the dovetail of sintered alpha silicon carbide and sintered silicon nitride have undergone both hot and cold spin test to failure. The silicon carbide exhibits 125% burst speed against 160% for silicon nitride. Static and cyclic loading tests of a compliant layer to distribute the contact load between the ceramic blade and rotor have identified L605 as the optimum material for the application. Other materials progressively extrude to failure at the expected temperature, whereas L605 tends to work harden, withstanding the cyclic loading while retaining enough compliance to protect the ceramic. A diffusion barrier of boron nitride is utilized at the dovetail to prohibit adhesion between the ceramic blade and the compliant layer.

During the period, regenerator disks of 1100°C (2012°F) rated alumina silicate have passed rig as well as engine tests, demonstrating thermal and aerodynamic performance comparable with that of the former 1000°C (1832°F) rated composition. Engine experience now totals over 400 hours. Specimen testing of this new composition verified that chemical stability is retained at the rated temperature by accurate monitoring of change in length per unit length upon temperature exposure. Development of the regenerator hot seal crossarm wearface has both overcome the previously reported delamination caused by oxidation at the plasma spray system bond coat and minimized distortion which contributes to excessive leakage under engine start-up and idle conditions. Seals of the 1900°F configuration have successfully completed rig and engine (428 hours) tests. The successful seals are of 85% nickel oxide/15% calcium fluoride composition with a barrier coat adjacent to the bond coat. Of more importance are friction and wear and distortion specimen tests which indicate that the 85/15 and 70/30 compositions of the nickel oxide/calcium fluoride family are candidates for the 981°C (1800°F) environment of the 2070°F engine configuration. Modulus of rupture testing of the regenerator disk matrix has identified three geometric variables contributing to strength loss: channel skewness, matrix distortion, and separator thinning. Initial NDE experiments are demonstrating the potential of X-ray, hot wire anomometry, and vibration profile in identifying strength-limiting geometric conditions.

*Lamilloy is a registered trademark of the General Motors Corporation.

Supporting these part-oriented activities have been basic ceramic material investigations into abradability, interface diffusion, and NDE. In a more comprehensive rig, abradability ratios of up to 8 to 1 with a metal rotor have been achieved with leached silicon carbide. Glass ceramic filler and silicon nitride specimens are also offering promise, but all materials must continue to show progress because 15 to 1 abradability ratios are required to permit close-tolerance tip clearance for improved engine operating efficiency. Experiments continue to identify NDE technologies capable of discerning the 10- to 100-micron critical flaw sizes of ceramics applied to the gas turbine engine. Photoacoustic spectroscopy, reflective high-frequency ultrasound, and acoustic microscopy show promise for flaws that are larger in degree and small in extent including voids, inclusions, and cracks. Ultrasonic velocity, ultrasonic attenuation, and differential spectroscopy are under study for microstructural variations.

The overall results of design, analysis, ceramic process development and ceramic component test continue to reflect favorable progress toward the second generation of the ceramic gas turbine engine to be operated at 1132°C (2070°F) during the next report period. The rig and engine testing also has been instrumental in promoting realized strength improvement of the existing materials and assessing emerging alternative materials. Further reports under Contract DEN3-17 will be issued semiannually. DDA has published the following reports as a part of the requirements of Contract DEN3-17: EDR 9519, EDR 9722, and EDR 9951. Copies can be made available upon request to NASA-Lewis Research Center, Cleveland, Ohio 44135.

II. ENGINE ASSEMBLY AND TEST

ASSEMBLY AND LABORATORY TEST ACTIVITIES

The test activities that occurred during this reporting period were conducted on 1900°F configuration ceramic components that successfully completed proof tests in rigs which simulated the most severe engine operating conditions; they were then tested in an engine for cyclic endurance. The engines used to evaluate the ceramic components are IGT 404-4 models rated at 1038°C (1900°F) gasifier rotor inlet temperature, modified to accept the ceramic parts. Major accomplishments and findings for the reporting period were:

- o Engines C-1 and C-2 accumulated 1671 hours, bringing the total CATE project ceramic hardware engine test time to 6270 hours.
- o Engine testing was conducted on the following ceramic components:
 - o Vanes - Carborundum, Pure Carbon
 - o Turbine Tip Shrouds - Carborundum, GTE Sylvania, Corning
 - o Regenerators - Corning, NGK (Japan)
 - o Rope Packing - 3M Co.
- o A new ceramic regenerator disk material was introduced which was successfully rig and engine tested. The thermal effectiveness increased 1% over the original disk hardware. Engine durability evaluation is continuing.
- o Component testing brought the maximum total times accumulated by a silicon carbide (Carborundum) vane and a thin-wall regenerator disk to 1499 and 3050 hours, respectively.

Table I is a summary of the total engine test hours accumulated since the start of testing.

TABLE I. ENGINE DURABILITY TIME OF CERAMIC COMPONENTS

<u>Component</u>	<u>Maximum hours for one component</u>	<u>Total durability hours</u>
Thick wall regenerators	1808	2829
Thin wall regenerators		
1000°C (1832°F) rated	3050	3917
1100°C (2012°F) rated	297	407
Gasifier turbine vanes		
Silicon carbide (Carborundum)	1499	2596
Silicon carbide (Pure)	293	293
Silicon nitride (AiResearch)	81	81
Gasifier turbine shroud		
Silicon carbide (Carborundum)	985	1546
Silicon nitride (GTE Sylvania)	113	113
LAS (Corning)	11	11

The ceramic component engine test activities during the reporting period are plotted in Figures 1 (engine test hours), 2 (gasifier turbine vane), 3 (tip shroud), and 4 (ceramic regenerator).

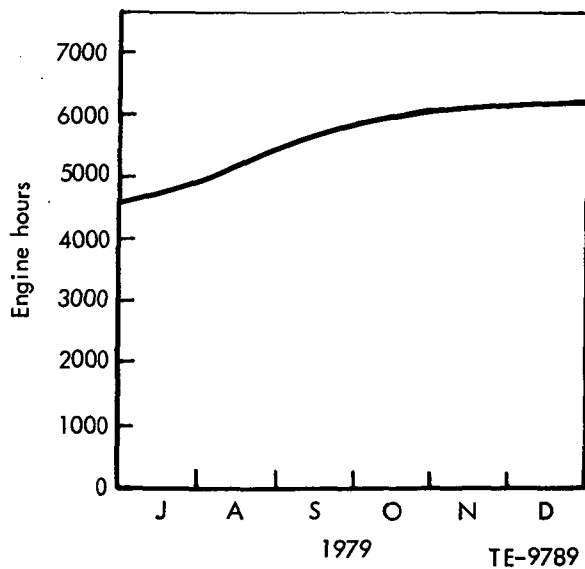


Figure 1. Engine test hour summary.

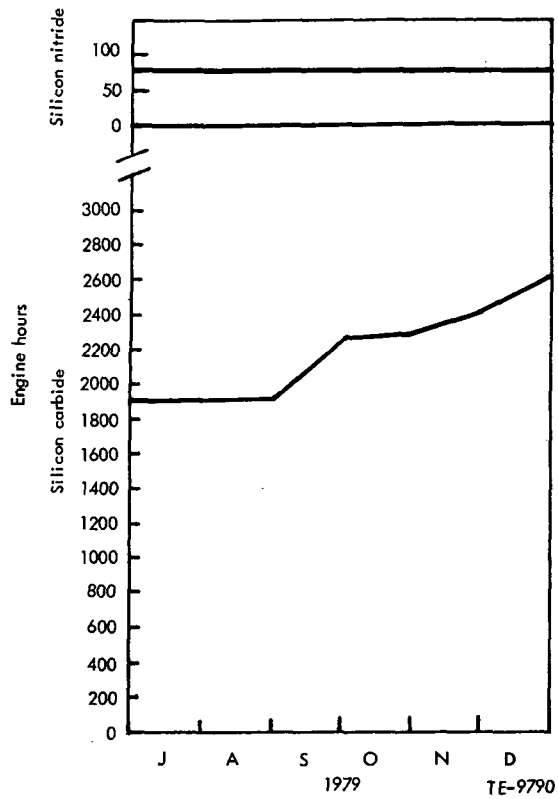


Figure 2. Gasifier turbine ceramic nozzle vane engine hours.

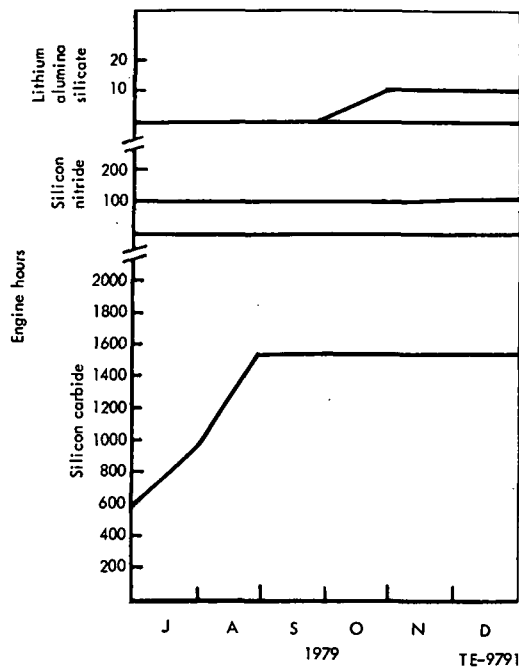


Figure 3. Gasifier turbine ceramic tip shroud engine hours.

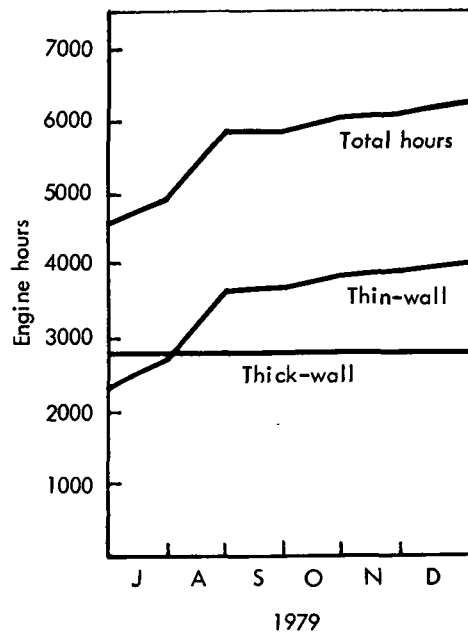


Figure 4. Ceramic regenerator engine hours.

Engine C-1

Engine C-1 accumulated 686 hours of testing for a total test time of 3118 hours. Silicon carbide (SiC) gasifier turbine vanes from two vendors were tested. All ceramic regenerator disks tested were thin-wall alumina silicate (AS) material, and the inboard regenerator seals featured crossarm wearface material of 70% NiO/30% CaF₂ or 85% NiO/15% CaF₂. The engine test activity was centered entirely on test stand durability and can be categorized into three tests as follows.

Test 1 - Test Stand Durability Testing of Ceramic Gasifier Vanes and Regenerators

This test program accumulated 393 hours of simulated truck cycle durability for ten silicon carbide gasifier turbine vanes, manufactured by Carborundum, and two thin-wall AS regenerator disks (1000°C (1832°F) material capability). The inboard regenerator seals used during the test had a plasma-sprayed crossarm wearface of 70% NiO/30% CaF₂ material. Table II provides the time breakdown for the ten vanes at the conclusion of Test 1. The vanes showed no evidence of distress following the test.

TABLE II. SUMMARY OF TOTAL TEST HOURS FOR TEN SILICON CARBIDE VANES IN
ENGINE C-1, TEST 1

Vane Serial Number	Total accumulated Test Hours	Comments
262	480	Carborundum 1st generation
B-7	1006	
B13	1006	Carborundum 2nd generation
B20	580	
B21	580	
C31-5	580	
C34-12	580	
C37-10	580	Carborundum 3rd generation
C38-6	580	
C39-8	580	

Table III provides a summary of the test times for the ceramic regenerator disks and the inboard and outboard regenerator seals at the conclusion of Test 1.

The wear rate of the inboard regenerator seal crossarm wearface has been monitored for all materials tested to date including 85% NiO/15% CaF₂, 70% NiO/30% CaF₂, and 85% NiO/15% CaF₂ with a barrier layer. Table IV provides the results of the wear measurements. These data do not represent a statistical computation because only a few parts of each material have been tested. Rather, they represent the projected wear life for each of the seal materials, derived by plotting a curve of wear measurements versus test hours and then taking the maximum allowable seal wear limit to determine projected wear life.

TABLE III. SUMMARY OF TOTAL TEST HOURS FOR THE REGENERATOR
COMPONENTS IN ENGINE C-1, TEST 1

<u>Regenerator disks serial number</u>	<u>Total accumulated test hours</u>	<u>Comments</u>
24	418	Corning 1000°C
25	515	AS thin-wall material
 <u>Inboard seals serial number</u>		
H985	416	Crossarm wearface
H948	588	70% NiO/30% CaF ₂
 <u>Outboard seals serial number</u>		
C492	390	
C493	515	

TABLE IV. PROJECTED SEAL LIFE BASED ON WEAR DATA FOR
INBOARD SEAL CROSSARM WEARFACE MATERIALS

<u>Seal wearface material</u>	<u>Projected life (hours)</u>
85% NiO/15% CaF ₂	6000
70% NiO/30% CaF ₂	5000-6000
85% NiO/15% CaF ₂ with barrier layer	Insufficient data available

Test 2 - Test Stand Durability Test of Improved Ceramic Gasifier Turbine
Vanes and Regenerators

Following Test 1, the engine was reconfigured with a new gasifier turbine nozzle assembly in which the metal vane holder had been modified to reduce secondary leakage and which contained ten silicon carbide vanes--two supplied by Pure Carbon Co. and eight by Carborundum Co. Four of the Carborundum vanes are fourth generation material. Also included in Test 2 were ceramic thin-wall AS material regenerator disks--one rated at 1100°C (2012°F), which is an increase in disk material temperature capability from 1000°C (1832°F). The other thin-wall ceramic regenerator was AS material rated at 1000°C (1832°F). Two inboard seals with a crossarm wearface material composition of 85% NiO/15% CaF₂ and a barrier layer were also tested.

Test 2 consisted of 128 hours of truck cycle durability, which was interrupted after four hours of testing by a failed silicon carbide vane (Figure 5). The failed vane was a first generation silicon carbide vane which had accumulated 1211 hours of engine testing. Engineering and Materials Research failure analyses have not conclusively determined the reason for failure. No evidence

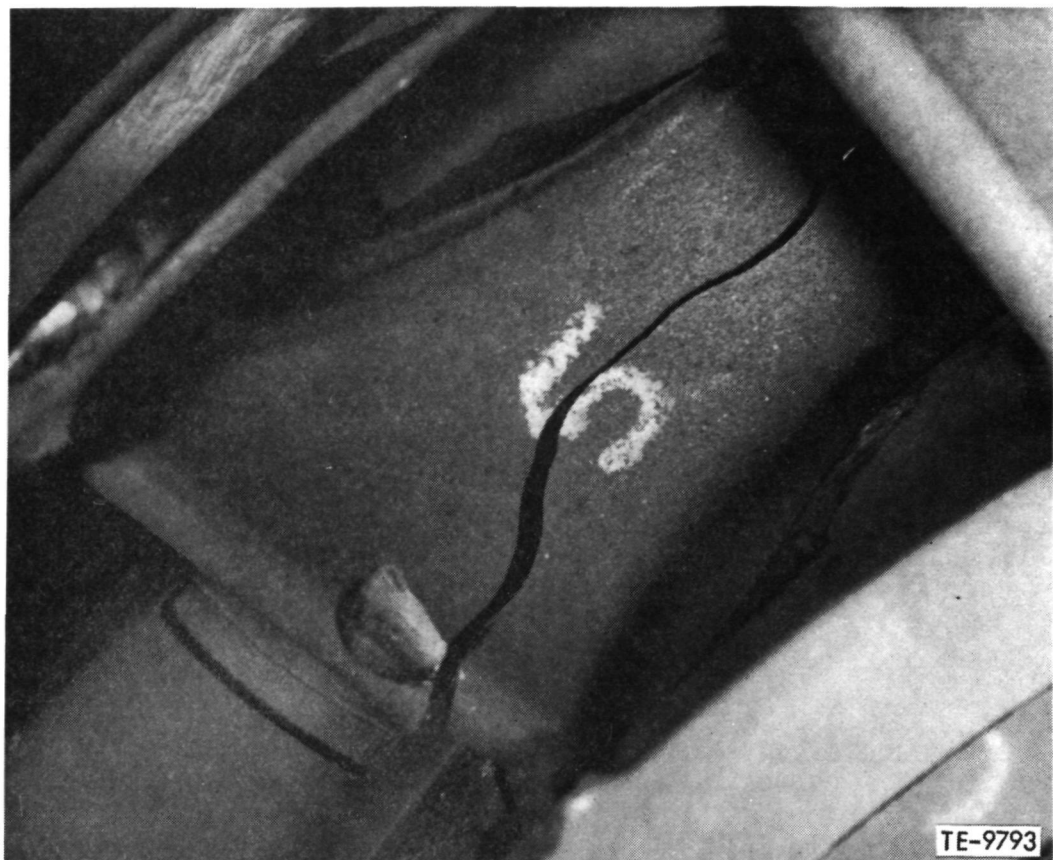


Figure 5. Failed silicon carbide vane.

of flaws or other material defects was found and no indication of load input from surrounding metal parts was evident on the failed vane. However, signs indicate that the plenum (which directs the burner outlet gas into the gasifier nozzle assembly) may have shifted position into the vane row at the location of the failed vane. The broken vane was replaced, the plenum shifting problem was resolved, and testing was continued without additional incidents.

At the end of Test 2, the electronic control T₆ thermocouples, which will be used to control the 1132°C (2070°F) and 1241°C (2265°F) engines, were installed in the engine and data were taken to correlate T₆ and T₄ temperatures. These data will be used to make the final trim adjustments and set up the first prototype T₆ control hardware.

Disassembly and inspection of the engine showed no evidence of distress in the ceramic vanes or regenerator components. Performance data analysis indicated that the compressor flow rate and the ceramic gasifier nozzle flow capacity did not match, so a new compressor system with a higher flow capacity was prepared for Test 3. The metal gasifier nozzle vane holder was further modified to reduce secondary leakage, and the engine was assembled.

ORIGINAL PAGE IS
OF POOR QUALITY

Test 3 - Test Stand Durability Testing of Improved Ceramic Gasifier Turbine Vanes and Regenerators and an Improved Compressor System

The engine accumulated 164 hours of test stand durability with the higher-flow compressor system and the ceramic components from Test 2. Table V summarizes the time accumulated by the ten vanes at the conclusion of Test 3. No distress in the vanes was evident.

TABLE V. SUMMARY OF TOTAL TEST HOURS FOR THE SILICON CARBIDE VANES IN ENGINE C-1, TEST 3

<u>Vane serial number</u>	<u>Total accumulated test hours</u>	<u>Comments</u>
232	1499	Carborundum 1st generation This vane has accumulated the most time of any of the SiC vanes
B6	823	Carborundum 2nd generation
B08	819	Carborundum 3rd generation
C29-7	398	
FX20234	293	
FX20235	293	Carborundum 4th generation
FX20242	293	
FX20249	293	
S1	293	Pure Carbon Co.
S3	293	(first Pure SiC vanes tested)

The total time accumulated by the ceramic regenerator components at the conclusion of Test 3 is shown in Table VI.

TABLE VI. SUMMARY OF TOTAL TEST HOURS FOR THE REGENERATOR COMPONENTS IN ENGINE C-1, TEST 3

<u>Regenerator disks serial number</u>	<u>Total accumulated test hours</u>	<u>Comments</u>
04	297	Corning 1100°C AS material
27	288	Corning 1000°F AS material
<u>Inboard seals serial number</u>		
H3032	302	Crossarm wearface 85% NiO/15% CaF ₂ with barrier layer
H3035	302	
<u>Outboard seals serial number</u>		
C479	2004	
C482	1994	

Engine C-2

During the reporting period engine C-2 accumulated 985 test hours, bringing the total engine test time to 1344 hours. Three ceramic gasifier turbine tip shrouds, thin-wall alumina silicate regenerators, and inboard regenerator seals with 85% NiO/15% CaF₂ crossarm wearface material were tested. All test activity was directed to test stand durability; it comprised the following four tests.

Test 1 - Test Stand Durability Testing of SiC Gasifier Tip Shroud and Ceramic Regenerators

This test program accumulated 964 hours of simulated truck cycle durability with a silicon carbide abradable gasifier turbine tip shroud, two thin-wall alumina silicate 1000°C (1832°F) material regenerators, and two inboard regenerator seals featuring a barrier layer crossarm wearface. Late in the testing, two thin-wall alumina silicate regenerators rated at 1100°C (2012°F) were installed along with two inboard seals featuring an 85% NiO/15% CaF₂ crossarm wearface with a barrier layer. Table VII provides a summary of the total time accumulated with the ceramic regenerator hardware at the end of Test 1.

TABLE VII. SUMMARY OF TOTAL TEST HOURS FOR REGENERATOR COMPONENTS IN ENGINE C-2, TEST 1

<u>Component and serial numbers</u>		<u>Total accumulated test hours</u>
Regenerator disks		
07 1000°C(1832°F)		3050
13 material		979
01 1100°C (2012°F)		85
02 material		74
Inboard seals		
H938 Barrier layer		949
H947 Barrier layer		1613
H3027 85% NiO/15% CaF ₂		74
H3028 85% NiO/15% CaF ₂		85
Outboard seals		
C490		1078
C491		977
C482		1697
C479		1707

The 1000°C (1832°F) high-time regenerator disk exhibited hot face deterioration. This disk had incurred numerous instances of secondary damage from debris from upstream incidences. It was retired at 3050 hours in favor of newer-composition core materials because it was showing progressive evidence of chipping--possibly the result of the secondary damage incidents.

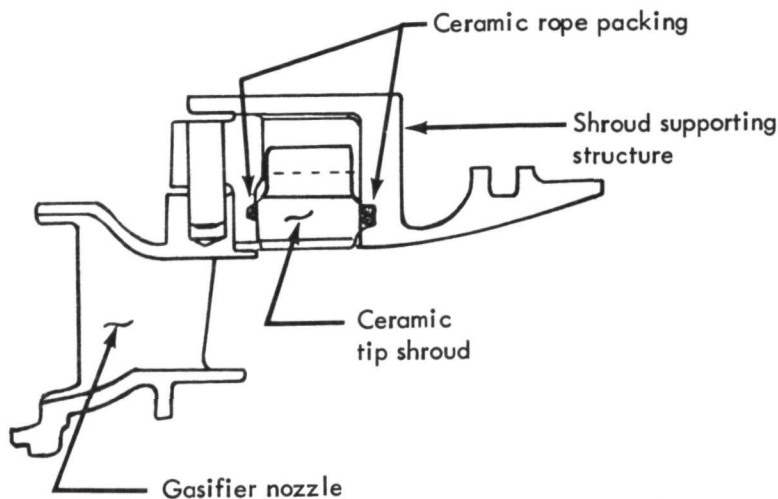
The seals were in good condition; their projected life is shown in Table IV. The 1100°C (2012°F) regenerators and 85% NiO/15% CaF₂ seals introduced late in the test were in excellent condition and were used in engine C-2 during Tests 2 and 3.

Although the abradable silicon carbide shroud was acceptable as a shroud ring structure, it was poor in terms of abradability. The shroud completed 964 hours during Test 1, bringing the total time to 985 hours with no evidence of distress. Ceramic rope packing was used to seal the front and aft faces of the shroud and prevent bypass leakage over the OD of the shroud. Figure 6 is a cross section of the 1900°F gasifier nozzle with a ceramic turbine tip shroud and the two ceramic rope packing seals. The ceramic rope packing is a 3M company alumina-boria-silica ceramic fiber and has exhibited excellent durability and sealing capability. After 985 hours of durability testing, no deterioration or shrinkage was evident in the rope packing and no loss in engine performance was noted during the test.

Engine C-2 was reconfigured with a new ceramic gasifier tip shroud made of lithium alumina silicate (LAS) with a foam cement abradable coating.

Test 2 - Test Stand Durability Test of LAS Gasifier Tip Shroud and Ceramic Regenerators

Engine C-2 accumulated 11 hours with one LAS tip shroud. The testing was divided into two builds and suffered from engine performance problems. The first build was a conservative approach, preventing a heavy gasifier rotor tip rub on the LAS shroud. A turbine tip clearance with the shroud was selected to give zero clearance at the worst known conditions. The poor engine performance was thought to have been caused by this clearance; therefore, another build was made with a larger-diameter turbine rotor which provided an interference condition of 1.52 mm (0.006 in.) at the worst known conditions.



TE-9795

Figure 6. Gasifier turbine nozzle with ceramic tip shroud and ceramic rope packing.

This configuration also resulted in poor engine performance, which raised questions about the porous foam cement ablatable coating on the shroud (see Figure 58, Section III).

The porous condition of the ablatable coating was suspected of allowing air to leak over the blade tips. To resolve that suspicion, a tip shroud which had been previously tested with acceptable engine performance was installed and tested (refer to the Test 3 discussion which follows).

The ceramic regenerator system utilized during Test 2 featured two 1100°C (2012°F) alumina silicate thin-wall regenerators and two inboard seals with 85% NiO/15% CaF₂ crossarm wearface material.

Test 3 - Test Stand Evaluation of Si₃N₄ Gasifier Tip Shroud and Ceramic Regenerators

Engine C-2 accumulated 10 hours with one Si₃N₄ gasifier tip shroud to evaluate engine performance problems previously encountered with an LAS gasifier tip shroud. The Si₃N₄ tip shroud had been previously tested with satisfactory engine performance. The performance results with the Si₃N₄ shroud were similar to those with the LAS shroud. To ensure that the ceramic regenerator parts were not involved in the performance problems, the entire set of regenerator parts was replaced with parts from engine C-1 which were known to have good leakage control. This change did not provide a performance improvement. A tracer powder was injected into the secondary path of the engine to determine where primary leakage was occurring. A flame spray grade (99.9% pure, -325 mesh) yttrium oxide powder was injected into the engine operating at 100% speed conditions. Subsequent disassembly and observation of the powder revealed several block cracks in a location which allowed compressor discharge air to leak into the engine exhaust. The block had been modified in the area where it had cracked, and the modification had weakened the structure enough to cause the cracks. The engine block will be replaced and test programs will continue. Table VIII summarizes the total test hours accumulated by the ceramic shrouds and regenerators used in Tests 2 and 3.

At the end of the reporting period the engine was being reconfigured to evaluate a new engine block cooling design which is required for operation at 1132°C (2070°F) turbine inlet temperatures.

COMPONENT RIG STATUS

The objective of the rig test program is to qualify all ceramic parts before engine testing. Any ceramic part deemed acceptable by NDE inspection is rig tested to conditions which simulate the most severe engine operating environment for that part. If the part passes the rig test and subsequent inspection, it has qualified for engine test.

During the reporting period, rig test activities included ambient and hot spin pit testing of various ceramic blade coupons and compliant layer materials, burner rig testing of ceramic gasifier turbine vanes and shrouds, and hot regenerator rig tests of ceramic disks and seal.

Table IX summarizes the number of ceramic components rig tested and those that qualified for engine testing.

TABLE VIII. SUMMARY OF TOTAL TEST HOURS FOR SHROUDS AND
REGENERATORS IN ENGINE C-2 AFTER TESTS 2 AND 3

<u>Component</u>	<u>Total accumulated test hours</u>
Gasifier turbine tip shrouds	
LAS shroud	11
Si ₃ N ₄ shroud	113
Regenerator system	
Disks	
Serial numbers	
01	110
02	98
Inboard seals	
Serial numbers	
H3027	95
H3028	106
Outboard seals	
Serial numbers	
C490	1099
C491	997

The special development inboard regenerator seals rig tested included parts with alternate methods of attaching the crossarm wearface to the substrate, a seal with an experimental salvage technique used to replace the crossarm wearface, and a seal modified to feature the crossarm leaf structure designed for the 982°C (1800°F) regenerator seals.

TABLE IX. CERAMIC COMPONENT RIG TEST SUMMARY

	<u>Number rig tested</u>	<u>Number qualified for engine testing</u>
Ceramic blade coupons		
Cold spin test - SiC coupons with compliant layer		
L605	1	
347SS	1	Tested to failure
IN 600	1	
Hot spin test - SiC coupons with compliant layer		
L605	1	Tested to failure
347SS	1	
Cyclic hot spin test - SiC coupons*		
with compliant layer		
L605	1 SiC coupon	
IN-600	5 compliant layers	
347SS	1 SiC coupon 3 compliant layers 1 SiC coupon 3 compliant layers	
Gasifier turbine vanes		
SiC - Carborundum	19**	0**
SiC - Pure Carbon	4	4
Gasifier turbine shrouds		
LAS - Corning	2	2
Alumina silicate regenerators		
Thin wall 1000°C(1832°F)	2	2
Thin wall 1100°C(2012°F)	4	4
Magnesium alumina silicate regenerator	1	0
Inboard regenerator seals	6	6
Special development seals	6	0

*The cyclic hot spin tests were not to failure speed. The objective was to determine compliant layer thinout. The L605 layer was superior, surviving 2500 cycles.

**These were NDE rejects tested to correlate NDE results to test results.

III. MATERIALS BEHAVIOR AND CHARACTERIZATION

INTRODUCTION

The objectives for this reporting period included the development of an experience base with ceramic materials, through laboratory testing and analysis, needed to support the design, inspection, and testing of ceramic components. Activities of work performed for this period included:

- o Examination of Pure Carbon Co. reaction-bonded silicon carbide materials for material characterization studies
- o Establishing the relationship between microscopic matrix structure and strength for the current alumina silicate regenerator disk material
- o Completion of the preliminary evaluation of the thermal stability of the new 1100°C (2012°F) alumina silicate matrix material
- o Completion of characterization studies of the second generation abradable seal materials
- o Nondestructive evaluation of the initial quantities of each of the 2070°F engine components
- o Continuation of development of new flaw detection techniques (reflective ultrasound, photoacoustic spectroscopy, and acoustic microscopy)

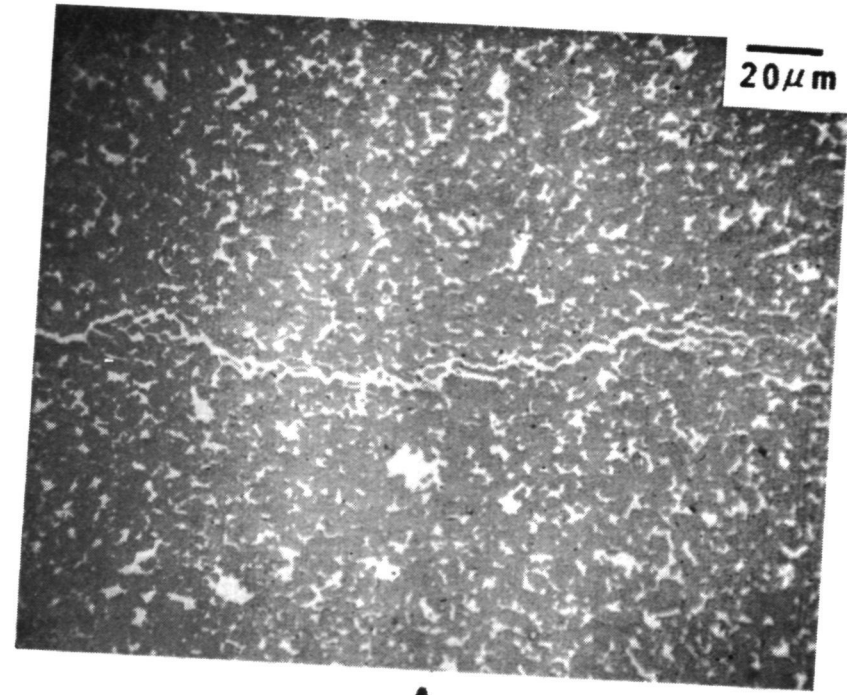
CHARACTERIZATION OF PURE CARBON SiC

A preliminary characterization effort directed at two Pure Carbon Company reaction-bonded silicon carbide (RB SiC) materials--one a slip cast product, the other an extruded product--has been completed. Material microstructure, strength characteristics, and oxidation behavior have been examined. The results of the preliminary investigation are described in this section.

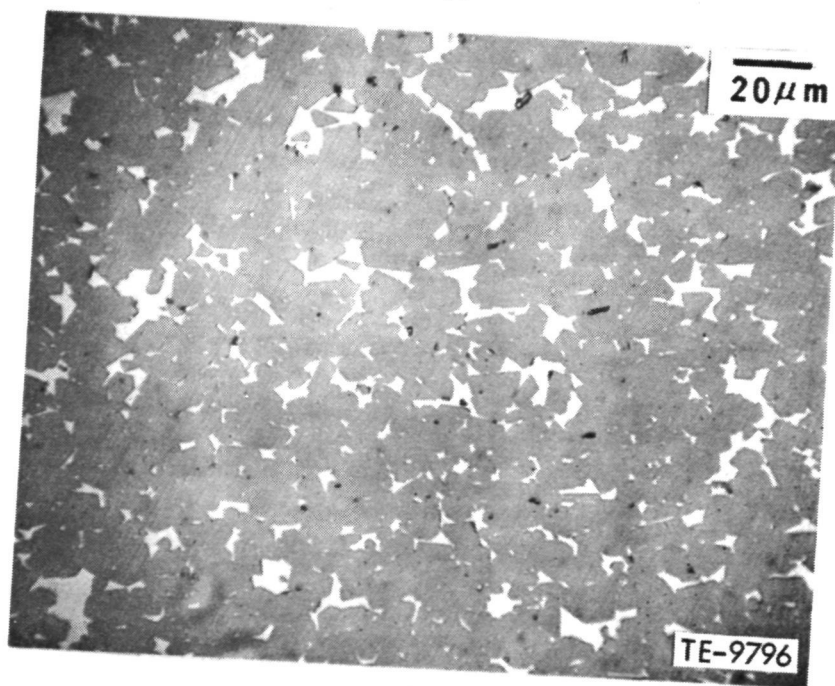
Microstructure

Pure Carbon's RB SiC materials have a microstructure consisting of a network of equiaxed SiC grains surrounded by free silicon. The detail of the microstructure is quite different for each of the two fabrication processes. The slip-cast reaction-bonded silicon carbide has a very fine-grained structure. The average grain size is 3.5 microns. The structure is generally uniform throughout. Occasionally, however, a thin lamination of free silicon is located 400-500 microns below the as-fired surface (Figure 7A). On the other hand, the extruded material has a much larger grain size as shown in Figure 7B. In this case the average silicon carbide grain diameter is approximately 11.6 microns or three times that found in the slip-cast product. The as-fired surface of the extruded material has, however, a silicon-rich layer approximately 300 microns in thickness, as shown in Figure 8.

The as-fired surface structure of both the slip-cast and extruded materials is quite similar. Figure 9 shows typical examples. Microprobe analysis shows barium and sulfur to be present in addition to silicon, along with small amounts of calcium and aluminum. The impurities tend to be concentrated in glassy puddles which are quite commonly found over the entire as-fired surface.



A



B

Figure 7. Microstructure of Pure Carbon reaction-bonded silicon carbide slip-cast (A) and extruded (B). White areas are free silicon.

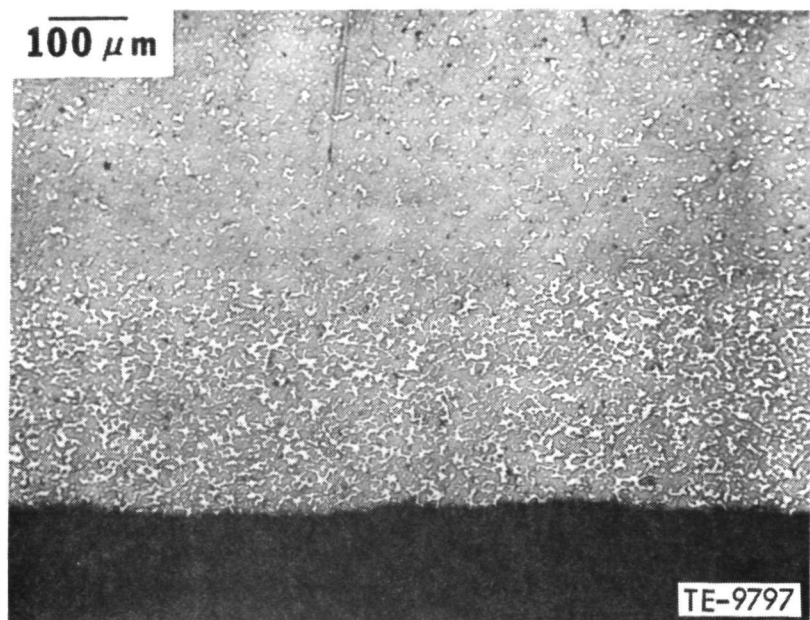


Figure 8. Photomicrograph of extruded Pure Carbon reaction-bonded silicon carbide showing a silicon-rich surface layer.

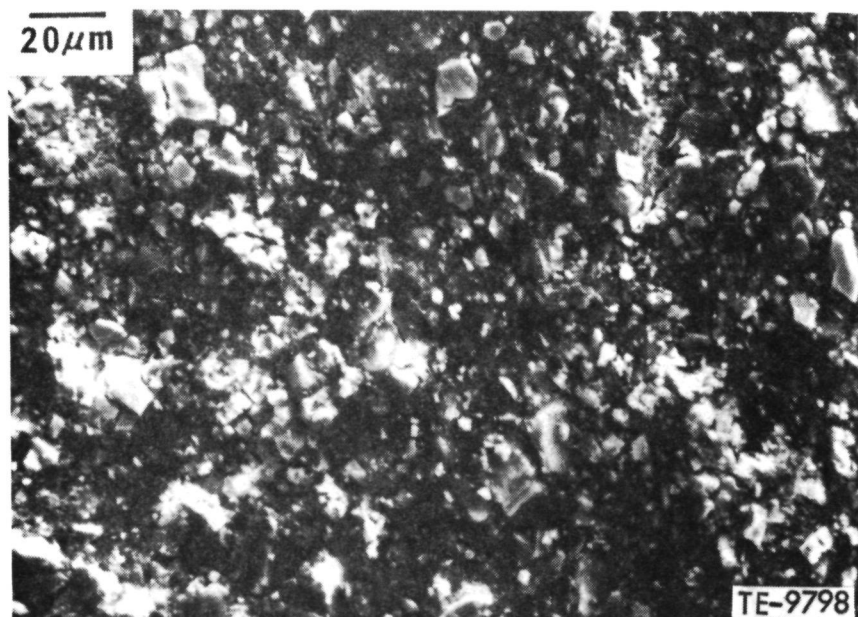


Figure 9. Surface structure of as-fired, slip-cast Pure Carbon reaction-bonded silicon carbide.

ORIGINAL PAGE IS
OF POOR QUALITY

Strength Characteristics

The bend strengths of the Pure Carbon extruded and slip-cast materials are summarized in Table X.

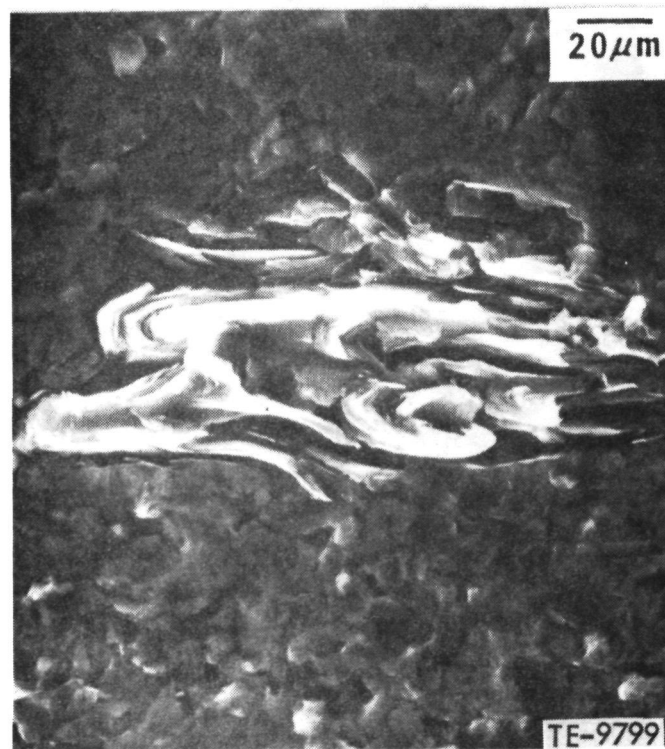
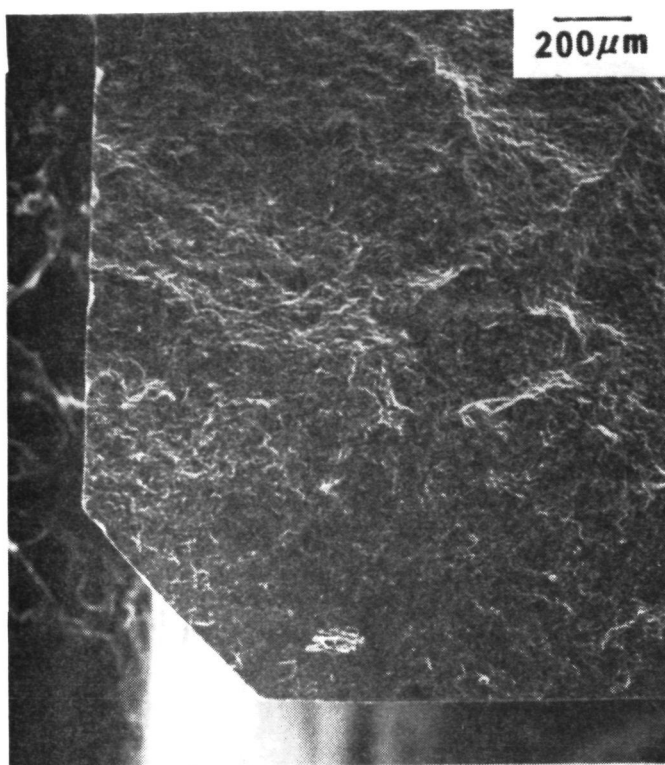
TABLE X. STRENGTH OF PURE CARBON REACTION-BONDED SILICON CARBIDE MATERIAL

<u>Material</u>	<u>No. Specimens</u>	<u>MOR, MPa(ksi)</u>	<u>Std. Dev, MPa(ksi)</u>
Slip Cast			
As Fired	29	266 (38.7)	50 (7.3)
Machined	10	469 (68.0)	78 (11.3)
Extruded			
As Fired	30	307 (44.5)	49 (7.1)
Machined	10	431 (62.5)	36 (5.2)

The strength for the as-fired surface condition of the slip-cast and extruded materials were 264 MPa (38.7 ksi) and 307 MPa (44.5 ksi), respectively. In the case of the slip-cast material, failure generally originated at the surface. The most common strength-controlling defects were glassy puddles. Failure also originated, on occasion, from silicon-filled subsurface laminations containing iron silicide particles. Such laminations become strength controlling when microporosity is associated with the iron silicide.

Failure also originated from surface sites for the extruded material. The strength-controlling defect in all cases was glassy puddles. The difference in strength between these two materials (significant at the 0.05 level) must be associated with differences in grain size and silicon content.

The average strength of the machined surface condition was similar for both materials (no difference exists at a 0.05 significance level). The slip-cast material failed exclusively from surface sites, presumably from machining flaws since no unusual microstructural feature could, in general, be associated with a given origin. However, in the case of the extruded material, failure originated at the surface and subsurface sites. Surface failures were associated with machining defects, whereas subsurface failures originated from carbon particles. A typical example of a subsurface origin is shown in Figure 10.



ORIGINAL PAGE IS
OF POOR QUALITY

Figure 10. Fracture surface of extruded, reaction-bonded silicon carbide showing a carbon particle at the failure origin.

Oxidation

The effect of oxidation at 1250°C (2282°F) was evaluated in preliminary fashion. Samples of each surface finish were exposed for 100 hours in ambient air. After exposure, changes in surface structure and the resulting effect on materials strengths were investigated.

After exposure, the surface of the as-fired, slip-cast material was covered by a crazed glass. Very large circular spots of approximately 2-mm (0.078 in.) diameter are visible in Figure 11. The oxide layer, in addition to silicon and oxygen, contains barium, calcium, and aluminum. An acicular phase which is free of barium was distributed throughout the oxide. The large glassy puddles generally contained high levels of calcium. Iron silicide was often present directly beneath the glassy bubbles.

The machined and oxidized slip-cast material was covered with a crazed oxide with numerous hills and bumps (Figure 12). These bumps contained high levels of calcium. No barium was found in the surface oxide, however.

The oxidized surfaces of both the as-fired and ground extruded material were similar to those found on the slip-cast material (Figure 13).

The change in strength after a 100-hour exposure for both the as-fired and ground surface conditions is summarized in Table XI.

TABLE XI. OXIDATION EFFECT ON STRENGTH OF PURE CARBON RB SiC MATERIALS*

<u>Material</u>	<u>No. Specimens</u>	<u>MOR, MPa(ksi)</u>	<u>Std. Dev, MPa(ksi)</u>
Slip Cast			
As Fired	5	277 (40.1)	87 (12.7)
Machined	5	424 (70.2)	87 (12.7)
Extruded			
As Fired	5	356 (51.6)	87 (12.7)
Machined	5	421 (61.1)	30 (4.4)

*100-hour exposure in ambient air at 1250°C (2282°F).

No significant change in strength occurred in either material regardless of surface finish. The as-fired and ground slip-cast materials failed exclusively from surface sites, either glassy puddles (Figure 14) or large grain (Figure 15). The extruded material also failed from surface sites, either glassy puddles in the case of an as-fired surface or oxidized bumps for ground surface (Figure 15).

CHARACTERIZATION OF REGENERATOR MATRIX MATERIALS

The regenerator core strength determination is particularly crucial because of the relatively low strength of alumina silicate, the complex structure of its triangular matrix, the thin cell walls [approx 0.089 mm (0.0035 in.)], and the necessity to establish strength parameters which can lead to effective nondestructive inspection techniques.

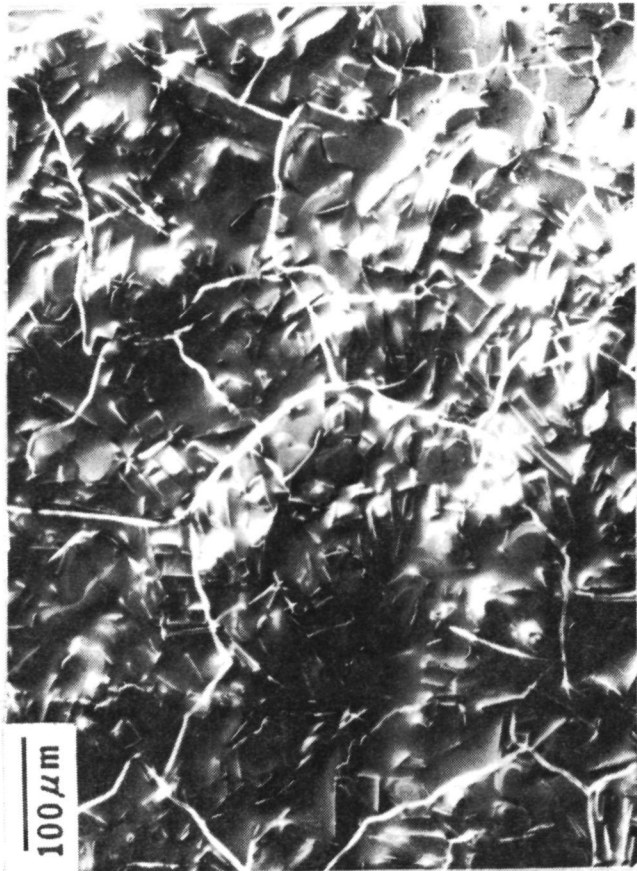
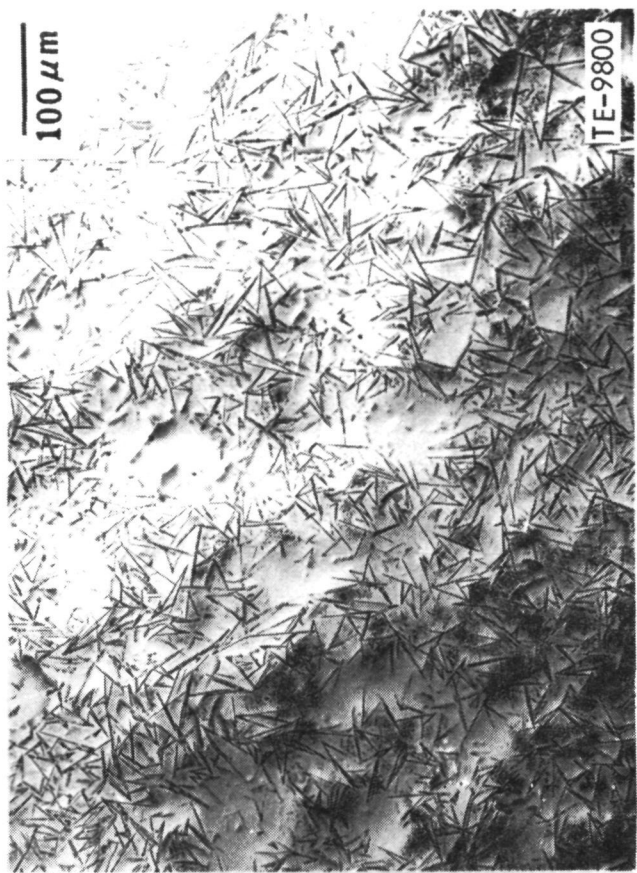
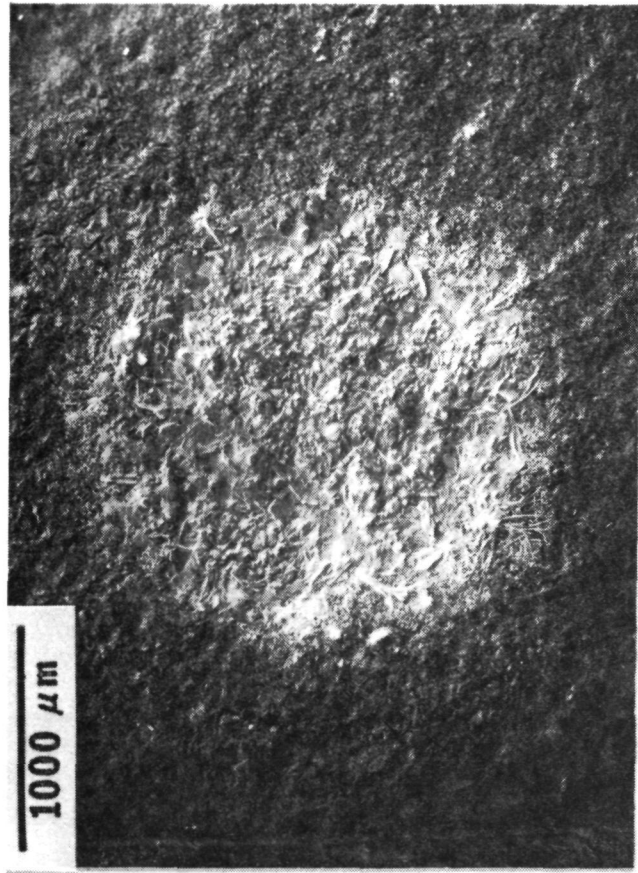


Figure 11. Surface structure of as-fired, slip-cast, reaction-bonded silicon carbide after exposure at 1250°C (2282°F) for 100 hours.

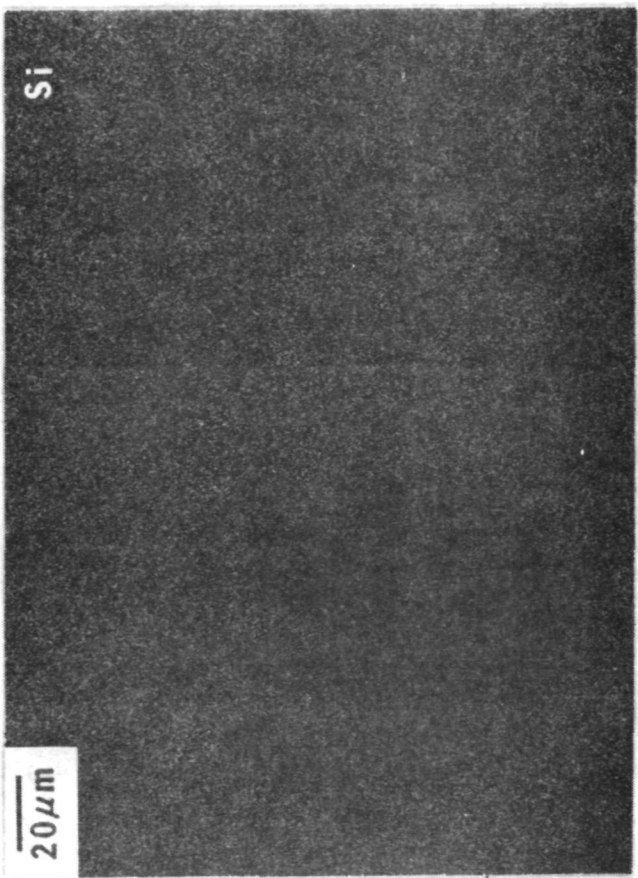
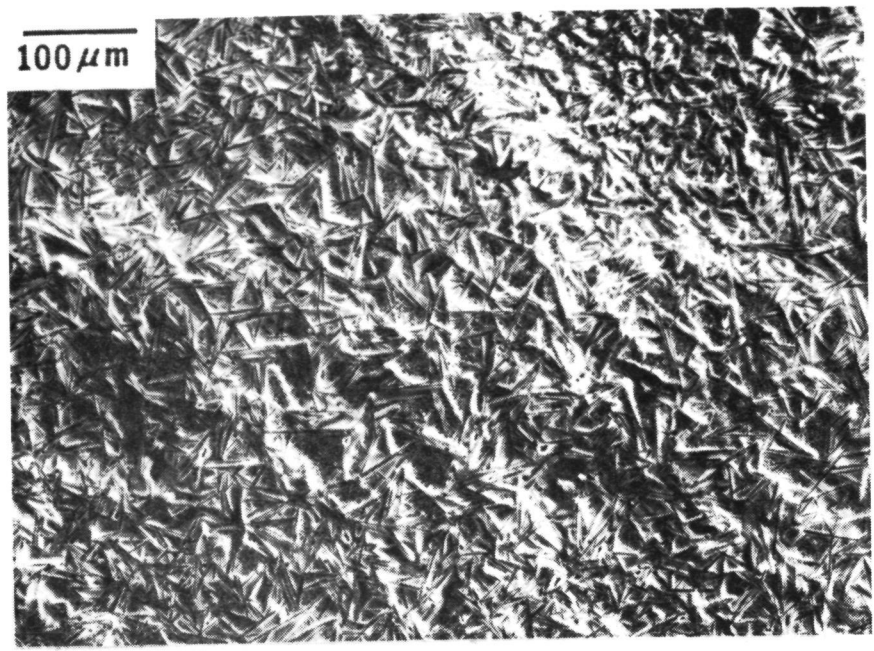
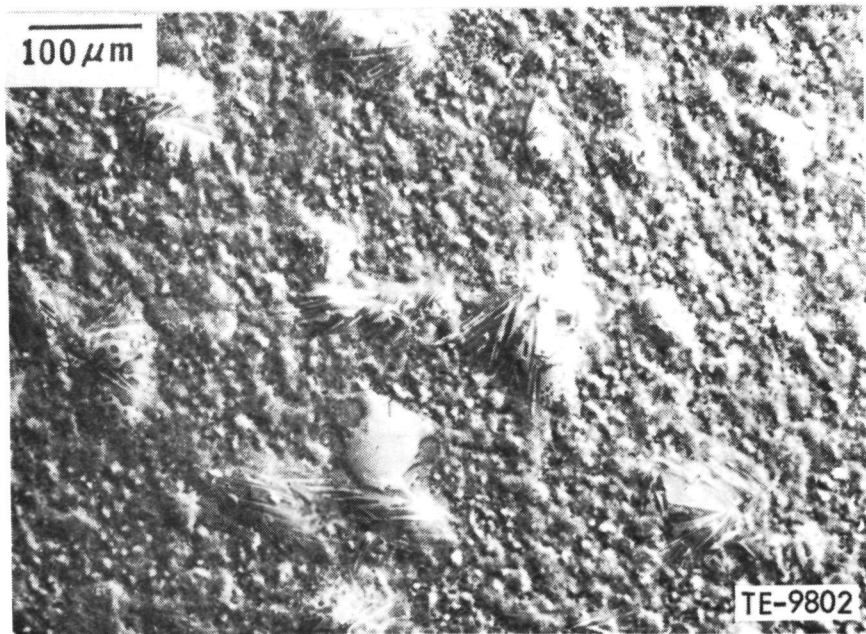


Figure 12. Surface structure of slip-cast and ground Pure Carbon RB SiC after exposure at 1250°C (2280°F) for 100 hours.



A



B

Figure 13. Surface structure of as-fired (A) and ground (B), extruded Pure Carbon RB SiC after exposure at 1250°C (2282°F) for 100 hours.

ORIGINAL PAGE IS
OF POOR QUALITY

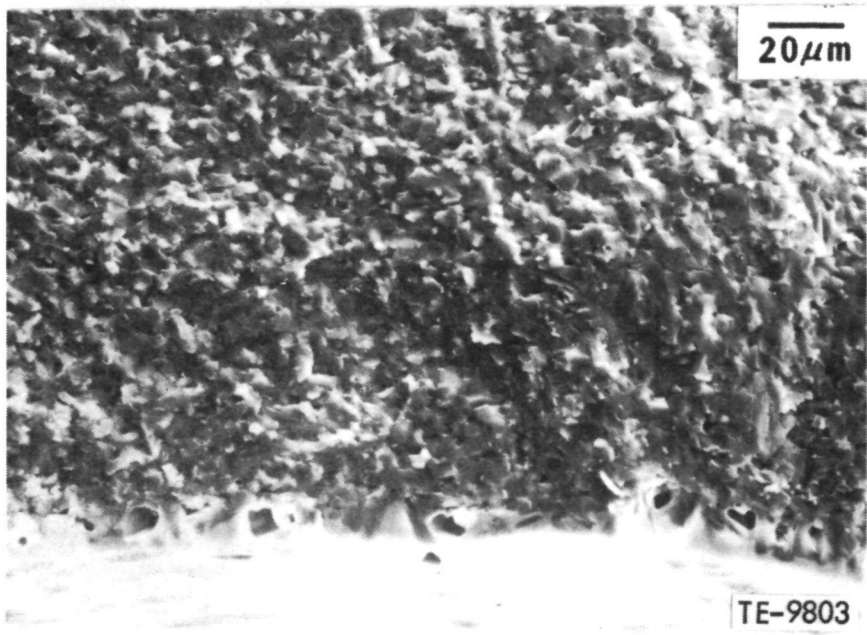
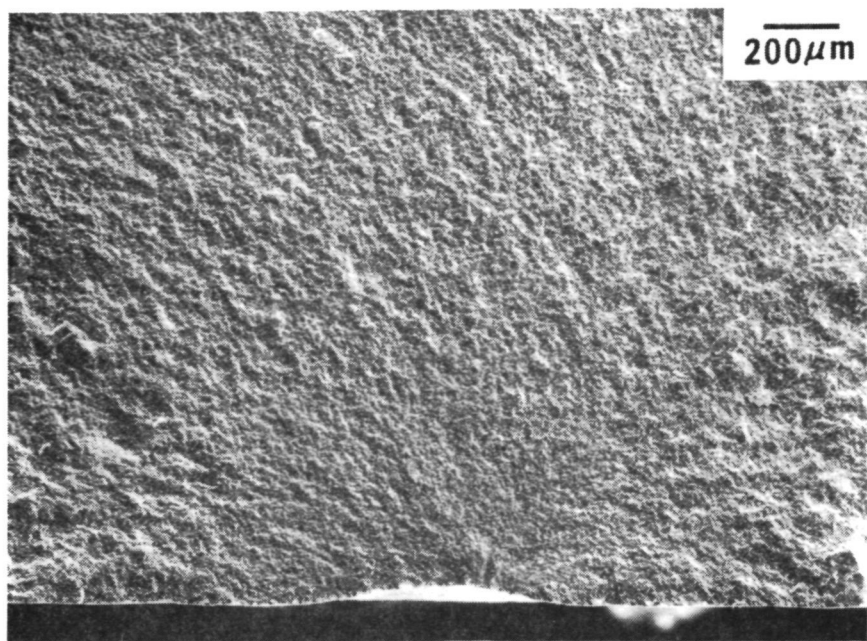


Figure 14. Fracture surface of slip-cast, oxidized Pure Carbon RB SiC showing glassy puddle at failure origin.

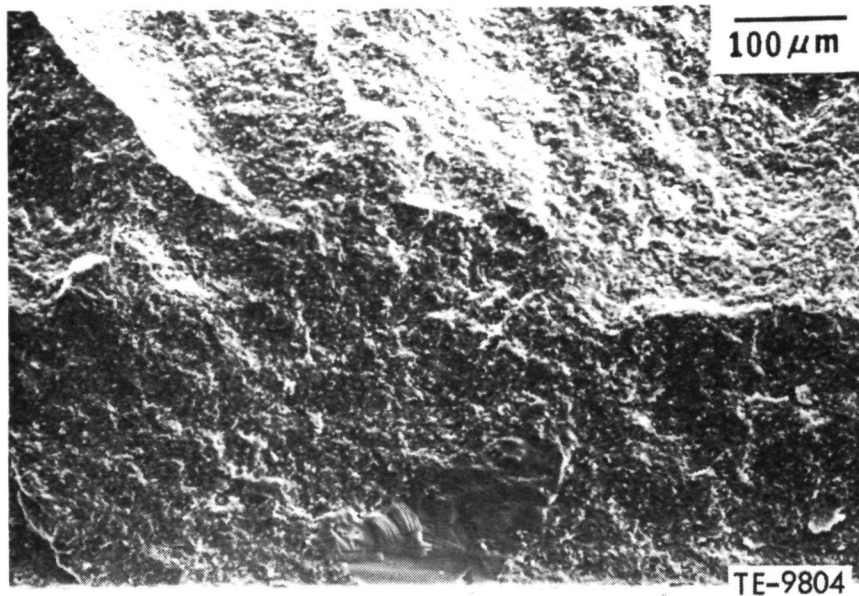


Figure 15. Photomicrograph of fracture surface of slip-cast, oxidized Pure Carbon RB SiC showing large grain at failure origin.

The as-received strength distribution of the current (1000°C) alumina silicate (AS) matrix material was established. Further, the effect of channel skew angle, cell distortion, and separator wall thickness on strength characteristics was examined. Finally, a preliminary evaluation of the strength and thermal stability of the new (1100°C) AS material was completed.

Alumina Silicate Matrix Strength

The results, in terms of disk-to-disk variation in MOR, for the as-received 1000°C (1132°F) AS material are summarized in Table XII. The values tabulated are for the mean MOR minus two sigma (-95% confidence limit) for the single variable correlation of channel skew angle and MOR. (The lower two sigma limit was used whether a significant correlation was shown or not.) Three important points are indicated by the tabulation. First, the possibility of two disk groups is indicated; disks 1, 2, 3, and 5 range from a high minimum of 1724 kPa (250 lb/in.²) to a low minimum of 800 kPa (116 lb/in.²) whereas disks 4 and 6 have a range from 855 kPa (124 lb/in.²) to 255 kPa (37 lb/in.²). Second, the intradisk strength variation is smaller than the interdisk variation. Third, while the intradisk strength variation is small, the location of the failure, in both cases, occurred in the indicated area of minimum strength, showing that the intradisk strength variation is significant with respect to practical stress levels.

As part of a major effort to establish the cause, or causes, for the failure of disk GM 15-05 (disk 6) in the regenerator test rig, the effects on strength of separator wall thickness, channel skew angle, and cell distortion at different radial positions were examined.

TABLE XII. 1000°C (1832°F) AS MATERIAL MATRIX VARIABILITY

	Sample radius, cm (in.)				
	30.5 (12.0)	25.4 (10.0)	20.3 (8.0)	15.2 (6.0)	10.2 (4.0)
<u>Disk</u>	<u>MOR, mean -2σ, kPa (1b/in.²)</u>				
1. HRD-AB-1	999 (145)	1069 (155)	999 (145)	979 (142)	1013 (147)
2. HRD-AB-2	1344 (195)	1186 (172)	1551 (225)	1227 (178)	1282 (186)
3. HRD-AB-3	Not available	1448 (210)	1724 (250)	1276 (185)	1379 (200)
4. GM 14A-23	Not available	552 (80)	793 (115)	655 (95)	{ 255 (37)}
5. HRD-AB-5	1317 (191)	876 (127)	800 (116)	816 (119)	1089 (156)
6. GM 15-05	{0-349 (0-50)*}	552 (80)	779 (113)	931 (118)	855 (124)

*Calculated; all other data are measured values.

The radii which correspond to the failure are marked { }. Disks identified as "HRD-AB-" are randomly selected; those designated "GM" are disks failed in the regenerator rig testing.

The first step was to test the MOR data for approximation of a normal distribution before proceeding with the analyses which depend on this approximation to predict, with reasonable confidence, the values of the three variables. The statistic K_3 , which is a measure of the skewness of a distribution, was calculated for two different cell sizes and varied from 0.084 to -0.053, giving a confidence level considerable better than 0.01 that the distribution is essentially normal. A multiple regression analysis was then performed, using wall separator thickness and skew angle as variables.

$$y = 1644.5 + 11.942.1x_w - 111.1x_s \quad (y = 238.5 + 43.3x_w - 16.1x_s)$$

y = modulus of rupture

x_w = mean separator wall thickness

x_s = channel skewness

This analysis shows that while both variables are significant, the separator wall thickness dominates the relation. Accordingly, a single regression equation relating the mean (for each test bar) separator wall thickness to MOR was calculated. The results are shown in Figure 16. The critical factor is the slope or regression coefficient of 76 560 kPa/mm (277.6 lb/in.²/in $\times 10^3$), indicating how sensitive the strength is to wall thickness in the matrix structure.

The grouping of the symbols for four radii illustrates the point that wall thickness varies with the radius; the thinnest wall at the outer radius is 25.4 cm (10.0 in.). Single regression equations were calculated for each of the axial positions, correlating the mean separator wall thickness and the radius. The regression line is plotted for all six axial positions - one is

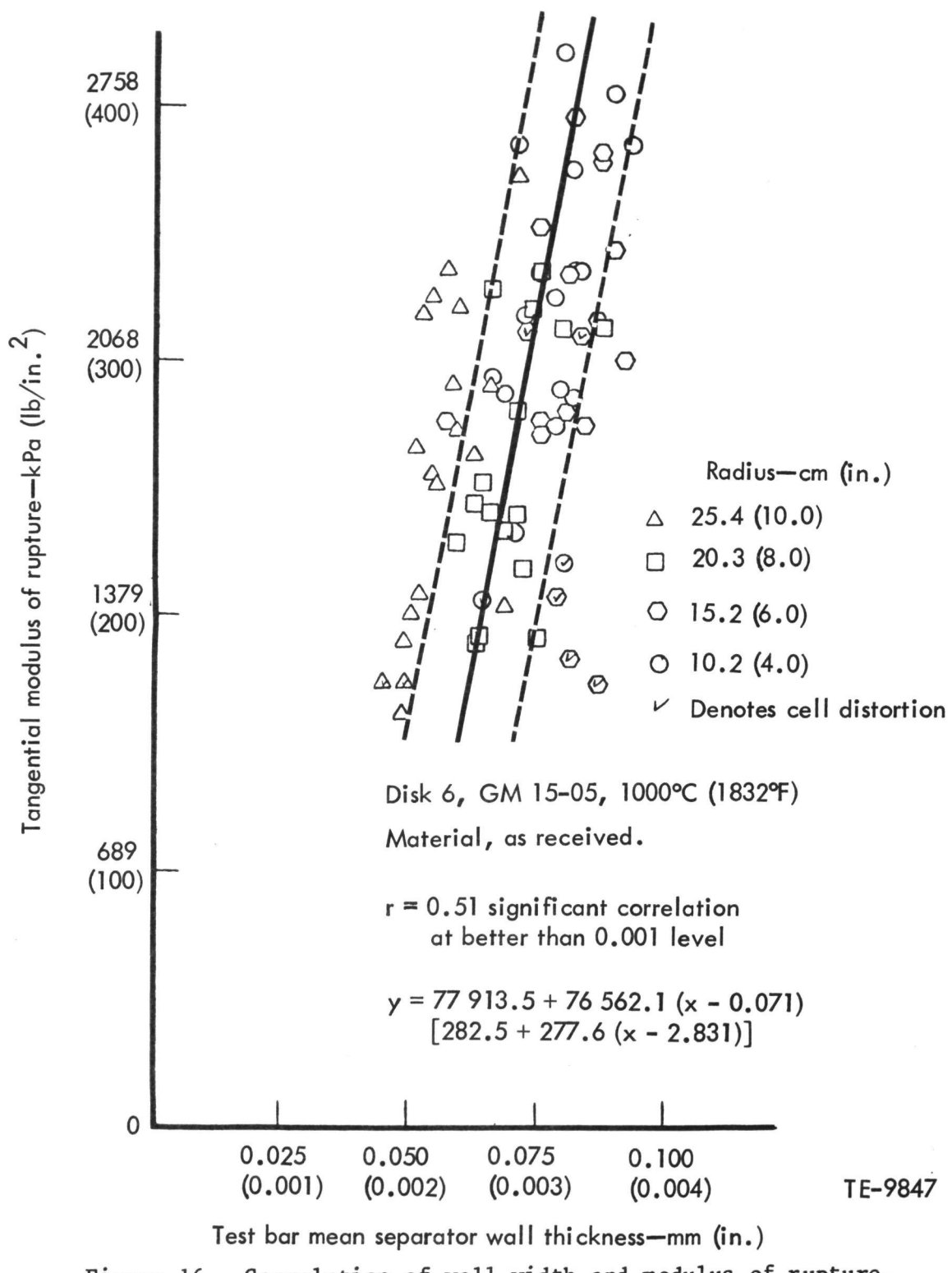


Figure 16. Correlation of wall width and modulus of rupture.

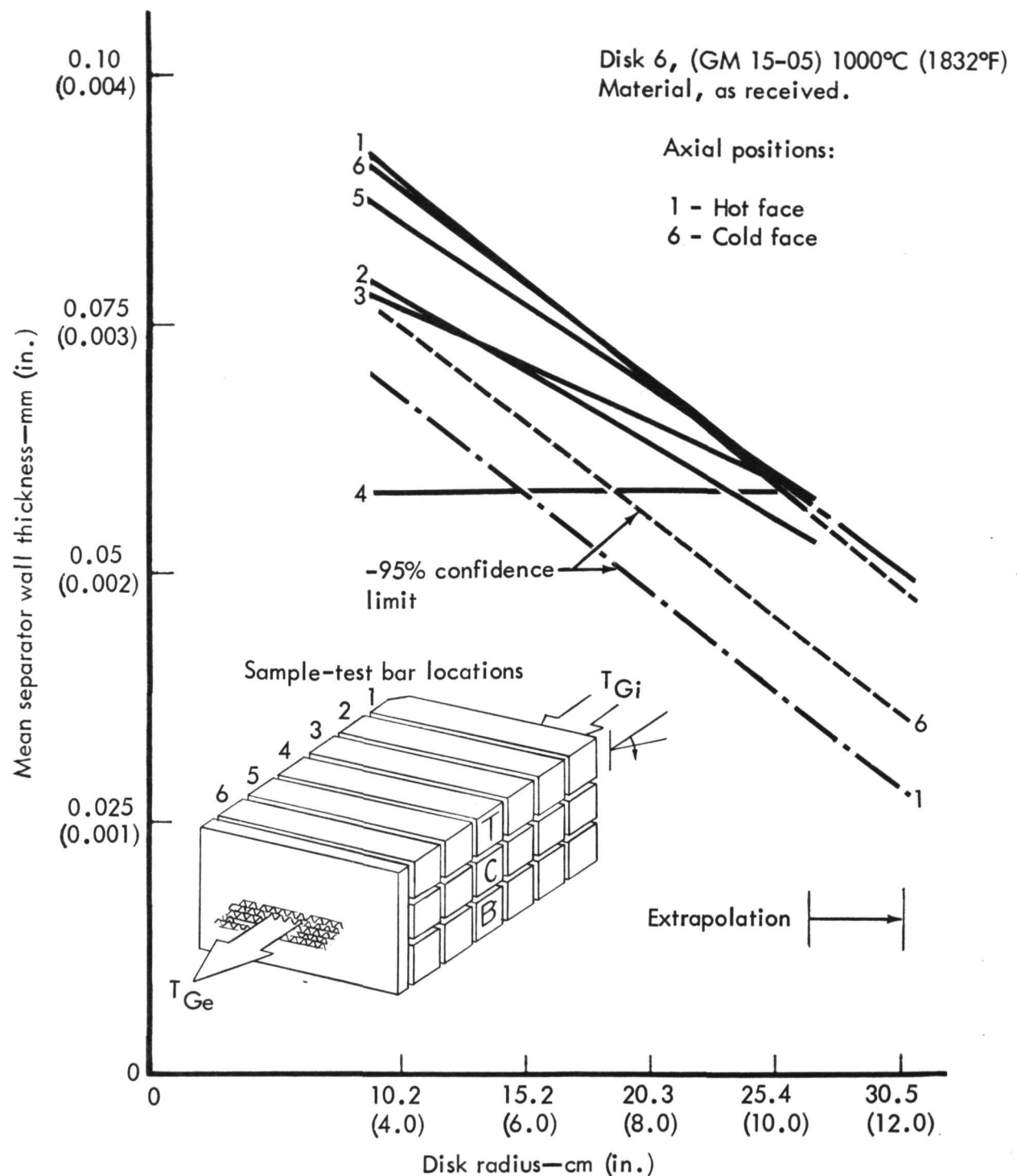
the hot face, six the cold face - with position four shown as a mean since the correlation significant level is below 0.10. In addition the minus 2σ (95%) limits are plotted for one and six (Figure 17). The mean line for the hot face extrapolated to 30.5 cm (12.0 in.) gives a wall thickness of 0.05 mm (0.002 in.) and an estimated strength of 358 kPa (52 lb/in.²) from Figure 16. The minus two sigma values have a probable wall thickness of 0.04 mm (0.0016 in.) and zero strength, extrapolated to the radius of the failure. The effect of cell distortion in either the overall correlation in Figure 16 or the correlation of wall thickness and MOR for the 25.4-cm (10.0 in.) radius is not significant.

Still incomplete multiple regression analyses of disks 1 and 5 have demonstrated that the effect of separator wall thickness is present in both MOR distributions. Interestingly enough, the channel skew angle is the dominant variable in disk 1, while the wall thickness is most important in disk 5.

Strength and Thermal Stability of the 1100°C (2012°F) AS Material Matrix

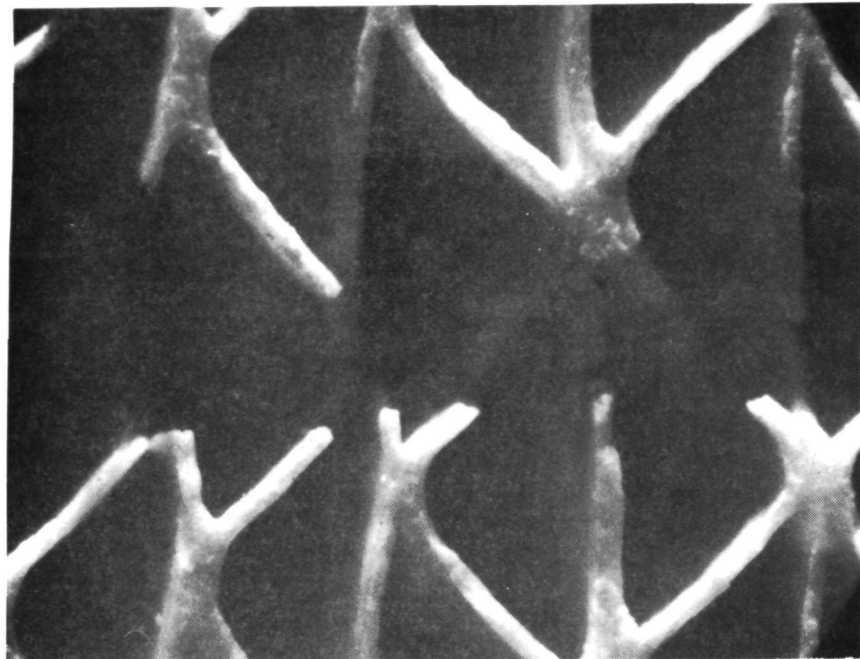
An improved alumina silicate (AS) thin-wall matrix material, rated at 1100°C (2012°F), was tested for MOR strength distribution, using the same techniques and approach used for the 1000°C (1832°F) matrix. The range of channel skew angles was well within the range seen in the 1000°C (1832°F) material (0.5 to 9.5°), and the sample cell distortion was zero while the separator wall thickness was slightly greater, with smaller variation, than that of disks 5 and 6 of the 1000°C (1832°F) material. The strength range, however, was much higher: Disk 5, 2097-1015 kPa (304-147 lb/in.²) and disk 6, 2792-1118 kPa (405-162 lb/in.²) for the 1000°C (1832°F) material as opposed to 4220-2271 kPa (612-329 lb/in.²) for disk 1 of the 1100°C (2012°F) matrix. Even though the range of strengths in the 1100°C (2012°F) disk is greater than that of the 1000°C (1832°F) material, the absolute level is high enough; relative to the probable stress, the lowest strength level is still very high. As yet incomplete statistical analyses indicate that the small increase in wall thickness does not account for the 85% increase in MOR for the 1100°C (2012°F) material. The fracture pattern in the 1100°C (2012°F) material is noticeably different; a very high percentage of the joint areas between the sinusoidal wall and the separator strips is involved. Figure 18 compares the macrofractography of a typical 1000°C (1832°F) test bar fracture and 1100°C (2012°F) fracture.

The comparison of resistance with thermal exposure of the 1000°C (1832°F) and the 1100°C (2012°F) rated materials is very difficult to relate to thermal exposure in the engine. A direct measurement of the improvement is to measure the permanent change in length ($\Delta L/L$) and plotting this against $1/T_{abs}$. This change in length is a measurement of the rate of phase transformation of aluminous keatite structure to the thermodynamically stable mullite and is practically useful since it can be related to the concurrent increase in the thermal coefficient of expansion--the cause of thermal stress cracking and fracture. Two disks, numbers two and five of the 1000°C (1832°F) material, were thermally exposed for ten hours to obtain some idea of the interdisk variability within a given material. The 1100°C (2012°F) material data are plotted for comparison in Figure 19. Considering the fact that disks 2 and 5 are separated in time by approximately a year, the indicated reproducibility is quite good.



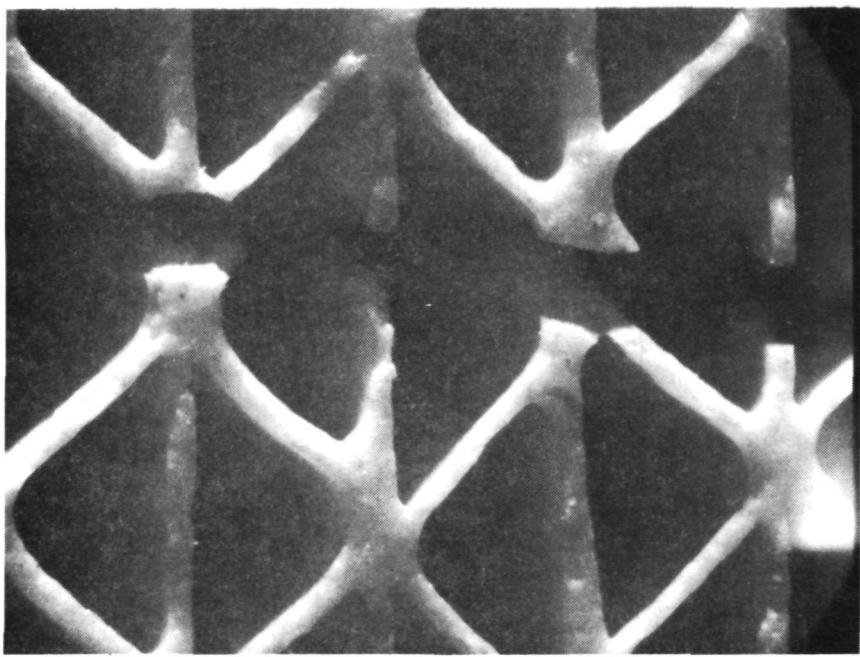
TE-9848

Figure 17. Correlation of mean separator wall thickness and disk radius.



Disk 6, HRD-AB, 1000°C (1832°F)
material; radius = 30.5 cm
(12.0 in.)

TE-9849



Disk 1, HRD-AC, 1100°C (2012°F)
material; radius = 30.5 cm
(12.0 in.)

Figure 18. Fracture comparison in typical test bars. (32X)

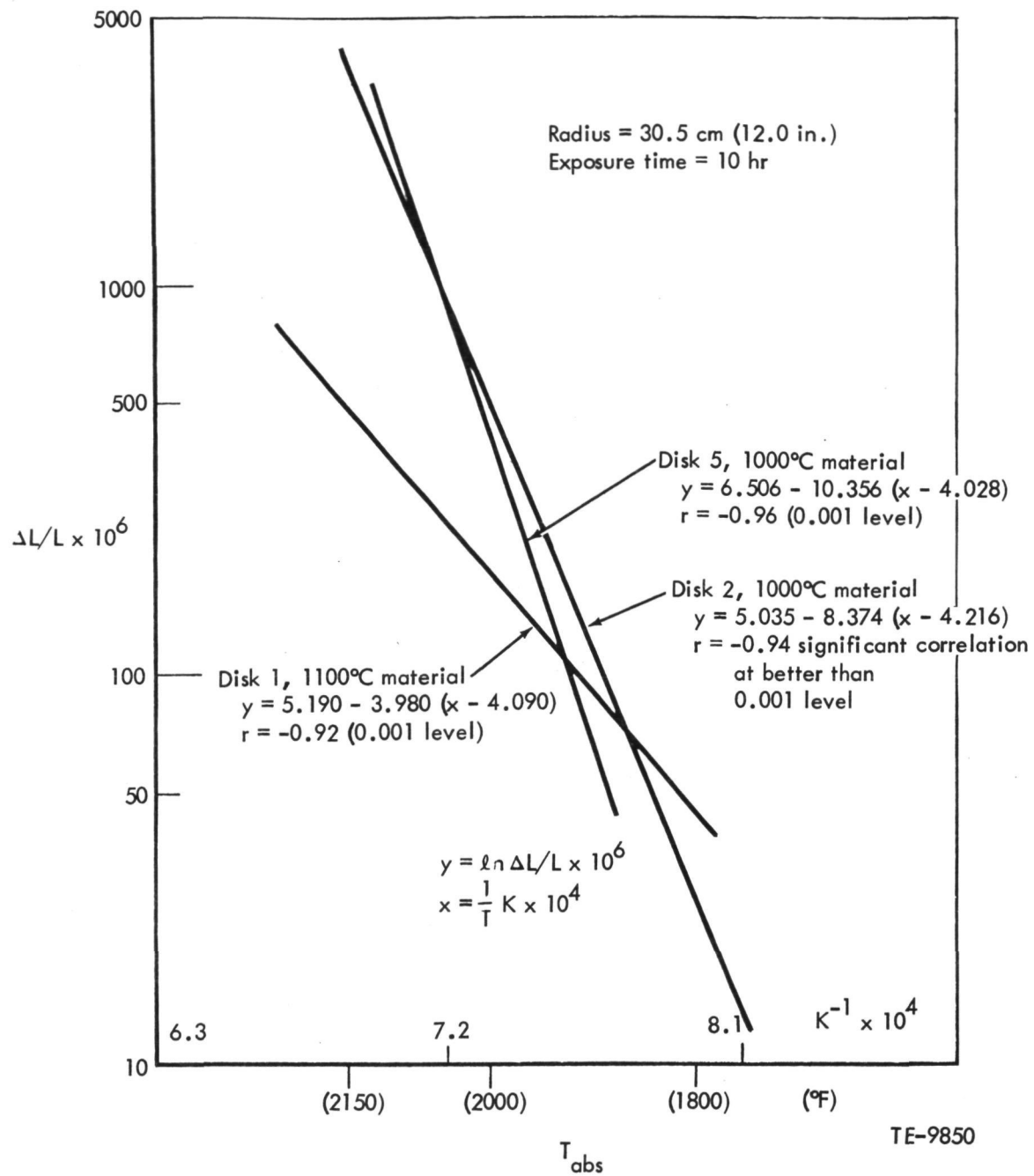


Figure 19. Comparison of phase transformation rate of 1000°C (1832°F) and 1100°C (2012°F) alumina silicate matrix materials.

The small spread in regression coefficient evident in the two 1000°C (1832°F) disks allows a high degree of confidence in evaluating the reduction in sensitivity to temperature level offered by the 1100°C (2012°F) matrix material, which is shown on the same plot. The quantitative comparison is shown by the reduction in regression from -10.4 and -8.7 to -4.0. There is a small increase in $\Delta L/L$ at the 1000°C (1832°F) level from 12 to 48 ppm for the 1100°C (2012°F) matrix, which is believed to be insignificant, while the increasing stability shown at temperatures above 1050°C (1925°F) includes the temperature critical acceleration cycles in engine application.

In the previous six-month report, the possibility of long-term changes in sample lengths at ambient storage conditions was raised. Analysis of the data has established that the apparent changes in length over extended periods of time are traceable to time drift in the measuring system calibration. The effect of this drift can be limited to approximately the reproducibility of the system (2-3 ppm) by shortening the interval from initial to final length measurement to four days or less.

Conclusions

The most important result of this reporting period is the separation and identification of the second factor, or variable, in determining the strength of the regenerator matrix--the separator wall thickness. This variable accounts for a major part of the disk variability unaccounted for by the channel skew angle and its concomitant fault, cell distortion. Further, the importance of accurately controlling this variable is very great since a very small increment in mean separator wall thickness, coupled with a reduction in the standard deviation, can result in a major increase in strength with only a small increase in ΔP .

Second, it is important to note that radial variations in strength, at the strength levels of the current disk population, make it very difficult if not impossible, to characterize a disk by a single measurement or localized "reference" MOR. Disks 4 and 6 failed under stress levels occurring in engine applications at two different radii and as a result of two different variables or fault systems. In this connection it is worth noting that analyses of failures, within the context of an estimate of disk population strength distribution, has yielded a major return in data base.

Finally, the first disk of the 1100°C (2012°F) material has demonstrated a major reduction in phase transformation rate due to thermal exposure when compared with the 1000°C (1832°F) matrix. This improvement is accompanied by an 85% increase in MOR. The correlations, to date, have not yet established causation.

CERAMIC ABRADABLE SEAL MATERIALS

Ceramic abradable materials development activity during this reporting period included the procurement and evaluation of a second generation of materials which are based on compositions reported in the previous semiannual progress report. These materials are specific formulations prepared by Coors, Corning, Carborundum, and GTE/Sylvania, and are modifications of materials previously evaluated and which were determined to warrant further consideration.

Cordierite

Coors Porcelain is developing a cordierite material for use as an abradable structure. Samples submitted to date are solid compacts with variations that result in changes in hardness and tensile strength but do not change the material density. Leakage through the material is therefore not anticipated to be a problem.

The softer of two cordierite samples (8H1) exhibited an R15Y hardness of 49 and abraded quite easily to a depth of 0.7 mm (0.028 in.) without any distress (Figure 20). The blade tips exhibited some blemishes (Figure 21) but had no measurable tip loss. The edges of the rub path were clean and distinct but fragile to the touch, breaking away very easily. This material experienced excessive damage (Figure 22) during the standard erosion test. The harder sample (8H2) had an R15W hardness of 90 and resulted in the development of a very severe wear scar during abradability testing (Figure 23). It should be noted that there is a significant difference in hardness between samples 8H1 and 8H2. Sample 8H2 required a change of two scales on the Superficial Hardness Tester (from 15Y to 15W) before a meaningful measurement could be recorded. The 8H2 wear scar was glazed and displayed both pullout and thermal cracking. Further metallic debris from the blade tip was imbedded in the wear track. The blade tips exhibited visual scoring (Figure 24), which did not appear to have any appreciable depth. A 0.013-mm (0.0005 in.) tip loss was measured. Maximum penetration of the cordierite was 0.25 mm (0.010 in.). The erosion test of this material resulted in a slight loss of material (Figure 25), which was significantly less than that lost during the testing of the 8H1 material.

Silicon Nitride

The silicon nitride material received from GTE/Sylvania is the second iteration from this supplier. This material was intentionally formulated to be excessively hard, with the intent of establishing an upper boundary for acceptable structures. Abradability performance was extremely poor for this sample, as shown in Figure 26. A moderate amount of metal debris was

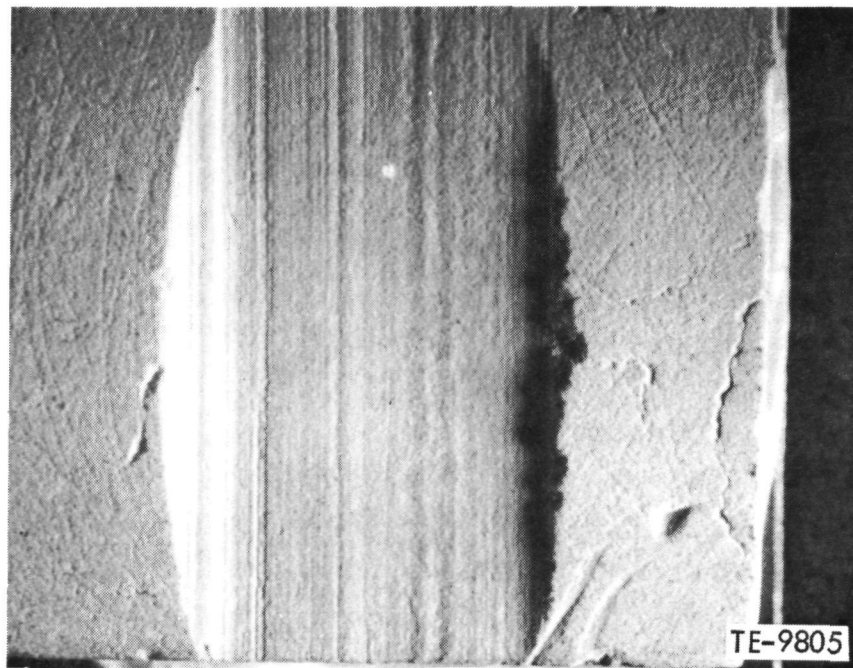


Figure 20. 8H1 cordierite--0.71 mm (0.028 in.) depth rub. (5X)

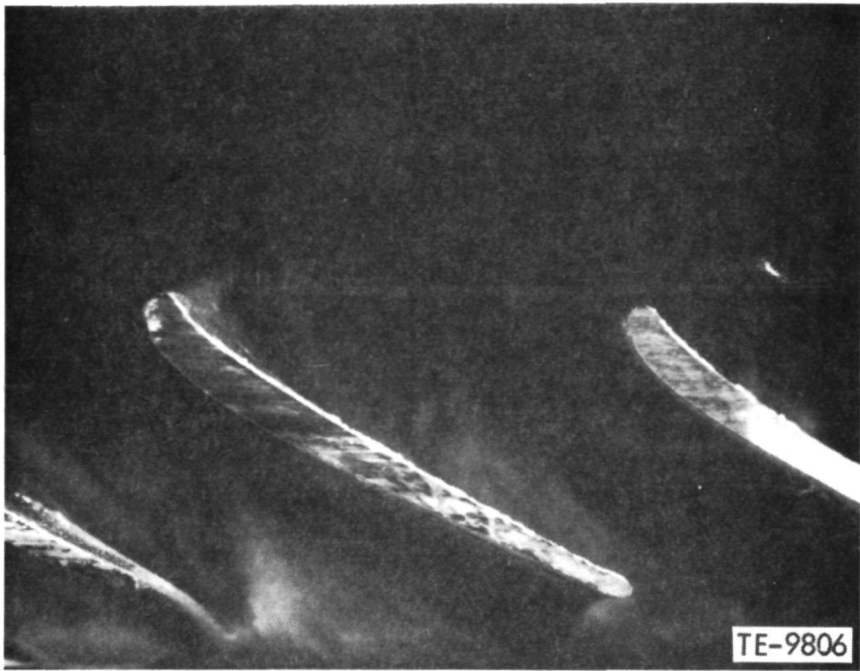


Figure 21. Mar-M246 blade tip after rub against 8H1 cordierite--zero blade tip loss. (5X)

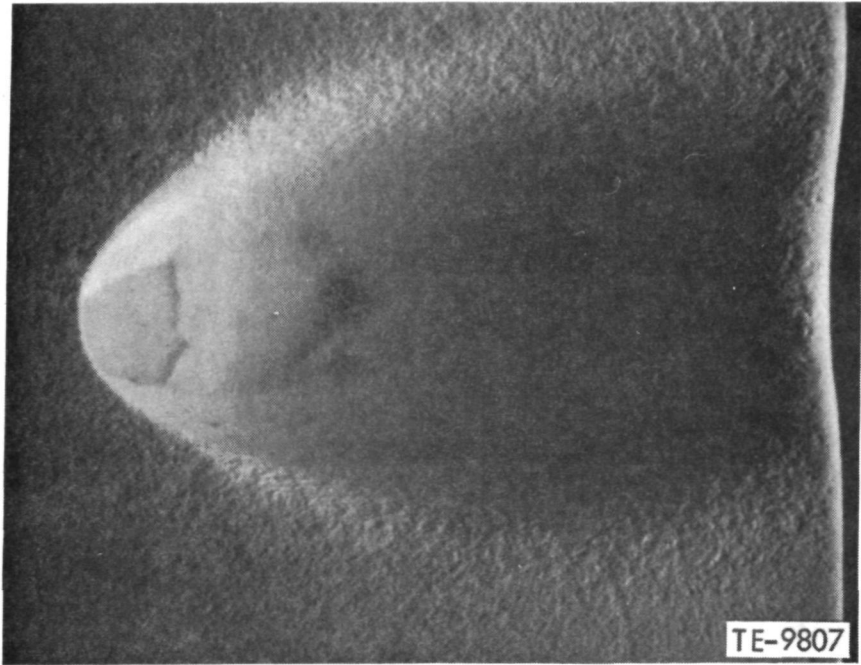


Figure 22. 8H1 erosion--45° impingement, 0.27 g/min dust flow. (5X)

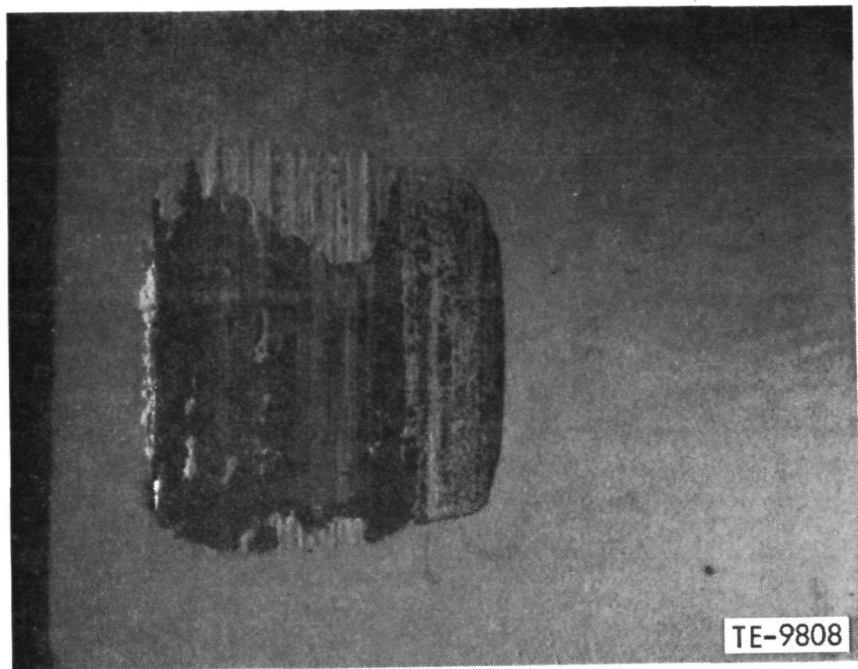


Figure 23. 8H2 cordierite--0.25 mm (0.010 in.) depth rub. (5X)

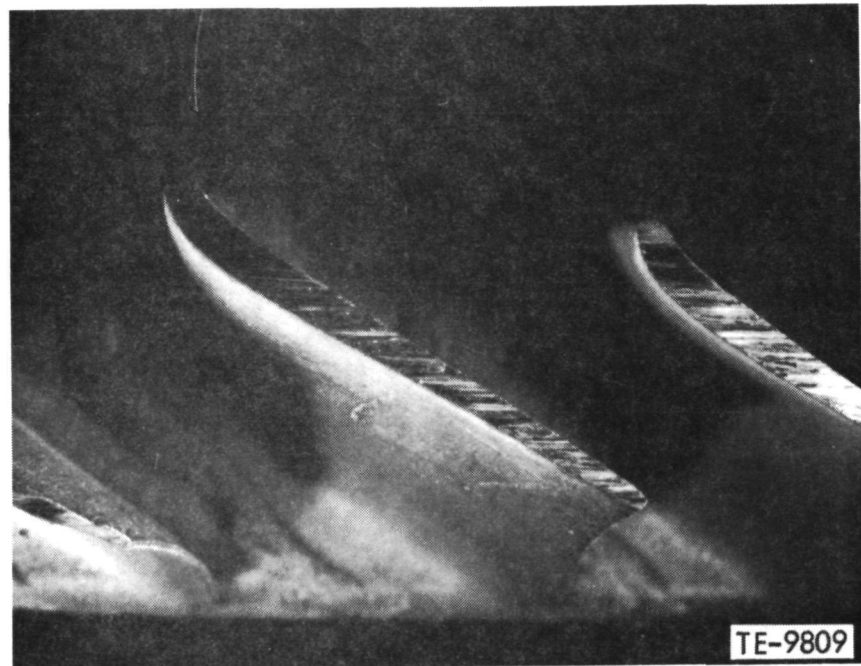


Figure 24. Mar-M246 blade tip after rub against 8H2 cordierite--0.013 mm (0.0005 in.) blade tip loss. (5X)

ORIGINAL PAGE IS
OF POOR QUALITY

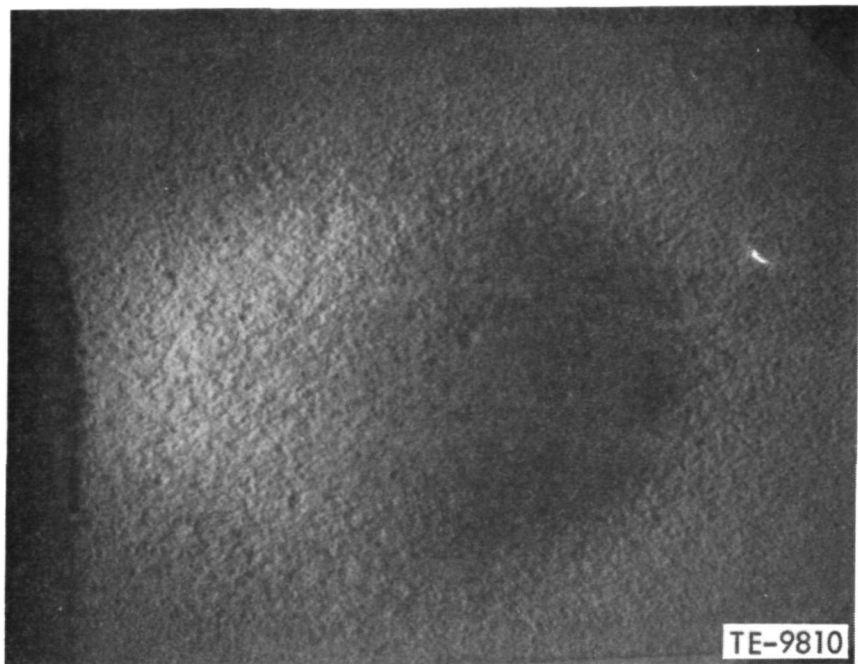


Figure 25. 8H2 erosion--45° impingement, 0.35 g/min dust flow. (5X)

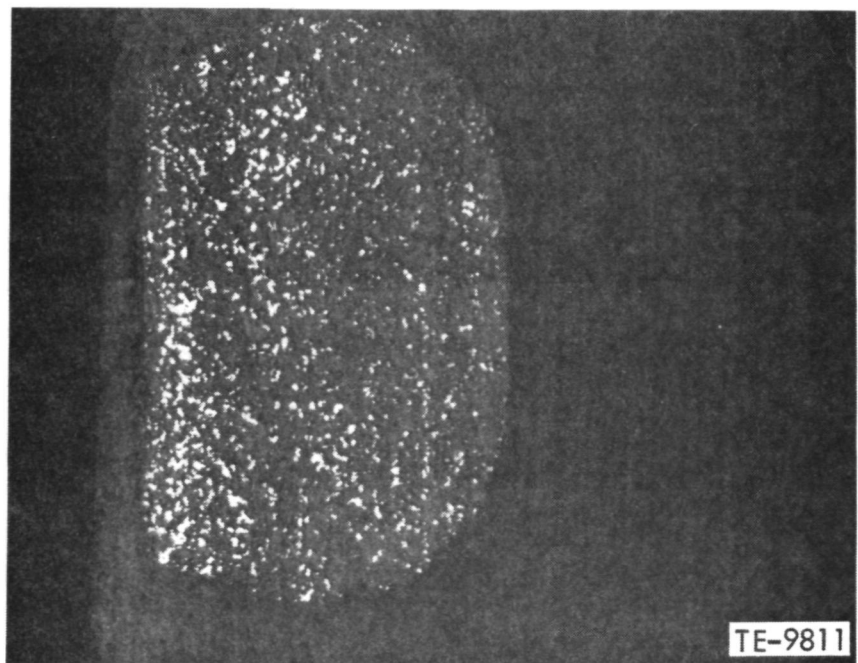


Figure 26. GTE silicon nitride--0.38 mm (0.015 in.) depth rub. (5X)

deposited in the rub track and, although the blade tips showed no evidence of scoring, they did experience a loss of 0.07 mm (0.0026 in.), corresponding to a rub depth of 0.38 mm (0.015 in.) in the silicon nitride. Erosion tests resulted in very minor surface damage to the specimen, as shown in Figure 27. Future specimens will be less dense, thereby enhancing abradability performance.

Reaction-Bonded Silicon Carbide

Samples of reaction-bonded silicon carbide submitted by Pure Carbon were evaluated for abradability and erosion performance. As a group, the Pure Carbon silicon carbide abradable materials performed significantly better than other silicon carbide samples previously examined. The behavior of these samples is generally characterized by an extremely clean postrub blade tip and a well defined wear track with various degrees of metallic deposits in the rub zone, depending upon the sample investigated. The ratio of rub depth/blade tip loss varied from infinity on sample II-1 to 9.3 on sample II-3. Figures 28 through 32 show the rub tracks and wear ratios. Figures 33 through 37 show the erosion test results. Close inspection of some of the samples revealed a two-step layer in the abradable coating. This was most prevalent in samples II-2 and II-3 (Figures 31 and 32). The zone of metal pickup can be seen to start at a finite distance below the surface of the material, particularly where this 0.13-mm (0.005 in.) thick surface layer ceases. Metallic debris can be seen in each of the samples shown in Figures 30, 31, and 32.

DDA CERAMIC TURBINE TIP SHROUD

While the various turbine shroud suppliers have been developing surface treatments and coatings which are compatible with respective products, a complementary effort within DDA seeks to apply a variety of alternate ceramic materials

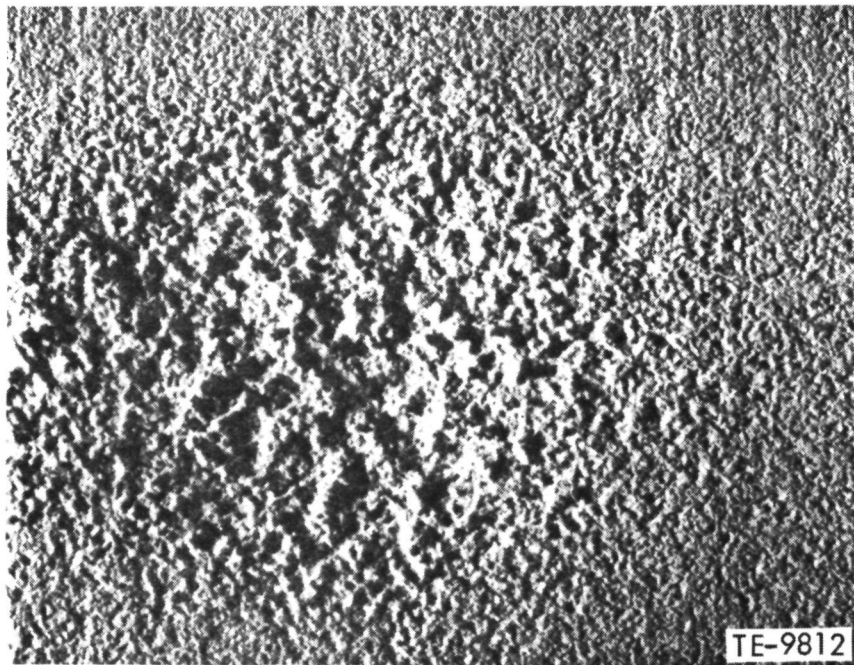


Figure 27. GTE silicon nitride erosion--45° impingement, 0.394 g/min dust flow. (5X)

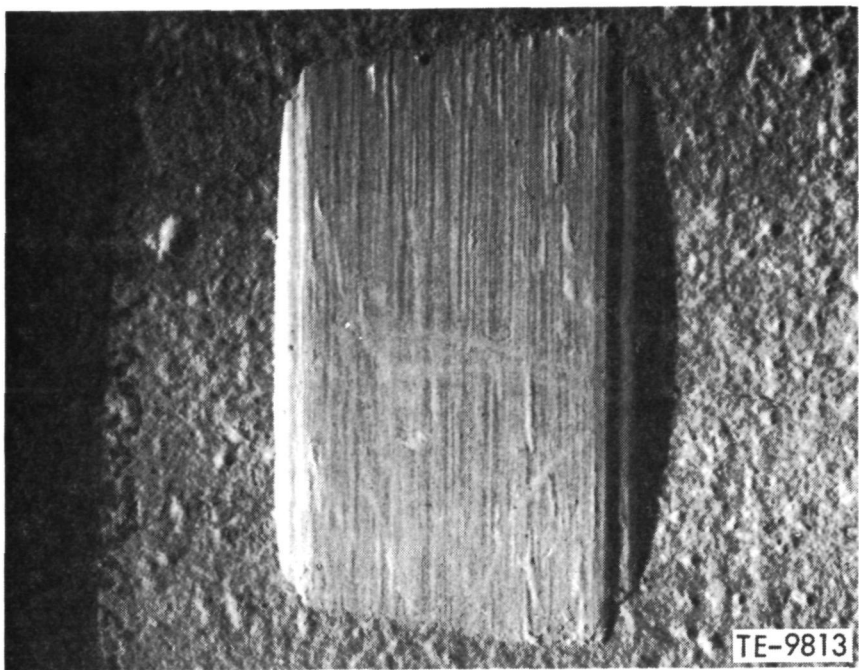


Figure 28. Pure Carbon RB SiC sample I-2--0.43 mm (0.017 in.) depth rub, 0.010 mm (0.0004 in.) blade tip loss. (5X)

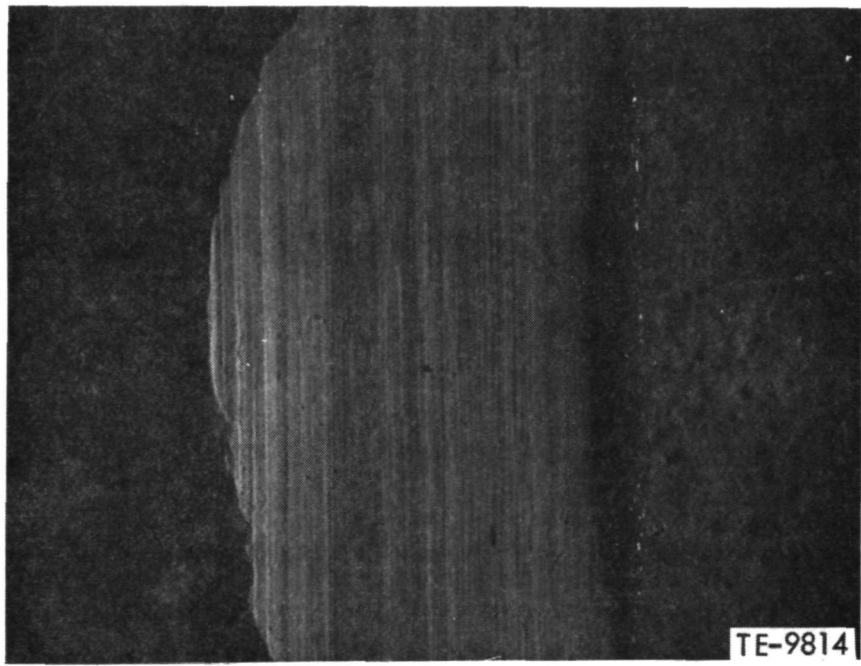


Figure 29. Pure Carbon RB SiC sample II-1--0.66 mm (0.026 in.) depth rub, zero blade tip loss. (5X)

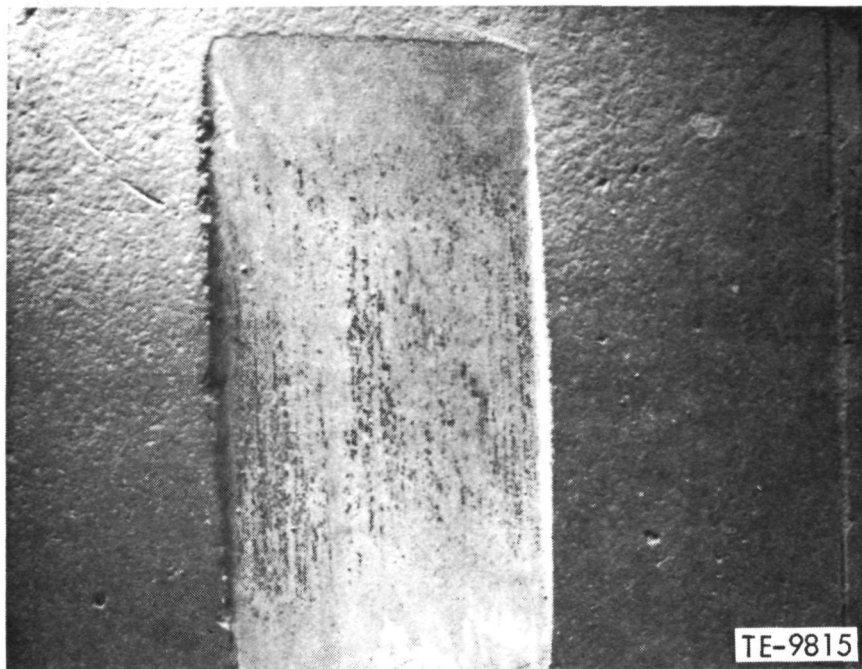


Figure 30. Pure Carbon RB SiC sample I-3--0.53 mm (0.021 in.) depth rub, 0.05 mm (0.0019 in.) blade tip loss. (5X)

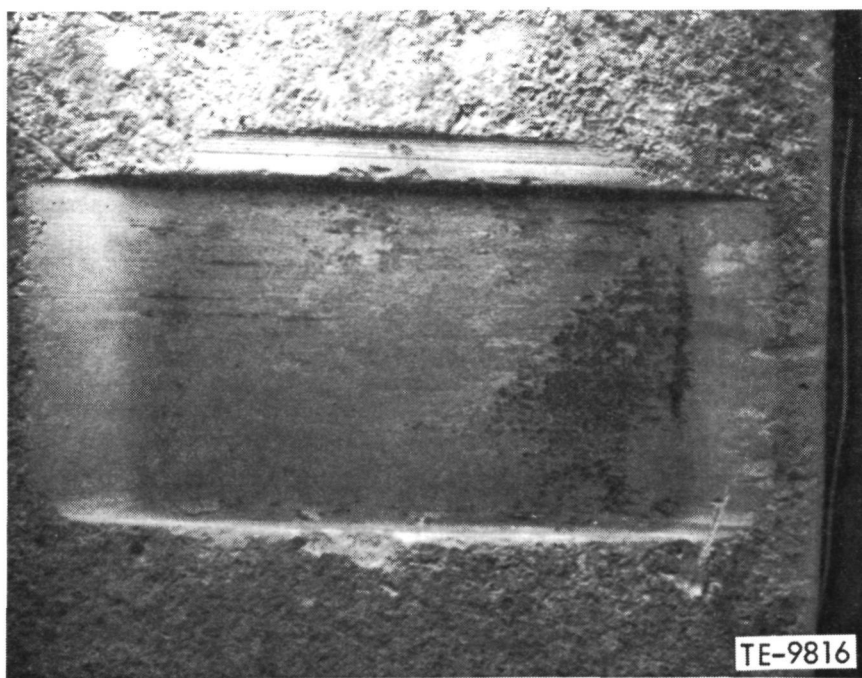
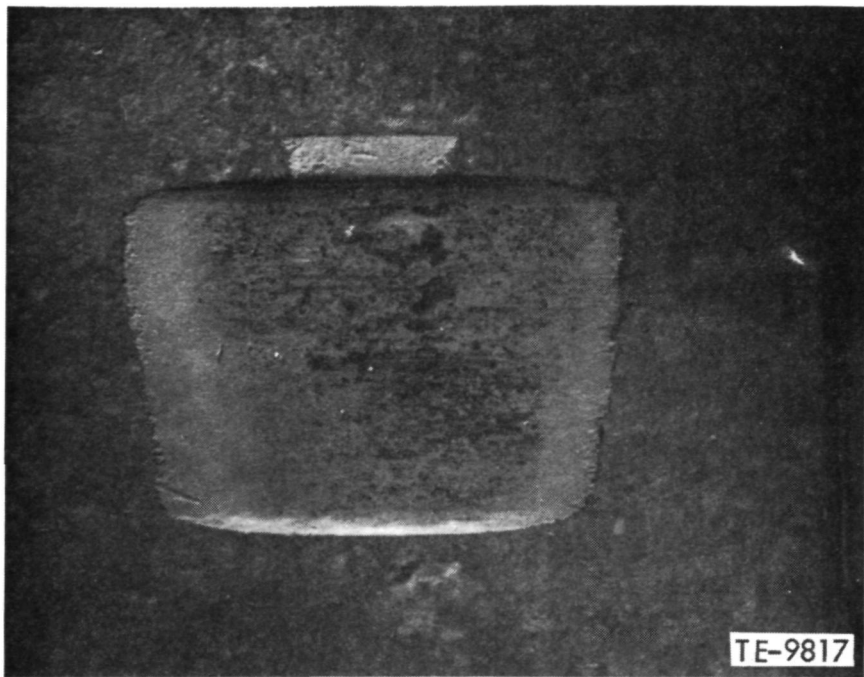


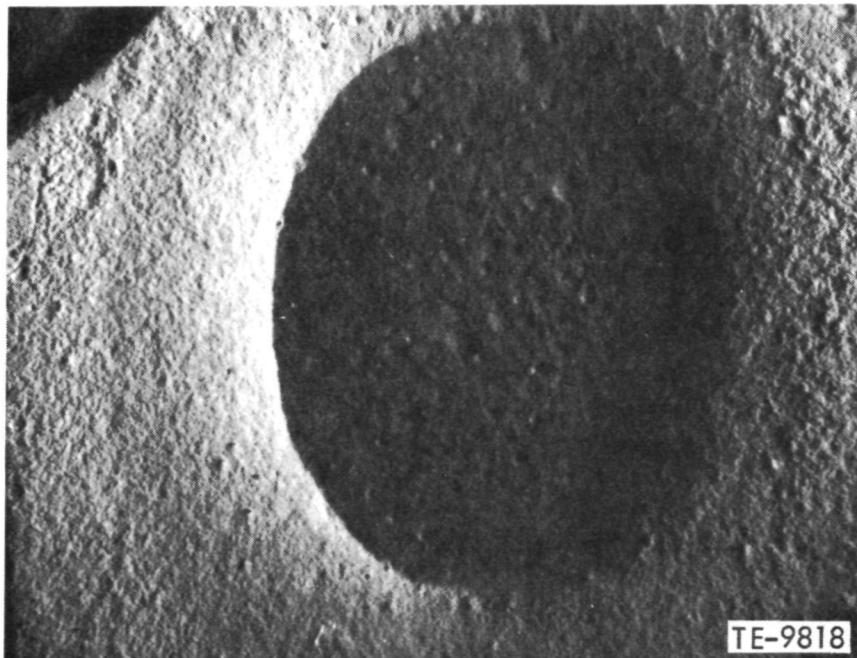
Figure 31. Pure Carbon RB SiC sample II-2--0.66 mm (0.026 in.) depth rub, 0.03 mm (0.0011 in.) blade tip loss. (5X)

ORIGINAL PAGE IS
OF POOR QUALITY



TE-9817

Figure 32. Pure Carbon RB SiC sample II-3--0.28 mm (0.011 in.) depth rub, 0.03 mm (0.0012 in.) blade tip loss. (5X)



TE-9818

Figure 33. Pure Carbon RB SiC sample I-2 erosion--45° impingement, 0.42 g/min dust flow. (5X)

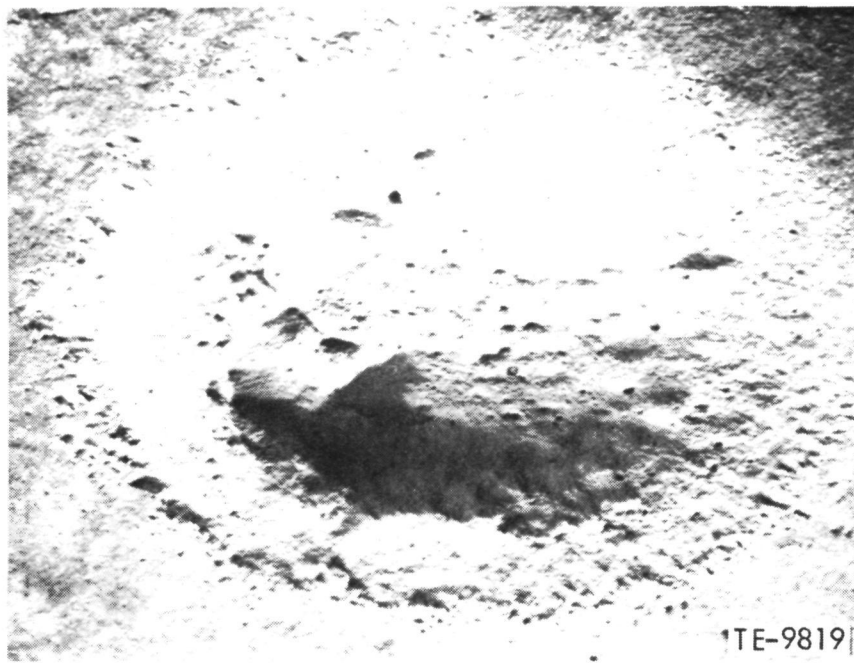


Figure 34. Pure Carbon RB SiC sample II-1 erosion--45° impingement, 0.307 g/min dust flow. (5X)

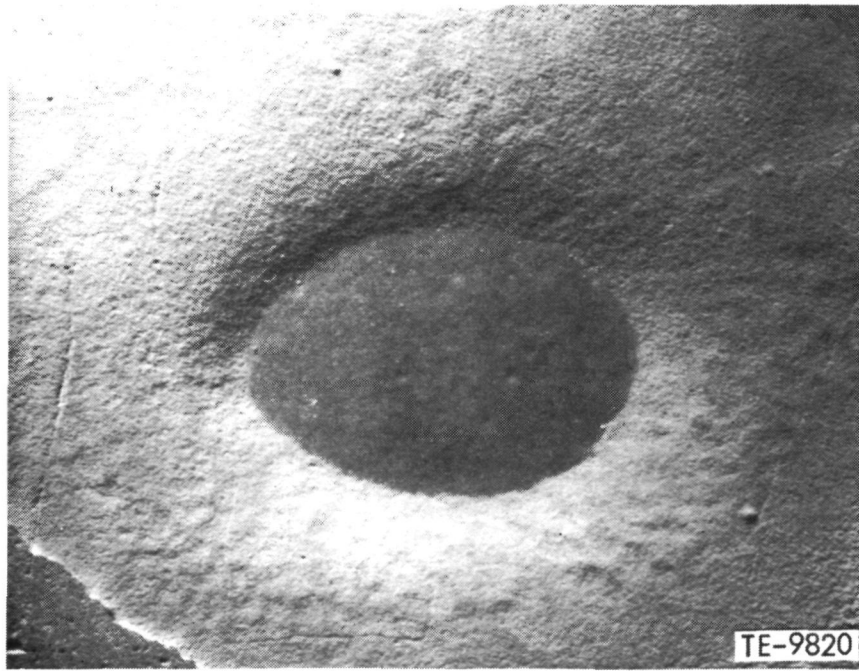


Figure 35. Pure Carbon RB SiC sample I-3 erosion--45° impingement, 0.533 g/min dust flow. (5X)

ORIGINAL PAGE IS
OF POOR QUALITY

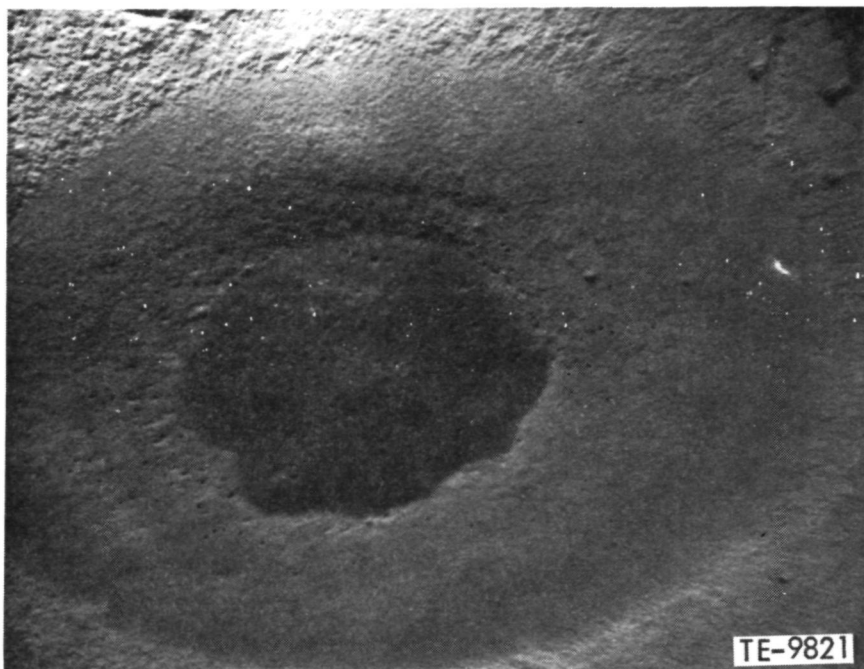


Figure 36. Pure Carbon RB SiC sample II-2 erosion--45° impingement, 0.270 g/min dust flow. (5X)



Figure 37. Pure Carbon RB SiC sample II-3 erosion--45° impingement, 0.377 g/min dust flow. (5X)

to substrates of silicon carbide and silicon nitride. Analysis of material requirements for compatibility with these substrates suggests that mullite and zircon have potential as candidate abradable seal materials. Each of these materials possesses the requisite thermal expansion characteristics with hardness values that are lower than either of the candidate shroud materials. True mullite is in the alumina silicate family as $3 \text{ Al}_2\text{O}_3 \cdot 2 \text{ SiO}_2$ and appears to be stable in the targeted operating temperature range. Present DDA work on mullite coatings is based on application of commercially available alumina filler papers and felts which are laminated to produce thicknesses of up to 1.52 mm (0.060 in.). Attempts to convert fiber and cementing components to an alumina silicate structure have been based on vacuum impregnation of the paper layers with colloidal silica solutions. The dried assembly is then fired in air to promote the mullite reaction.

A parallel effort to produce a zircon coating is being pursued through bonding yttria-stabilized zirconia felt or woven cloth layers to a silicon carbide coupon. Vacuum impregnation of the cemented layers is again employed to infuse the low-density felt and cloth with colloidal SiO_2 to promote the zircon reactions upon firing the coupons in air. Figures 38 and 39 display the cemented coatings described.

The "cemented" coatings were all fired about 1600°C (2910°F) and were too dense and hard for abradable seal use. Adjustments of fabrication and process variables are being investigated to improve the suitability of cemented systems for abradable seal applications.

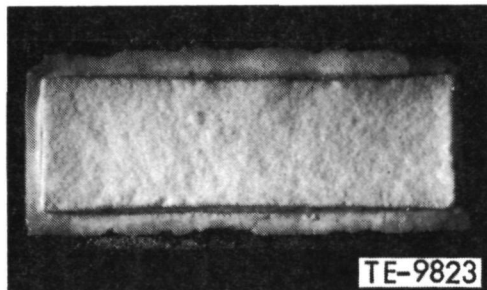


Figure 38. Aluminum silicate coating bonded to silicon carbide coupon. (1.1X)

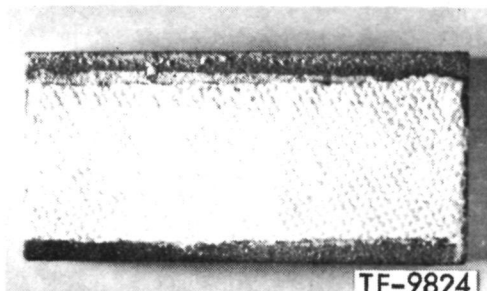


Figure 39. Zirconium silicate coating bonded to silicon carbide coupon. (1.1X)

Additional coating investigations have included mullite and zircon (zirconium silicate) applied by a plasma spray process on the as-fired surface of Norton NC-400 slip-cast silicon carbide coupons. Powder particles classified by size to satisfy the plasma spray gun parameters will be required before work can continue with that system.

A dual-density coating has also been applied to an NC-400 coupon. The initial coating of Metco 202 NS (yttria-stabilized zirconia) was applied 0.006 cm (0.015 in.) thick, followed by a "low-density" 0.010 cm (0.025 in.) coating of Metco 202 NS codeposited with Metco 600 polyester powder. The polyester powder "filler" has been used in other DDA abradable seal programs where the polyester has been burned out in a postspray operation. Further work will seek to lower still more the density of the coatings displayed in Figures 40 and 41.

Additional coating development in support of the total DDA effort has been included in a purchase order for work to be done at Deposits and Composites, Inc. The coating will incorporate hollow carbon spheres dispersed in a chemical-vapor-deposited coating of silicon carbide material. The thin carbon hollow spheres will, of course, rapidly oxidize in operation, but the resultant coating provides a way of lowering the density of the SiC matrix to improve abradability. The closed-pore, low-density coating is expected to provide a leak-free seal coating surface. Future efforts will include substitution of CVD Si_3N_4 as the matrix material.

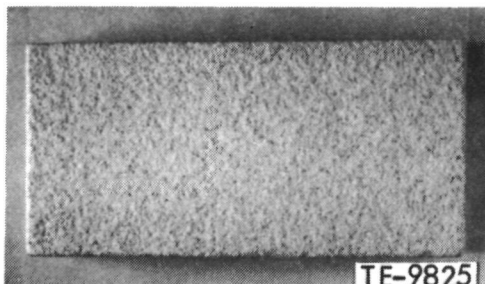


Figure 40. Plasma-sprayed zircon coating on silicon carbide coupon C-3.
(1.15X)

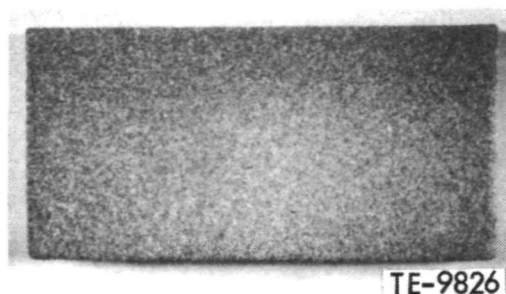


Figure 41. Dual-density zirconia coating on silicon carbide coupon C-7.
(1.2X)

NONDESTRUCTIVE EVALUATION

Nondestructive evaluation is used both as a step in qualification of parts for engine use and a source of data to promote process development at the ceramic source. During component development each material is characterized, NDE is applied to finish parts, test bars are evaluated, and qualification tests (mechanical and thermal) are run on each part before a part is ready for introduction to the engine environment. To make ceramic materials viable in the mass production environment of the automotive product, nondestructive evaluation, failure surface topography, chemical analysis, and microstructure examination serve as data to be related back to the ceramic source to revise processing and/or implement process controls to overcome the strength-limiting defects revealed. In addition, NDE technology development is underway to provide a technology base to permit economical high volume inspection of ceramic parts capable of identifying flaws down to critical size.

Current NDE techniques and equipment have been applied during this development phase to ceramic materials. These include X-ray, ultrasonic, 30-power visual, and fluoropenetrant techniques. At best, these have been able to disclose only gross flaws. The minimum practical flaw size detectable has been 300 microns, whereas critical flaws are much smaller. In addition, no single candidate was able to find all flaws present. Thus, a need was identified to define NDE criteria and evaluate potential technologies which could be applied to ceramics in the near term (5 years in the future).

A survey was conducted by Technology Associates Inc. to identify technologies which could be applied to ceramic materials. The critical flaw size in ceramic materials varies from about $25 \mu\text{m}$ to $100-200 \mu\text{m}$ over the temperature range of the gas turbine engine. Detection and resolution of flaws in ceramics are difficult for two reasons. First, the high acoustic velocity in ceramic materials; the wavelengths of acoustic signals are increased several fold over corresponding wavelengths in metals. Since current commercial ultrasonic test equipment operates in the 20-MHz range, the wavelength of such an acoustic signal in a ceramic is on the order of $500 \mu\text{m}$, which is substantially larger than the critical flaws to be detected. Although detection of the presence of flaws may be possible, the resolution of flaws smaller than the wavelength is generally not possible. Second, grain sizes of ceramics vary from $5 \mu\text{m}$ in hot-pressed materials to $100 \mu\text{m}$ in cold-formed materials, producing disturbances in the propagating waves that are comparable with those resulting from a flaw. Since the effect of the flaw upon strength is both a function of its size and location, it is necessary that NDE be capable of locating and classifying flaws with precision.

A summary taken from the Technology Associates report entitled "Survey of the NDE Techniques Applicable to Flaw Detection in Ceramic Turbine Parts" is as follows:

"Success of current efforts to develop ceramic materials for high-performance applications such as gas turbines is strongly dependent on the concurrent development of suitable nondestructive evaluation (NDE) procedures. The primary materials being studied for this application are silicon carbide (SiC) and silicon nitride (Si_3N_4). These ceramics are brittle and their strength is greatly affected by the presence of defects such as cracks, inclusions and voids in the material. Processing techniques have not progressed to the point

where such defects can be eliminated and therefore the feasibility of using these materials depends on the availability of suitable NDE techniques to separate defective components from nondefective components."

Based on a review of current NDE techniques, it is evident that there is no presently available procedure capable of carrying out the necessary detection and classification of flaws in ceramic turbine parts. However, there are several new techniques and extensions of old techniques that offer considerable promise of meeting the necessary performance criteria. These are reviewed briefly here.

Reflective ultrasound provides the most direct approach to the flaw detection problem. By increasing the operating frequency by a factor of 2 to 5 over current systems and by employing special signal processing techniques, it appears possible to achieve the necessary sensitivity and to obtain an adequate, though far from optimum, resolution capability. More extended research will be required to provide the refinements ultimately desired.

Surface acoustic wave technology has made great strides in recent years and is rapidly becoming a well established discipline. The potential of this approach to detection of surface cracks and subsurface flaws is great but the state of the art has not yet reached the point where it is directly applicable to the problem of flaw detection in ceramics. Research should be encouraged along these lines, but a near-term solution does not appear likely.

Photoacoustic spectroscopy is a technique in which sound generated by a pulsed laser beam impinging on a surface is measured by a sensitive transducer. The character of the sound is altered by the variations in the physical characteristics of the surface, such as cracks, roughness, and various flaws. The resolution and sensitivity are determined by the laser spot size and power and appear adequate for the present application. This technique appears to offer considerable promise for detection of surface and near-surface flaws in ceramic parts.

Optical holography as an NDE technique has developed greatly in recent years and offers a promising approach to detection of surface cracks and flaws in ceramic materials. In one promising technique an interference pattern is generated by laser light reflected from the surface for unstressed and stressed conditions. For a flaw-free specimen the fringe patterns are regular and comparable with those of other similar parts. The presence of flaws causes perturbations that can be detected visually or by automated procedures. Appreciable development work will be required to perfect this technique, but the sensitivity and resolution are adequate for this application.

Computerized tomography has become a major new tool in medical X-ray analysis because of its ability to produce images of the internal structure of tissue. The same technique is directly applicable to NDE of ceramics but would require the design of specialized equipment due to the great differences in material properties and required sensitivity and resolution between the medical and NDE applications. A careful cost analysis would be required to determine the feasibility of this approach. The use of ultrasonic tomography does not appear feasible at this time due to the need for very high acoustic frequencies and the difficulties encountered due to refraction at the object's surfaces.

Ultrasonic holography has been found useful in a number of NDE applications. This technique generates an image of the internal structure of an object by converting an acoustic hologram (interference pattern) into an optical hologram and then reconstructing an optical counterpart of the acoustic image. At the present time the sensitivity and resolution of such systems is substantially below that required for application to ceramic turbine parts. In future years, when such systems can be operated at 100-500 MHz, this may be an extremely useful tool for flaw characterization.

Microwave scanning has been shown experimentally to have the capability of detecting in ceramics flaws on the order of tens of microns. The experiments were carried out by using carefully prepared specimens, and the extension of this technique to irregularly shaped parts may be difficult. However, it is a technique that should be considered as potentially useful in the future because of its very high sensitivity. One drawback is that it is useful only in nonconducting materials such as silicon nitride.

DDA, under the Ceramic Applications in Turbine Engines project, is performing feasibility experiments in some of the aforementioned techniques to further establish their feasibility as ceramic material NDE techniques.

NDE DEVELOPMENT

During this report period, work continued in the development of various flaw detection techniques for Class I type of flaws (voids, inclusions, cracks). These techniques--reflective ultrasound, scanning photoacoustic spectroscopy (SPAS), and scanning laser acoustic microscopy (SLAM)--are described in the following paragraphs.

Reflective Ultrasound

High-frequency ultrasound flaw detection studies of silicon-based ceramic, using a C-scan technique, was initiated. Figure 42 shows a C-scan imaging system. The system consists of an x-y scanner, a 75.0-MHz broadband pulser/receiver, a gated peak detector, and a 50.0-MHz nominal frequency focused transducer. The transducer had a focal length of 4.13 cm in water.

Two identically seeded billets of hot-pressed silicon nitride (NC-132) were acquired from the Norton Company. The nominal size of the billets was 15.2 cm x 15.2 cm x 0.625 cm (6 in. x 6 in. x 0.250 in.). The seeds were placed in the center of the billet thickness. Iron, silicon, boron nitride, and graphite were selected as seed materials because they have been found to be common fracture controlling sites. Figure 43 shows the locations and nominal sizes of the seeds.

One billet (#1301) was machined by Norton after the hot pressing, while the other (#1302) was unmachined. The density and surface finish of the machined billet were found to be 3.27 g/cc and 9 to 13 rms, respectively. For the unmachined billet, the density was 3.25 g/cc and surface finish was 150 to 800 rms. Figure 44 shows the photomicrographs of the surfaces of the machined and unmachined billets. The surface roughness of the unmachined billet is quite obvious.

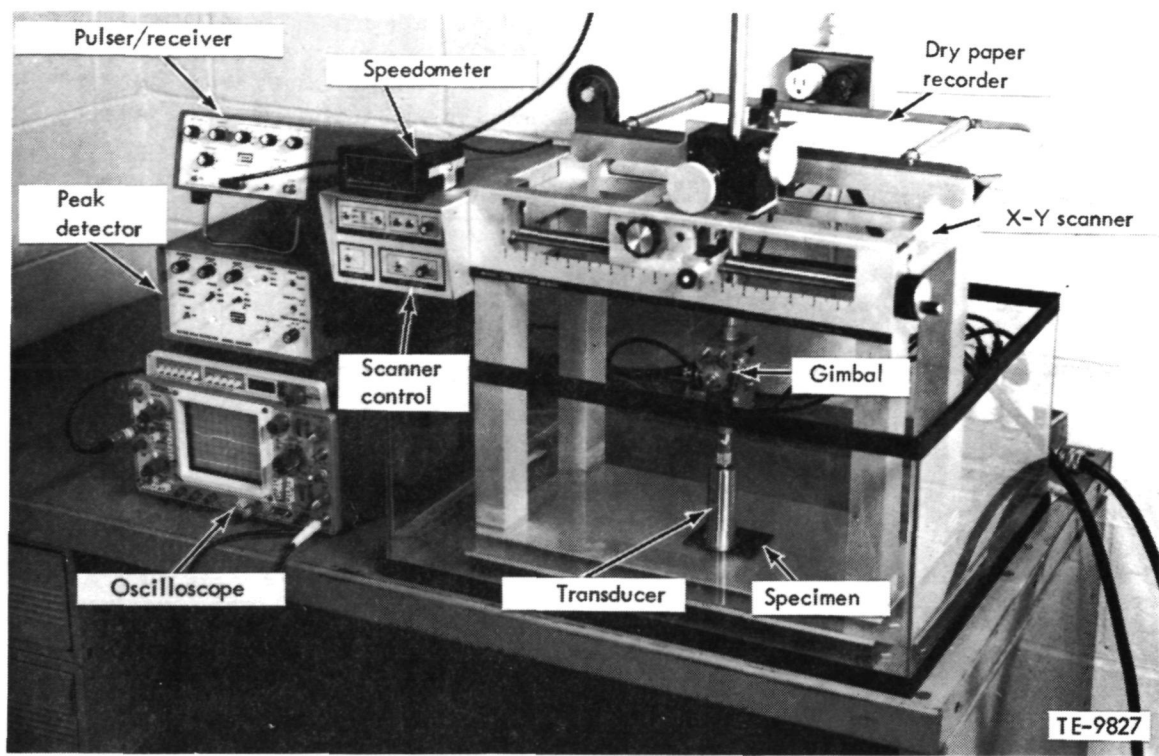


Figure 42. High-frequency ultrasonic C-scan system for flaw detection in structural ceramics.

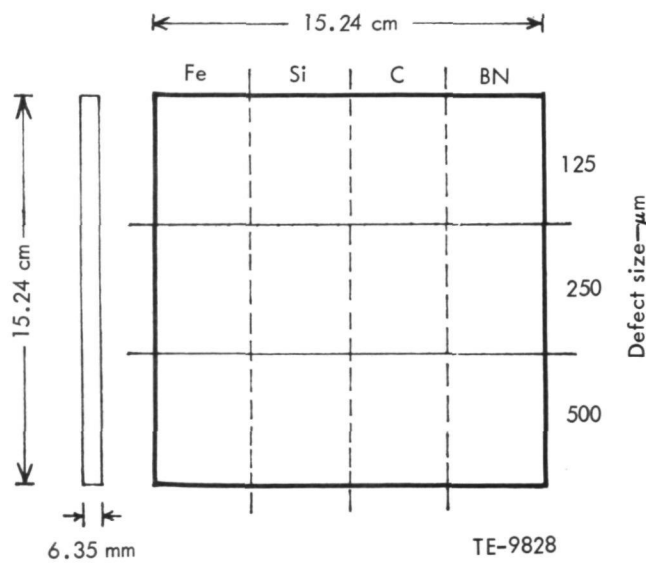


Figure 43. Schematic layout of the seeded defects in NC-132 billets.

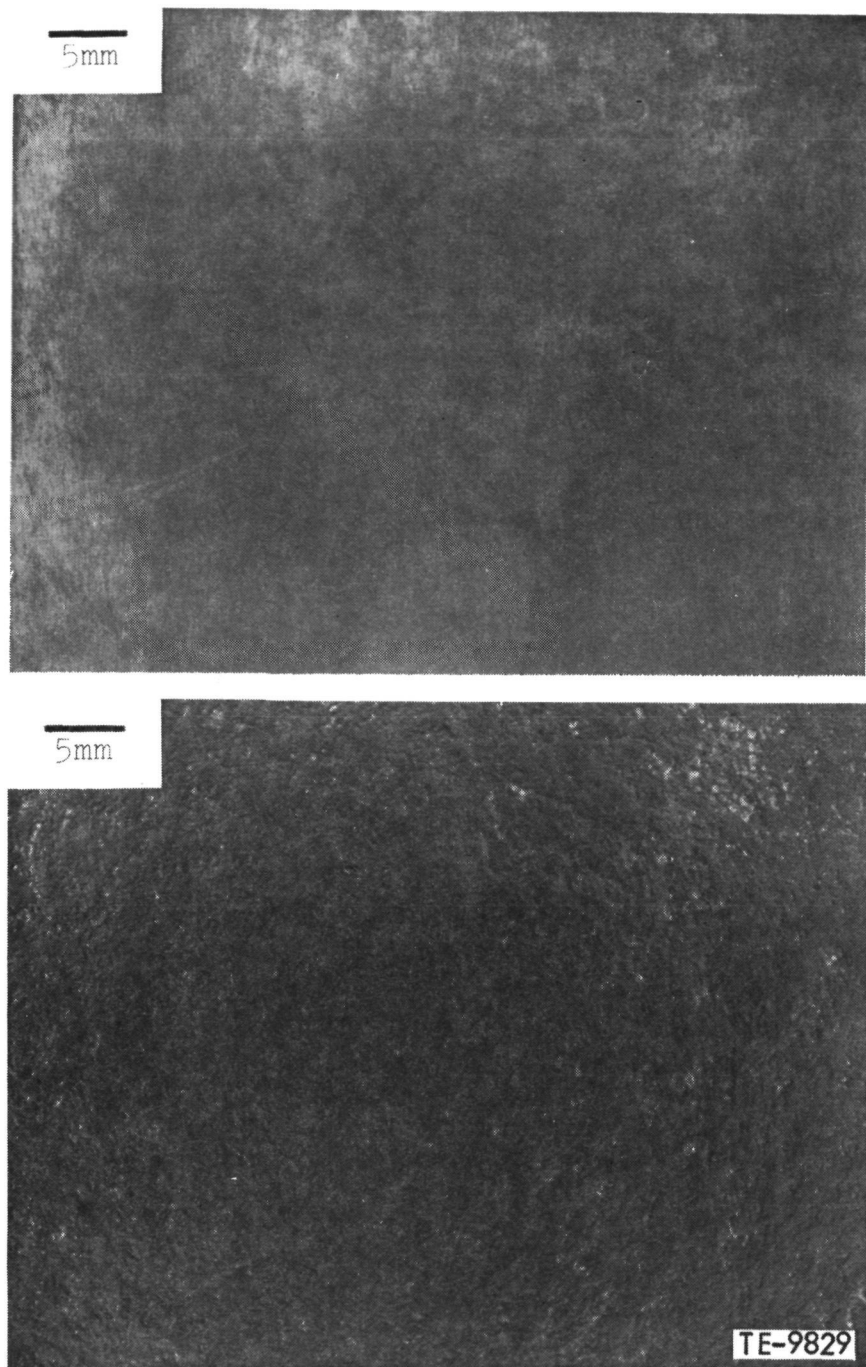
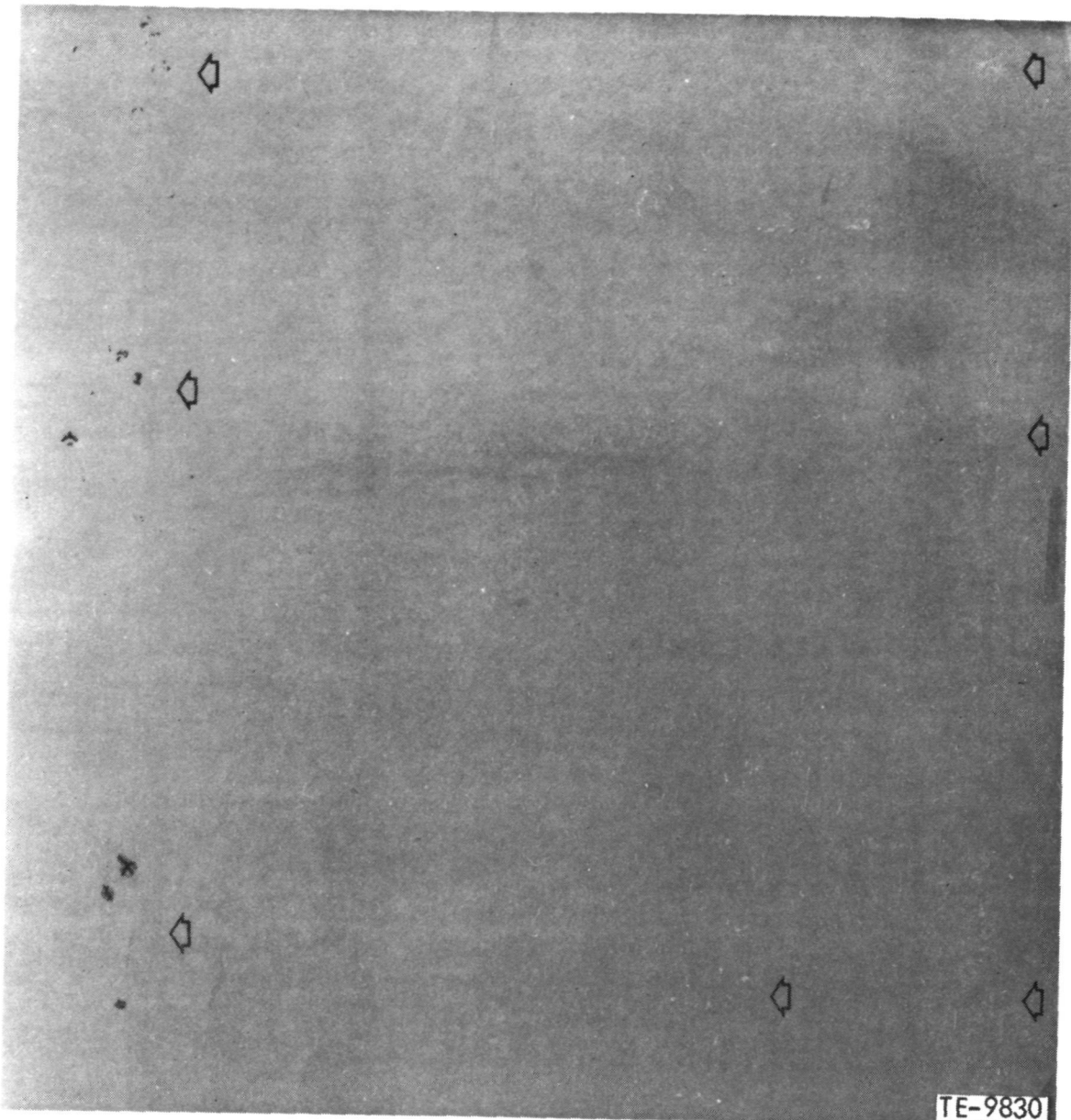


Figure 44. Photomicrographs showing surface roughness of NC-132 seeded billets.

Both billets were radiographed, using a Norelco X-ray system that had a glass window and a focal spot diameter of 2.5 mm (0.1 in.). The best results were obtained at 60 kv and 8 mA, using M-type Kodak film. Figures 45 and 46 show the positive of the radiographs of machined and unmachined billet, respectively. The dark areas represent high-density inclusions; the light areas are low density inclusions. Table XIII shows that the X-ray film density was quite uniform for the machined billet (#1301). Both the iron (Fe) and boron nitride



TE-9830

Figure 45. X-ray radiograph of machined, seeded billet (S/N 1301) of NC-132.

(BN) flaws were detected in all the three sizes. Silicon and graphite seeds were detected only in the $500 \mu\text{m}$ (0.020 in.) size. The sensitivity of the radiographic technique was 2.22% for Fe and BN and 8.9% for Si and graphite (C). Signal-to-noise (contrast) ratio was the greatest for iron and lowest for silicon. Figure 46 shows that the surface roughness of the as-fired billet (#1302) was excessive and caused large thickness variations which resulted in a radiograph of randomly varying film density. Only iron seeds were detected. Other low-density seeds, which were detected in the machined billet, were masked by the variation in the X-ray absorption.

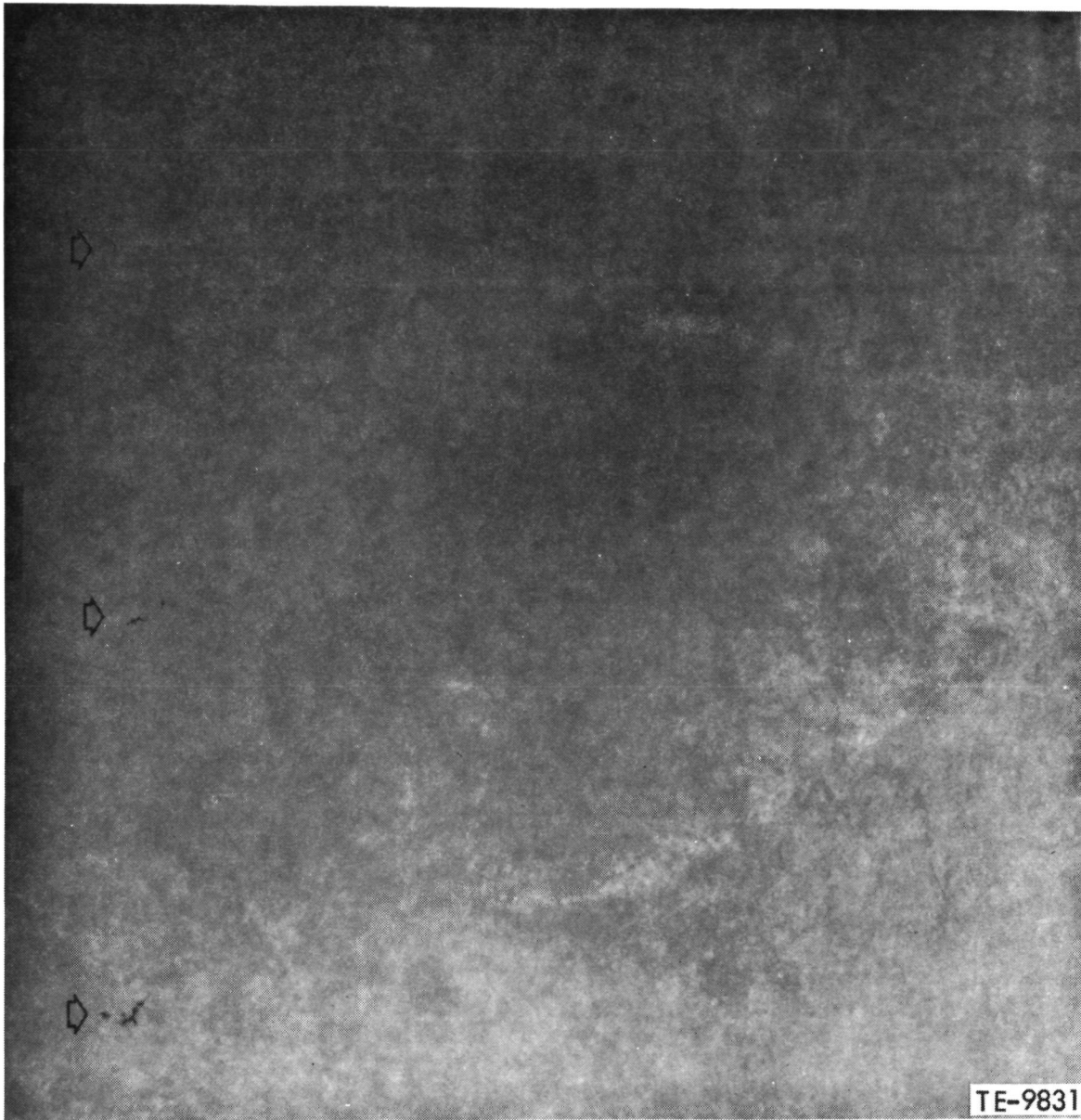


Figure 46. X-ray radiograph of unmachined, seeded billet (S/N 1302) of NC-132.

The machined seeded billet (#1301) of NC-132 was evaluated in the longitudinal mode, using the ultrasonic C-scan system shown in Figure 42. The water path was maintained at 6.4 mm, and the transducer was focused in the center of the specimen thickness. The transducer was scanned at 2.54 cm/s and incremented by 0.125 mm at the end of each scan line. The electronic gate was placed between the front surface and first back surface reflections. The transit time from the transmit pulse to the front surface reflections was blanked to eliminate any spurious signals and the gate was triggered by the front surface echo. The front surface dead zone was measured to be about 110 ns, while the back surface dead zone was found to be 30 ns. The analog output of the peak detector was measured to be linear and the threshold detected to write a

TABLE XIII. X-RAY EVALUATION OF SEEDED BILLETS OF NC-132

Type of billet	Defect size (μm)	Type of defect seed*				X-ray detection sensitivity
		Fe	Si	Graphite	Bn	
Machined (No. 1301) Thickness: 5.72 mm (0.23 in.)	125	D	ND	ND	D	2.22% (Fe, BN)
	250	D	ND	ND	D	
	500	D	D	D	D	8.9% (graphite)
Unmachined (No. 1302) Nominal thickness: 6.25 mm (0.25 in.)	125	D	ND	ND	ND	2.22% (Fe)
	250	D	ND	ND	ND	
	500	D	ND	ND	ND	

*D = detected; ND = not detected

C-scan. Figure 47 shows a C-scan of three types of seeds (Fe, Si, and C) of 125 and 250 microns in the machined billet (#1301) of NC-132. The BN seeds were also detected. Numerous defects, both coalesced and individual, of all the three types of seeds of 125 μm and 250 μm were detected. (Note: the silicon and graphite defects were not detected by X-ray radiography.) The signal-to-noise ratio was 5 to 1 or more. It was also observed on the A-scan that the rf amplitude of the large number of flaws was below the threshold of 50 mV used in the present experiment. By decreasing the threshold, it should be possible to detect flaws smaller than 125 μm .

Scanning Photoacoustic Spectroscopy (SPAS)

Two specimens were evaluated by SPAS, utilizing the flaw detection system described in the previous semiannual report. One specimen was of alpha-silicon carbide ($\alpha\text{-SiC}$) and the other of reaction-bonded silicon nitride (RBN 122). Both the specimens, 12.7 mm x 6.35 mm x 1.5 mm (0.5 in. x 0.25 in. x 0.06 in.), had a reference black line and an artificially induced Knoop indentation as a simulated surface flaw. The specimens were scanned parallel to their length starting from the reference line.

Figures 48 and 49 show the results of the photoacoustic scan along with the scanning electron micrograph of the detected flaws. The photomicrographs of the unpolished surfaces of the nitride and the polished surface of alpha-silicon carbide did not reveal any apparent radial cracks at the surface emanating from the contact zone. The indentor-induced surface spalling was more in $\alpha\text{-SiC}$ and less in RBN 122. The length (2C) of the indentations was 133 μm for $\alpha\text{-SiC}$ and 255 μm for the RBN 122 specimen.

The PAS signal from both the black line and the indentation was larger in RBN 122 than in $\alpha\text{-SiC}$. The thermal diffusivity of nitride is lower than $\alpha\text{-SiC}$. Therefore, it is heated locally to a much higher temperature and, hence, produces a higher photoacoustic signal. In the case of the indentations, the

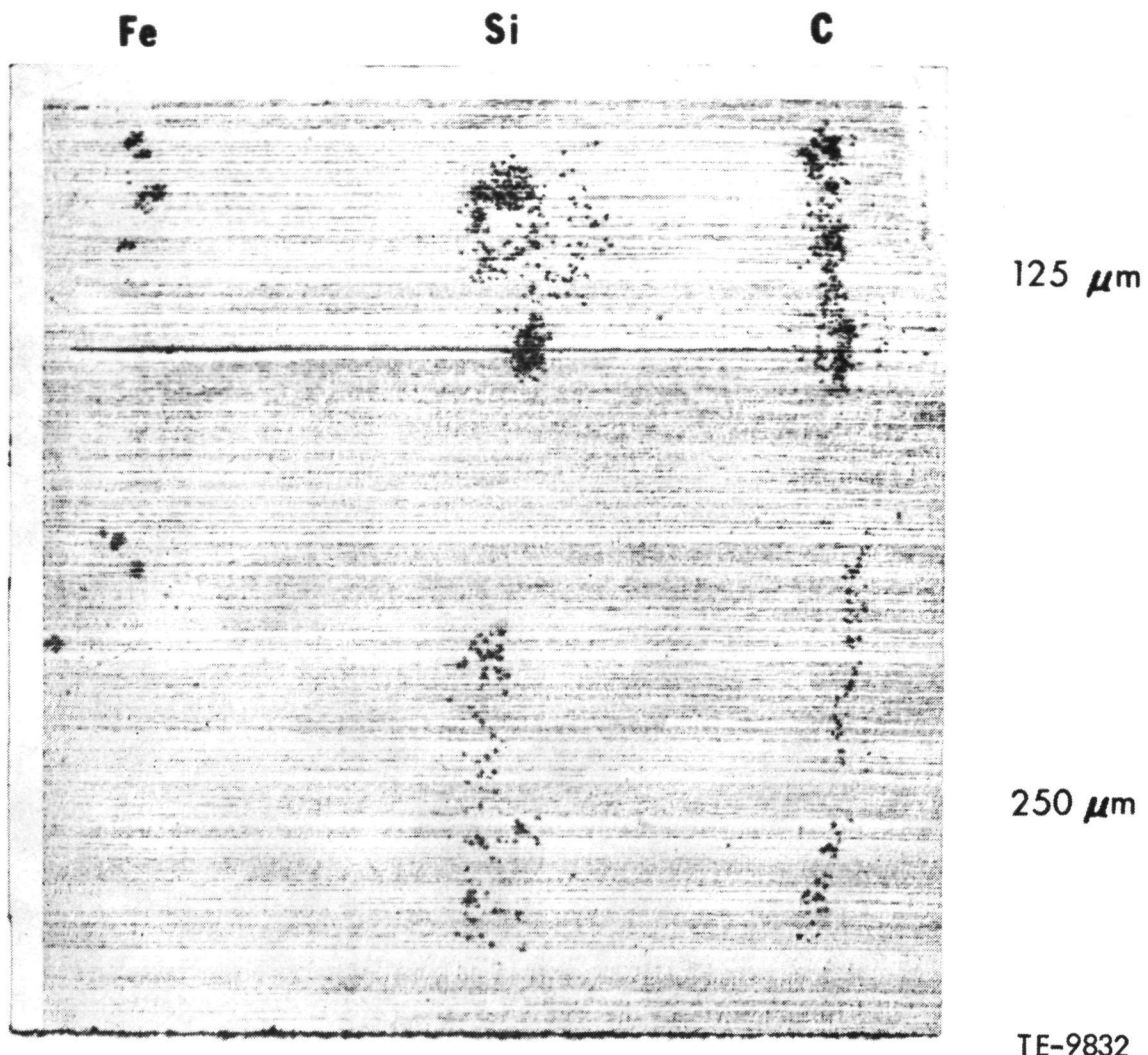


Figure 47. Ultrasonic C-scan of machined billet (S/N 1301) of NC-132 (longitudinal mode).

subsurface microcracking further decreases the thermal diffusivity and increases the PAS signal. Other parameters which may contribute to the higher photoacoustic signal in silicon nitride are differences in the grain size distribution and chemical composition through their effect on the optical and thermal properties.

A naturally occurring flaw (Figure 49) was detected in the RBN 122 specimen. Its location and linear distance from the black line was confirmed by visual examination. The natural defect was revealed by microscopic (SEM, optical, and visual) analysis to resemble a lap. Energy dispersive analysis of X-ray (EDAX) of the lap region showed no abnormal peaks. Therefore, the lap alone was probably responsible for the detected PAS signal.

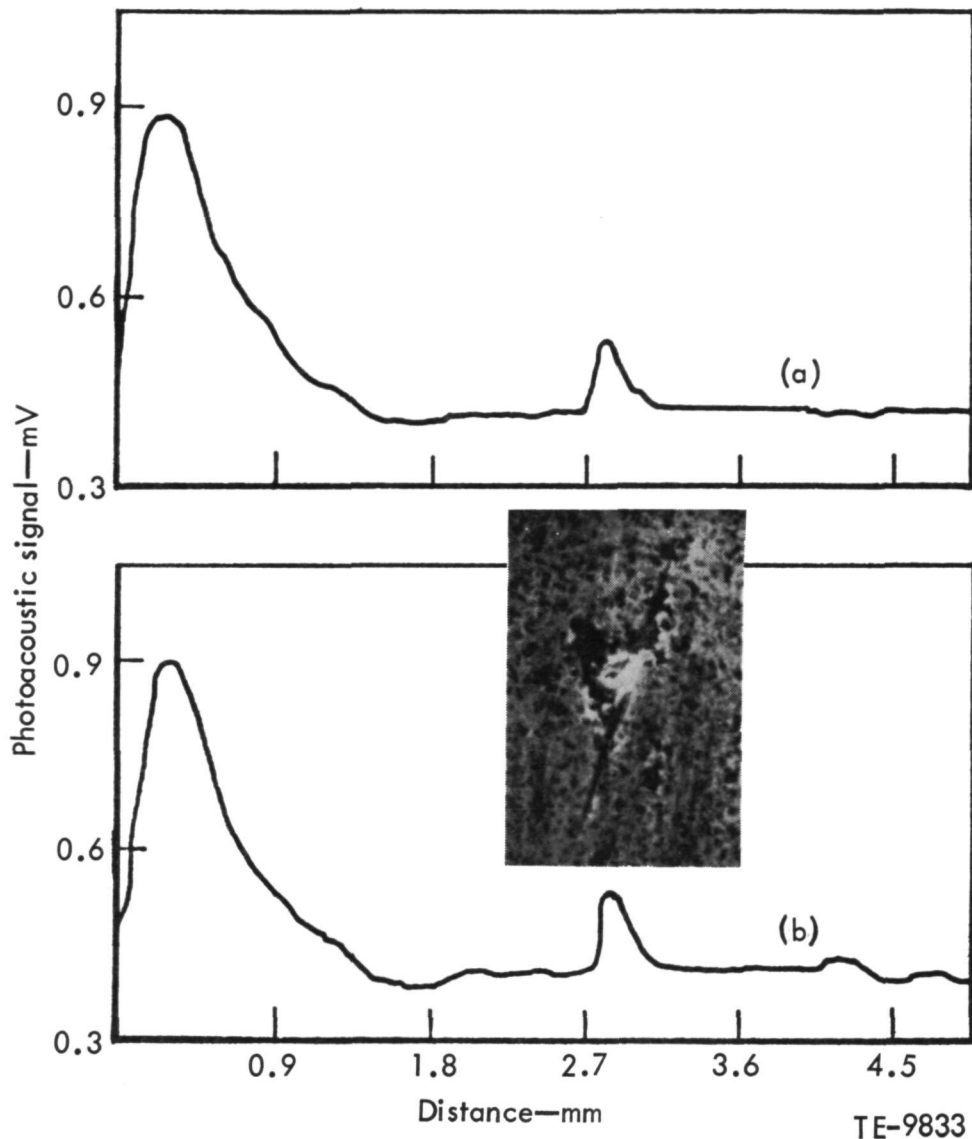


Figure 48. Photoacoustic signals from successive scans of a microhardness indentation in alpha silicon carbide.

The repeatability of detecting and locating the flaws was excellent (Figures 48 and 49) with respect to the amplitude of the photoacoustic signals and their signal-to-noise ratio. The distance between the signals was in good agreement with the measured linear distance between the flaws under an optical microscope at 50X.

Acoustic Microscopy (SLAM)

Several sources of artifacts were revealed during the characterization of modulus-of-rupture bars of sintered silicon carbide. A systematic investigation discovered four sources which caused disturbances in the acoustic image:

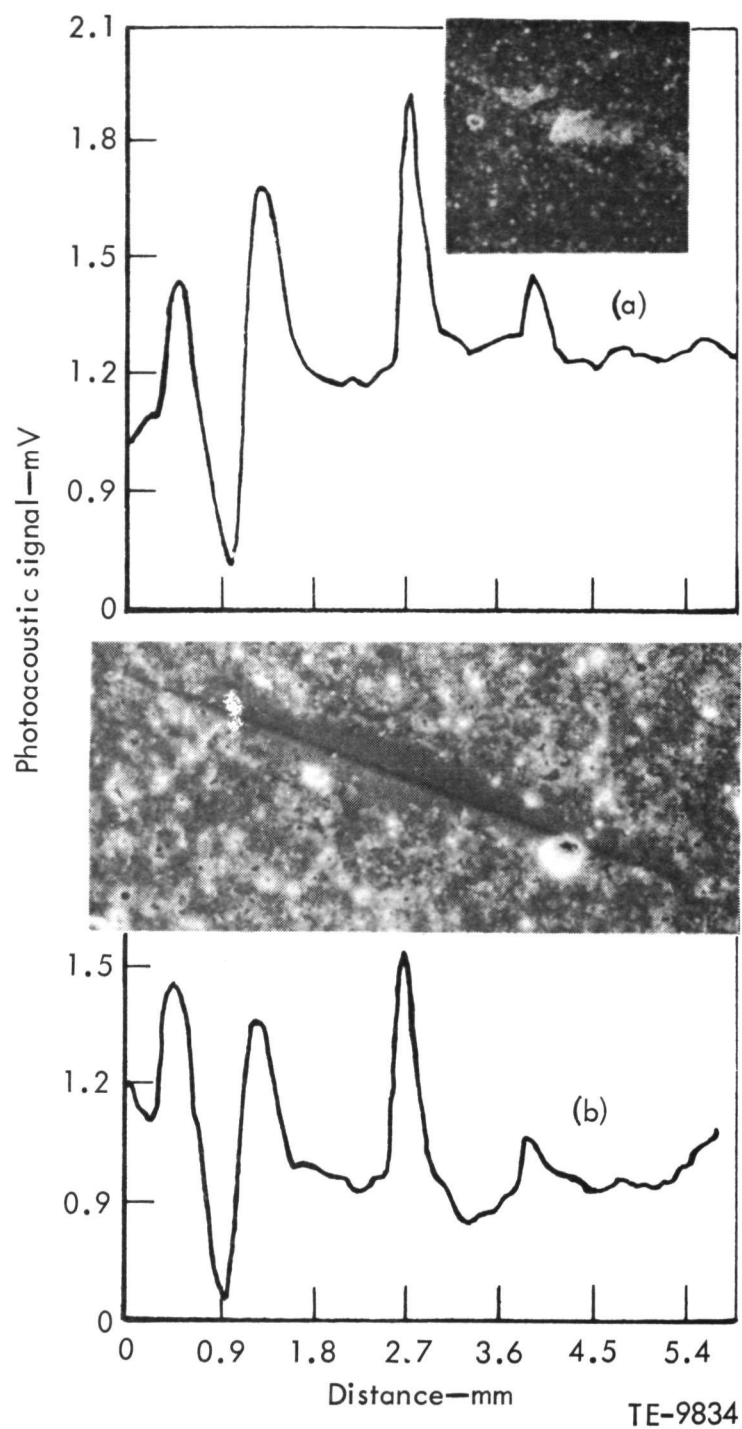
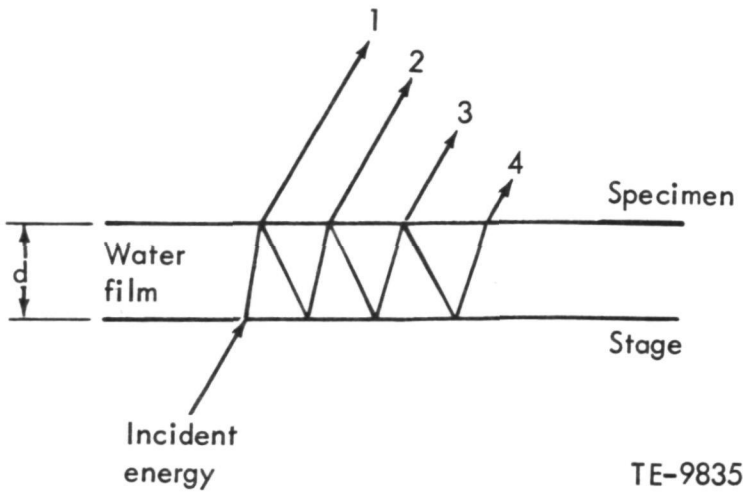


Figure 49. Photoacoustic signals from successive scans of a microhardness indentation in reaction-bonded silicon nitride (RBN 122).

- (1) The first type of artifact was an interference in the water film between the stage of the microscope and the silicon carbide specimen (Figure 50). This film, which is on the order of a few microns in thickness, generates constructive and destructive interference depending on the local dimensions of the gap. This phenomenon is



TE-9835

Figure 50. Reverberations in water film between stage and specimen. Phase of 1, 2, 3, and 4 depends on film thickness "d."

best detected by tilting the specimen with respect to the stage of the microscope (Figure 51A). This artifact was eliminated by increasing the water path (Figure 51B).

- (2) The second type of artifact, one which we have termed "edge effect," was produced by a portion of a beam reflecting from the side of the specimen and interfering with the direct beam (Figure 52). This produced a series of interference lines parallel with the edge of the specimen. Edge effect tends to obscure defects occurring at the edge of the specimen. This type of interference is reduced and/or eliminated by tilting the specimen around its long axis and increasing the water film thickness. It can also be modified by rotating the specimen 180° on the stage of the microscope. This type of interference may be associated with the side lobes of the source transducer.
- (3) The third type of phenomenon observed is the launching of the surface wave on the lucite mirror block (Figure 53). There seems to be no evidence that the surface wave is interfering with the visualization of the specimen or specimen defects. The surface wave is also not a consistent finding. It is easily eliminated by moving the mirror slightly with respect to the specimen.
- (4) The fourth type of artifact was due to mirror defects. These defects can produce image irregularities which are indistinguishable from defects in the specimen. These can presently be readily detected by moving the mirror with respect to the specimen. The mirror should be supported on the superstructure so that the defects in the mirror are stationary or fixed in the field as the specimen is advanced. Only the defects in the field of view in the specimen will move. The microscope stage has been modified for this mode of operation.

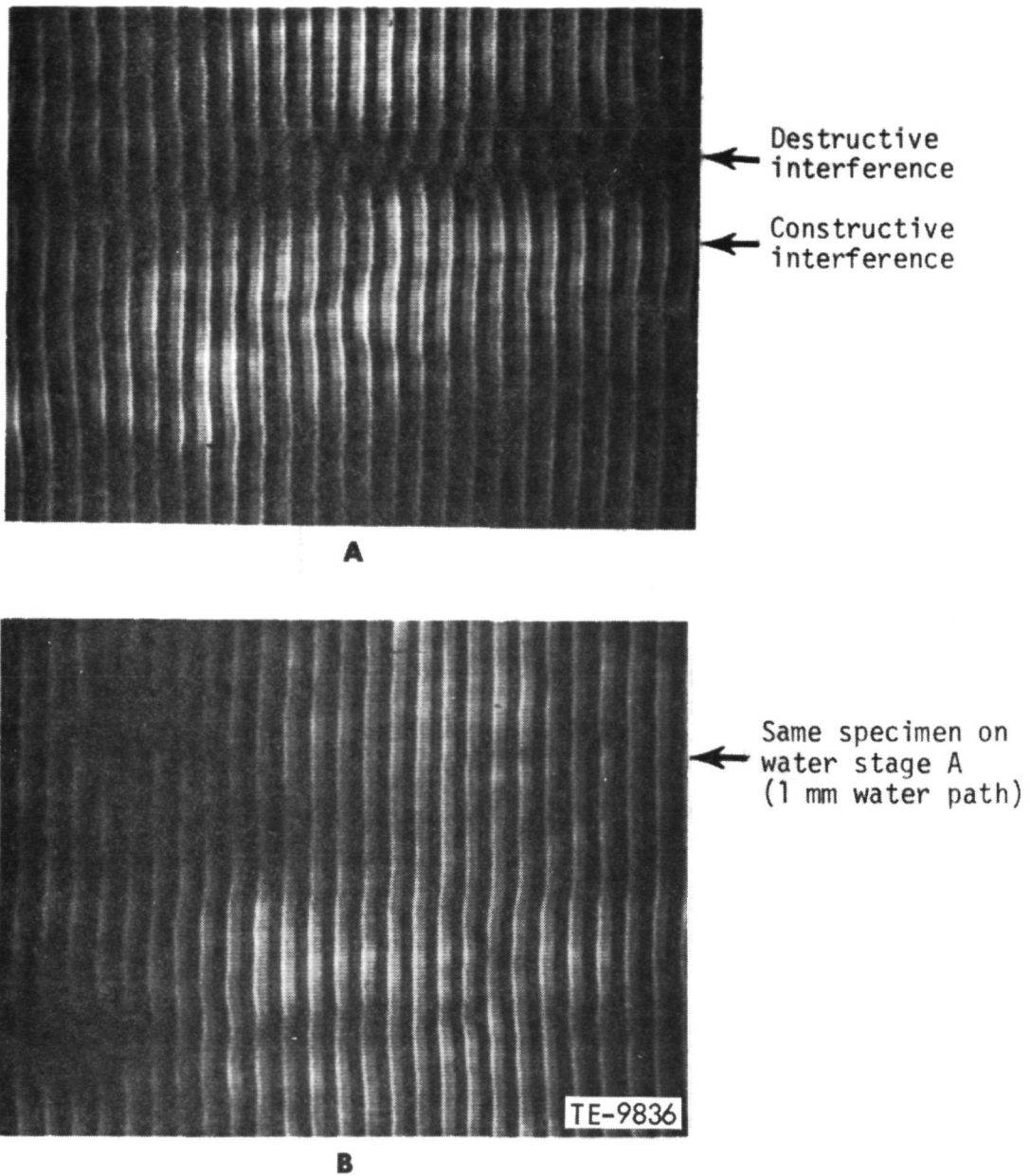
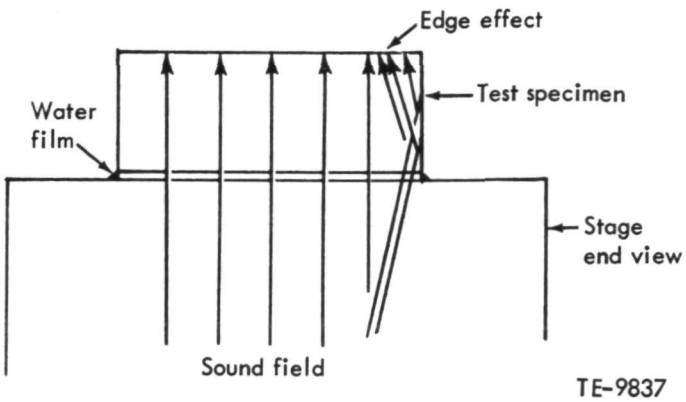


Figure 51. Water film between stage and specimen: (A) interference of reverberations; (B) elimination of interference by increasing water path (50-100 λ).

Three lucite washers (or water stages) with thickness of 1 mm, 1.3 mm and 1.6 mm were prepared to provide a relatively long water path between the stage and the specimen. Optimum results were obtained by the 1-mm thick "water stage." This water path tends to eliminate the interference phenomenon (Figure 54) and considerably reduces the edge effect.



TE-9837

Figure 52. Schematic diagram of acoustic interference associated with "edge effect."

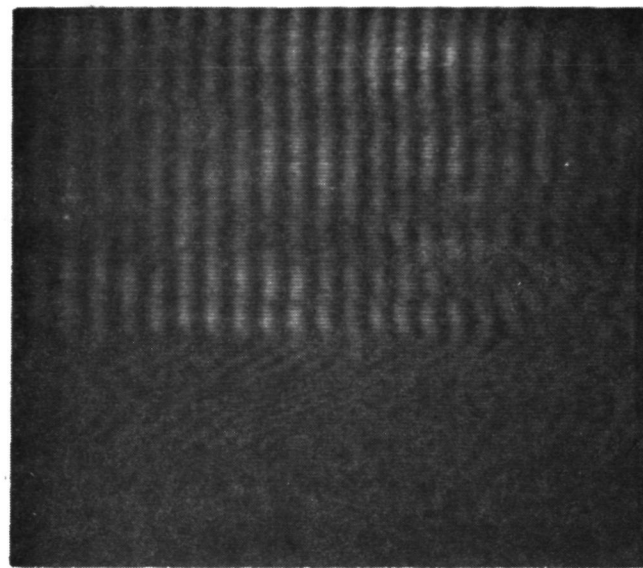
COMPONENT NONDESTRUCTIVE CHARACTERIZATION

During this reporting period small quantities of each of the 2070°F engine components were received and nondestructively characterized. A group of silicon nitride blade coupons was also evaluated. Tables XIV through XVIII summarize the results obtained with these components for which the characterization work has been completed.

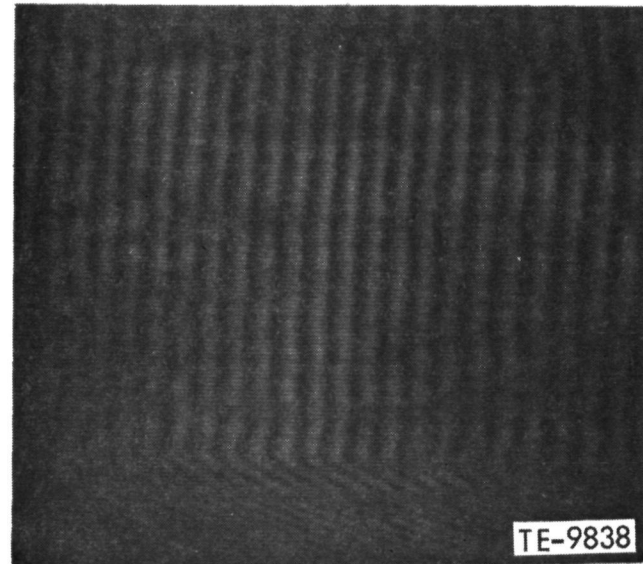
TABLE XIV. NONDESTRUCTIVE CHARACTERIZATION OF GASIFIER VANES

<u>Material</u>	<u>Quantity</u>	<u>X-ray*</u>	<u>FPI</u>	<u>Visual (10-30X)</u>
EX131232 α-SiC $\rho = 3.15 \text{ g/cc}$ Carborundum	45	30 NI, 15 LDI, 15 NI, others 1 with large minor pits; 2 through-crack airfoil cracks	12 with "mudcracking" on LE & TE, 18 NI; others with usual chips and pits	
EX130157 RB SiC $\rho = 2.94 \text{ g/cc}$ Carborundum	21	14 NI; 1 HDI, 6 LDI	19 NI, 2 with small pits	9 NI, others with minor chips

*LDI = low-density indications; HDI = high-density indications; NI = no indications.



A



B

Figure 53. Interferogram of specimen scanned along two edges in the midspan:
(A) edge toward back of stage; (B) specimen rotated 180° with edge in front
of stage.

ORIGINAL PAGE IS
OF POOR QUALITY

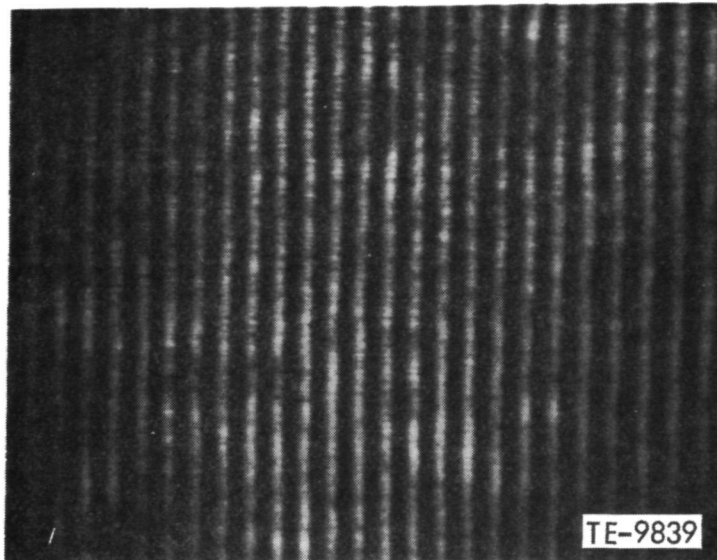


Figure 54. Interferogram of an alpha SiC specimen with a 1-mm (0.04 in.) thick water stage.

TABLE XV. NONDESTRUCTIVE CHARACTERIZATION OF GASIFIER BLADES

<u>Material</u>	<u>Quantity</u>	<u>X-ray*</u>	<u>FPI</u>	<u>Visual (10-30X)</u>
EX130180 <i>a</i> -SiC $\rho = 3.14 \text{ g/cc}$ Carborundum	18	12 NI, 3 with cracks, 3 LDI	4 NI, 14 minor pits	4 NI, 18 with usual chips
EX131235 <i>a</i> -SiC $\rho = 3.15 \text{ g/cc}$ MOR = 221 MPa (48 ksi) Carborundum	49	15NI, 34 LDI	3 NI, 4 with large porous areas, 42 minor pits	25 NI, 24 minor pits and chips

*NI = no indications; LDI = low-density indications.

TABLE XVI. NONDESTRUCTIVE CHARACTERIZATION OF HOT FLOW PATH COMPONENTS

<u>Material</u>	<u>Quantity</u>	<u>X-ray*</u>	<u>FPI</u>	<u>Visual (10-30X)</u>
EX130158	15	9 NI, 6 NDI	6 crazing on OD, 7 NI	6 occasional edge chips, 9 NI
Ring--Vane Retaining blanks	"As-fired"			
RB SiC				
$\rho = 2.99 \text{ g/cc}$				
Carborundum				
EX131230	6	4 NI; 2 HDI and LDI	3 minor pits, 3 NI	6 NI
Ring--Vane Retaining KT SiC	"As-fired"			
$\rho = 3.14 \text{ g/cc}$				
Pure Carbon				
EX130159	10	LDI	3 blanks NI, 7 porous areas pits; 1 fin.	No visual exam on blanks; 1 fin. part two areas with insuffi-
Support-- Vane Inner blanks	"as-fired"			cient stock for
RB SiC	1	NI	crack in base of two lugs	machining
$\rho = 2.97 \text{ g/cc}$	finished			
Carborundum	part			
EX132415	10	LDI	4 blanks NI, 6 crazing and pits on OD	No visual exam on blanks; 1 fin. part tool chatter
Support-- Vane Outer blanks	"as-fired"			marks around slots in OD
RB SiC	1	NI	& ID; 1 fin. part three pits	
$\rho = 2.97 \text{ g/cc}$	finished			
Carborundum	part			
EX130156	2	2 LDI	1 NI, 1 minor pit	ID of each shroud etched to form abradable layer
Shroud				
RB SiC				
Carborundum				

*HDI = high-density indications, LDI = low-density indications, NI = no indications

Approximately 75 additional components are currently in process and have not completed all phases of NDE at this time.

TABLE XVII. NONDESTRUCTIVE CHARACTERIZATION OF STRUT SHELLS

<u>Material</u>	<u>Quantity</u>	<u>X-ray*</u>	<u>FPI</u>	<u>Visual (10-30X)</u>
EX125684	15	15 NI	15 minor pits, 2 with long through cracks	6 NI, 2 with cracks, 7 with minor pits
REFEL SiC				
$\rho = 3.09 \text{ g/cc}$				
Pure Carbon				
EX130179	121	21 semifinished parts, severe cracks & LDI; 100 blanks, LDI	21 semifinished parts, cracks; 99 blanks NI, 1 blank pits	Considerable cracking visible on ID of 21 semifinished parts; 100 blanks NI
α -SiC				
$\rho = 3.15 \text{ g/cc}$				
Carborundum				

*NI = no indications; LDI = low-density indications.

TABLE XVIII. NONDESTRUCTIVE CHARACTERIZATION OF SILICON NITRIDE BLADE COUPONS

<u>Material</u>	<u>Quantity</u>	<u>X-ray*</u>	<u>FPI</u>	<u>Visual (10-30X)</u>
EX125681	23	19 NI, 4 LDI	6 NI, 17 pits	2 NI, 21 small pits
3502 Si ₃ N ₄				
$\rho = 3.22 \text{ g/cc}$				
MOR = 475 MPa (69 ksi)				
GTE				

*NI = no indications; LDI = low-density indications.

SHROUD ABRADABILITY

Abradability testing of shrouds required imbedding a portion of the ring in urethane plastic for attachment to the test rig. In this manner, the test wheel could be placed inside the ring and the shroud moved into the rotating blades. This test arrangement is shown in Figure 55.

Based upon the results of abradability and erosion tests previously performed on samples of Corning LAS foamed type 1050 cement, three abradable blade tip shrouds were purchased for engine evaluation. These shrouds, P/N EX 130193, were scheduled for abradability tests prior to being released for engine use. They were intended to be identical with respect to the abradable coating; however, when they were examined, it was obvious that the density of the coating on one of the shrouds (FX 23083) was very different from that of the remaining two (FX 23081, 23082), its porosity being extremely open. Figures 56 and 57 are views of the surface structure of shrouds FX 23081 and FX 23083 in which the differences are readily apparent.

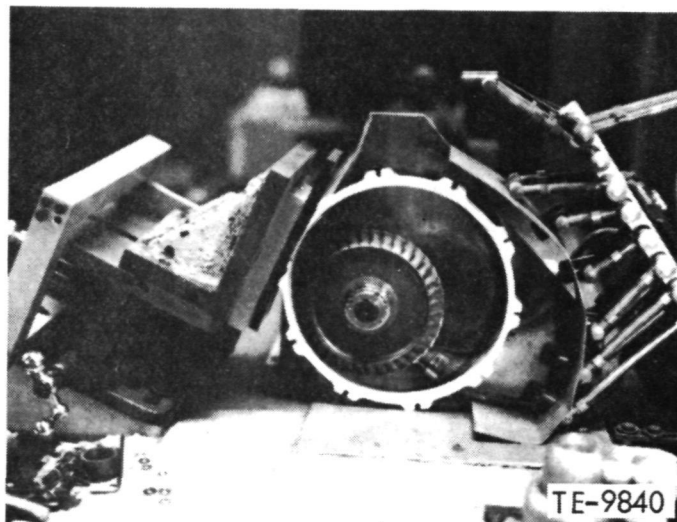


Figure 55. Low-speed abradability test rig.

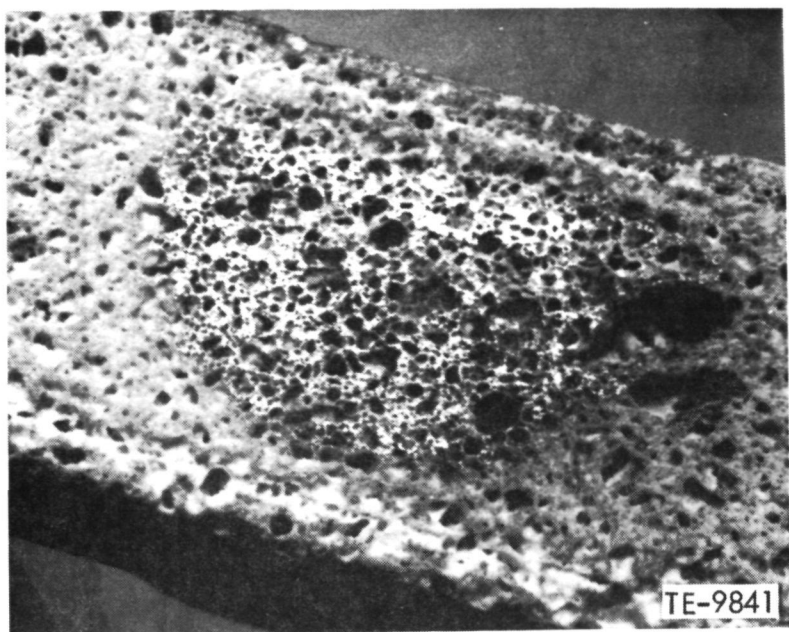


Figure 56. LAS shroud FX 23081. (5X)

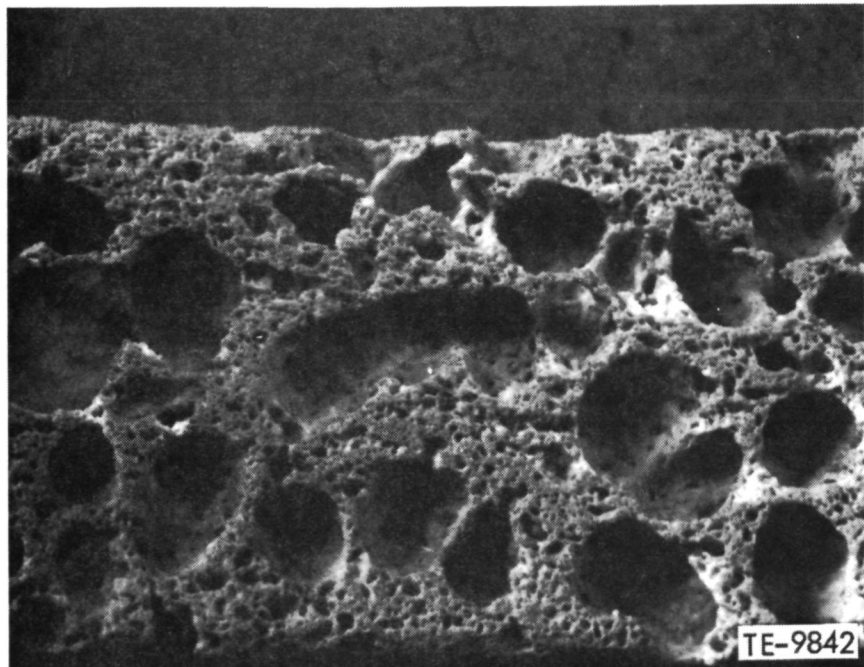


Figure 57. LAS shroud FX 23082. (5X)

ORIGINAL PAGE IS
OF POOR QUALITY

Testing of shroud FX 23082 resulted in a 0.58-mm (0.23 in.) rub depth (Figure 58) with a loss of blade tip material of approximately 0.025 mm (0.001 in.). The quality of the abradable coating in this shroud was very uniform. The abradability of shroud FX 23083 was found to be somewhat better than that of FX 23082, probably because of the unusually large percentage of void area present. A rub dept of 0.43 mm (0.017 in.) was achieved with no loss in blade tip material. The absence of blade material loss is probably the result of the relatively small amount of LAS in the actual contact zone. Erosion loss of the normally dense material (FX 23082) is shown in Figure 59. This loss is not considered severe although the erosion rate in the vicinity of the larger pores appears to be accelerated.

Reaction-Bonded SiC Shroud (P/N EX 130156)

Two reaction-bonded silicon carbide shrouds were received from the Carborundum Company. These shrouds were of the newer 2070°F configuration, with a bulk density of 2.88 g/cc. Testing of the shrouds in selected areas showed them to be very similar in abradability performance, resembling the 2.88-g/cc samples previously tested. Figures 60 and 61 show the abradability rubs on each shroud. Two different rub patterns can be seen in Figure 60 as a result of the varied nature of the seal surface.

In some areas the surface appeared etched or spongy. Rubs were made in areas which appeared normal as well as in areas with the etched-type surface. Total depth for the two rubs was 0.69 mm (0.027 in.), with a blade tip loss of 0.08 mm (0.0032 in.). The abradable surface of the second shroud (Figure 61) had a completely different appearance with respect to color and texture. The color of the abradable surface on the first shroud was black; the second one was green. The black color and surface variations in the first shroud were attributed to contamination during the leaching operation. There was no difference in abradability performance between the first and second units, as can be seen in Figure 61. Metallic debris is present in the wear track, and blade tip loss was 0.025 mm (0.001 in.) for a depth rub of 0.178 mm (0.007 in.).

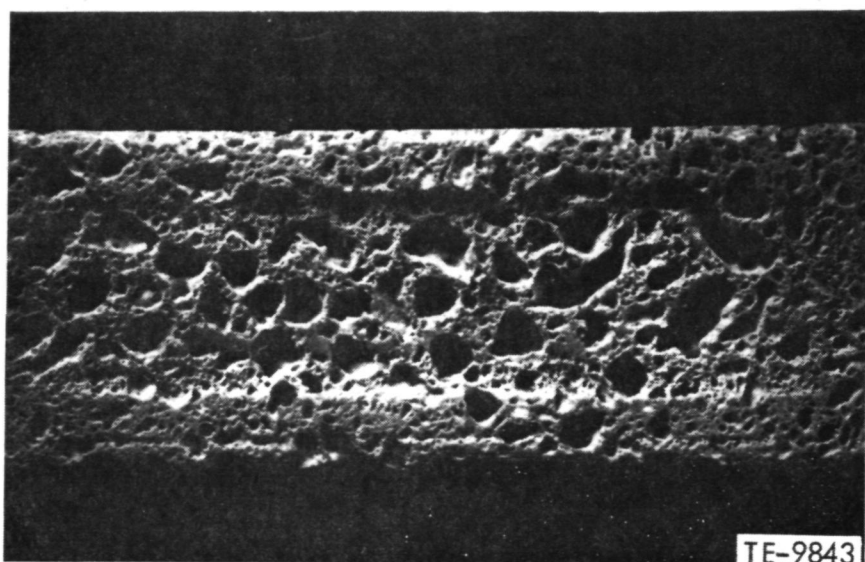


Figure 58. Shroud FX 23082--Corning LAS foam abradable layer--0.58-mm (0.023 in.) rub depth, 0.025-mm (0.001 in.) blade tip loss. (3X)

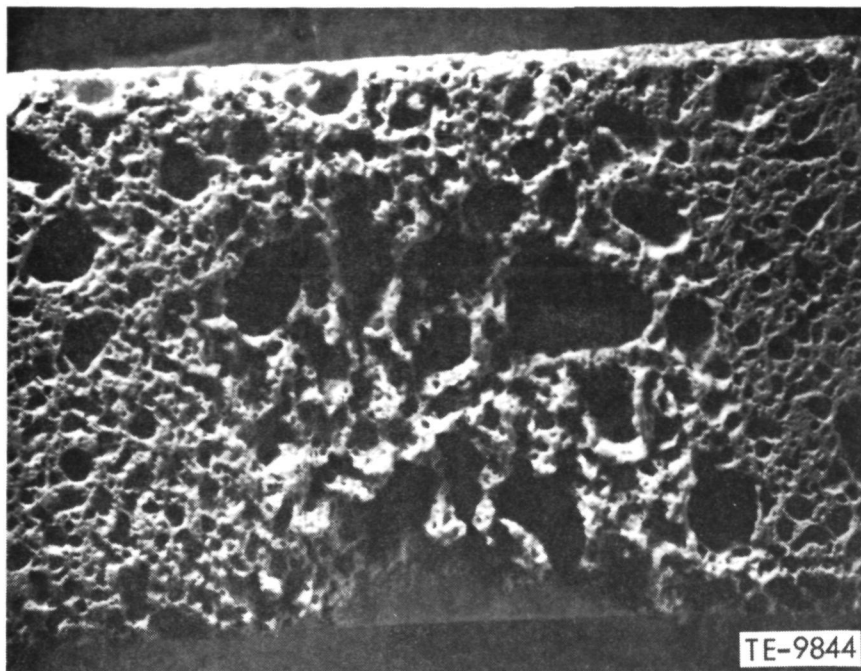


Figure 59. LAS shroud FX 23082 erosion test (0.34 g/min). (5X)

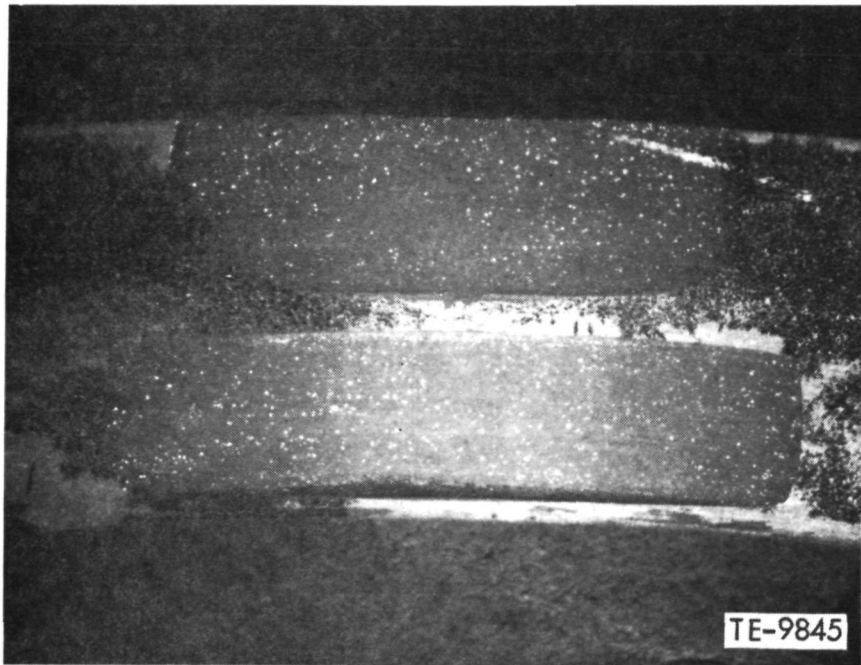


Figure 60. Carborundum shroud FX 23782--0.69-mm (0.027 in.) rub depth,
0.08-mm (0.0032 in.) blade tip loss.

ORIGINAL PAGE IS
OF POOR QUALITY

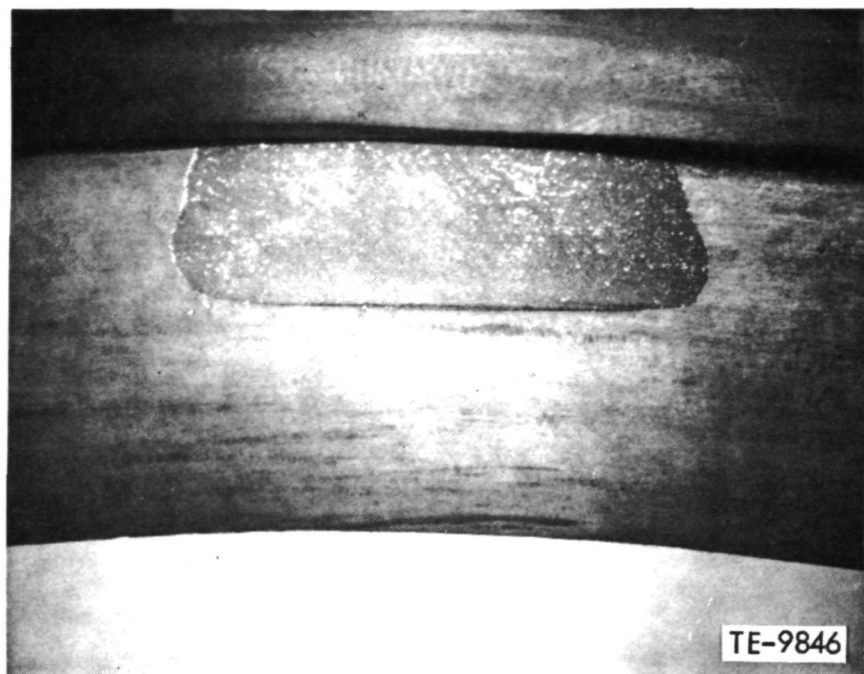


Figure 61. Carborundum shroud FX 23781--0.178-mm (0.007 in.) rub depth, 0.025-mm (0.001 in.) blade tip loss.

CERAMIC MACHINING DEVELOPMENT

Machining development work has been directed at defining the potential of conventional machining methods. The bulk of the testing has involved various grades of silicon carbide. Silicon nitride has been more prone to chipping than silicon carbide.

General grinding, jig grinding, and ultrasonic machining have been proved effective in machining fired ceramic components. These operations establish the capability of producing all of the present generation of ceramic components except for the dovetail portion of the blade.

General Grinding

Internal, rotary, and regular surface grinding techniques have been developed and are being used to manufacture ceramic components at this time. Conventional form grinding has been tested, but this method has been found to cause high levels of part chippage and unsatisfactory surface finishes. Form grinding, using a crush dressable diamond wheel in conjunction with creep feed grinding techniques, has performed very well. The ground samples had a 3-5 rms surface finish with no chipping. Creep feed grinding will be used to machine the ceramic blade dovetail.

The grinding tests have shown that G ratios, (in.³ of stock removed/in.³ wheel lost) of 50 or better are readily attainable when resin-bonded wheels are used. Metal-bonded wheels achieve G ratios of 100 or better.

Jig Grinding

Basic jig grinding trials with diamond-plated mandrels have established the necessary machining parameters. Testing of metal- and resin-bonded mandrels will be conducted as soon as the tooling is received. Tolerances closer than 0.012 mm (0.0005 in.) can be held with resultant surface finishes in the range of 0.15 m (6 rms) to 0.32 m (13 rms). This provides machining capability for straight or radially generated edge machining, open-ended slots, and through-slots with starter holes.

Ultrasonic Machining

Ultrasonic machining techniques have been developed to allow irregular-shaped holes to be machined within a 0.025-mm (0.001 in.) tolerance band. Surface finishes of 0.125 m (5 rms) to 0.20 m (8 rms) are readily obtainable.

New tool designs are being developed to decrease the time required to change the tooling during the machining cycle. Presently, each tool is brazed onto a toolholder before it can be used. This consumes more time than the actual machining. Initial tests of the new tool concepts have shown very good potential. It is expected that the new tool designs and overall process improvements will make this process very competitive.

IV. CERAMIC TURBINE COMPONENTS

INTRODUCTION

The activities that took place during this reporting period involved ceramic component design analysis, fabrication of 2070°F ceramic components, and process development effort at the Carborundum Company. The following are the major accomplishments and findings for this period:

- o Completion of 3-D finite element analysis of the 2070°F vane inner support rings. The probability of survival is calculated to be 0.9989 (11 failures/10,000 parts).
- o Completion of work to develop a simplified finite element model for evaluation of alternate blade designs.
- o Fabrication of silicon carbide strut shells and vane retaining rings by Pure Carbon Company.
- o Fabrication of silicon carbide inner and outer support rings, strut shells, 2070°F vanes, and abradable turbine tip shrouds by the Carborundum Company.
- o Successful hot spin proof testing of ceramic blade coupons.
- o Cyclic spin testing to evaluate blade dovetail compliant layer material was completed. L605 was determined to be an acceptable material.
- o Initial fabrication of a silicon carbide plenum was completed by the Carborundum Company.

GASIFIER TURBINE NOZZLE

2070°F Design

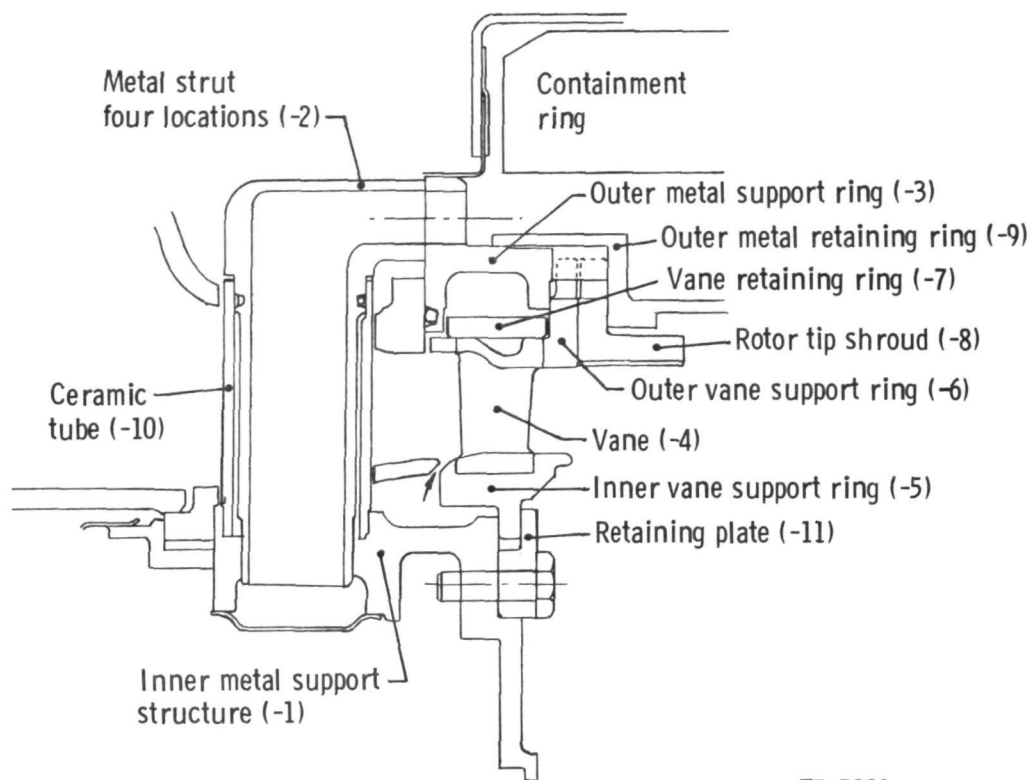
The 1132°C (2070°F) gasifier turbine nozzle design activities involved ceramic component probability of survival analysis and coordination of component fabrication. The Carborundum Company continued its efforts under subcontract to fabricate 1132°C (2070°F) turbine components of silicon carbide.

Nozzle Component Analysis

The 1132°C (2070°F) gasifier turbine nozzle design (Figure 62) consists of 6 ceramic parts. Four of these parts were subjected to probability of survival analysis and 2 were not considered because of the less severe gas conditions around the parts. The results of the analyses for the vane (-4), the abradable turbine tip shroud (-8), and the outer vane support rings (-6) were presented in the previous semiannual report. The inner vane support analysis (-5 and Figure 63) was completed during this reporting period and is presented in this section along with the continued analyses of the vane and outer vane support ring.

The finite element model of the inner vane support ring (Figure 64) included 4 vane pockets and represents 1/7 of the total ring.

Probability of failure analysis was completed for the heat-up transient condition defined in Figure 65. The material characteristics used in this analysis were for reaction-sintered silicon carbide. The steady-state heat transfer analysis of the inner support ring resulted in a maximum component temperature



TE-5808

Figure 62. 2070°F ceramic vane assembly.



TE-9876

Figure 63. Inner vane support ring.

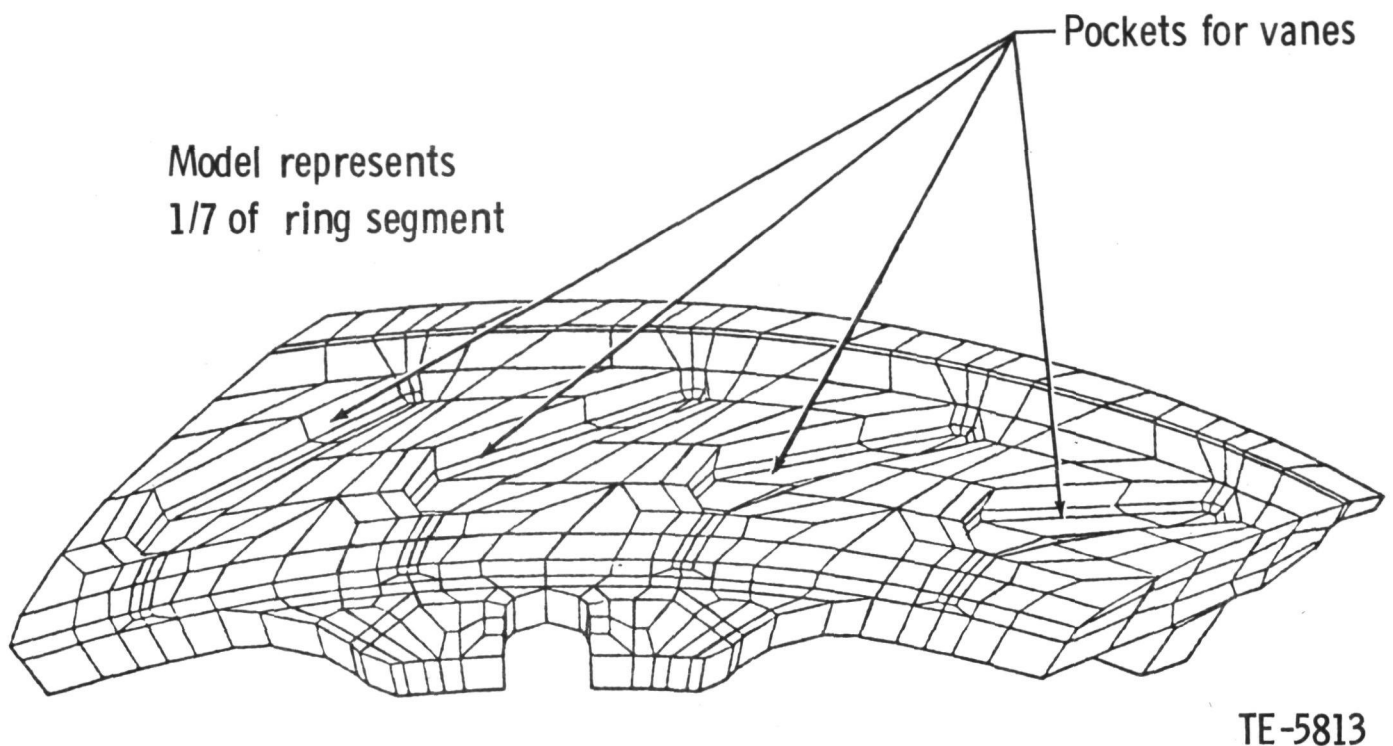


Figure 64. Finite element model of ceramic inner vane support ring.

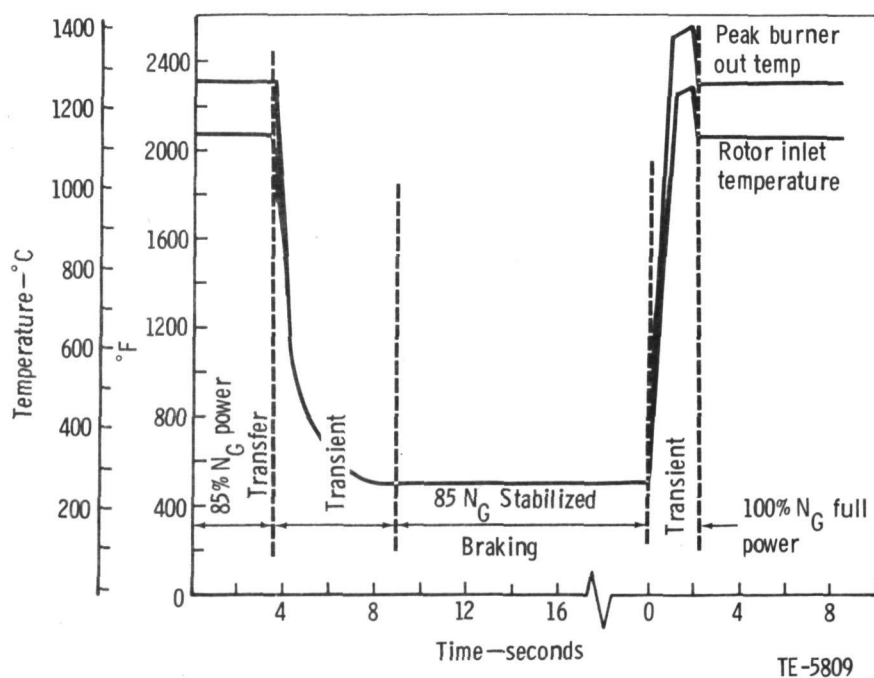


Figure 65. CATE 2070°F engine thermal transients for heat transfer analysis.

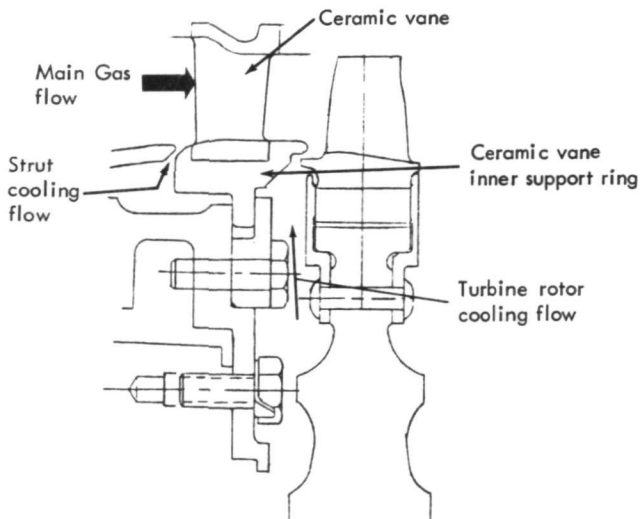
of 868°C (1595°F). This steady-state operating temperature is the lowest of any of the ceramic components analyzed to date. This is due to the turbine cooling air flow running up the back face and the strut cooling air flowing across the front face of the ring (Figures 66 and 67).

Transient heat-up thermal analysis of this ring was also conducted. From the steady-state analysis, it was determined that the coolest portion of the ring would be the ID axial retaining flange, and that the hottest point would be on the flow path surface. The temperatures for nodes representing these two points appear in Figure 68. The maximum temperature differential of 135°C (243°F) occurs at 8 seconds after initiation of the transient. The temperature distribution at 8 seconds appears in Figure 69 and was used as the basis for a stress analysis, which resulted in the stress distribution shown in Figure 70.

The peak maximum principal stress of 114.04 MPa (16.54 ksi) occurs on the ID axial retaining flange. With this stress distribution and the material strength properties of reaction-sintered silicon carbide--MOR = 366.8 MPa (53.2 ksi) and $m = 8$ --the probability of success for the heat-up thermal transient is $P_s = 0.998901$ or 1 failure in 1000 components tested. A similar analysis on the cool-down transient resulted in a probability of survival of 0.999767.

The design goal based on competitive warranty requirements was a 0.999756 probability of survival. The heat-up transient survival rate at 0.998901 does not meet the reliability goal. As with all other components, the inner vane support ring will be burner rig proof tested to the critical thermal transients before engine testing, thereby attaining the required probability of survival upon installation in the engine.

With the completion of the inner ring, the initial probability of failure analysis package including the vane, shroud, outer vane support ring, and inner vane support ring is completed. Table XIX presents a summary of the results of the analysis. The outer vane support ring has the lowest probability



TE-9877

Figure 66. Ceramic vane inner support ring environment.

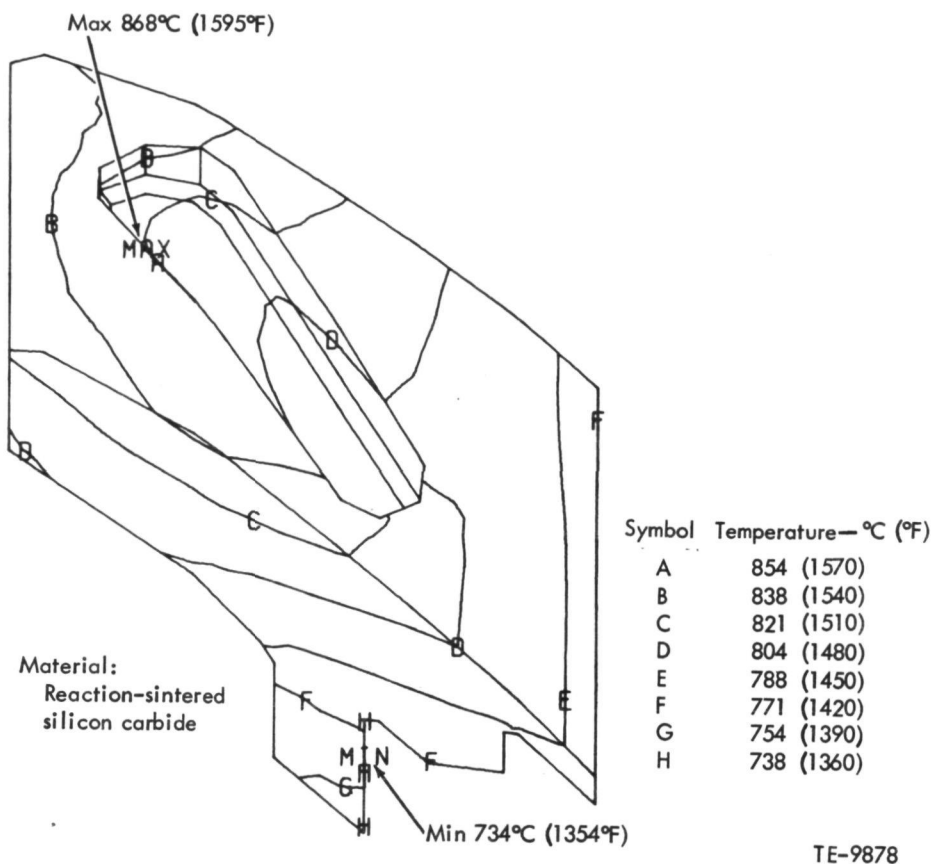


Figure 67. Ceramic vane inner support ring steady-state temperatures (1/28 of total ring).

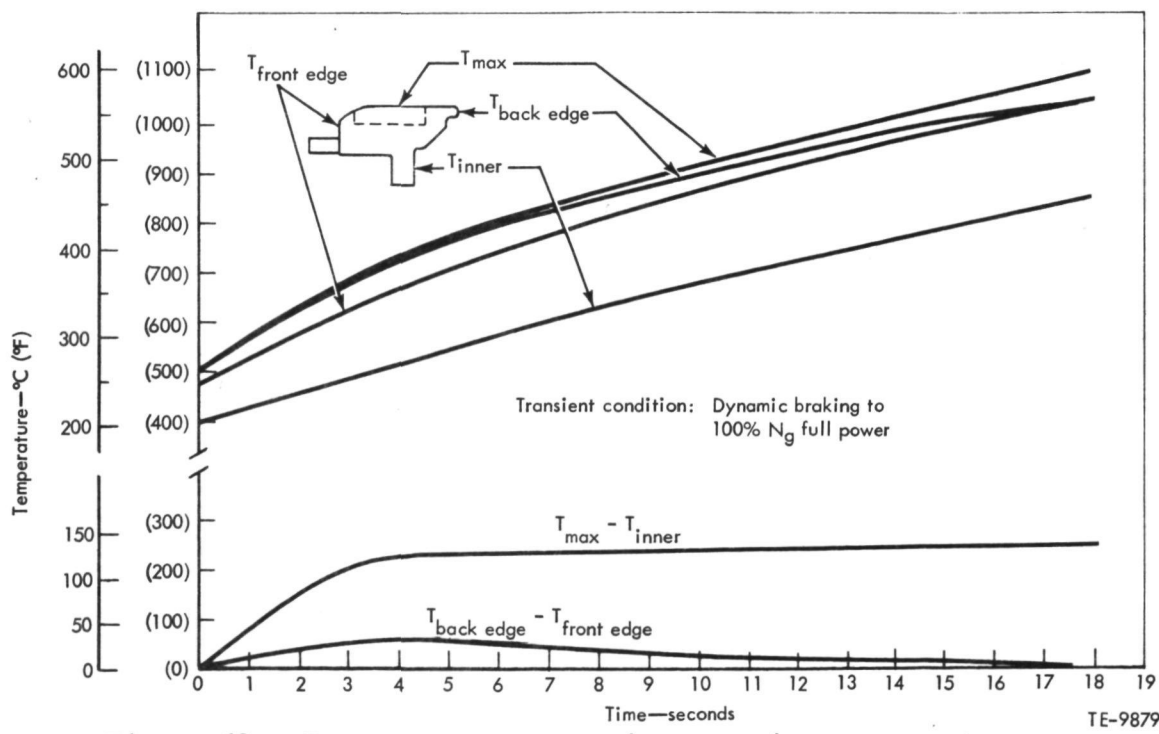


Figure 68. Inner vane support ring transient temperatures.

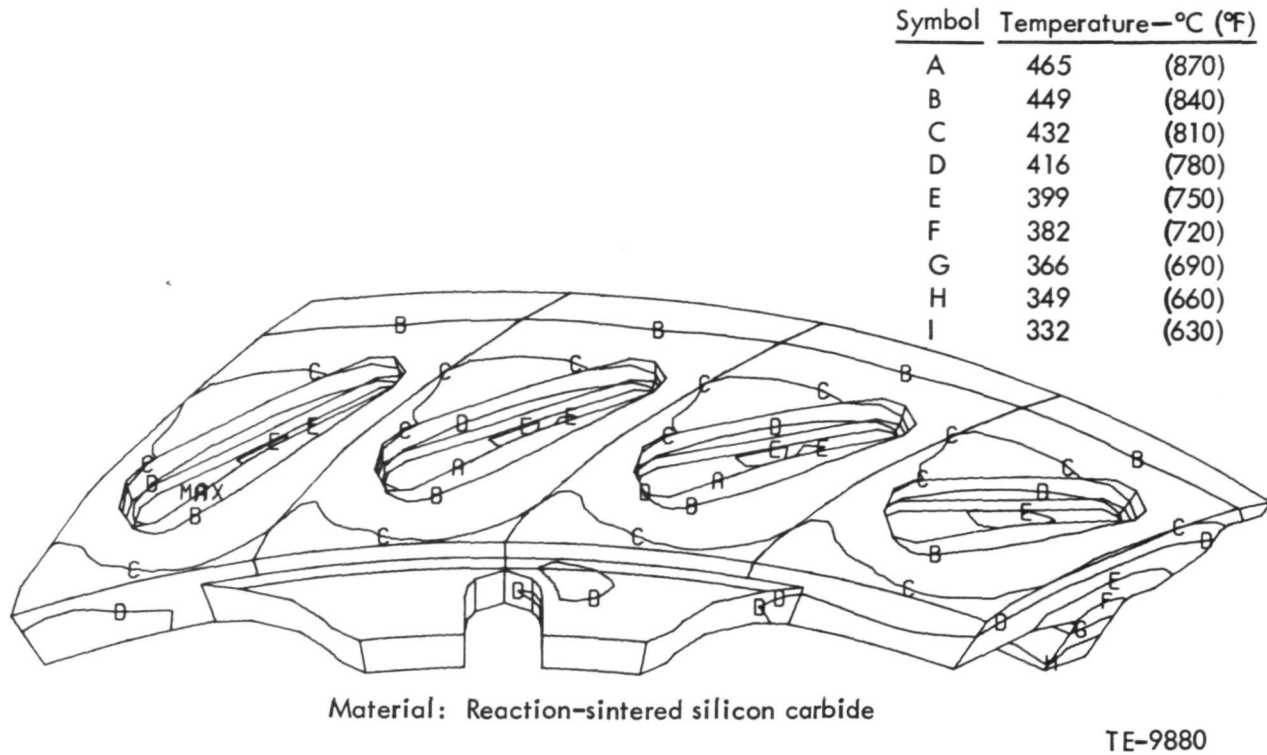


Figure 69. Inner vane support ring temperature distribution at 8 seconds into heat-up thermal transient.

TABLE XIX. SUMMARY OF GASIFIER TURBINE NOZZLE CERAMIC COMPONENT ANALYSES

<u>Component</u>	<u>Probability of survival*</u>	<u>Maximum principal stress, MPa (ksi)</u>	<u>Transient generating stress</u>	<u>Design goal**</u>
Vane	0.985918	368.18 (53.40)	Heat-up, dynamic braking to 100% power	0.999974
Shroud	0.999999	77.70 (11.27)	Heat-up, dynamic braking to 100% power	0.999941
Inner vane support ring	0.998901	114.04 (16.54)	Heat-up, dynamic braking to 100% power	0.999757
Outer vane support ring	0.762592	381.62 (55.35)	Cool-down, 85% N _G to dynamic braking	0.999757

*Based on a reaction-sintered silicon carbide material strength represented by a MOR of 366.80 MPa (53.2 ksi), m = 8.0.

**Design goal is based on production reliability and warranty requirements.

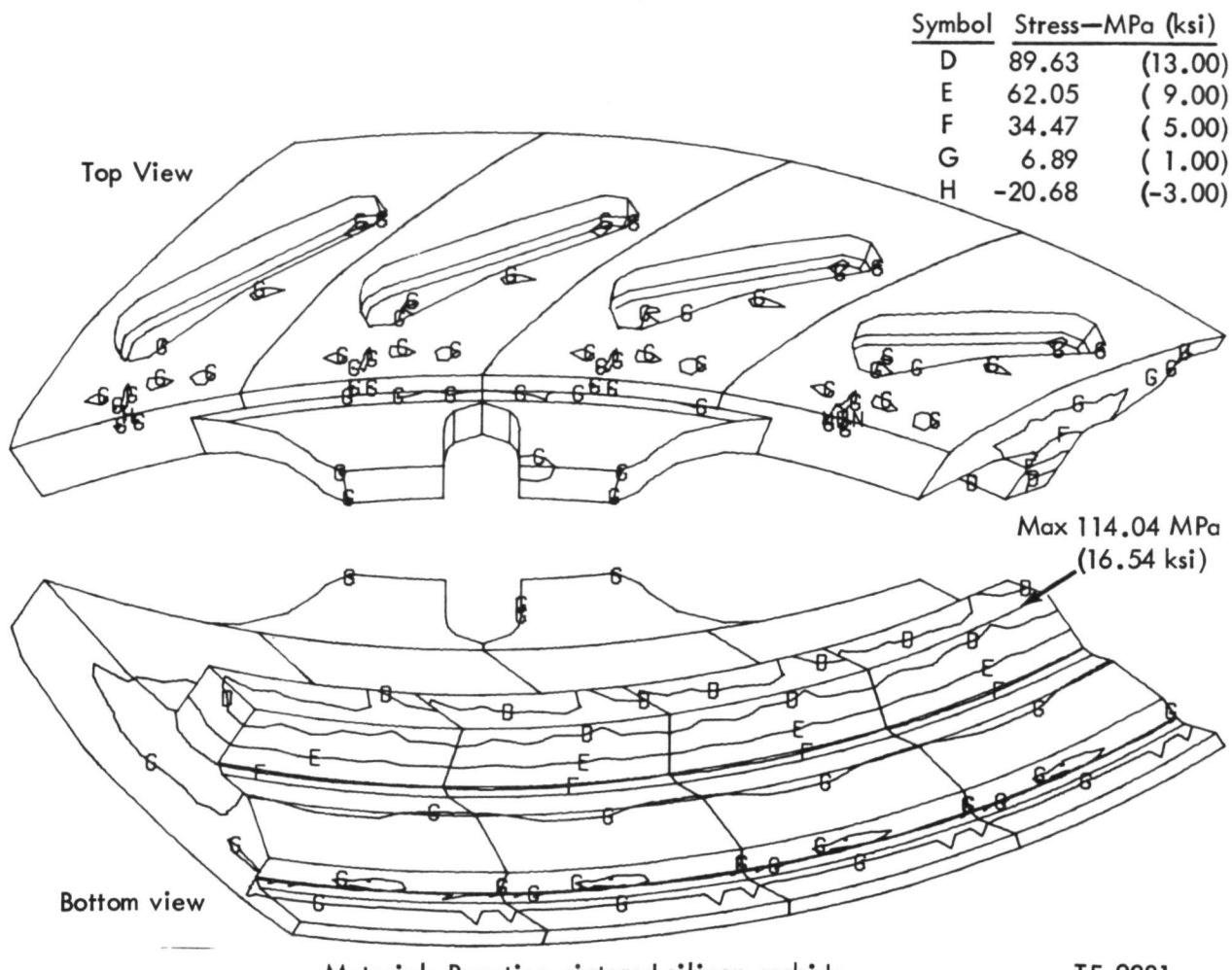


Figure 70. Inner vane support ring maximum principal stress distribution at 8 seconds into heat-up thermal transient.

of survival at 0.762592. The probabilities of survival for the vane (0.985918) and the outer support ring (0.762592) were low enough that they warranted further analysis. Follow-on analysis programs have been planned and initiated to investigate methods to increase the survival rate for these two components. It must be recognized that these predictions are based upon the material properties as they stood at the initiation of the analysis. Process development is continually improving the realizable strength which, in turn, will improve the probability of survival.

The follow-on vane analysis is being conducted with revised heat transfer coefficients on the vane platform ends. The initial analysis of the vane was made with insulated vane platforms (both inner and outer) as a worst case approach. Subsequent secondary flow analysis has determined that from 0.4 to 1.4% of the primary gas flow can pass over just the outer vane platform. This definitely does not result in an insulated vane platform. Therefore, a

reanalysis will show a vane that is more evenly heated, with lower thermal gradients, lower thermal stresses, and a higher probability of survival. This reanalysis is presently undergoing heat transfer analysis.

The follow-on analysis of the outer vane support ring determined that its low probability of survival (0.762592) was due to different thermal response rates between the front and rear portions of the ring. The thin front edge responds to flow path gas temperature changes faster than the more massive rear flange. The resultant differential thermal expansion produces the internal loads and stress which yield the low survival rate. Three modifications to the outer support ring are being investigated to address this problem.

The first modification to the vane outer support ring is to block the secondary flow over the front edge of the ring (Figure 71). This will reduce the heat input to the less massive front edge and tend to equalize the thermal response rates of the two ring sections. The second and third modifications are to slot the ring on the front edge at the vane through-hole, which is the peak stress point (Figure 72). This breaks up the hoop integrity of the front section of the ring and allows differential thermal expansion without creating the internal loads. A probability of success analysis will be conducted for the ring cut in two different manners (7 and 28 equally spaced cuts). The modeling revisions for these modifications have been completed, and the models are undergoing heat transfer analysis.

Carborundum Process Development

Carborundum (CBO) continues under subcontract to develop stationary silicon carbide components. The objective of this subcontract is to conduct the necessary process development of silicon carbide materials to produce ceramic vanes, shrouds, and support rings for the 1132°C (2070°F) CATE engine.

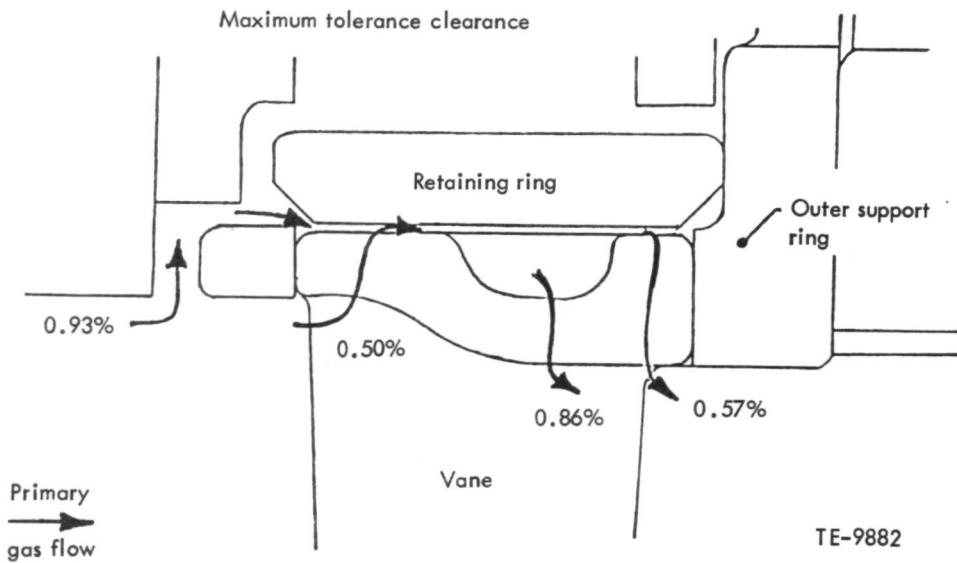


Figure 71. Secondary gas flow over 2070°F ceramic vane and outer support ring.

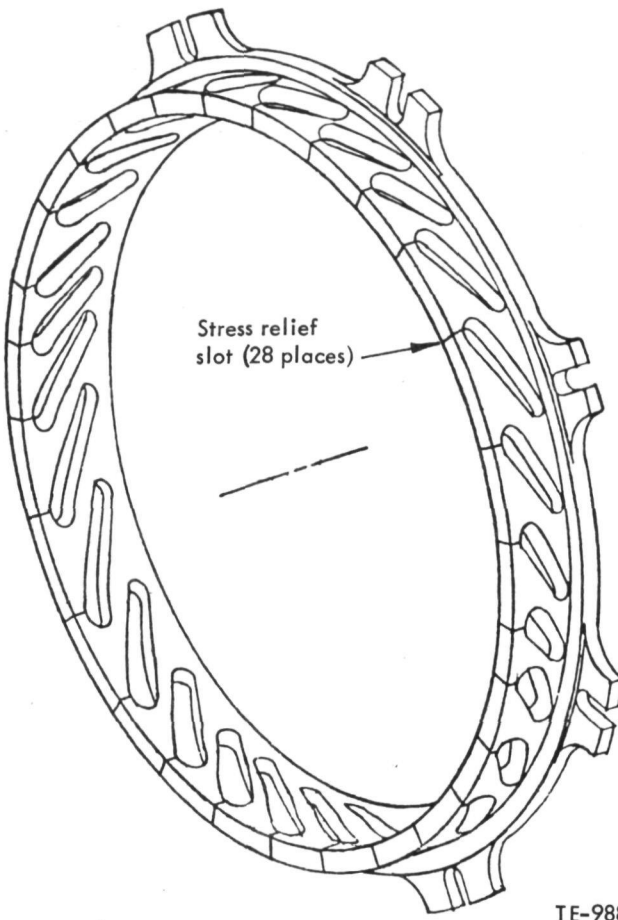


Figure 72. Outer vane support ring (split in 28 places).

Carborundum's work on the 1132°C (2070°F) gasifier turbine components is divided into four tasks. Task I, the ceramic blade, is reported under a subsequent heading. Tasks II through IV, the stationary ceramic components, are defined as follows:

- Task II - Vane development
- Task III - Shroud, inner support ring, and outer support ring development
- Task IV - Material variation investigation

The material used in Tasks II and III is reaction-sintered silicon carbide. In Task IV, the basic reaction-sintered silicon carbide material is subjected to several process variations which affect the microstructure and strength. Also in Task IV, a vane will be fabricated from sintered alpha silicon carbide.

Work in the previous reporting periods involved the design and procurement of molds and molding of initial parts for each of the tasks. The following is a report of the progress made in each of the tasks.

Task II - Vane Development

The activities relative to the ceramic vane involved an evaluation of 15 reaction-sintered silicon carbide vanes, representing the initial fabricating process. NDE and dimensional inspection was completed at DDA. Three of the vanes had X-ray indications (two with low density and one with high density). In Zyglo crack detection, DDA found the vanes clean where CBO found very fine line indications on four vanes. Visually, both DDA and CBO noted numerous nicks and scratches from the hand grinding operation to remove the excess silicon. Measured density on these vanes was 2.94 g/cc. Dimensionally these vanes were acceptable except for the inner platform and the first two airfoil sections (A-A and B-B), which appear to have twisted at the trailing edge in the direction to uncamber the vane. Carborundum felt that this could happen when the green molded vane is lifted out of the tool. Six vanes reflecting revised handling procedures were subsequently dimensionally checked without significant improvement. This should not significantly affect aerodynamic performance, but it will require some hand blending on the vane to fit the master vane platform contour gage. Tool modification will correct this problem.

Failure analysis of base-line (per process routing in the previous semiannual report, Table XXIV) bonded silicon carbide test bars found that many failure sites were associated with the lack of microstructural uniformity. The primary flaw type is a graphite inclusion or a void left by the oxidation of the graphite cluster at high temperature. The existence of the graphite inclusion indicated a lack of complete mixing in the preparation of the molding compound. To address this problem, a hammer milling step was added to the process routing as item 2C in the aforementioned process routing. It was found that the hammer milling tends to give a more homogenous microstructure due to a more uniform mixing of the molding compound.

Carborundum has completed bend tests of the base-line material and the material made under the revised process routing. Table XX presents a summary of Carborundum's test data at 20°C (68°F), 1100°C (2012°F), and 1300°C (2372°F). These bars were made by transfer molding. Note that adding hammer milling to the process increases the average test bar strength by 52 to 143 MPa (7 to 21 ksi). However, the low Weibull Moduli (2.87 to 6.00) indicate the presence of strength-limiting flaws in some test bars that were not found by NDE.

Processing has begun for the final 56 reaction-sintered silicon carbide vanes that will complete this task. These vanes will include the hammer milling processing step that previous testing had shown to increase material strength. Delivery of these vanes is expected during the next reporting period.

Task III - Ring Structure Development

Task III is divided into subtasks that cover three different ceramic ring structures:

- Task IIIa - Abradable turbine tip shroud
- Task IIIb - Inner vane support ring
- Task IIIc - Outer vane support ring

TABLE XX. CARBORUNDUM TRANSFER-MOLDED, REACTION-SINTERED SILICON CARBIDE STRENGTH CHARACTERIZATION

4-point bend test results summary* - MPa (ksi)

	Room Temp		1100°C (2012°F)		1300°C (2372°F)	
	base line	hammer milled	base line	hammer milled	base line	hammer milled
Mean value	314.54 (45.62)	392.21 (57.03)	355.91 (51.62)	406.58 (58.97)	308.68 (44.77)	499.95 (65.26)
Standard dev	82.67 (11.99)	103.35 (14.99)	85.56 (12.41)	151.89 (22.03)	60.26 (8.74)	117.28 (17.01)
Weibull Modulus	3.32	2.87	4.73	2.24	6.00	3.89
Number of bars	50	50	20	20	20	20
High strength value	487.46 (70.72)	500.08 (72.53)	562.47 (81.58)	642.52 (93.19)	510.56 (74.05)	588.67 (95.38)
Low strength value	98.25 (14.03)	96.73 (14.03)	262.69 (38.17)	95.42 (13.84)	215.12 (31.20)	262.21 (38.03)

Hammer milling added to material processing.

*Carborundum test data - bar size 3.18 x 6.35 x 50.8 mm (0.125 x 0.250 x 2.0 in.) 1/3 point loading, with center span of 12.70 mm (0.5 in.)

In Figure 62, these components are -8, -5, and -6, respectively. Fabrication of these rings requires similar processing procedures, but handling and machining problems will involve different approaches. Task IIIa includes a study of how variations of the material composition affect the abradability of the ceramic turbine tip shroud. Thus, a general discussion on the forming of the rings will be presented, followed by details unique to the individual parts.

All three rings are formed by warm compression molding of a cylindrical ring, baking, soft (green) machining to near net shape, siliconizing, and final machining (diamond grinding or ultrasonic). The tooling to form a cylindrical ring is a simple set of ID and OD rings with a cylindrical plunger. In addition to molding a simple ring and soft machining a part, a casting and a complex compression molding technique were to be tried on the inner vane support ring (Task IIIb). The complex compression molding technique has since been dropped due to uneven shrinkage in bake-out.

Since the casting technique has not been previously demonstrated, there is no specific process routing for the casting process. The process routing for the ring structures fabricated from the simple tool appears in Table XXV of the previous semiannual report. The aforementioned process for forming ring structures was the starting method of fabrication; to date there have been no changes.

Task IIIa--Abradable Turbine Tip Shroud

The basic function of the turbine tip shroud is to control the rotor tip clearance. Rather than trying to hold the shroud diameter precisely on the rotor center with a fixed radial clearance, it is easier to allow the rotor to cut (abrade) its own required clearance. Ceramic material is desirable in this application because its low coefficient of expansion does not require cooling to control its diametral growth, but then the flow path surface must be abradable. To address this requirement, a part of the work completed in the previous reporting period involved the evaluation of a matrix of abradable reaction-sintered silicon carbide coupons.

Both DDA and Carborundum evaluated the abradability coupons, and Carborundum evaluated the MOR bars. The detailed results of the evaluation of the abradability coupons and MOR bars are reported in Section III and in the previous semiannual report. The basic results were that materials at the 2.95-g/cc density were found not abradable. The metal test rotor would gall and transfer rotor material to the test coupon. The 2.82-g/cc material was very abradable.

Previous engine testing of ceramic shrouds at DDA had confirmed that the 2.95-g/cc material is not abradable. Additional shrouds of the 2.91- and 2.84-g/cc density material were ordered and delivered during this reporting period. The 2.91-g/cc density shrouds were blanks to be finish machined at DDA into 1900°F configuration parts. Of the four blanks ordered, three were delivered. All three blanks were finish machined at DDA. Surface treatment for abradability at Carborundum resulted in two good shrouds and one broken in the leaching process. These two 1900°F configuration parts have not yet been burner rig proof tested or evaluated for abradability. After these two tests are completed, one of the parts will be incorporated into the engine test program. The 2.84-g/cc density shrouds were selected for the 2070°F configuration based on the abradable matrix evaluated in the previous reporting period.

The material used for the turbine tip shroud is identical with that used for the inner and outer vane support rings except that it is molded to a lower density. This lower density allows it to be siliconized to a lower final density, which gives the necessary abradability after acid treatment. An unexpected difficulty arose after the baking process used to carbonize the resin binders. At this point the shrouds are "green machined" to final size, but the low-density material was relatively weak and shrouds were broken in the machining. This problem was reduced by using a graphite ring to surround the shroud blanks as they were clamped in the chuck jaws. The problem could also be reduced by changing the mix composition so that it can be pressed to a high green density while still obtaining a low final density. This can be done by two methods: (1) substituting a lower char yield resin or (2) adding elemental silicon powder right into the mix.

During the current reporting period two turbine tip shrouds of the 2070°F configuration were delivered to DDA. Measurements prior to abradability showed the material density to be 2.87 and 2.88 g/cc as opposed to the desired 2.84-g/cc goal. Possible causes of the density variation are that (1) the green molded body may be nonuniform in density so that green machining would increase the density of the final part through the removal of lower-density

excess stock material or (2) the difference in the 2.85- and 2.88-g/cc densities is only 0.04 g/cc or 1.4%. It may not be possible to control densities of large-diameter ring structures to any greater degree of accuracy.

The Material Laboratory evaluated the abradability of these two shrouds. The evaluation is reported under the Abradable Seal Material Development heading in Section III (ref Figures 60 and 61).

Carborundum completed 4-point bend tests at 20°C (68°F) and 1100°C (2012°F) of the abradable shroud material. The bars were made by warm compression molding plates to a 2.84-g/cc density and then cut into test bars. The results of these tests appear in Table XXI. Note that the strength of this material at room temperature is equal to that of the transfer-molded material, but its 1100°C (2012°F) strength of 510.14 MPa (73.99 ksi) is 103 MPa (15 ksi) higher than that of the vane material. Experience has indicated that warm-compression-molded material is expected to be stronger than the transfer-molded material.

TABLE XXI. CARBORUNDUM COMPRESSION-MOLDED, REACTION-SINTERED SILICON CARBIDE STRENGTH CHARACTERIZATION

4-Point Bend Test Summary* - MPa (ksi)

	<u>Room Temp</u>	<u>1100°C (2012°F)</u>
Mean value	389.76 (56.53)	510.14 (73.99)
Standard dev	44.13 (6.40)	105.56 (15.31)
Weibull Modulus	9.59	5.38
Number of bars	20	20
High strength value	454.71 (65.95)	695.75 (100.91)
Low strength value	277.58 (40.26)	368.04 (53.38)

Note: 2.84-g/cc material density required for abradability

*Carborundum test data - bar size 3.18 x 6.35 x 50.8 mm (0.125 x 0.250 x 2.0 in.) 1/3 point loading, with center span of 12.70 mm (0.5 in.).

Task IIIb--Inner Vane Support Ring

In the previous reporting period, 10 rough machined inner vane support rings and 10 blocks of material for qualification test bars were delivered to DDA. As was reported in Task III, three fabrication techniques were to be tried for making the reaction-bonded silicon carbide turbine vane inner support ring:

- (1) Warm compression molding of a simple ring, baking the ring to char the thermoset resin, machining the ring to size, and subsequent siliconizing and final grinding
- (2) Plastic forming the complex shape, using the turbine vane's transfer molding mix, and siliconizing plus final grinding
- (3) Thixotropic casting a semifluid mix into a rubber mold (the mold is made from a slightly oversize ring pattern), siliconizing, and final grinding

All three of these methods incorporate a final grinding step to achieve the final form and dimensions. The amount of final grinding has a profound influence on the component cost; therefore, it is desirable to make the green body as close to the final size and shape as possible.

The inner support ring has 28 blind hole pockets into which the vanes are inserted. The first fabrication method of warm compression molding with green machining can form these pockets by either machining the green body (preferably after baking to char the resin) or by machining in the final siliconized state. The plastic forming technique (2) and the thixotropic casting technique (3) can produce the rings with the holes molded in place. Because of the high confidence level in technique 1, it was used to fabricate rings for DDA rig and engine tests. A separate study in this Task investigated ultrasonic machining of the vane pockets. Techniques 2 and 3 were investigated for their potential in reducing machining costs when higher quantitites of rings were produced. The results of techniques 2 and 3 follow.

Technique 2, Plastic Forming - Two plastic forming methods could be used for making the inner support rings with a flowable mix:

- (1) Warm compression molding
- (2) Transfer molding.

The 28 vane pockets could be molded in with either method; however, the molding tool is complex and costly. Simple, square cross-section rings were molded from the vane transfer molding mix.

The first two (IIIc and IIId) rings broke during mold unloading, but the third and fourth ones were crack-free. The surface finishes were poor, so the inner and outer diameters of both rings were lathe machined. The bottom and top surfaces were also faced true. Both rings were baked in a vacuum furnace to 1000°C (1832°F) to pyrolyze the resin binders. Table XXII summarizes the dimensional results.

The large amounts of shrinkage, the shrinkage inconsistency, and the amount of out-of-roundness indicates that this plastic molding approach does not appear to be successful; it will not be pursued further.

Technique 3, Thixotropic Casting - Carborundum's proprietary thixotropic casting technique was considered to be a possible method for making turbine rings which have complex geometries.

TABLE XXII. DIMENSIONAL CHANGES IN PLASTIC-MOLDED VANE SUPPORT RINGS

Type	Green Outside <u>Diameter</u>	Baked Outside Diameter <u>Maximum</u>	<u>Minimum</u>	Out-of- Roundness <u>Max-Min</u>
Outer Support Ring	271.31 mm (10.7 in.)	260.35 mm 10.2 in.)	256.92 mm (10.1 in.)	3.43 mm (0.14 in.)
Inner Support Ring	223.77 mm (8.8 in.)	216.92 mm (8.5 in.)	214.76 mm (8.4 in.)	2.16 mm (0.09 in.)
Inner Support Ring	151.26 mm (6.0 in.)	147.96 mm (5.8 in.)	147.45 mm (5.8 in.)	0.51 mm (0.02 in.)
	192.79 mm (7.6 in.)	189.48 mm (7.5 in.)	187.83 mm (7.4 in.)	1.65 mm (0.06 in.)

An aluminum pattern of the inner support ring was made without the scallop and slot features. Based on previous work, 1.5% total shrinkage from the pattern to the final siliconized piece was allowed.

A rubber mold was cast from the aluminum pattern and, in turn, a thixotropic Sic casting was made with this mold. The casting had numerous air bubbles and voids (see Figure 73). However, it was siliconized to get an indication of the dimensional change with this shape. This casting was siliconized according to the same process routing procedures used for the warm-compression-molded inner support rings (see Figure 74). The green casting was marked at the three points of diameter measurement so that the diameters before and after siliconizing would correspond to each other. Table XXIII summarizes the dimensional changes. The worst out-of-roundness was only 0.44 mm (0.017 in.) for the fired ring.

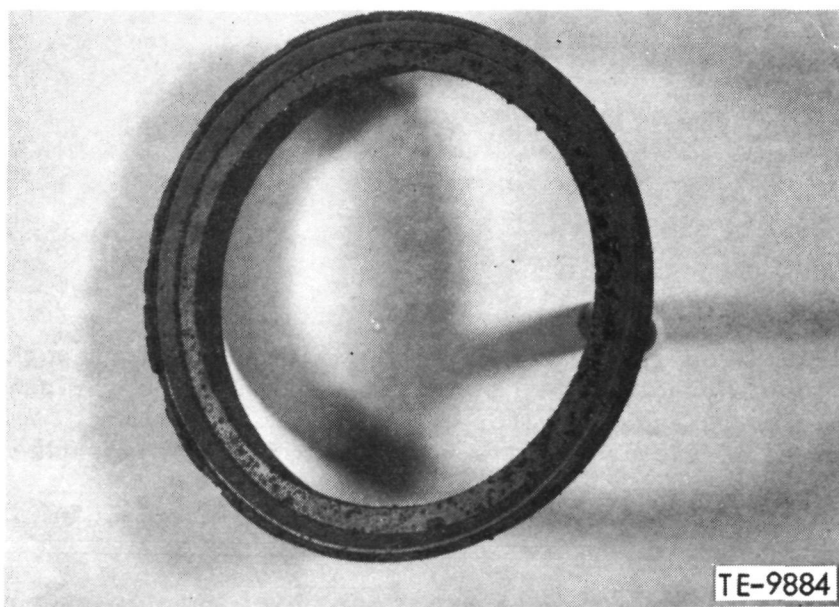


Figure 73. Thixotropic cast inner vane support ring showing numerous air bubbles and voids.

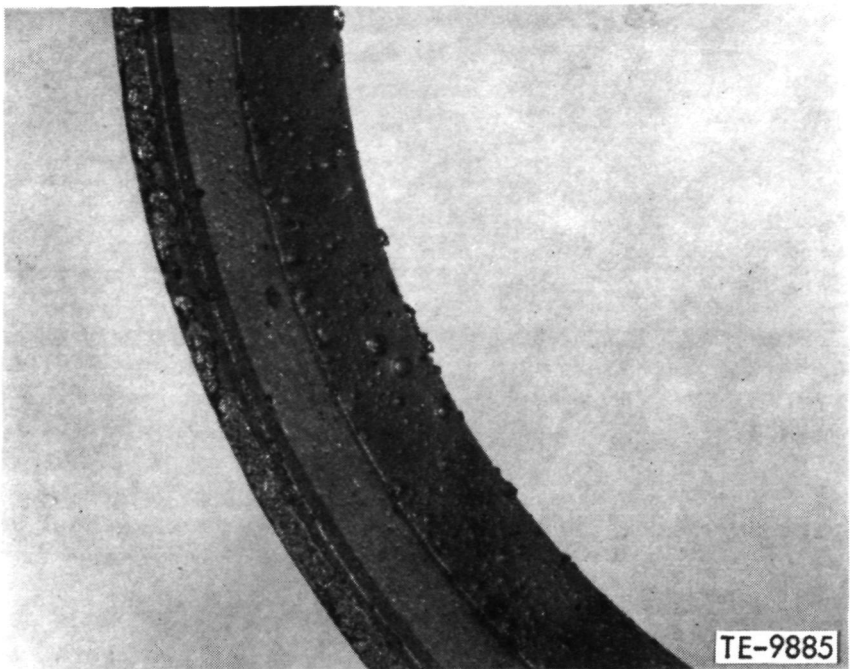


Figure 74. Thixotropic cast inner vane support ring after siliconizing.

TABLE XXIII. DIMENSIONAL CHANGES IN THIXOTROPIC CAST INNER SUPPORT RING--
mm (in.)

<u>Diameter</u>	<u>Green Out-of-Round Min Dia/Min Dia</u>	<u>Final Out-of-Round Max Dia/Min Dia</u>	<u>Avg. Final Diameter</u>	<u>Print Dimensions</u>
A	0.58 (0.023)	0.36 (0.016)	179.55 (7.07)	176.0/176.8 (6.93/6.96)
B	0.12 (0.005)	0.40 (0.016)	168.55 (6.65)	168.4/169.2 (6.63/6.66)
C	0.15 (0.006)	0.33 (0.013)	156.52 (6.16)	155.6/156.4 (6.13/6.16)
D	0.51 (0.020)	0.44 (0.017)	191.66 (7.55)	187.98/188.38 (7.40/7.45)

These dimensional results are highly encouraging. Previous work has shown that the air bubble problem can be greatly reduced. The shrinkages were much less than anticipated and, therefore, the ring was oversize. A new pattern would be required if usable parts were to be made by this technique.

Flat plates of this material were cast to provide material for test bars to be tested during the next report period.

Additional rings will be cast to further investigate the dimensional uniformity--both within a ring and between rings. Thixotropic casting is capable of producing the part with the holes and scallops formed, and the preliminary investigation indicated that this may be a viable production technique.

As stated previously, technique 1 was used to form the rings for rig and engine tests. This requires machining the vane pockets in either the green or the siliconized state. The hole shape, which is to mate with the turbine vane platform, lends itself to ultrasonic machining.

A 2400-watt Sheffield Cavitron ultrasonic machine was used to study both green and siliconized machining. The green (baked to pyrolyze the resin) inner support ring segment was rigidly mounted on a holding fixture located below a tubular cutting tool. Its rounded, rectangular shaped dimensions were 20.32 x 11.94 mm (0.8 x 0.08 in.) outside and 16.10 mm x 10.13 mm (0.63 x 0.40 in.) on the inside. This was not the vane platform shape; however, it was reasonably close to give a representative test.

The operator adjusted the frequency and positioned a flexible spout to flood the area between the cutting tool and the work with a slurry of boron carbide and water. Boron carbide of 320 grit was used for this test. The gap between the cutting tool and the work piece can be varied about one-tenth millimeter by varying the grit size. The tool was gravity fed, and the penetration rate was enhanced by drawing a vacuum on the hollow cutting media directly under the cutting portion of the tool.

Three holes were made for a cutting rate study; the average material rate was calculated to be 0.124 cc/minute. The tool wear was less than 0.0025 mm (0.00009 in.). Figure 75 shows the outer view of the green inner support shroud after it was machined. The tool entered the ring from the outside surface and exited through the inner surface. Some chipping of the inside occurred, but this can be minimized by supporting the inner surfaces with a rigid sleeve and filling the gap between the sleeve and the ring with stacking wax.

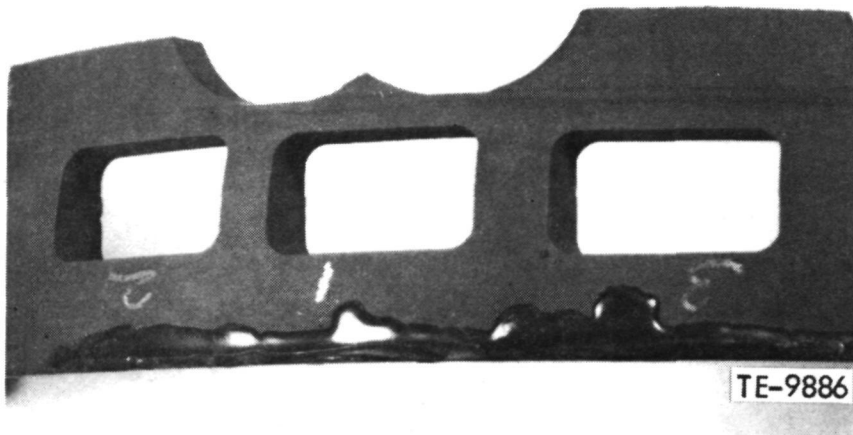


Figure 75. Outer view of green inner ring, ultrasonic machined holes.

The siliconized specimen was secured to the holding fixture, using the same tooling, and three holes were machined through. The stock removal was 0.027 cc/minute--approximately one fifth the machining rate of the green material. Again, some chipping was noted on the inside edges.

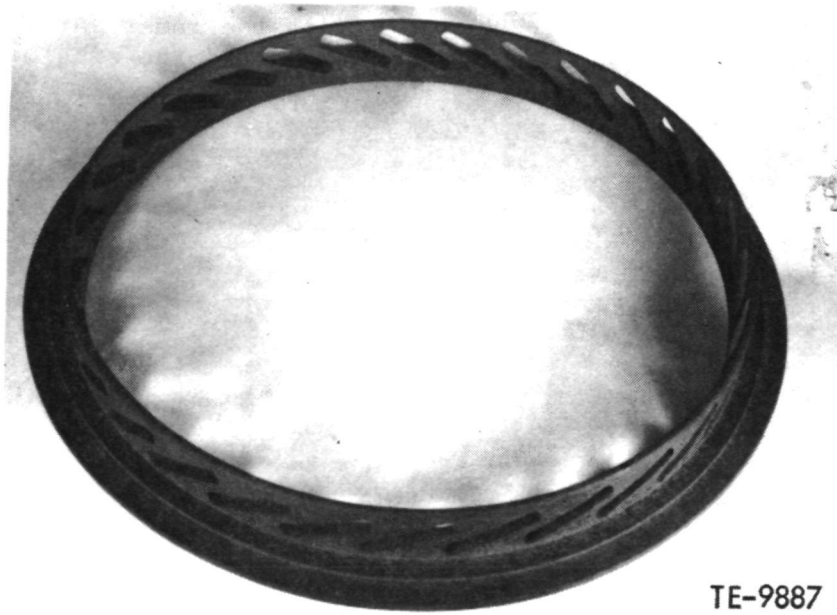
Since almost no distortion occurs when green material is siliconized, it appears to be advantageous to do the ultrasonic machining in the green state. A green Task IIIc outer support ring was machined with 30 rectangular 6.35 mm x 30.23 mm (0.25 in. x 1.19 in.) holes. This ring also was not supported on the inside surface and edge chipping was again experienced. The ring was siliconized by the process routing procedure and then sandblasted to remove residual silicon metal (see Figure 76). Visual Zyglo examination revealed no cracks. Tasks IIIB, Inner Support Ring, and IIIc, Outer Support Ring, both use ultrasonic machining in the green states as part of their manufacturing procedure.

The first fully machined inner vane support ring was completed in October 1979. NDE of this ring and delivery of additional rings are expected in January and February 1980.

Task IIIc--Outer Vane Support Ring

The outer support ring is formed by compression molding a simple shape, followed by baking, green machining, reaction sintering, and final machining. Tooling for simple compression molding of the vane outer support ring was to be the same as that used for the fabrication of the turbine tip shroud.

At the end of the reporting period, DDA had received one finish machined outer vane support ring (Figure 77). Additional finished rings are expected early in 1980.



TE-9887

Figure 76. Outer ring after ultrasonic machining, siliconizing, and sandblasting.

ORIGINAL PAGE IS
OF POOR QUALITY



TE-9888

Figure 77. Finish-machined vane outer support ring.

Carborundum has conducted material strength characterization tests of the warm-compression-molded material. Billets, 63.5 mm x 63.5 mm x 9.5 mm (2.5 in. x 2.5 in. x 3/8 in.), were molded to the same green density as that desired for the rings, and these billets were processed according to the rings process routing. The billets were diamond wheel cut into 12 test bars per billet. In the summaries of the results (Tables XXIV and XXV), the bars are identified by billet number and bar number.

Four-point bend tests were conducted at room temperature, 1100°C (2012°F), and 1300°C (2372°F) in air for both Tasks IIIb and IIIc. Table XXIV presents a summary of the average test bar strengths for each billet at the various temperatures tested. NDE had found numerous test bars which had porosity. These porous bars came from specific billets (identified in the table with asterisks). It is apparent that those plates with porosity have significantly lower strength. Table XXV presents a summary of the strength distribution data for only nonporous billets.

TABLE XXIV. AVERAGE STRENGTH RESULTS OF WARM-COMPRESSION-MOLDED, REACTION-SINTERED SILICON CARBIDE BILLETS**

(2.97-g/cc density)

	<u>200°C (68°F)</u>	<u>1100°C (2012°F)</u>	<u>1300°C (2372°F)</u>
Task IIIb Milestone 10			
Billet No./ number of test bars	10B/13	17A/10	19B/10
Average of billet test bar strength, MPa (ksi)	271.17* (39.33)	458.43 (66.49)	516.00 (74.84)
	11B/13 248.83* (36.09)	18B/10 337.64* (48.97)	20B/10 518.97 (75.27)
	14B/13 188.50* (27.34)		
	17B/13 281.10* (40.77)		
Combined average	247.38 (35.88)	398.03 (57.73)	517.59 (75.07)
Task IIIc Milestone 8			
	32A/12 479.94 (69.61)	5B/10 297.44* (43.14)	30B/12 466.78 (67.70)
	32B/12 479.67 (69.57)	29B 461.19 (66.89)	33B/8 483.74 (70.16)
	34A/12 458.93 (66.56)		
	33A/12 450.64 (65.36)		
	5B/2 343.50* (49.82)		
Combined Average	462.36 (67.06)	379.28 (55.01)	473.69 (68.69)

*NDE detected porosity

**Carborundum test data - bar size 3.18 x 6.35 x 50.8 mm (0.125 x 0.250 x 2.0 in.) 4 point bend, 1/3 point loading, outer span 38.1 mm (1.5 in.)

TABLE XXV. 4-POINT BEND TEST SUMMARY, COMBINED RESULTS OF NONPOROUS MATERIALS--MPa (ksi)*

	<u>10°C</u> <u>(68°F)</u>	<u>1100°C</u> <u>(2012°F)</u>	<u>1300°F</u> <u>(2372°F)</u>
Mean Value	468.55 (67.69)	459.79 (66.69)	495.51 (71.87)
Standard deviation	8.08	4.02	7.41
Weibull modulus	9.63	18.84	10.88
Number of bars	48	20	40
High strength value	556.32 (80.69)	516.60 (74.93)	593.34 (86.06)
Low strength value	314.39 (45.60)	411.67 (59.71)	333.35 (48.35)

*Carborundum test bar data - bar size 3.18 x 6.35 x 50.8 mm (0.125 x 0.250 x 2.0 in.) 4 point bend, 1/3 point loading, outer span 38.1 mm (1.5 in.)

The reason for the existence of the porosity is not fully understood. The billets made for Tasks IIIb and IIIc were molded from the same lot of molding powder, and the green densities of all the plates were nearly identical. The amount of cover mix used in the siliconizing step (180%) may be near the lower limit, and a higher amount may be necessary to achieve 100% yields. The only disadvantage of such an increase is that more excess silicon has to be removed from the parts. While this might add a small amount of time to the process, it is definitely worthwhile to the alternative of incomplete siliconization and the resultant porosity. The amount of cover mix will be increased to improve subsequent yields.

Task IV--Material Variation Investigation

The purpose of Task IV is to evaluate test bars and material properties made from variations to the basic reaction-sintered silicon carbide material used in Task II. Vanes fabricated from the materials showing the most promise will be burner rig tested. Eight variations were evaluated in the previous reporting period: a combination of material composition variations (bimodal grain, 1; silicon doping, 3; high purity silicon, 4; and high silicon amount, 7) and process variations (hammer milled, 5; hammer milled plus warm molded, 6; and high free silicon outer layer, 2) which would lead to microstructural changes. Standard material was used as a control to give a total of eight materials. (Refer to Table XXVII in the previous semiannual report.) With the exception of Variation 2 (high free silicon outer layer), all the variations were made into test bars without difficulty.

The results of the 4-point bend tests of tests bars at room temperature (refer to Table XXVIII in the previous semiannual report) indicate that the strongest variations were standard materials which were hammer milled (Variations 5 and 6) and the bimodal material (Variation 1). The doped silicon materials (Variation 3) and the high free silicon material (Variation 7) were clearly weaker than the others. The high-purity silicon was also higher in strength than the standard material.

From the test results, it was clear that several variations are promising. A material investigation matrix (Table XXVI) was defined to study these variations further. Also, three of the variations showing promise (1, 4, and 5) are being made into 1900°F vanes and test bars for evaluation. Fifteen vanes of each of these compositions have been fabricated with test bars. These are being evaluated by NDE and will then be exposed to the burner rig proof test.

TABLE XXVI. REDEFINED MATERIAL VARIATION MATRIX

	<u>1000-Mesh SiC</u>	<u>35% 1000-Mesh SiC + 65% 500-Mesh SiC</u>
Hammer Milled	Variation 5 (Repeat)	Variation 9
Hammer Milled & Air Impact Milled	Variation 10	Variation 11
Hammer Milled & Air Impact Milled & Low Free Silicon		Variation 12 Variation 13 (same as variation 12 except that all free silicon is removed)

Carborundum has fabricated 2070°F configuration vanes and test bars for each of the material variations defined in Table XXVI.

Also included in Task IV is the fabrication of alpha silicon carbide vane. In the 2265°F engine, some vanes will be exposed to temperatures above the limit of the reaction-sintered silicon carbide material. For this reason, it was felt that experience should be gained with the fabrication of an alpha silicon carbide vane. The higher shrink rate of the alpha silicon carbide requires a separate molding tool. This tool was fabricated in the last reporting period.

In the current reporting period, Carborundum delivered 45 alpha silicon carbide vanes (2070°F configuration) and matching test bars. Table XXVII presents the results of the NDE.

TABLE XXVII. NONDESTRUCTIVE CHARACTERIZATION OF GASIFIER VANES

<u>Material</u>	<u>Quantity</u>	<u>X-ray*</u>	<u>FPI</u>	<u>Visual (10-30X)</u>
α -SiC	45	30 NI, 15 LDI;	15 NI, others	12 with "mud-cracking" on
EX131232		1 with large	minor pits; 2	LE & TE, 18 NI,
$\rho = 3.15$ g/cc		through-crack	airfoil cracks	others with usual chips and pits
Carborundum				

*LDI = low density indications, HDI = high density indications, NI = no indications

Dimensional inspection of the alpha vanes revealed that the vanes did not shrink as anticipated. This did not significantly affect the airfoil profile or thickness, but it did show up in the overall length of the airfoil and the radial height of the vane. These two items should not hinder the aerodynamic performance of the vane but will affect the mechanical fit of the vane into the support ring vane pockets. The length and height of the vane will have to be hand blended to match the vane platform contour.

Burner Rig Tests

In the current reporting period, two Corning LAS 1900°F turbine tips shrouds were exposed to five cycles each in the burner rig proof test. Both shrouds passed without failure. Both rings were evaluated for abradability as reported in Section III. The shroud with the best abradability was selected for engine test.

GASIFIER TURBINE BLADE

Design Objective

The objective of this activity is to design a ceramic-bladed gasifier turbine rotor for the engine. Design detail and most analyses had been completed in the two previous six-month reporting periods. The rotor is designed for operation at 1132°C (2070°F) rotor inlet temperature with potential for operation at 1241°C (2265°F). The rotor fits the existing shaft mounting features and is adapted to the space limitations in the engine. Emphasis has been placed on achieving high turbine efficiency, which requires airfoils designed specifically for the 1132°C (2070°F) and 1241°C (2265°F) engine performance cycles. Determination of blade design acceptability is based on a probabilistic evaluation, using 3-D finite element analysis techniques.

Effort in this reporting period centered on analytical determinations of spin test effectiveness in improving blade reliability. The development of a simplified finite element model that could be used to evaluate alternate blade designs was also begun.

Design Approach

The previously completed blade and rotor design is presented for reference in Figure 78. The blade is designed for injection-molded sintered silicon carbide or silicon nitride with as-fired surfaces and machining limited to critical features as indicated. Blades are retained in a single-lobe dovetail configuration. An 0.18-mm (0.007 in.) thick metal compliant layer (not shown) is utilized at the ceramic blade/metal rotor interface. The following is the approach to completing analytical evaluations of spin proof, dynamic effects, and proof plus dynamic effects.

Spin Proof Testing

A calculation method has been established which allows the determination of component reliability in an engine operating condition subsequent to a proof test. The calculation of the probability of surviving a prescribed load condition after the structure is proof tested is as follows:

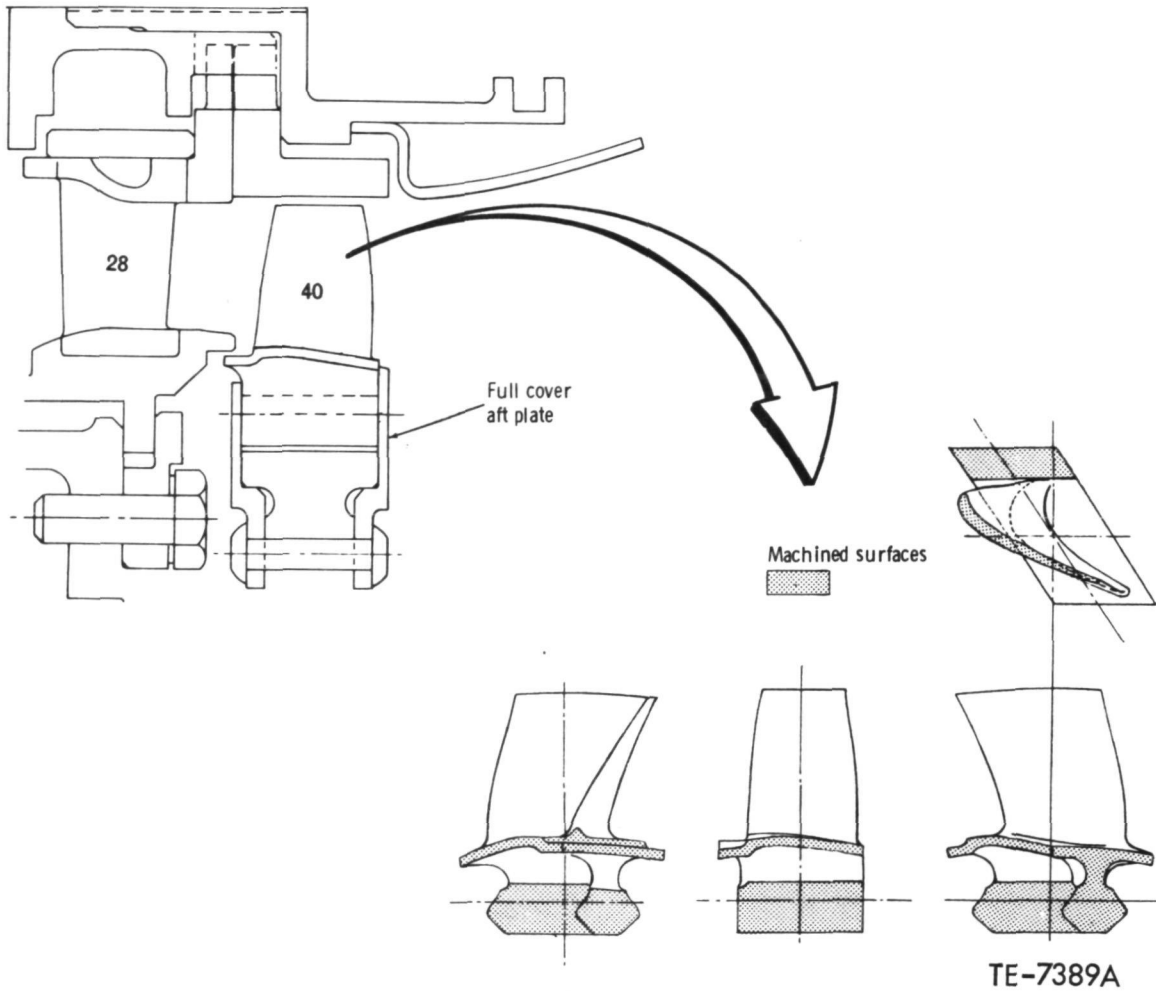


Figure 78. 2070°F ceramic blade geometry.

$$P_s = e^{-R_R + R_p} \quad \text{Probability of survival}$$

$$R_R = \frac{\sigma_p - \sigma_u^m}{\sigma_o} \quad \text{For load condition } (\sigma_R \text{ principal stresses}) \quad (1)$$

$$R_p = \frac{\sigma_R - \sigma_u^m}{\sigma_o} \quad \text{For proof test } (\sigma_p \text{ principal stresses})$$

σ_o , σ_u , m are Weibull material constants

If R_p is greater than R_R , then $P_s = 1$

σ_R and σ_p are greater than 0

Equation (1) is integrated over the surface and volume of the structure (in this case over each element of the finite model). The stresses (σ_R) at each integration point are stored on tape when the probability of survival is calculated for the desired load condition. This tape is used as input for the proof test run, and the stresses are combined in the probability calculation. If, at any point, the proof stress is greater than the load condition stress,

the probability will be 1.0. This equation combines all of the principal stresses disregarding the direction. This assumes that a flaw will fail at a given stress no matter what the direction of the stress. In view of this assumption, it is necessary that the proof test simulate the running load condition as closely as possible. Therefore, a spin test is recommended for proof.

The 2070°F blade design has the highest probability of failure in the transient condition which occurs at 3 seconds into an acceleration from stabilized braking to maximum power. This worst case operating condition was evaluated with a range of proof test speeds, and an improvement in blade reliability was noted. Failure probability was determined for airfoil and attachment substructures as well as for the total blade. The results obtained are presented in Table XXVIII.

TABLE XXVIII. EFFECTS OF PROOF TEST SPEED ON BLADE RELIABILITY

Proof Test Speed	% Blades Lost in Proof	Probability of Failure		
		Airfoil	Attachment	Total
Zero (no proof test)	None	0.0008	0.017	0.0178
36,905 RPM (100%)	00.7%	0.0005	0.0028	0.0033
40,000 RPM (108%)	2.7%	0.00029	0.00024	0.00053
43,250 RPM (117%)	10%	0.00021	0.000015	0.00023
48,280 RPM (131%)	50%	0.00017	0.0000001	0.00017

It is apparent that increasing spin proof speed continues to improve attachment reliability throughout the speed range evaluated but little improvement in airfoil reliability is realized above 40,000 rpm (108%). A comparison of airfoil stress distribution due to thermal and centrifugal loads during the 3-second acceleration shows a significantly different distribution during cold spin, which involves centrifugal loads only. Significant airfoil "tilt" is provided in the 2070°F blade design to minimize airfoil peak stress during engine transients and, as a result, the lower portion of the airfoil pressure surface remains at a low stress during spin test regardless of speed--i.e., airfoil bending stress is offsetting simple P/A centrifugal load stress on the airfoil pressure surface. Therefore, some small portions of the airfoil are not being proof tested even at high spin speed. However, overall blade reliability is improved with spin proof testing, and it appears that a proof test speed of 43 250 rpm (117%) will provide satisfactory rotor reliability ($P_f = 0.00023$) for initial engine testing (Rotor $P_f = 0.00023 \times 40 = 0.0092$).

Blade Dynamics

Another analysis procedure has been developed which will assist in evaluating the effects of blade vibration on reliability. This analytical methodology allows a dynamic stress to be combined with a static stress distribution previously established for an engine operating condition. Since vibratory stress level in the engine cannot be calculated, range of peak vibratory stress level distributions were computed for the blade fundamental mode. These were combined with the static stress distribution computed for engine operation at $N_g = 79\%$ (29 000 rpm) and $T_4 = 1132^\circ\text{C}$ (2070°F). This condition corresponds to an anticipated interference point at 28th engine order (vane passage frequency) and blade first bend frequency (14 854 Hz). Once the combined dynamic and static stress distribution is established, blade reliability can be determined using Weibull analysis techniques. Results achieved by this procedure are summarized in Table XXIX.

TABLE XXIX. EFFECT OF DYNAMIC STRESS ON BLADE RELIABILITY

Peak Dynamic Stress	Probability of Failure		
	Airfoil	Attachment	Total
+ Zero (steady state, $N_g = 79\%$)	0.00003	0.00022	0.00025
+40.0 MPa (5.8 ksi)	0.00005	0.00073	0.00078
+80 MPa (11.6 ksi)	0.0001	0.0026	0.0027
+159.3 MPa (23.1 ksi)	0.001	0.023	0.024
+318.5 MPa (46.2 ksi)	0.05	0.48	0.51

These results indicate that high vibratory stress could have a significant and adverse effect on blade reliability and that failure would probably occur in the attachment portion of the blade. The ceramic blade reliability shown was computed without benefit of a spin proof test, which will improve reliability. To determine this effect, computer routines were combined to determine blade reliability with dynamic plus static stress but with recognition of a previously completed spin proof test. A spin proof test speed of 117% (43 250 rpm) was selected for evaluation, and the effects of the proof test are summarized in Table XXX.

Results indicate a dramatic improvement in reliability at lower dynamic stress levels but, as might be expected, the probability of failure is not greatly improved at very high dynamic stress levels. Further review of results indicates that desired blade reliability of $P_f = 0.00025$ (Rotor $P_f = 0.00025 \times 40 = 0.01$) can be met if proof tested blade dynamic stress does not exceed +153 MPa (22.1 ksi). This is felt to be a sufficient vibratory stress tolerance for initial engine testing.

TABLE XXX. EFFECT OF SPIN PROOF AND DYNAMIC STRESS ON BLADE RELIABILITY

<u>Peak Dynamic Stress (Dovetail)</u>	<u>Probability of Failure</u>	
	<u>Without Proof Test</u>	<u>With Proof Test</u>
+Zero (steady state, $N_g = 79\%$)	0.00025	3.0×10^{-7}
+80 MPa (11.6 ksi)	0.0027	3.03×10^{-6}
+159.3 MPa (23.1 ksi)	0.024	0.00034
+318.5 MPa (46.2 ksi)	0.51	0.133

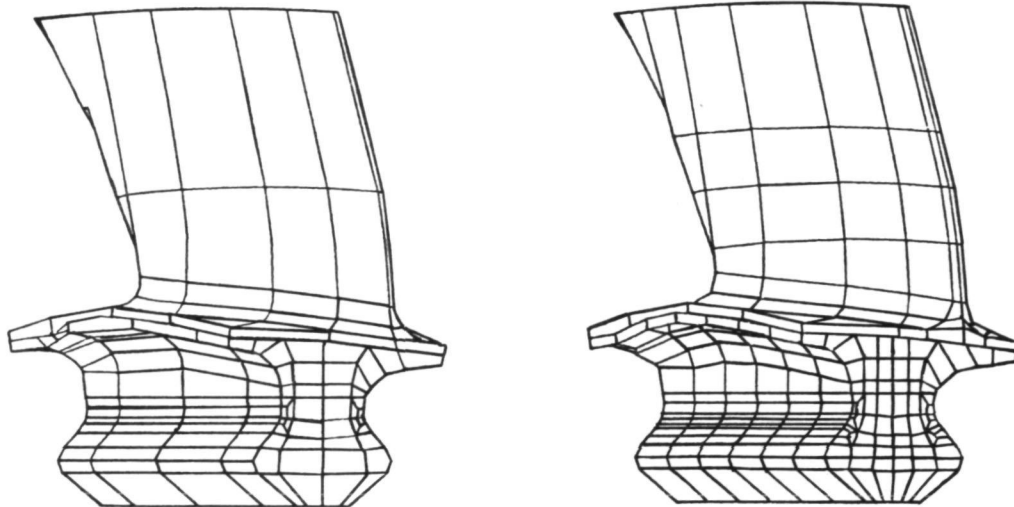
Alternate Blade Design

Design attention is presently directed toward an alternative configuration to the current 20700F blade. Recent effort has focused on simplification of the existing 3-D finite element model to reduce computation cost and time. It is intended that the simplified model represent the current blade geometry. Results with the simplified model will be compared with those of the existing more sophisticated model. Simplification basically means reduction in the number of elements in the low stress gradient regions.

A simplified version of the finite element model has been completed (Figure 79). The total number of elements has been reduced from 649 to 263, and the anticipated computation costs are reduced by nearly 90%. However, the model has not been completely checked out, and its acceptability will depend upon comparisons of stress distribution and reliability parameter comparisons with the original model. When an acceptable revised model has been developed, revision to blade geometry will be evaluated using the new modeling technique. The objective of the redesign is to improve reliability of the blade without compromise in aerodynamic performance. One approach to reducing attachment peak stress and reliability involves reduction of the broach or hub setting angle. This can be achieved through blade airfoil revision (perhaps without a vector diagram change, which would affect the first vane shape). The airfoil radial alignment to the stalk can also be changed and evaluated. Airfoil stack revision may also be appropriate, with more emphasis placed on a design approach that improves proof test effectiveness.

A preliminary aerodynamic study indicates that hub setting angle can be reduced with a blade airfoil design which suits the current vector diagram. The following findings have evolved from this early study:

- o Revised radial throat distribution could reduce hub setting angle by about 5° and reduce blockage in the gas path hub
- o Reducing the airfoil number from 40 to 38 could also reduce hub setting by 5°
- o Reduced airfoil hub section area could reduce hub setting. One example was evaluated and a 2° hub setting angle reduction was found possible. This "thin airfoil" approach also reduced dovetail load by 6% but airfoil hub stress would increase by about 16%.



Simplified blade model
 Airfoil elements: 69
 Dovetail elements: 184
 Total elements: 263

Original blade model
 Airfoil elements: 189
 Dovetail elements: 460
 Total elements: 649

TE-9893

Figure 79. 2070°F blade computer model simplification.

The parametric studies will continue to support aerodynamic changes which may have to accompany the 2265°F (1241°C) configuration design and are available to be applied in the event of durability or performance problems with the current design as development testing proceeds.

Spin Testing

Testing of silicon carbide spin coupons and compliant layers has continued in this reporting period. The purpose of this test series, conducted at elevated temperature, was to aid in selection of a compliant layer material prior to its use in the rotor configuration. Overspeed-to-failure tests and cyclic spin tests were completed to evaluate compliant layer and SiC coupon performance.

Hot spin testing with the SiC spin coupons was conducted at 677°C (1250°F), which is slightly higher than the anticipated attachment temperature in the 2070°F engine. The desired rotor temperature is obtained by using resistance heating elements located with the rotor in an insulated chamber. Chamber air temperature has been shown to be in close agreement with the disk temperature, which was determined by using rotating thermocouples. Rotating thermocouple data were obtained by using slip-ring signal transmission at rotor speeds up to 50 000 rpm. After this correlation was established in initial testing, subsequent testing was based on chamber air temperature indication and rotating instrumentation was deleted.

Overspeed-to-Failure Tests

The first three tests completed were overspeed to failure with each of three compliant layers. In each test, the silicon carbide coupon dovetail and the compliant layer contact surfaces were coated with boron nitride spray to provide a lubricant and a diffusion barrier. This procedure was developed during static compliant layer testing and was reported last period. Spin coupon and compliant layer are mounted in a single-slot test wheel as in previous cold testing. Wheel and coupon assembly are rotated at 12 000 rpm until the desired temperature is obtained (heating requires about 100 minutes to reach 677°C (1250°F)). With temperature maintained, rotor speed is slowly increased until failure occurs. This procedure was followed with 347 stainless steel, L605, and IN-600 compliant layer details. Hot spin failure speeds along with previously completed room temperature silicon carbide spin results are presented in Table XXXI. The average of three hot tests is within 1.7% of the average of seven cold spin tests, and none of the compliant materials seems clearly superior.

TABLE XXXI. SPIN TEST SUMMARY

<u>Coupon Material</u>	<u>Serial No.</u>	<u>Compliant Layer Material</u>	<u>Failure Speed (RPM)</u>
<u>Cold Spin Test Summary (completed in May 1979)</u>			
SiC	12	IN-600+BN	35 800
SiC	13	IN-600+BN	37 500
SiC	14	IN-600+BN	38 100
SiC	15	IN-600+BN	42 600
SiC	16	IN-600+BN	38 800
Average of 5			<u>38 560</u>
SiC	17	L605+BN	38 100
SiC	18	347SS+BN	42 800
Average of 7			<u>39 100</u>
<u>Hot Spin Testing Summary* (November 1979)</u>			
SiC	22	347SS+BN	39 100
SiC	23	L605+BN	38 500
SiC	25	IN-600+BN	41 750
Average of 3			<u>39 783</u>
Average of 10			<u>39 305</u>

*677°C (1250°)

Each of the three failed coupons has been examined for unusual conditions which could have had a significant effect on failure speed. The following comments are pertinent to the failure analysis of these coupons:

- o Coupon No. 22 failed at 39 100 rpm, using a 347 stainless steel compliant layer (Figure 80). The primary failure origin, indicated by arrow, is in a zone of high predicted stress (near the peak stress location), and no major flaw was found at this origin. Presumably, the fracture at the surface was a result of machining damage.

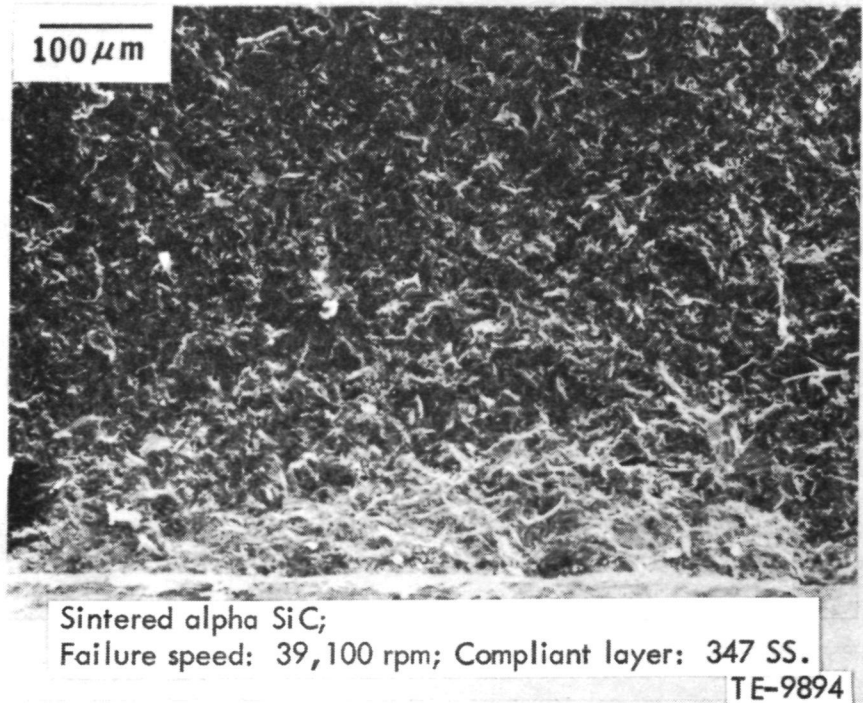
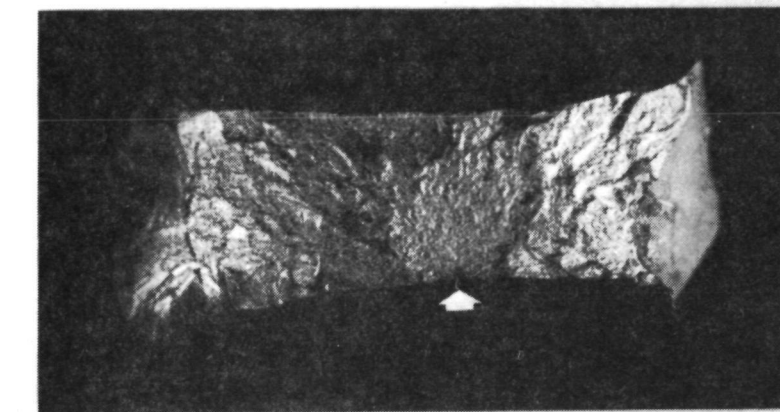


Figure 80. Spin coupon No. 22.

- o Coupon No. 23 failed at 38 500 rpm, using L605 material as the compliant layer (Figure 81). The primary failure originated at the surface in a zone of high stress near the peak stress location but, again, no flaw could be found.
- o Coupon No. 25 failed at 41 750 rpm, using an IN-600 material compliant layer (Figure 82). Primary failure originated at a rounded pore located at the predicted peak stress location. This pore is typical of those which control strength in material qualification test bars that were cut from billets along with the spin coupons.

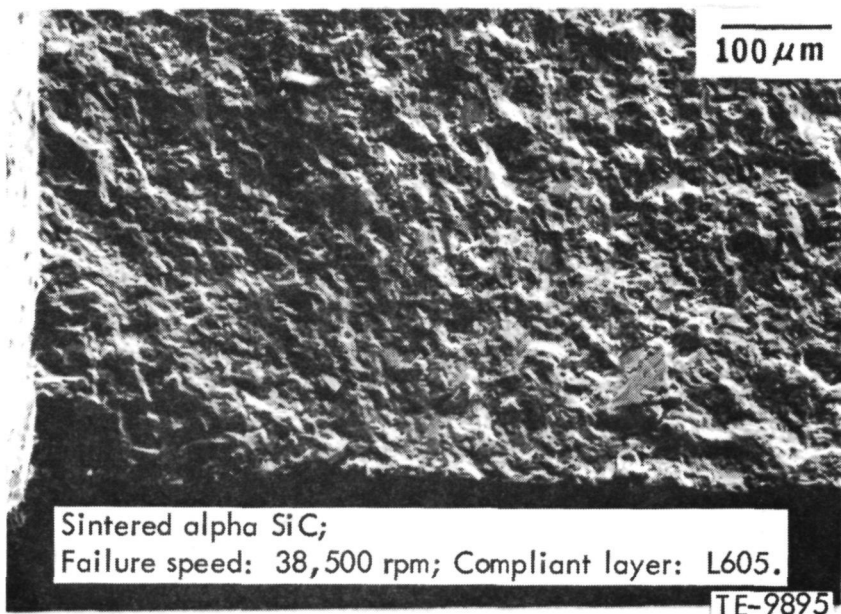
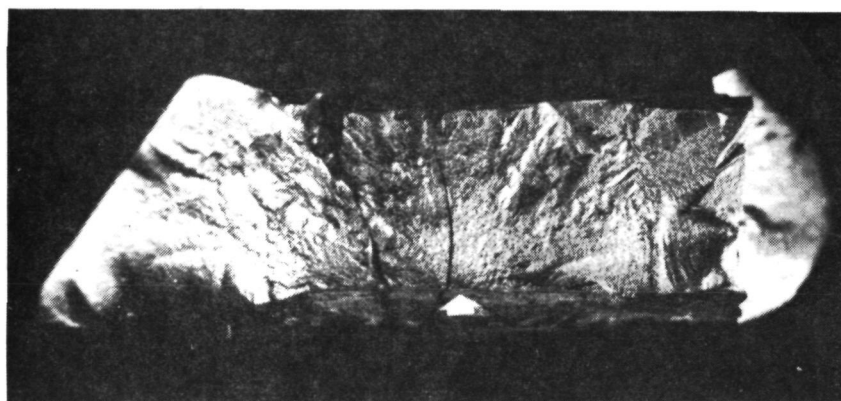
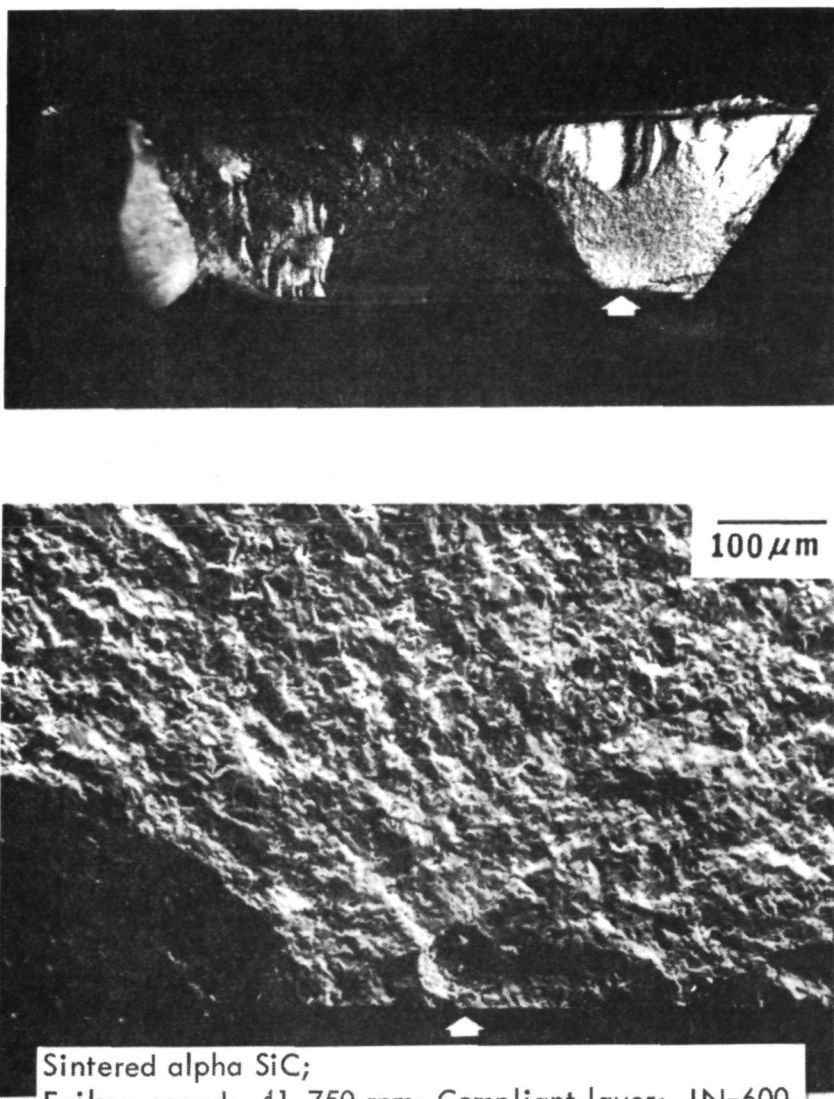


Figure 81. Spin coupon No. 23.

ORIGINAL PAGE IS
OF POOR QUALITY



Sintered alpha SiC;
Failure speed: 41,750 rpm; Compliant layer: IN-600.
TE-9896

Figure 82. Spin coupon No. 25.

Cyclic Spin Tests

In this test series, the rotor assembly temperature is maintained at 677°C (1250°F) and rotor speed is cycled between 500 and 30 800 rpm (100% attachment load speed). After each test, the compliant layer and coupon were photographed and the thickness change of the layer was determined. Compliant details were replaced after each test and were never reinstalled for additional testing. Results of thickness change measurements are presented in Figure 83, which depicts the maximum thickness change found in each case. The original thickness was 0.18 mm (0.007 in.). The following is a discussion of the results obtained with each material:

ORIGINAL PAGE IS
OF POOR QUALITY

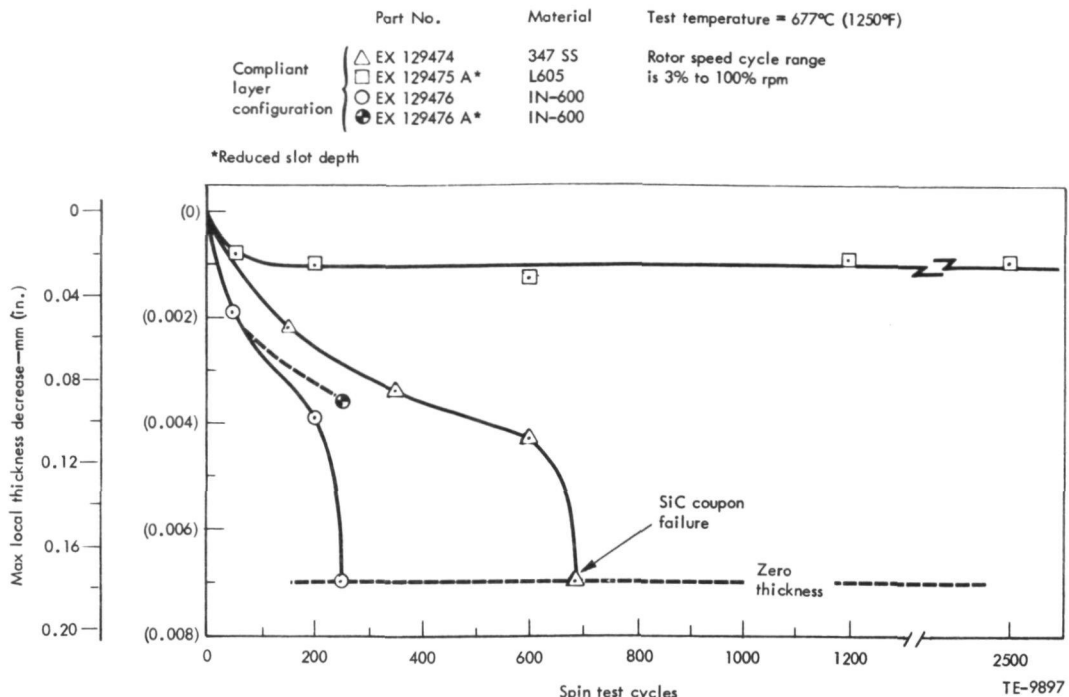


Figure 83. Hot cyclic spin evaluation of compliant layers.

- o Inconel 600 Compliant Layer

This material seems to be compliant, but cyclic testing resulted in complete thin-out in 250 cycles. The posttest appearance of IN-600 compliant layers is shown in Figure 84. Considerable distortion of the compliant layer is evident at 200 cycles, and it becomes very severe with complete thin-out to zero thickness at 250 cycles. Distortion and thin-out seem to be adversely affected by two weight reduction slots in the lower portion of the compliant details. IN-600 compliant layers with reduced slot depth were available, and performance did improve as evidenced by a repeat of the 250-cycle test. Measured thickness change with reduced slot depth geometry was 0.091 mm (0.0036 in.), which is an improvement over the deep slot version (Figure 83).

- o 347 Stainless Steel Compliant Layer

This material is also compliant, but excessive thin-out again resulted in cyclic testing. After 600 cycles, the maximum local thickness reduction was 0.11 mm (0.043 in.). An attempt to run a greater number of cycles with a new compliant detail resulted in complete thin-out and failure of the ceramic coupon at 684 cycles (Figure 85). The compliant layer details available for test were of the "deep slot" configuration, and it is believed that cyclic life could be extended by a reduction in slot depth; however, this has not been pursued because of the more favorable characteristics of L605.

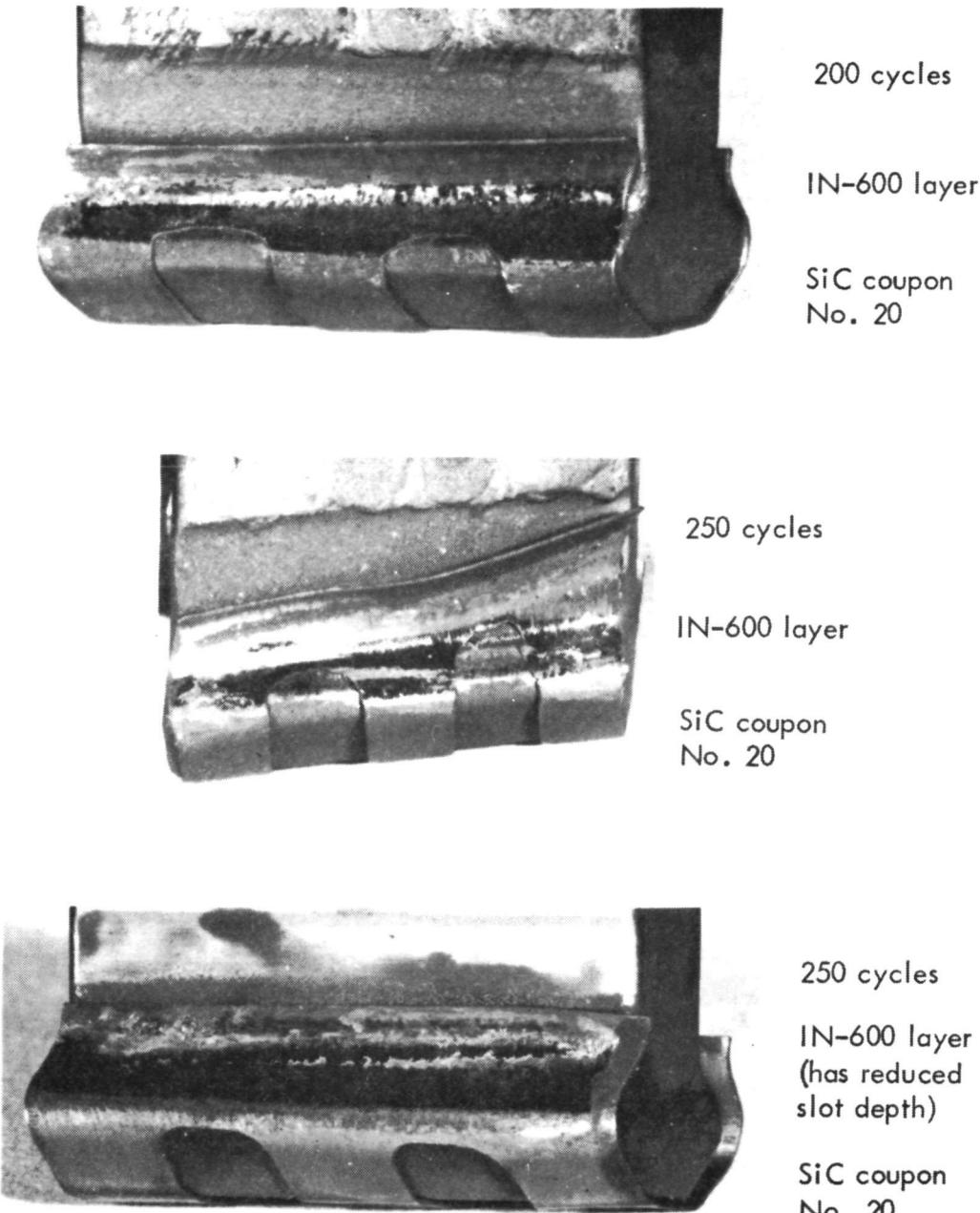


Figure 84. Hot cyclic spin test of IN-600 compliant layer.

Closer examination of the failed spin coupon No. 20 reveals the relationship between compliant layer thin-out position and coupon fracture origin (Figure 86). Failure originated at a point of local contact between test disk and ceramic coupon. Multiple horizontal cracks, shown in Figure 87, are located at the failure origin and are typical of high Hertzian stress failures in brittle materials.

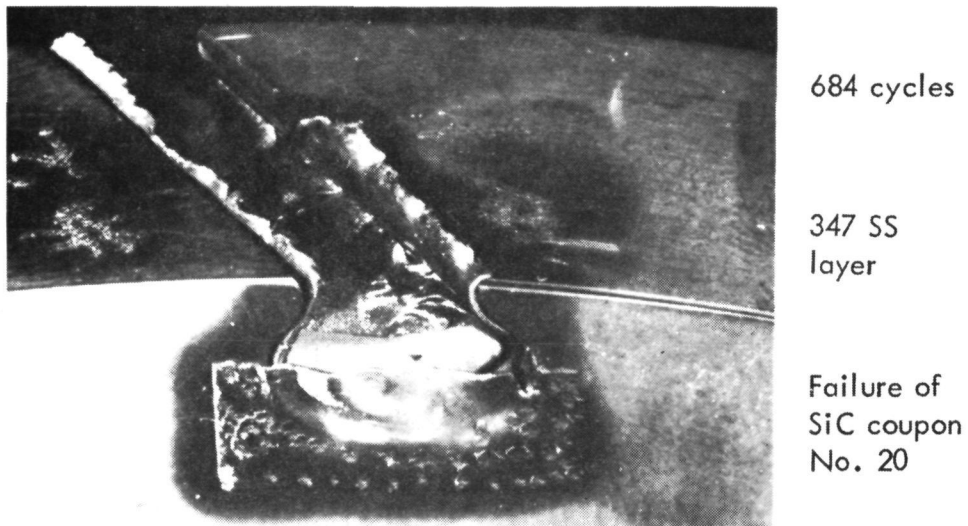
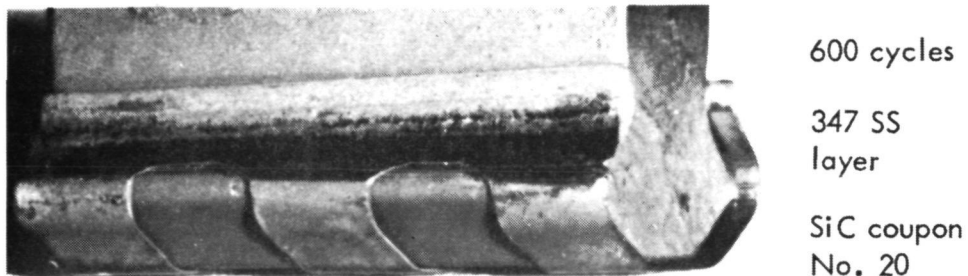
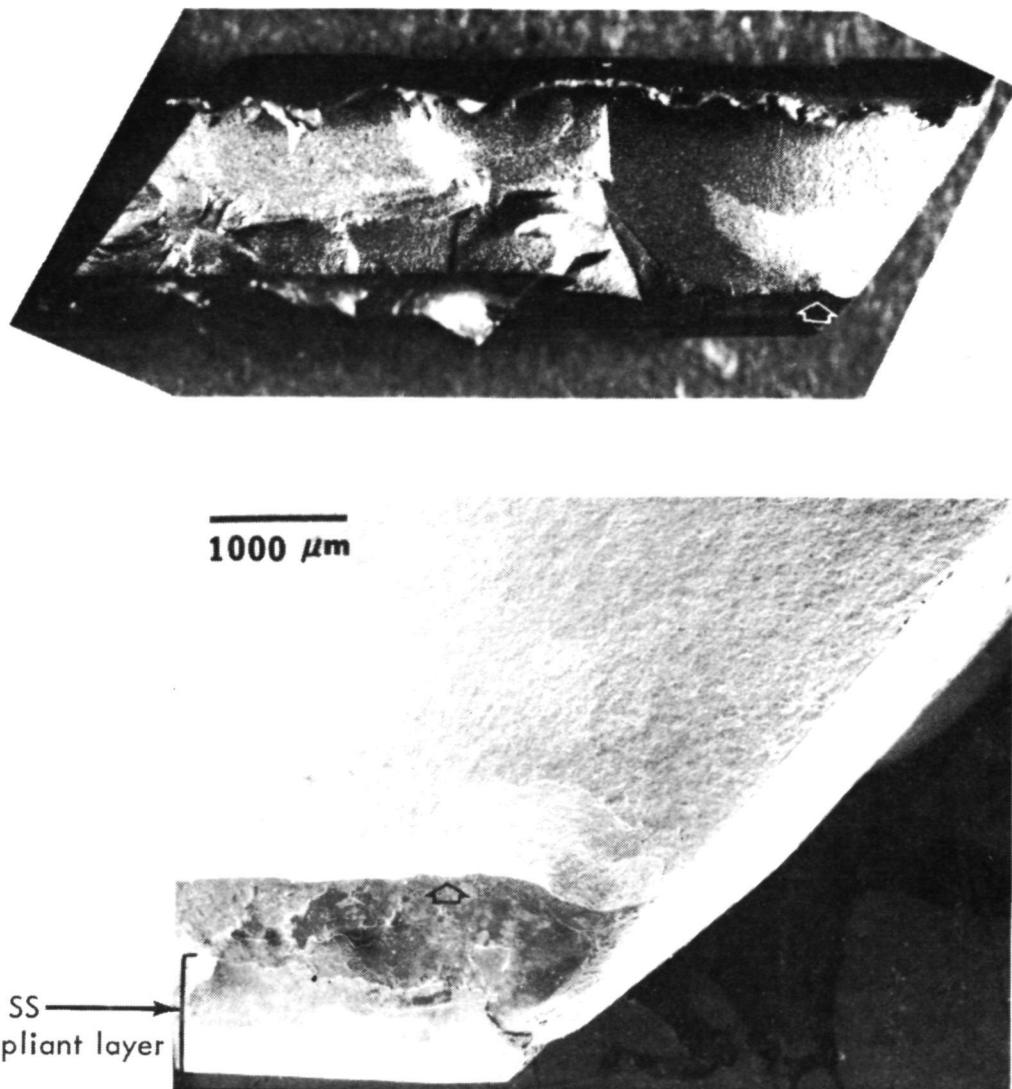


Figure 85. Hot cyclic spin testing of 347 stainless steel compliant layer.

o L605 Compliant Layer

This cobalt-base material used in an annealed condition seems to be the most promising for use as a compliant layer. After a 50-cycle test, the maximum local thickness reduction was 0.03 mm (0.0008 in.) and additional cyclic testing provided similar results up to 2500 cycles (see Figure 83). All L605 compliant layers tested were of the reduced slot depth configuration and all were in excellent condition (see 2500-cycle part in Figure



Sintered alpha SiC;
Failed at 684 cycles; 677°F (1250°F) TE-9900

Figure 86. Spin coupon No. 20.

88). The initial annealed condition of L605 provides adequate compliance, based on contact pattern evidence and on overspeed-to-failure results. Work-hardening characteristics provide resistance to continued thin-out after the initial contact impression is made. None of the materials tested exhibited metal-to-ceramic or metal-to-metal bonding or fretting.

Based on these results, L605 has been selected for compliant layers to be used in the initial testing of blades in rigs and engines. It will also be used in near-term spin testing of silicon nitride spin coupons and silicon carbide prototype blades. The use of boron nitride spray for the initial lubrication seating of the conforming surface is felt to be beneficial and will be continued.

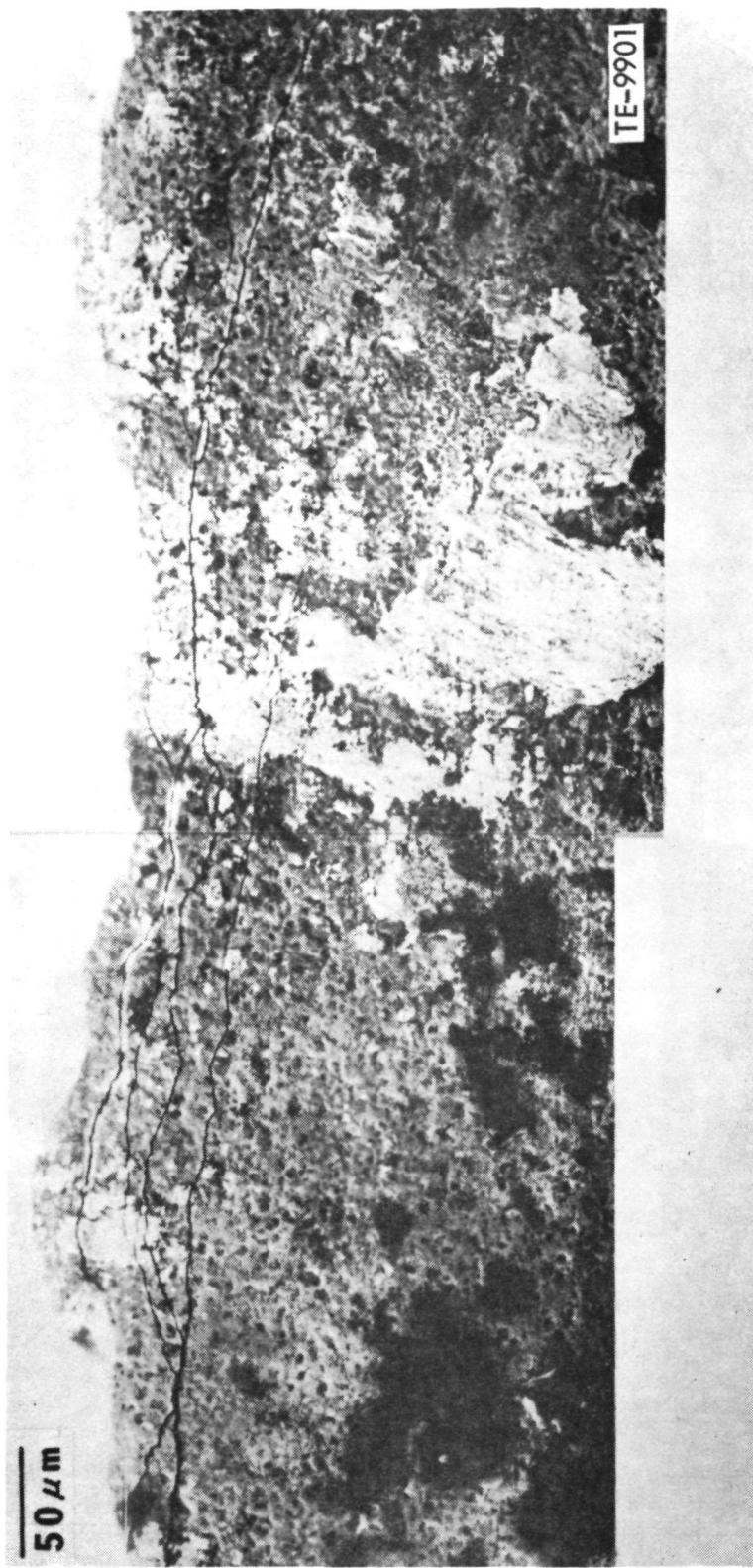
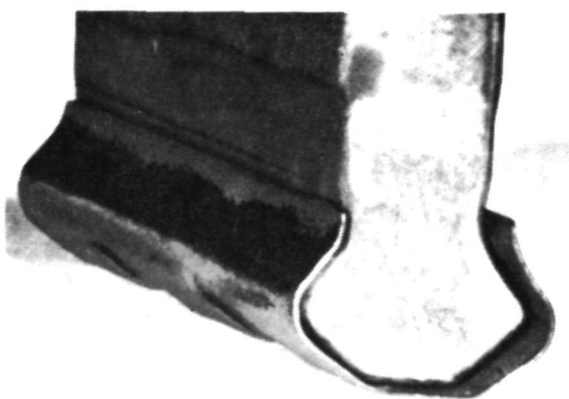
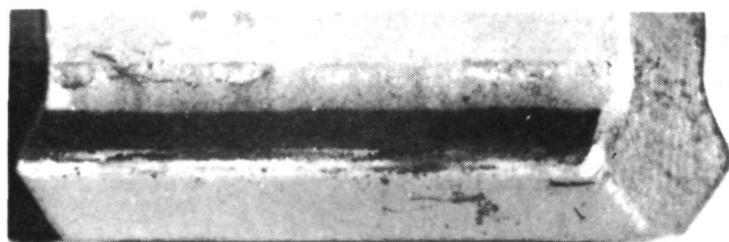


Figure 87. Multicrack at peak stress area in spin coupon No. 20.

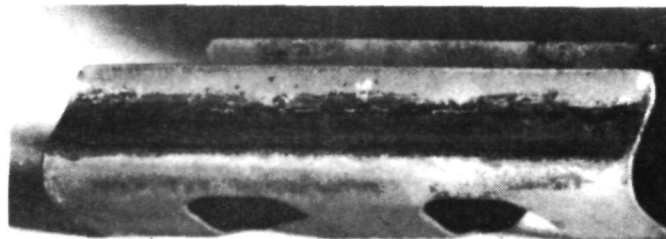
ORIGINAL PAGE IS
OF POOR QUALITY



Coupon and layer after 2500 cycles



SiC coupon No. 20 contact pattern



L605 compliant layer contact pattern
(has reduced slot depth) TE-9902

Figure 88. 2500-cycle hot spin test of L605 compliant layer.

Carborundum Process Development

The program to develop a ceramic turbine blade process was initiated at the Carborundum Company in March of 1978. The purpose of this program is to optimize injection-molded sintered alpha silicon carbide manufacturing processes for fabrication of a gas turbine blade. The immediate goal is to provide blades suitable for operation in the 2070°F CATE engine test program. Blade design and process requirements are to have the intrinsic capability ofulti-

mate development to meet production reliabilities at low part cost. The initial effort was pursued with a prototype blade configuration, but work has now been transferred to the 2070°F engine blade design. Process development during this reporting period has advanced dramatically, and process parameters have now been established which produce blades of acceptable shape and quality for initial bench, rig, and engine testing. The following is a discussion of significant events in this development.

Details of injection mold tooling design features for the 2070°F blade were reported in the last period, but significant items to keep in mind include:

- (1) Single blade and single MOR bar cavities are provided, and these are fed in parallel from a main runner.
- (2) Molded blade and bar bodies are 16.3% oversize to account for shrinkage anticipated at sintering.
- (3) Two methods of gating or filling the blade cavity are provided: a side fan gate or an end stem gate (both located at the blade dovetail).
- (4) The tool is readily adaptable to either a reciprocating screw injection molding machine or a plunger press.

This tool was available in the previous reporting period, but because of minor dimensional discrepancies and die closure problems related to a warped base plate it was returned to the supplier for repair. Acceptable tooling became available at Carborundum in August 1979, and a major effort to optimize process parameters for the specific 2070°F configuration has been completed since that time.

Molding

Optimization of molding parameters was approached with a trial and error technique in which parameters were varied and fifteen blades were molded for each set of conditions. The changeable parameters were:

- o Injection machine
- o Mold temperature
- o Material temperature
- o Injection pressure
- o Gate configuration

Starting with a New Britian screw machine and the end gate configuration, pressure was initially fixed and the mold temperature was varied about a given material temperature. The material temperature was then adjusted upward incrementally, providing three levels of mold temperature for each of the three levels of material temperature (Table XXXII).

The next series of experiments involved varying the injection pressure around the two best conditions with respect to total number of passing blades and bars from the first nine experiments. The experiments selected were 3 and 4, (11 and 14 were repeats of 3 and 4). Experiments 16, 17, and 18 were repeats of 11, 15, and 14 except for the use of the fan gate.

For the last experiments (19 through 27), a Tempcraft plunger press was used. It was impossible to translate all of the parameters of the New Britain to the Tempcraft. However, the approximate Tempcraft molding conditions for blades were known from experience. In general, mold temperatures were lower to minimize blistering, and pressures were lower. The material temperatures used were the same, and the total injection time plus hold time was the same as the injection, hold, and cooling times for the New Britain.

For all experiments but one (No. 21), an air shot was taken before molding each pair. Blisters generally occur if this practice is not respected, particularly on the New Britain; they are probably the result of temperature increase during residence time.

Inspection

After molding, the parts were inspected visually at 8 to 40X. Those passing visual (most failures were due to blisters on blades and cracking on bars) were evaluated by X-ray.

Baking

All molded parts passing visual and X-ray inspection were baked out at the same time.

Inspection

After baking, the blades were inspected visually at 8 to 40X.

Sintering

After a proprietary presintering treatment, the blades from experiments 3, 4, 12, 13, and 16 were sintered in a continuous furnace to minimize batch-to-batch variations. Preliminary testing to determine optimum loading arrangement was carried out. Two preliminary capsules were run, providing a 3.16-g/cm³ average density for the desired loading arrangement. The density obtained is higher than that of blades heretofore sintered in the periodic furnace.

Blade Yield: Five of the seven best groups based on the highest number of good blades through baking (at least 10 out of 15) were processed through final inspection (visual, Zyglo, and X-ray).

The molding conditions for these groups, although not identical, are reasonably close. In general, low to moderate material temperatures, high mold temperatures, and high injection pressures, using the end gate on the New Britain, appear best.

Bar Yield: At least two-thirds of the bars made on both the New Britain and Tempcraft turned out to be good after baking (i.e., no apparent defects). In general, low material temperatures, moderate to high mold temperatures, and moderate injection pressures appear to be best.

TABLE XXII. CERAMIC BLADE INJECTION MOLDING OPTIMIZATION EXPERIMENTS

Exp No.	Matl Temp °C (°F)	Mold temp °C (°F)	Pressure kPa (psig)	Gate	Machine	Molded Qty	Visual X-Ray Good Blades Molded	X-Ray Good Blades Sintered	Visual Zyglo Good Blades Sintered	X-Ray Good Blades Sintered	Visual Good Bars Molded	X-Ray Good Bars Molded	ρ Bars Sintered (g/cc)	
							Visual Good Blades Baked	X-Ray Good Blades Sintered	Visual Good Blades Sintered	X-Ray Good Blades Sintered	Visual Good Bars Baked	X-Ray Good Bars Molded		
1	146.1 (295)	26.7 (80)	3447.4 (500)	End	NB	15	13	4	3.14	14	14	14	3.13	1.3
2	146.1 (295)	37.8 (100)	3447.4 (500)	End	NB	15	13	9	3.14	7	7	7	3.15	
3	146.1 (295)	48.9 (120)	3447.4 (500)	End	NB	15	13	12	3.14	14	14	14	3.14	
4	157.2 (315)	48.9 (120)	3447.4 (500)	End	NB	15	13	12	3.15	8	8	6	3.11	
5	157.2 (315)	37.8 (100)	3447.4 (500)	End	NB	15	10	8	3.16	0	0	0	3.11	
6	157.2 (315)	26.7 (80)	3447.4 (500)	End	NB	15	11	8	3.16	9	1	1	3.15	
7	168.3 (335)	26.7 (80)	3447.4 (500)	End	NB	15	10	5	3.16	13	4	4	3.16	
8	168.3 (335)	37.8 (100)	3447.4 (500)	End	NB	15	12	9	3.16	5	5	5	3.16	
9	168.3 (335)	48.9 (120)	3447.4 (500)	End	NB	15	11	8	3.16	10	10	10	3.15	
10	157.2 (315)	48.9 (120)	24.13.2 (350)	End	NB	15	75	5	3.17	7	7	7	3.15	
11	157.2 (315)	48.9 (120)	3447.4 (500)	End	NB	15	15	15	3.17	15	15	15	3.15	
12	157.2 (315)	48.9 (120)	4481.6 (650)	End	NB	15	15	15	3.16	12	12	12	3.15	
13	157.2 (315)	48.9 (120)	4481.6 (650)	End	NB	15	11	11	3.15	2	2	2	3.14	
14	157.2 (315)	48.9 (120)	3447.4 (500)	End	NB	15	12	11	3.16	9	9	9	3.16	
15	157.2 (315)	48.9 (120)	24.13.2 (350)	End	NB	15	7	6	3.17	9	9	9	3.15	
16	157.2 (315)	48.9 (120)	3447.4 (500)	Fan	NB	15	13	13	3.16	12	12	12	3.15	
17	157.2 (315)	48.9 (120)	24.13.2 (350)	Fan	NB	15	9	5	3.16	9	9	9	3.14	
18	157.2 (315)	48.9 (120)	3447.4 (500)	Fan	NB	15	13	8	3.17	11	9	9	3.15	
19	146.1 (295)	37.8 (100)	7584.2 (1100)	Fan	T	15	10	2	3.15	4	2	2	3.12	
20	146.1 (295)	37.8 (100)	8963.2 (1300)	Fan	T	15	6	3	3.17	5	4	4	3.15	
21	146.1 (295)	37.8 (100)	8963.2 (1300)	Fan	T	15	8	2	3.14	1	1	1	3.13	
22	157.2 (315)	37.8 (100)	8963.2 (1300)	Fan	T	15	7	6	3.15	6	5	5	3.14	
23	157.2 (315)	37.8 (100)	8963.2 (1300)	Fan	T	15	11	8	3.16	12	11	11	3.15	
24	157.2 (315)	37.8 (100)	7584.2 (1100)	End	T	15	12	9	3.17	10	10	10	3.14	
25	157.2 (315)	37.8 (100)	6205.3 (900)	End	T	15	13	9	3.17	11	9	9	3.16	
26	146.1 (295)	37.8 (100)	7584.2 (1100)	End	T	15	12	11	3.16	10	8	8	3.15	
27	146.1 (295)	37.8 (100)	6205.3 (900)	End	T	15	13	0	3.15	12	9	9	3.15	

Dimensional Evaluation

All sintered blades from experiments 3, 4, 12, 13, and 16 were evaluated at DDA for conformance to airfoil shape drawing requirements. The results of this evaluation are as follows:

Experiment No.	Number Evaluated	Number Acceptable	Acceptance Rate
3	10	4	40%
4	9	4	44%
12	14	3	21%
13	11	9	82%
16	13	5	38%

Although the sample size is small for each group, the highest yield was clearly produced by experiment No. 13. These results were based on airfoil tip evaluation only; the principal criterion for unacceptable parts was excessive airfoil twist relative to the blade root (attachment and stalk). The blades from Experiment 13 were subsequently evaluated more thoroughly, and 9 of 11 were still found within drawing limits.

Visual, Zyglo, and X-ray examination of the experiment 13 blades at DDA correlates fairly well with the results reported by Carborundum. DDA found seven parts of acceptable quality; CBO would accept eight (one additional blade was rejected by X-ray at DDA). Two of the "good" quality parts were rejected by the dimensional evaluation for an overall yield of 5 of 11 or 45% after sintering. This yield rate will be reviewed continually as additional parts are made. Current plans are for Carborundum to supply 90 finish-machined blades plus 140 without machining.

Some 2070°F blades produced prior to the molding optimization are being machined on required surfaces to establish fixturing and machining technique. The first of these parts is shown in Figure 89. The blade shown is machined on required surfaces except at the blade tip and the platform forward lip seal. Inspection indicates that machined surfaces are correctly located relative to the airfoil.

In summary, the blade process development program at Carborundum has established a suitable fabrication process. Current indications are that the mold through sinter yield may be 33%, which must be improved for production, but it appears that blades of satisfactory quality and accurate shape can be produced for the current program. The strength of injection-molded silicon carbide as provided by current process parameters is yet to be established, but each blade being made (230 currently ordered) will be accompanied by a MOR test bar. The bars have as-fired and ground opposite faces to allow strength determination for both types of surface conditions. This quality of bars can provide a statistically adequate determination of strength variation.

Preceding page blank

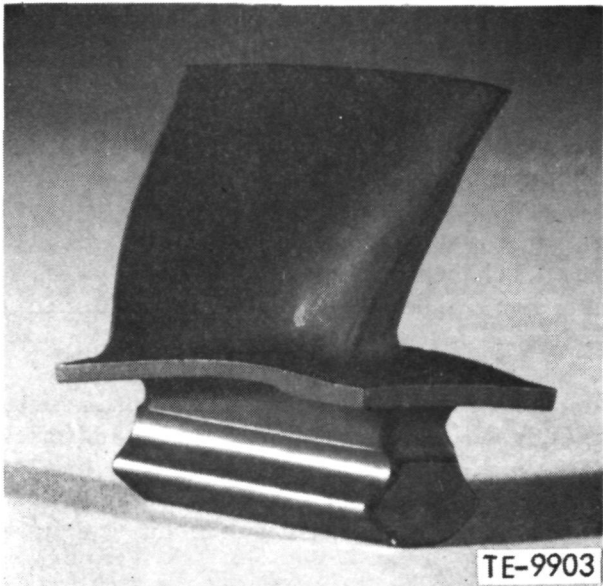
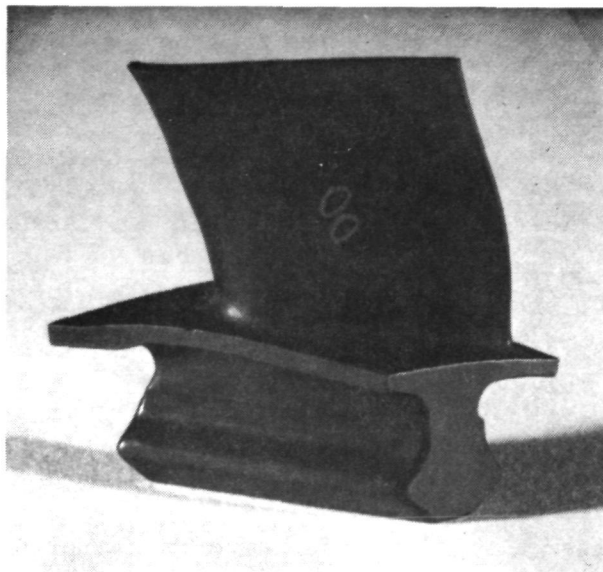


Figure 89. Partially machined 2070°F silicon carbide blade.

GASIFIER TURBINE INLET PLENUM

The ceramic plenum design has been completed, and fabrication is under way at the ceramic suppliers (Norton Co. and Carborundum Co.). Wooden patterns have been fabricated, molds have been prepared, and plenums have been cast and cured at Carborundum. An initial attempt has been made to sinter a plenum without fixturing in a "production" furnace. The plenum was sintered intact but exhibited distortion from incomplete shrinkage during sintering. Further effort is awaiting the availability of a new furnace which will improve process control.

ORIGINAL PAGE IS
OF POOR QUALITY

V. CERAMIC REGENERATOR DEVELOPMENT

INTRODUCTION AND SUMMARY

Development of the ceramic regenerator and its mating face seals continued to increase their durability and temperature capability. The major accomplishments and findings for the reporting period were:

- o Seal and regenerator engine testing was continued.
- o A new design for attachment of the regenerator drive gear was completed and fabrication was begun.
- o Three regenerator disk failures were analyzed to be the result of low strength caused by very thin and distorted separator strips.
- o Various techniques for detecting thin and distorted separator strips in regenerator disks were being investigated.
- o A new three-piece high-temperature inboard regenerator seal design was completed and fabrication was begun.
- o A solution for delamination of the inboard seal crossarm wearface was demonstrated with acceptable leakage.
- o Regenerator seals and disks were tested in the hot rig as follows:
 - 6 inboard seals with new wearface
 - 4 new higher-temperature (1100°C) disks
 - Numerous seals with experimental crossarms
 - A disk composed of extruded segments
- o A new higher-temperature [982°C (1800°F)] hot rig was designed and fabricated

REGENERATOR DISK

Disk Gear Adapter

The previous semiannual report showed a new scheme for the adapter attaching the driving ring gear to the ceramic regenerator disk. Figure 90 shows this scheme, which not only simplifies gear attachment but also provides protection of an exposed disk corner against handling damage.

Disk Failures

Rim Cracking

The previous report described a new disk rim finishing technique and coating cement to forestall circumferential cracks in the first two wraps of the disk. The change in rim coating cement alone has not entirely eliminated these cracks but does prevent the generation of debris from the cracks. Such debris had been a severe life-limiting factor on seal wear. One disk, which utilizes one cement for both rim coating and rim face filling to eliminate processing difficulties and incompatibility between the standard two cements, has accumulated 301 hours of engine operation with excellent results.

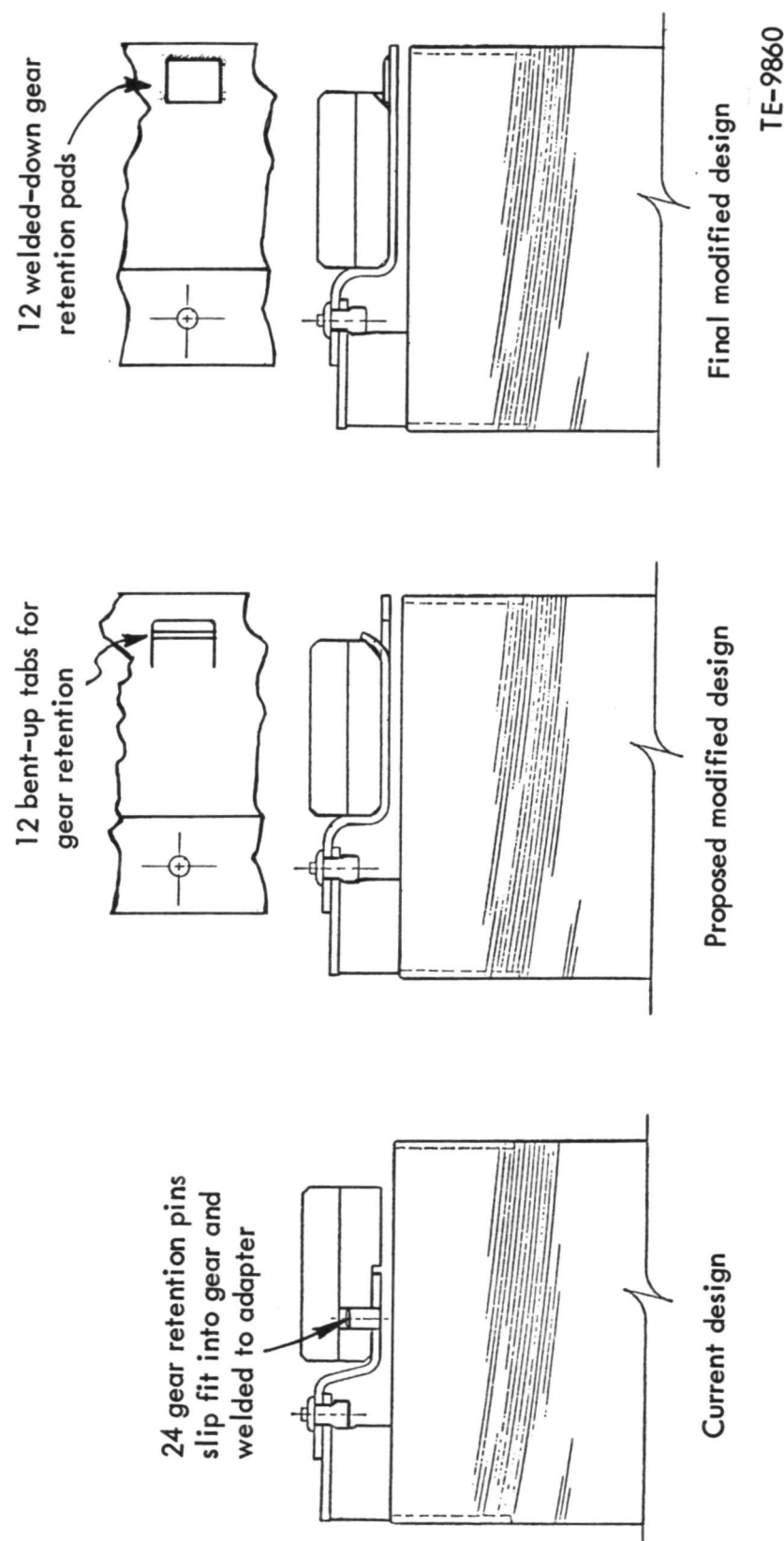


Figure 90. Changes introduced into ring gear mounting adapter to protect edge of ceramic matrix.

Broken Disks

Two Corning disks have completely broken in their initial hot rig test and one disk has acquired a 35-cm (14 in.) long by 1.3 cm (0.5 in.) deep circumferential crack in engine running. Failure analysis attributes all three failures to either thinness or distortion of the flat separator strip. The disk matrix is formed by a flat strip and a corrugated strip spirally wrapped together. Thinness or distortion of the flat sheet results in a severe loss of strength. All three disks failed in the area of greatest loss in strength. Figures 91 through 94 show the failures. All failures were induced by circumferential cracks resulting from the weakness of the separator strips.

The two disks which were completely broken in the regenerator rig had each run about 5 hours at lower speeds and failed after about 45 minutes at 100% engine speed conditions. The 100% speed represents the maximum pressure and torque but not the maximum temperature encountered by a disk. At the radii where these failures occurred, stress analysis shows that pressure loads are by far the dominant stress producer. Consequently, a 30% overpressure proof test has been incorporated into the hot rig test of each set of seals and disks.



Figure 91. Regenerator disk hub failure encountered during hot rig running.

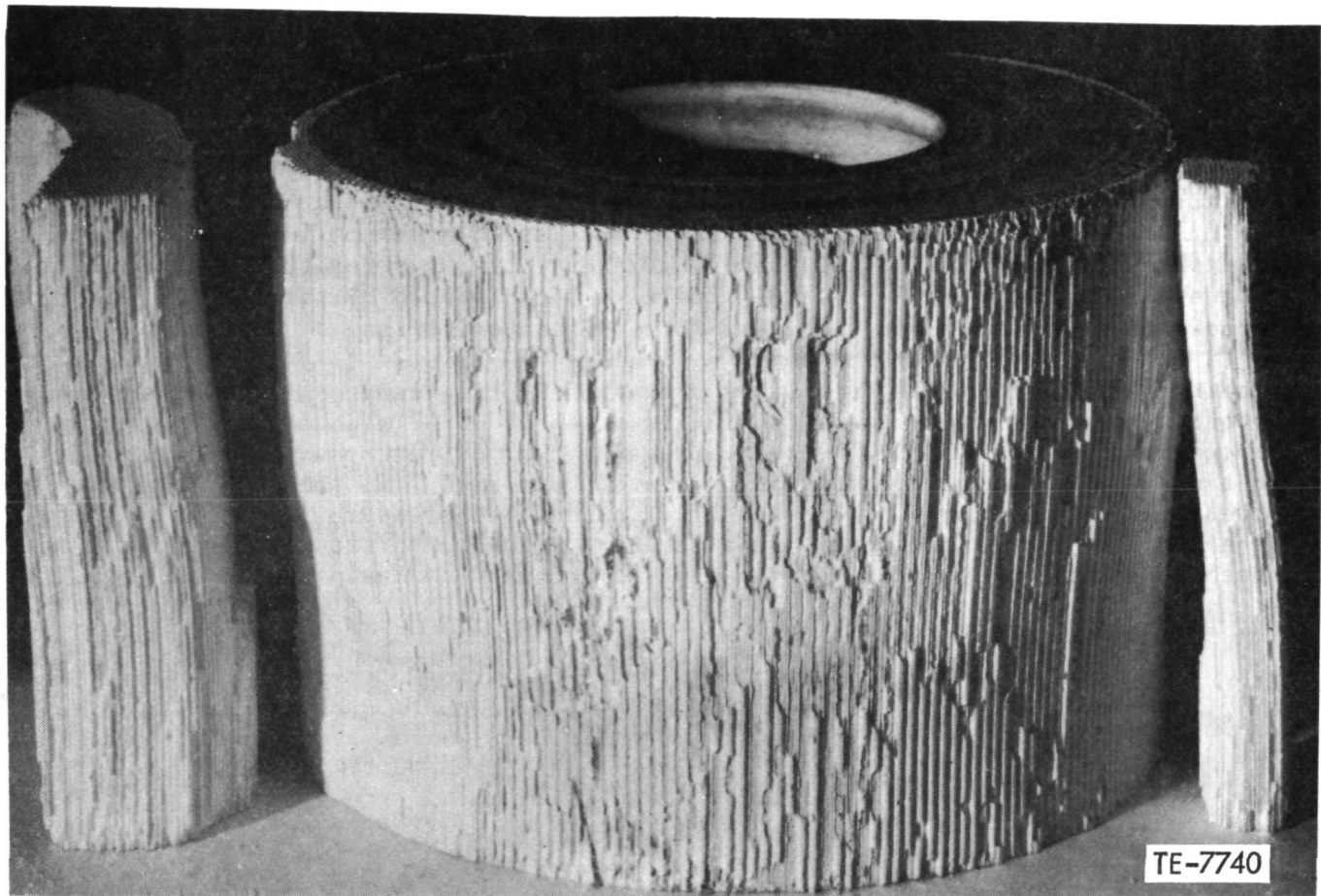


Figure 92. Close-up of hub showing unusual passage slant.

Thermal stresses are maximum and predominant in the rim area where the seals establish high temperature gradients. The first disk failed in the matrix just outside the hub joining cement at about 5.6 cm (2.2 in.) radius as shown by Figures 91 and 92. Modulus of rupture (MOR) samples taken throughout the disk showed that the matrix strength was very low in the area near the failure. The low matrix strength was the result of a combination of distortion and thinness in the flat separator strip. Details of this investigation are covered in Section III of this and the previous semiannual report. Figure 95 illustrates distortion of the separator and its effect on strength. This distortion was found to be closely associated with an unusual "S" shape of the disk passages (Figure 92). The separator distortion takes place at the inflection point in the "S." Normally, disk shrinkage in firing produces a single curvature in the passages instead of this double curvature.

The second disk failed at about the 28-cm (11 in.) radius, as shown in Figure 93. This disk also had the abnormal "S" shaped passages and consequent separator distortion; however, it was milder near the failure area than elsewhere and not judged to be responsible for the failure. Correlation of matrix strength and wall thickness demonstrated that this failure was the result of thin separators. Regression coefficients show a very strong dependency of

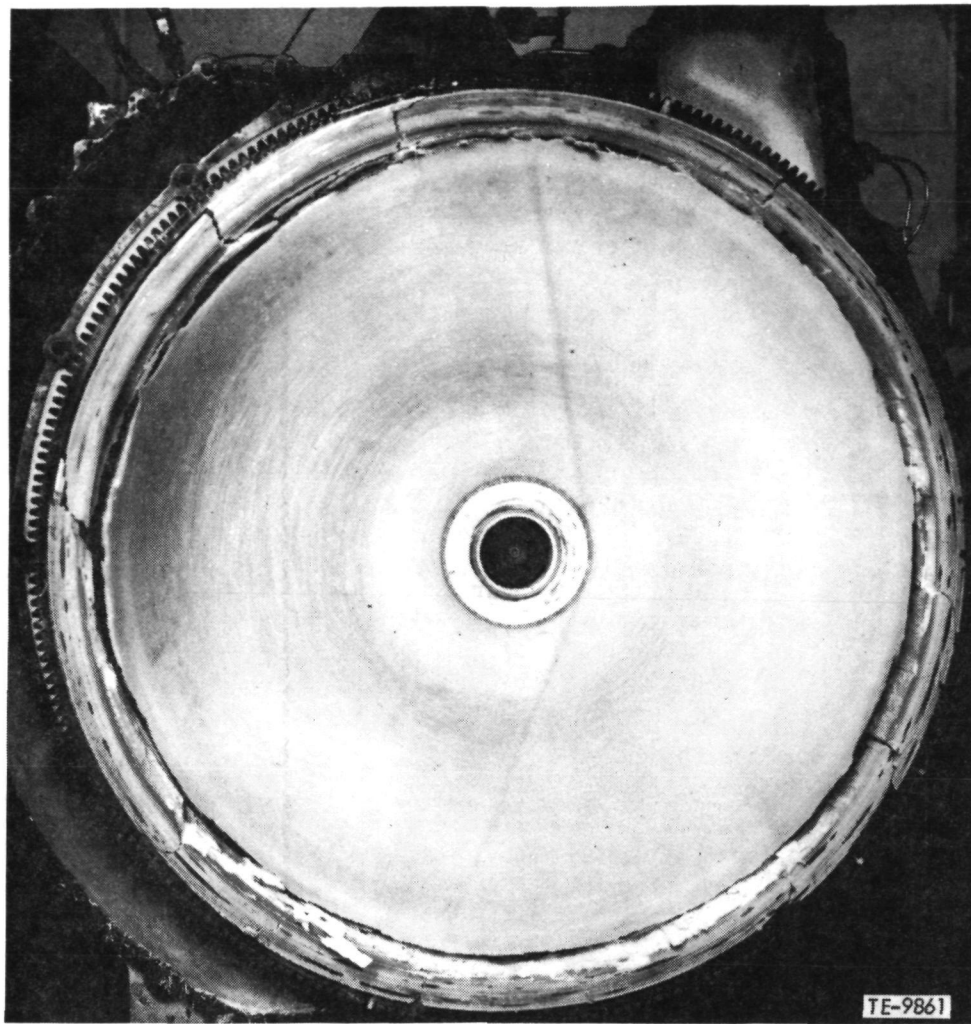


Figure 93. Failed ceramic regenerator disk (DOE transit coach project).

strength on wall thickness, suggesting that a limit must be established. These test results and analyses are discussed in Section III under Regenerator Materials Evaluation.

The third failed disk developed a 35-cm (14 in.) circumferential crack at the 25-cm (10 in.) radius (Figure 94), resulting from an exceedingly thin separator strip less than 0.025 mm (0.001 in.) thick instead of the normal 0.066 mm (0.0026 in.). This failure amounted to a disintegration of the flat separator strip with the adjacent corrugated strips left intact.

Because of the involvement of "S" shaped passages and separator strip thinness in disk failures, inspection procedures for the detection of these deficiencies are being developed.

ORIGINAL PAGE IS
OF POOR QUALITY

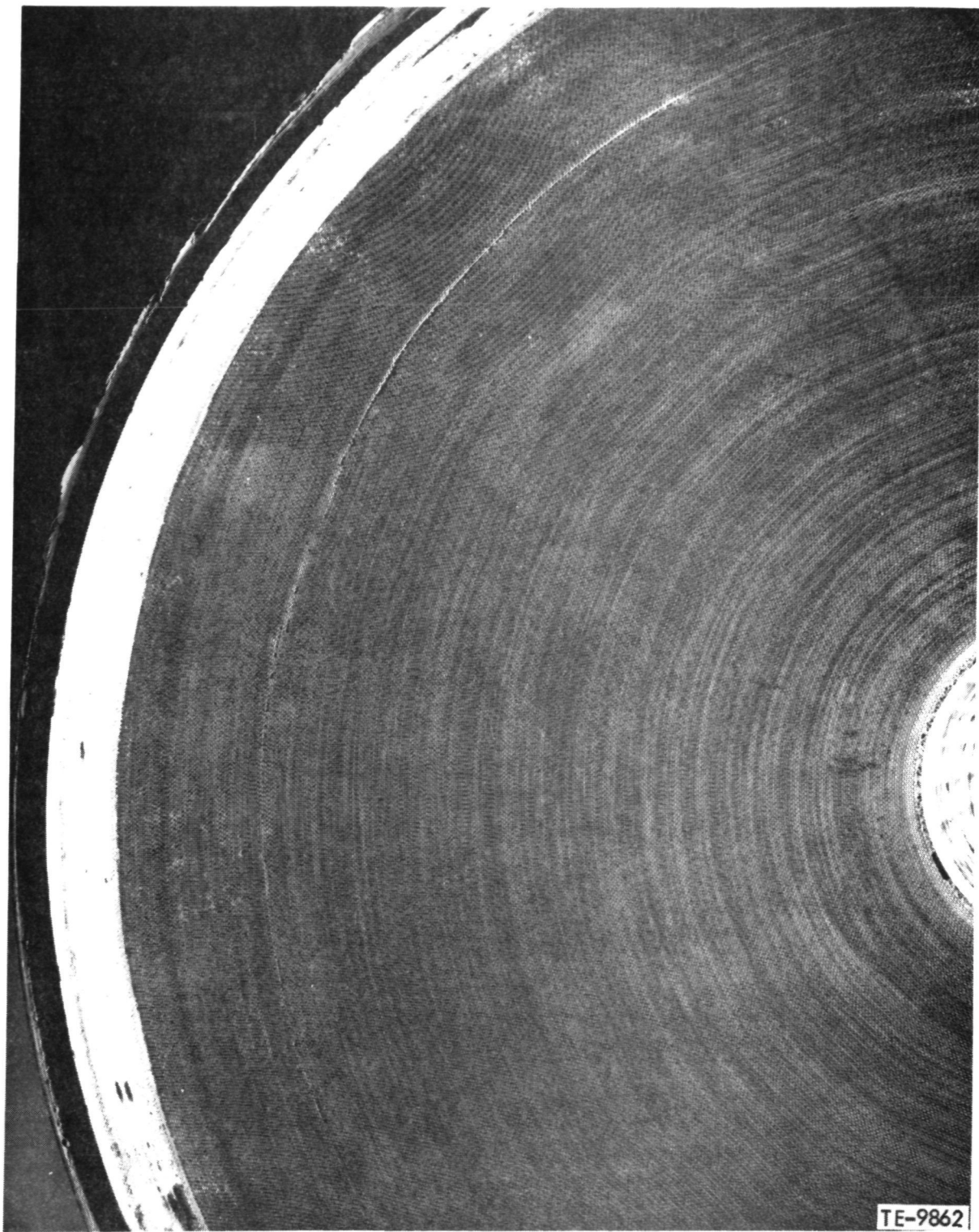
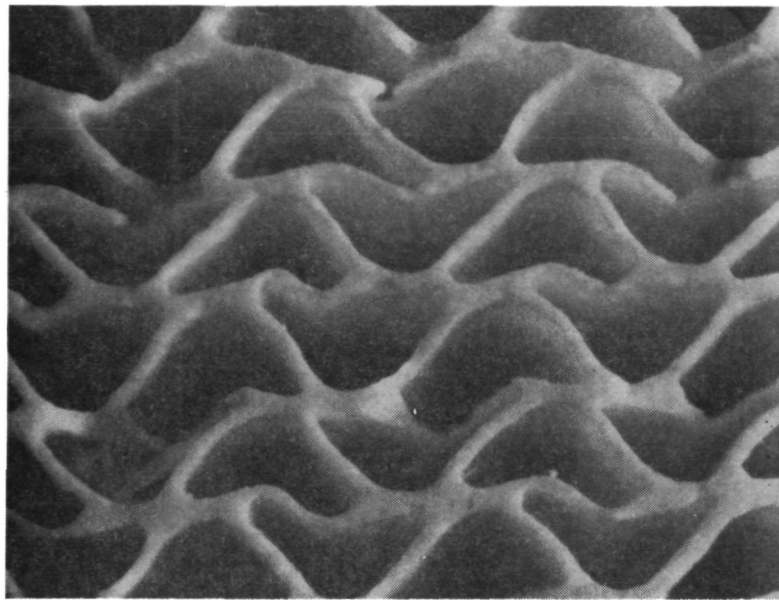
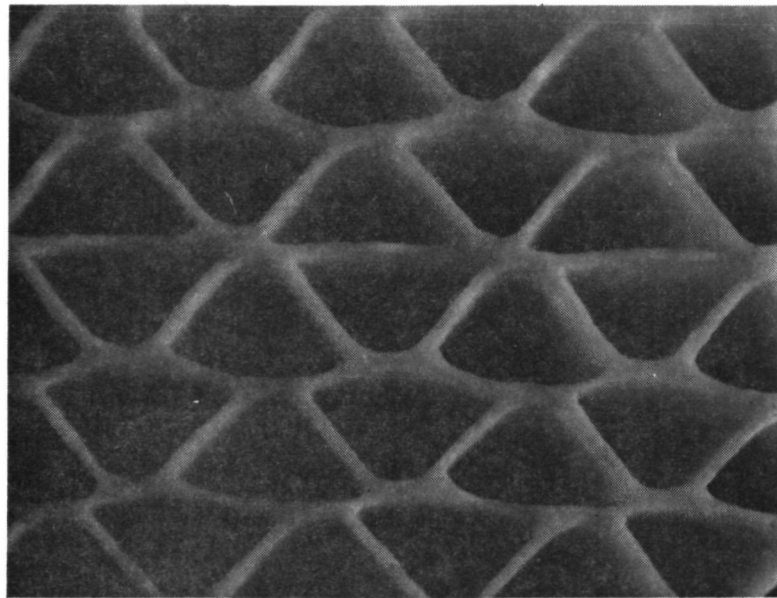


Figure 94. Cracked ceramic regenerator disk (DOE transit coach project).



Test bar B₄; radius = 10.1 cm (4.0 in.);
MOR = 704 kPa (101 psi)



Test bar T₆; radius = 10.1 cm (4.0 in.);
MOR = 1481 kPa (215 psi) TE-7735

Figure 95. HRD-AB disk 4, alumina silicate matrix, sample 1.

NGK-Locke Disk Failure in Hot Rig

The first NGK-Locke extruded composite matrix failed during rig testing. The failed core is shown in Figure 96. This disk is a composite construction of 27 extruded segments. It is a magnesium alumina silicate (MAS) material and has a triangular matrix with 0.127-mm (0.005 in.) thick walls. The disk ran for 3.17 hours and had completed 50 through 90% free-shaft conditions as defined in Table XXXIII.

ORIGINAL PAGE IS
OF POOR QUALITY

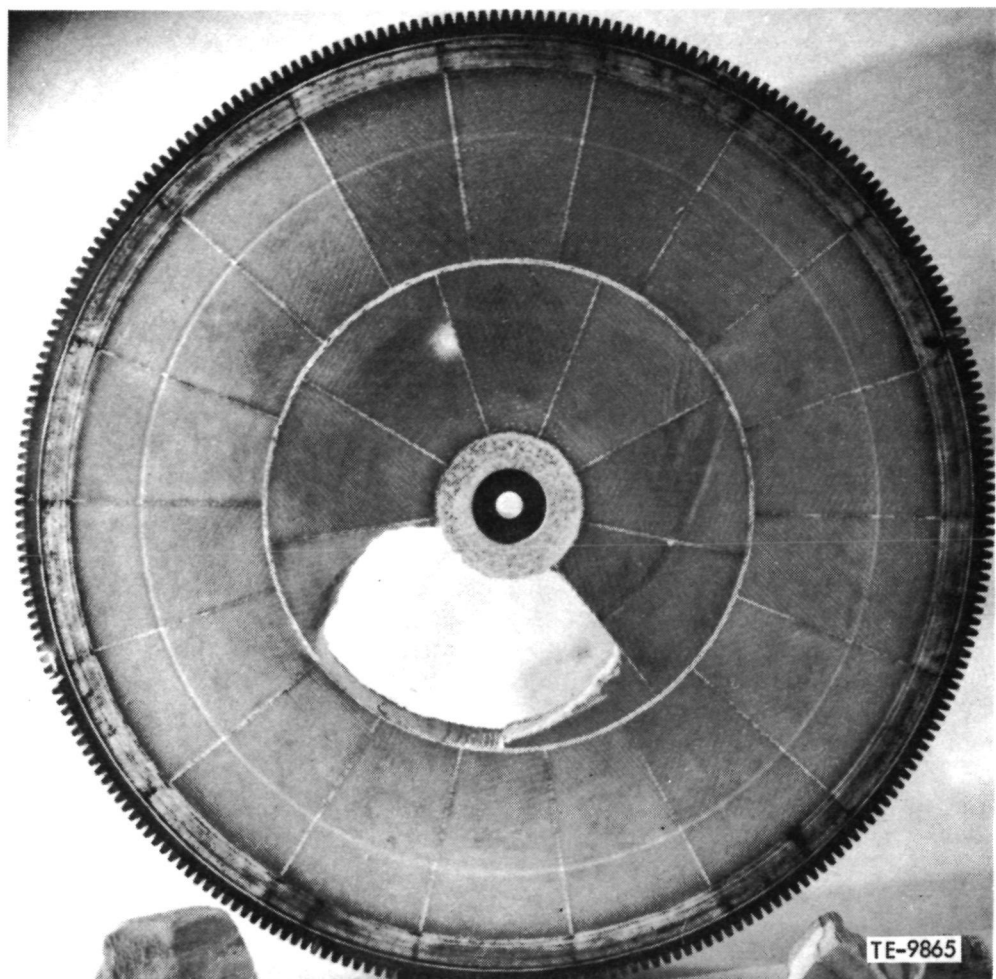


Figure 96. Failed NGK regenerator disk after 3.17 hours of rig testing.

TABLE XXXIII. FREE-SHAFTING RIG TEST CONDITIONS

Gasifier Speed, %	50	60	70	80	90	100
Air Inlet Pressure, kPa psi	38.6 (5.6)	64.8 (9.4)	97.9 (14.2)	142.7 (20.7)	203.4 (29.5)	282.7 (42.0)
Air Inlet Temp, °C °F	71 (159)	92 (198)	114 (237)	142 (287)	172 (341)	205 (401)
Gas Inlet Temp, °C °F	515°C (959°F)	543 (1009)	537 (999)	556 (1033)	590 (1094)	641 (1186)

Gas inlet pressure within 13.8 kPa (2.0 psi) of atmospheric throughout test range. The failure occurred in going from the 90 to 100% condition.

Slight cracks were visible in the circumferential cement joint between the inner and outer matrix sections before the disk was tested. NGK-Locke has related that cementing of the circumferential joint is a known problem area and has agreed to supply two more cores with changes to the cement process at a later date.

Disk Inspection

X-Ray

X-ray techniques have been developed to detect "S" shaped disk passages which cause flat separator strip distortion and loss of strength in the matrix. Wires are inserted through passages to enhance contrast. Inspection of 22 disks has shown three disks with "S" shaped passages of a severity equal to that found in the failed disk. Corning, the disk vendor, is making arrangements for X-ray inspection.

Microscopic

A microscopic technique for detection of thin separator strips was proposed to Corning; they are evaluating its feasibility in their process. Statistical analysis of the effect of separator strip thickness on matrix MOR toward a suitable limit for thickness is continuing.

Anemometer

An investigation is under way to determine whether a survey of local flow rates will detect areas with thin walls or distorted separator strips. A very sensitive anemometer covering an 8-mm (0.25 in.) diameter flow area is used. Preliminary results indicate high sensitivity to thin walls but not to distorted separators. Correlation analysis is in process.

Natural Frequency

Tests are in process to determine whether natural frequencies and mode shapes of the regenerator disk will detect and locate weak spots. Excitation is provided by an electromagnetic shaker with the disk mounted at the hub. Preliminary results are encouraging in that one of six disks has distinctly lower frequencies and odd mode shapes suggestive of weak spots.

Disk Stress

Both completed disk failures occurred while running at maximum pressure rather than maximum temperature in the hot regenerator rig. Previous stress analyses, as previously reported, had shown no significant effect of pressure or pressure-induced gear and seal loads on disk stress. The failures at maximum pressure gave reason to reexamine the previous analyses. Several factors came to light:

1. Matrix strength data from NASA CR-135330 (page 95), published since the previous analysis, show that radial compressive strength is appreciably lower than radial MOR, which was the only radial strength available initially.
2. The previous stress model employed simplifying assumptions which should be eliminated in light of new concerns:
 - a. Low pressure was applied throughout the interior of the matrix instead of confining low pressure to one sector as established by the diametral seal.
 - b. Concentrated gear and seal loads were confined to one direction instead of their true multidirection.

The stress model is being modified to improve its accuracy. In the meantime, preliminary results show that pressure-induced stresses predominate throughout the region of the failures and will reach very significant levels compared with now published radial compressive strength. Nevertheless, the three failures to date have been shown to be the results of disk deficiencies.

REGENERATOR SEALS

3-Piece High-Temperature Seal

During this reporting period final design and stress analysis of a new 3-piece inboard regenerator seal for high-temperature operation were completed and fabrication was begun. This seal is designed to have reduced thermal distortion for lower leakage and wear.

The major source of regenerator seal stress and distortion is the radial temperature gradient across the rim of the inboard seal. Figure 97 shows the regenerator disk and seals at the rim. The inside diameter of the seal, exposed to exhaust gas, runs hotter than the outside diameter, which is exposed to compressor discharge air. The resultant stresses cause yielding of the seal platform in hot areas. Distortion of the seal results in locally accelerated wear and leakage. Distortion takes the form of out-of-plane and coned buckling of the rim and crossarm bow.

A new concept is utilized in the 3-piece seal design, shown in Figure 98, to counteract the rim temperature gradient.

The pattern of seal temperatures necessary for this analysis was extrapolated from seal temperature measurements at temperatures midway between the current standard 774°C (1425°F) and future 982°C (1800°F) level.

During this report period, this seal crossarm cooling concept was tested on a modified current seal at current temperatures. Results suggest that cooling may be adequate at higher temperatures.

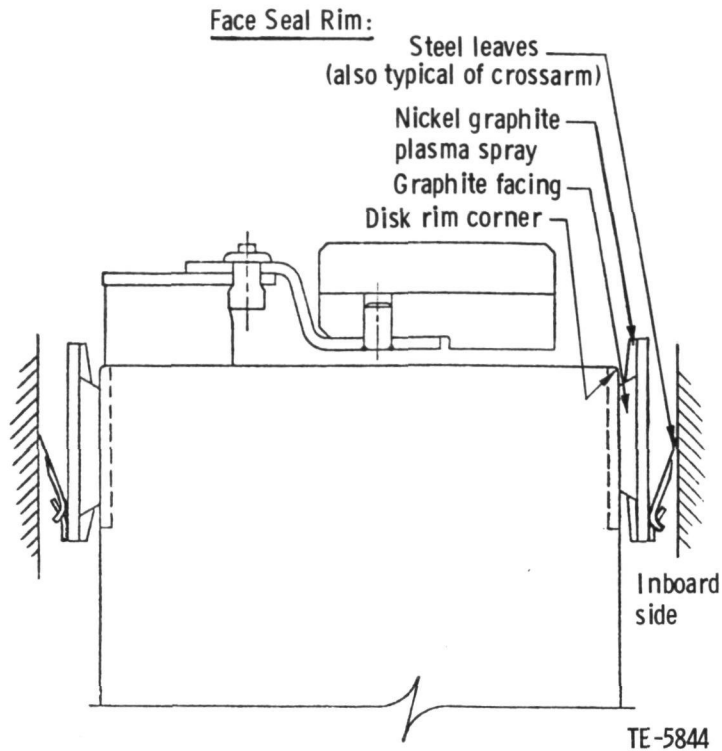


Figure 97. Cross section of regenerator disk rim, drive gear, and face seal rims.

NiO/CaF₂ Plasma-Sprayed Wearface

During this report period, sufficient test experience was acquired with the new 85% NiO/15% CaF₂ inboard crossarm wearface with an interlayer to demonstrate that the delamination problem had been solved and that acceptably low leakage was achieved. The development of this coating system to prevent oxidation of the bond coat promoted by the CaF₂ content was described in the previous semiannual report. The first 10 seals of the new configuration showed acceptable average leakage values as follows:

<u>Engine Speed Condition</u>	<u>Average of 10 Leakage</u>
50% Idle	6.9%
70%	3.6%
100%	4.1%

Efforts were continued to obtain still lower leakage by reducing both permanent and nonpermanent thermal distortion from thermal expansion mismatch between wearface and substrate. Increase in the CaF₂ content was known to improve the expansion match but also to aggravate delamination tendency. Increased CaF₂ aggravates delamination because it promotes oxidation of the bond coat and because, when mechanically mixed with the NiO, it tends to

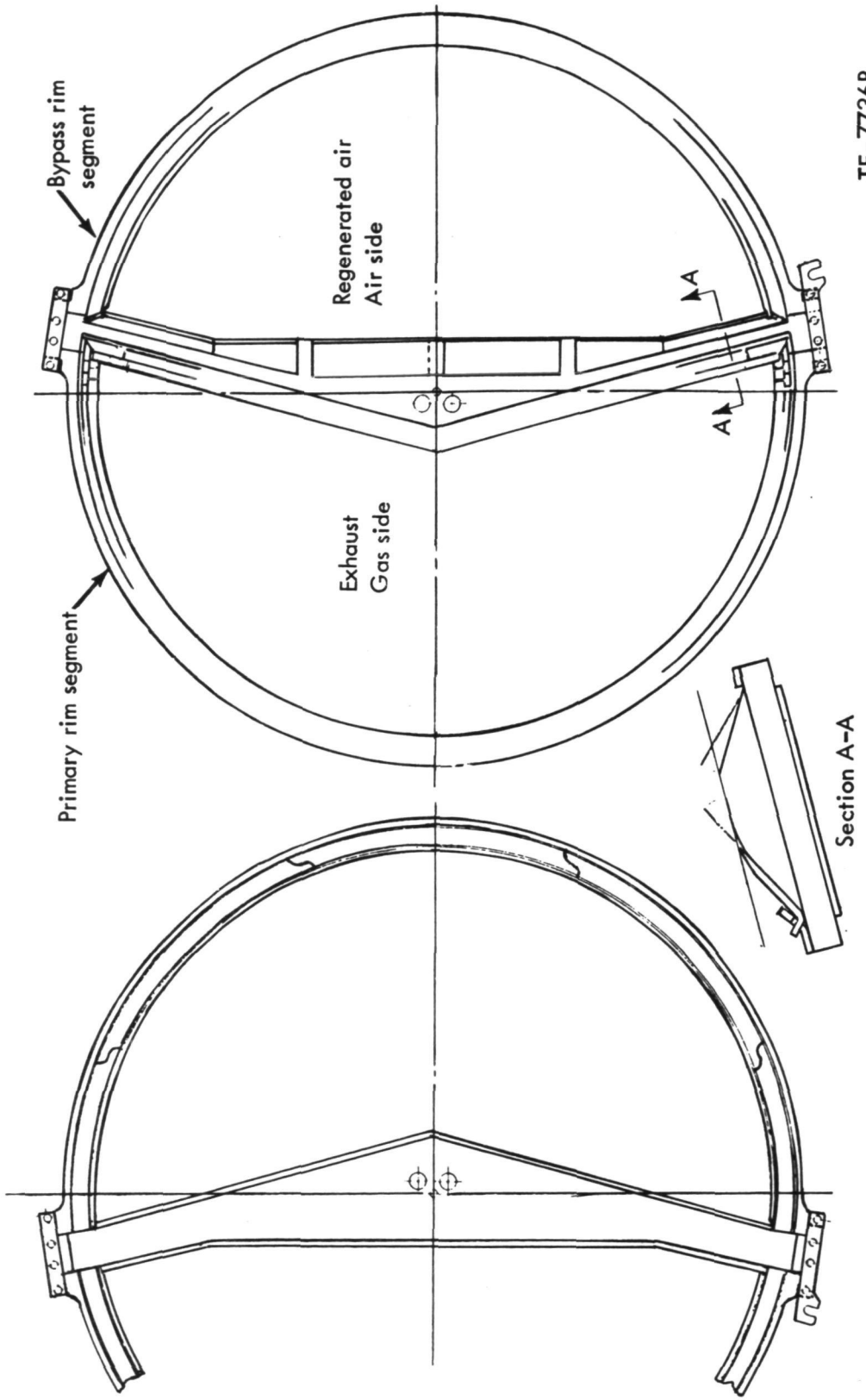


Figure 98. Regenerator inboard seal.

stratify producing planes of low shear strength. New composite NiO/CaF₂ spray powders were received near the end of the report period. These powders range from 10 to 40% CaF₂ content, allowing optimization. In the interim, development has proceeded with the mechanically mixed powders.

A crossarm with 65% NiO/35% CaF₂ wearface was produced. It demonstrated lower thermal distortion and short-term delamination resistance to 871°C (1600°F). Delamination resistance to thermal cycles and mechanical impact was demonstrated. On this basis, several seals with 70% NiO/30% CaF₂ wearface were ordered.

Seals with the crosswise bow in the crossarm are ground flat when finished but reacquire about 1/3 of their initial bow when run. Two of these seals were reground after running and showed no further bowing; however, no leakage improvement was realized. This suggests that nonpermanent thermal distortion must predominate.

Friction and wear of the 85% NiO/15% CaF₂ and 70% NiO/30% CaF₂ were compared at 871°C (1600°F) for the mechanically mixed powders with the following results:

<u>Material</u>	<u>Seal wear per 100 hr</u>	<u>Disk wear per 100 hr</u>	<u>Coefficient of friction</u>
70% NiO/30% CaF ₂	0.100 mm (0.0040 in.)	0.190 mm (0.0075 in.)	0.34-0.58
85% NiO/15% CaF ₂	0.036 mm (0.0014 in.)	0.038 mm (0.0015 in.)	0.33-0.42

Higher friction and wear with the 70% NiO/30% CaF₂ was not expected, based on results at lower temperatures. It may be that CaF₂ stratification in the mechanically mixed powders is responsible; therefore, better results are anticipated with the new composite powders.

Mixing of NiO and CaF₂ powders in the spray nozzle was tried, but this produced even worse stratification than mechanical premixing.

A seal was made and tested with 85% NiO/15% CaF₂. Leakage was as good as but no better than in early 70% NiO/30% CaF₂ seals which had suffered delamination. A leakage and flatness check after 331 hours of engine running showed the following increases:

<u>Engine Speed Condition</u>	<u>Initial Leakage</u>	<u>Leakage after 331 hr</u>
50% idle	4.1	11.8
70%	2.1	6.7
100%	3.6	4.9

The final leakage would be classed as only fair and is similar to the worst new single-coated 85% NiO/15% CaF₂. The crossarm had also acquired a 0.51-mm (0.020 in.) lengthwise bow and a 0.051-mm (0.002 in.) crosswise bow. The bow was concave with respect to the wearface which is opposite to that for standard single-coated seals. This seal is also discussed under "Hot Performance Rig Testing."

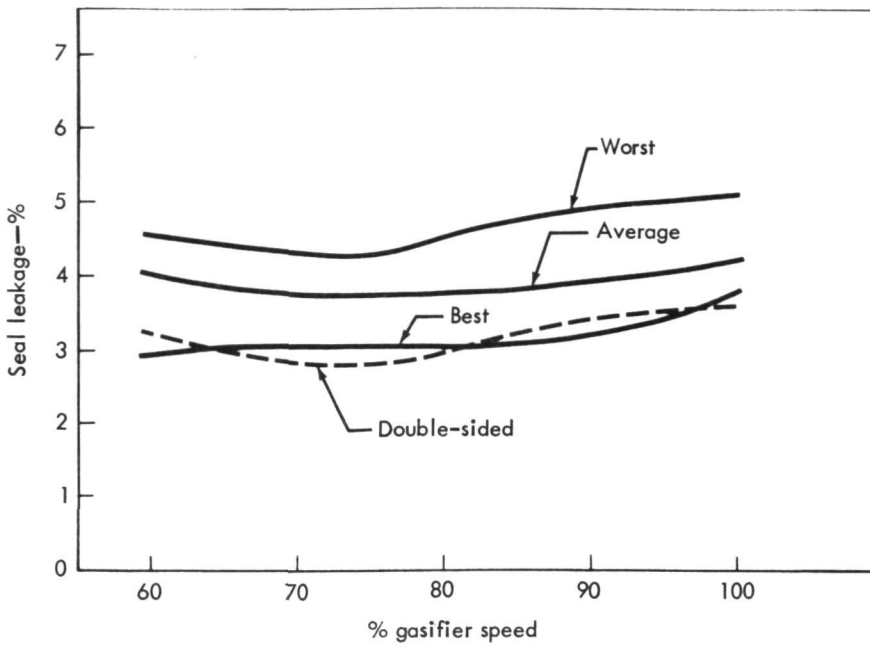
HOT PERFORMANCE RIG TESTING

Hot rig testing during this period consisted mainly of the qualification of six inboard seals with 85% NiO/15% CaF₂ crossarm wearface and four Corning 9461 AS material thin-wall disks capable of running at 1100°C (2012°F). A number of other regenerator parts were also rig tested as described in the following discussion.

Leakage performance data from the six CATE program inboard seals with 85% NiO/CaF₂ crossarm wearface are shown in Table XXXIV. Also included in this table are seven seals of identical design purchased and tested under other programs. (These are the seals run with the 15-XX serial number disks.) The 60-100% speed points in this chart are power transfer conditions and represent the bulk of engine operating conditions. The 50% free-shaft points give an indication of how the seals perform during starting and engine idle conditions. The first 50% column in the chart was run immediately preceding the power transfer testing; the last 50% column immediately following it. Figure 99 is a plot of the 60-100% data for the worst and best as well as the average of the fourteen seals in Table XXXIV. Also included in the table and in Figure 99 is data from the initial testing of an inboard seal with 85% NiO/15% CaF₂ plasma spray on the crossarm. Figure 100 presents the initial test results of this seal as well as the rig test results after the seal had been engine tested for 331 hours. The leaf side of the seal is shown in Figure 101.

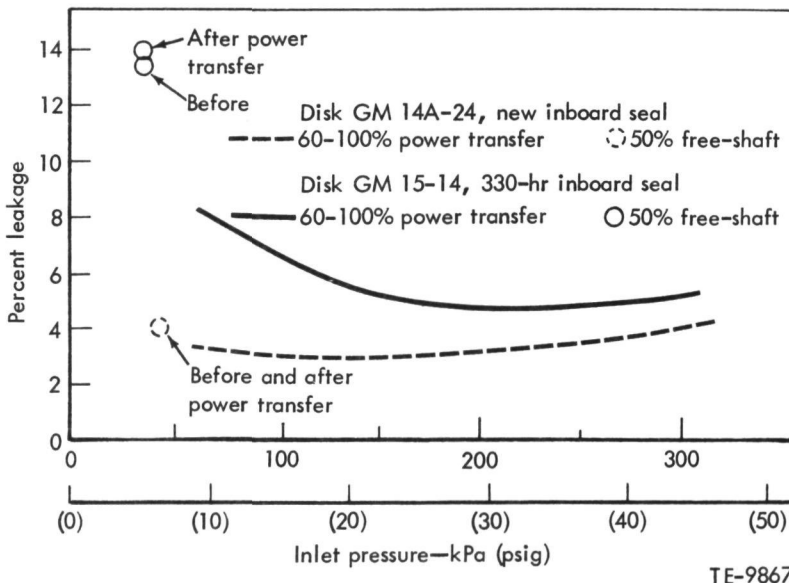
TABLE XXXIV. LEAKAGE OF 85/15 INBOARD REGENERATOR SEALS

Inb'd Seal	Outb'd Seal	Disk	50FS	60	70	80	Gasifier Speed 90	100	50FS
H3027	C491	16A-02	18.1		3.6	3.8	4.0	4.4	9.1
H3028	C490	16A-01	6.5	4.0	3.8	3.6	4.1	4.5	4.1
H3032	C479	14A-25	5.6	3.9	3.7	3.7	4.0	4.1	5.8
H3035	C482	16A-04	8.2	4.5	4.3	4.5	4.9	5.1	4.8
H3037	C514	15-04	4.9	2.9	3.0	3.0	3.2	3.8	4.1
H3036	C505	15-10	4.9	2.9	2.7	2.9	3.4	3.5	4.1
H3039	C492	14A-24	4.1	3.2	2.8	2.9	3.4	3.6	4.1
H3031	C396	15-01	7.6	4.5	4.4	4.3	4.3	4.5	3.7
H3038	C493	16A-03	---	4.9	4.2	3.9	3.6	3.8	7.8
H3029	C481	14A-26-SC	4.9	4.8	4.1	3.7	3.7	3.9	6.5
H3040	C524	15-15	4.0	3.3	3.4	3.6	3.6	4.0	5.6
H3041	C531	15-13	8.7	4.2	3.7	3.6	3.7	4.0	---
H3042	C511	15-11	7.8	6.0	4.1	4.7	4.5	4.8	7.7
H3043	C532	15-18	5.8	3.9	3.7	3.6	3.7	4.2	---
Average			7.0	4.0	3.7	3.7	3.9	4.2	5.6



TE-9866

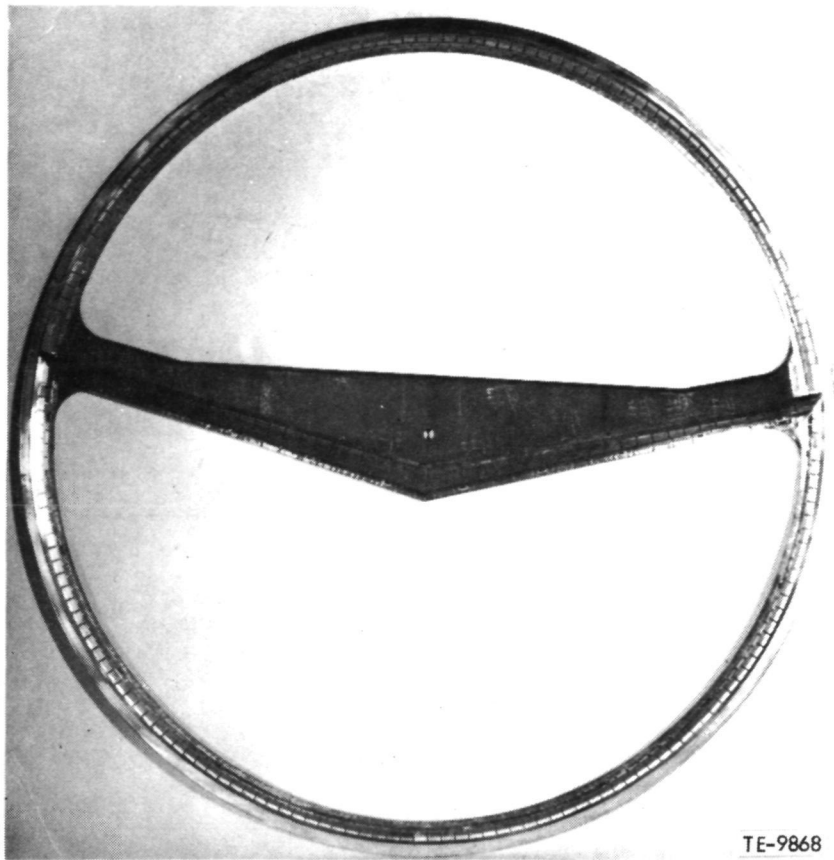
Figure 99. Leakage of inboard seals with 85% NiO/15% CaF₂ crossarms sprayed by DDA.



TE-9867

Figure 100. Retest of crossarm seal.

Table XXXV is a list of recently tested ceramic regenerator disks including the four 9461 material disks received this period. This table shows the disks from the same series of tests as shown in Table XXXIV. Both tables present the data in chronological order of testing. Also, the testing of disk 14A-27-SC has been added to Table XXXV. It does not appear in Table XXXIV because it was tested with hot seal H3032, which appears with disk 14A-25. Again, the



TE-9868

Figure 101. Leaf side of inboard seal.

disks with the prefix 15 serial numbers were not fabricated or tested under the CATE project and are not discussed in this report, but they are of the same design and are included to give a broader base for comparison of the 9461 material disks. Figure 102 is a comparison of average effectiveness and pressure drop for the four 9461 material disks tested against the average of eleven 9460 material disks. The X's along the airflow axis of the plot are 60, 70, 80, 90, and 100% gasifier speed.

Other types of disks tested this period include an extruded composite disk made by NGK-Locke and two Corning thin-wall AS disks of 9460 material incorporating an improved rim coating technique.

The improved coating technique, as shown in Figure 103, uses QF180 cement to coat the outside diameter of the disk for protection of the matrix and to fill the outer 1 inch of peripheral matrix face in order to provide acceptable surface conditions for the seal. The standard practice is to use QF180 cement to fill the face and a separate cement to coat the outside diameter. Rim delamination problems encountered on some disks have been attributed to the incompatibility of rim coating and face fill at the point where they meet at the edge of the disk rim. After rig testing of two disks and limited engine testing of one disk, the single-cement rim coating and face fill process appears to be a significant improvement over previous processes.

TABLE XXXV. EFFECTIVENESS AND PRESSURE DROP OF RECENTLY TESTED DISKS

Disk	Inb'd Seal	Outb'd Seal	Comment	Percent Gasifier Speed								
				60	70	80	90	100				
16A-02	H3027	C491	9461 Material	η (%)	98.6	96.8	97.0	95.5	93.3			
				ΔP (%)	2.5	3.25	3.85	4.70	5.65			
16A-01	H3028	C490	9461 Material		98.1	97.1	97.6	96.3	93.4			
					2.50	3.00	3.65	4.45	5.45			
14A-25	H3032	C479	9460 CATE		92.6	97.5	96.3	94.8	92.5			
					2.38	2.83	3.45	4.25	5.18			
15A-04	H3035	C482	9461 Material		98.9	98.0	97.0	95.6	93.3			
					2.50	2.92	3.54	4.36	5.35			
14A-27SC	H3032	C479	All QF180 Coating		98.5	97.5	96.3	94.9	92.9			
					2.49	2.98	3.61	4.35	5.31			
15-04	H3037	C514	9460 Bus		97.2	96.3	95.1	93.7	91.7			
					2.46	2.90	3.56	4.38	5.30			
15-10	H3036	C505	9460 Bus		98.6	97.8	96.4	94.7	92.5			
					2.21	2.61	3.18	3.93	4.78			
14A-24	H3039	C492	9460 CATE		98.4	97.2	95.4	94.2	91.7			
					2.22	2.61	3.19	3.93	4.81			
15-01	H3031	C396	9460 Bus		98.6	97.6	96.0	94.0	91.4			
					2.04	2.42	2.95	3.60	4.45			
16A-03	H3038	C493	9461 Material		99.2	98.2	96.9	95.1	93.0			
					2.57	2.93	3.55	4.31	5.24			
14A-26SC	H3029	C481	All QF180 Coating		98.4	97.2	95.7	94.3	91.8			
					2.46	2.94	3.57	4.39	5.29			
15-15	H3040	C524	9460 Bus		98.5	97.5	96.3	93.8	91.4			
					2.07	2.61	3.09	3.77	4.58			
15-13	H3041	C531	9460 Bus		98.3	97.7	96.5	95.0	92.5			
					2.40	2.51	3.39	4.10	4.94			
15-11	H3042	C511	9460 Bus		99.3	97.7	96.5	94.8	92.5			
					2.14	2.68	3.24	3.91	4.83			
15-18	H3043	C532	9460 Bus		97.7	96.8	95.7	94.2	91.3			
					1.95	2.38	2.83	3.49	4.29			
				15 Disk Average	98.5	97.4	96.3	94.7	92.3			
					2.32	2.79	3.37	4.13	5.03			
				9461 4 Disk Average	98.7	97.6	97.1	95.6	93.3			
					2.52	3.03	3.65	4.46	5.42			
				9460 11 Disk Average	98.4	97.3	96.0	94.4	92.0			
					2.25	2.71	3.28	4.01	4.89			

A regenerator disk made up of a number of extruded sections cemented together to form a complete disk was rig tested. The results of this testing are reported under "NGK Regenerator Disk Failure," which appears earlier in this section.

A number of experimental inboard seals were rig tested. Four of these, with test results shown in Figure 104, had NiO/CaF₂ plasma sprayed over Metnet. Metnet is a 5% dense metal foam material made of iron, nickel, and chrome. The Metnet is brazed to the metal seal platform and filled with chromite-potassium silicate before being covered with plasma-sprayed NiO/CaF₂. All four seals in Figure 104 have a 0.152-cm (0.060 in.) thick platform with 0.140-

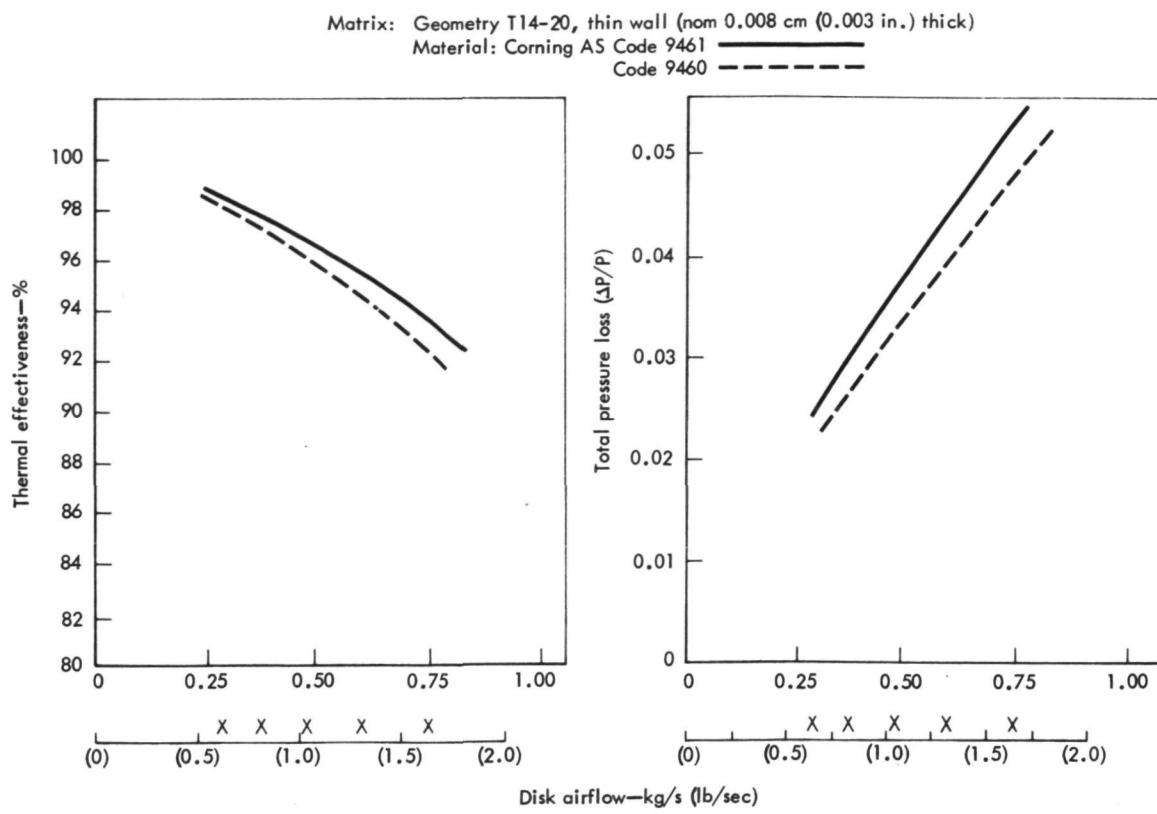


Figure 102. Effectiveness and pressure drop vs airflow.

TE-9869

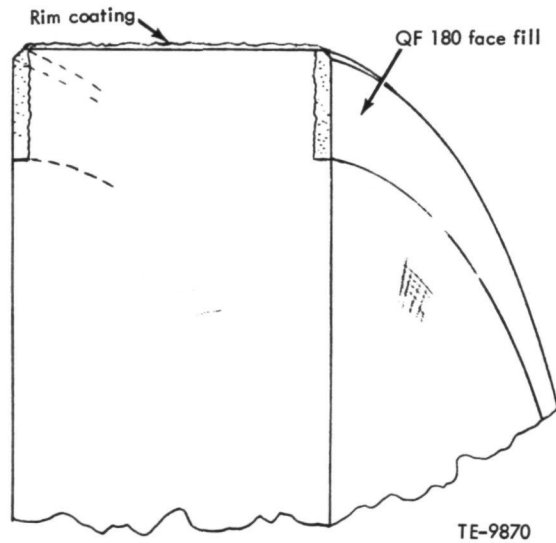


Figure 103. Disk rim coating and face fill process.

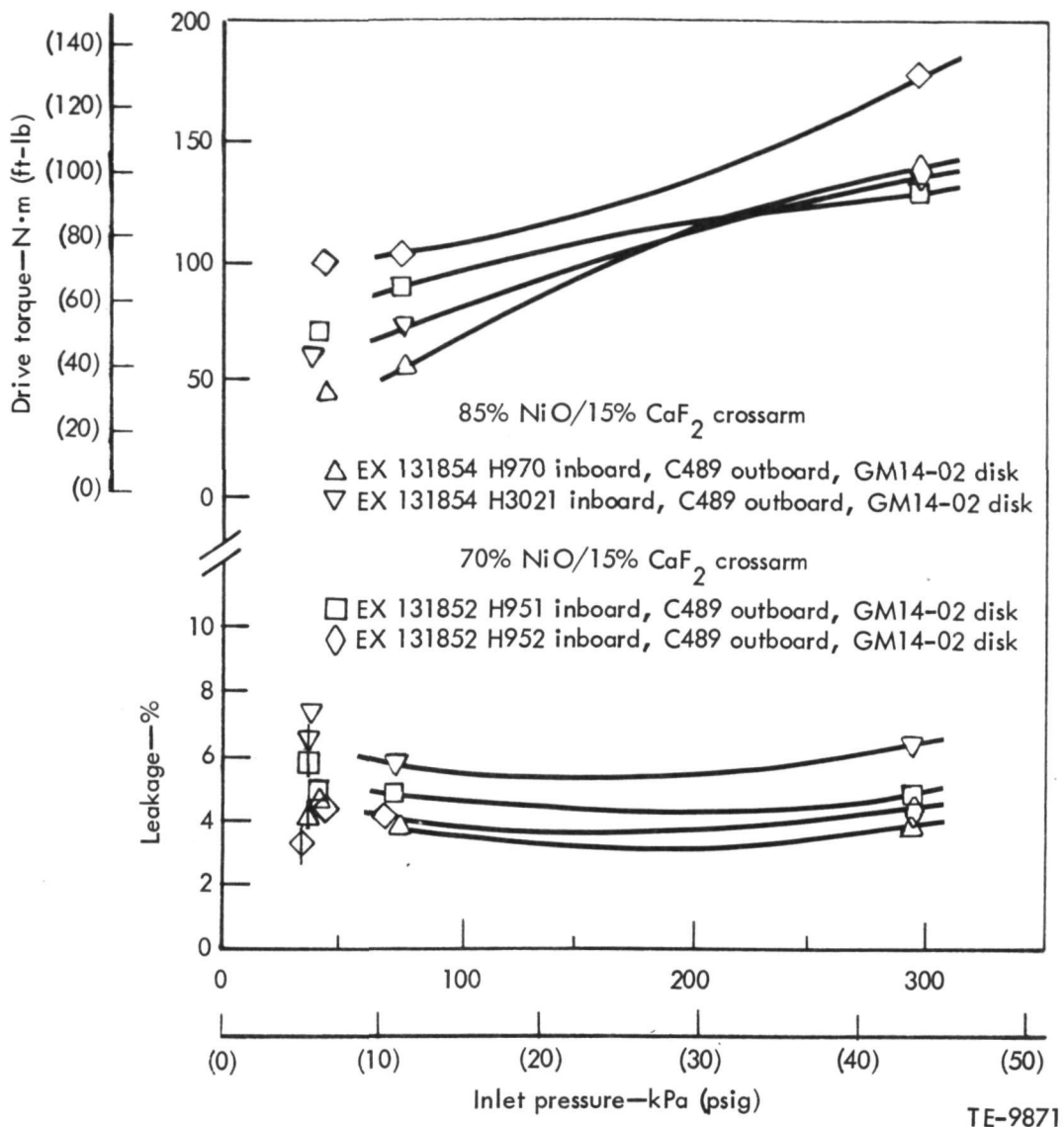


Figure 104. Hot rig performance of inboard regenerator seals with crossarms of NiO/CaF₂ plasma sprayed over Metnet.

0.165 cm (0.055-0.065 in.) of Metnet and 0.076-0.102 cm (0.030-0.040 in.) of NiO/CaF₂. Two were sprayed with 85% NiO/15% CaF₂ and the other two with 70% NiO/30% CaF₂. The purpose of the Metnet is to provide a compliant layer to divorce the higher-expansion plasma-sprayed wearface from the metal seal platform, which offers advantages in remedying delamination and minimizing thermal distortion.

The curves in Figure 104 were taken at 60-100% power transfer engine conditions. The points at the low end of the curves are at engine 50% free-shaft conditions, which approximate idle--the open points being taken before the power transfer curve, and the points with vertical slashes after the 100% power transfer points.

The three seals for which test data are shown in Figure 105 are one-piece in-board seals with 70% NiO/30% CaF₂ crossarm wearface plasma-sprayed directly to an Inconel 625 seal platform. They have the same construction as the current standard CATE inboard seals except that the crossarm platform is 0.406 cm (0.160 in.) thick and the rim platform 0.254 cm (0.100 in.) thick as opposed to the standard respective crossarm and rim thicknesses of 0.317 cm (0.125 in.) and 0.152 cm (0.060 in.). The wearfaces of both seals H989 and H991 were disbonded subsequent to the testing of Figure 105.

The wearface of seal H990 was still bonded after the rig test; the seal was subsequently reworked to the configuration which will be used in the 982°C (1800°F) 3-piece seal design. This permitted preliminary testing of the cooling circuit up to 787°C (1450°F), the temperature limit of the current

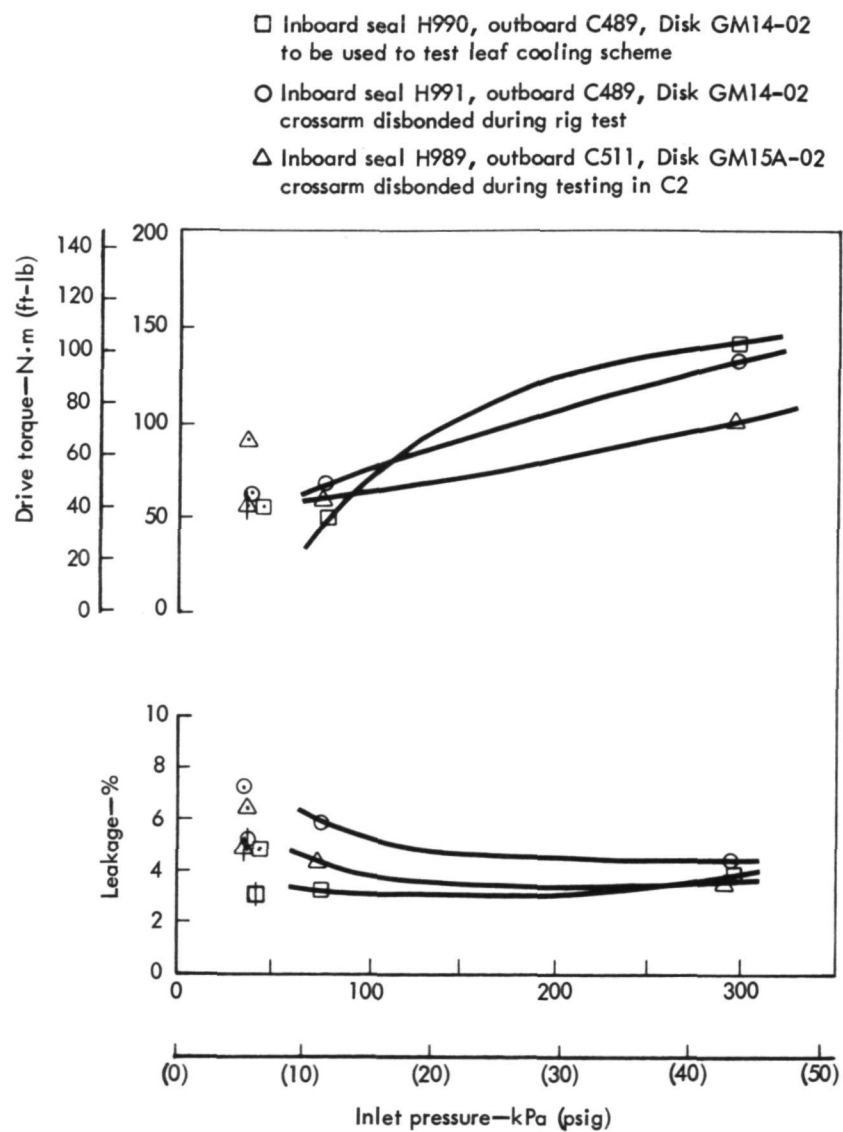


Figure 105. Hot rig performance of thick-platform inboard regenerator seals with 70% NiO/30% CaF₂ crossarm wearface.

TE-9872

rig. The results of this testing are discussed under "Three-Piece High-Tem-
perature Seal." Figure 106 shows seal H990 with the thermocouple wiring in
place.

Figure 107 shows the leakage results of a test of a seal (EX131861, S/N H991) conceived as a rework procedure for failed crossarm wearface. This seal was originally manufactured with a crossarm wearface of 70% NiO/30% CaF₂. When tested, the wearface disbonded from the seal as it also did from five other 70% NiO/30% CaF₂ seals. The crossarm wearface of seal H991 was replaced while the crossarm remained welded into the seal assembly. The new wearface is an 85% NiO/15% CaF₂ wearface; the main difference between the crossarm in this seal and new crossarms made as separate pieces is the deletion of the 787°C (1450°F) heat treatment which cannot be done on a finished seal with leaves and rim graphite wearface in place. Based on the poor low-pressure leakage results shown in Figure 107, this process is not being pursued further at this time.

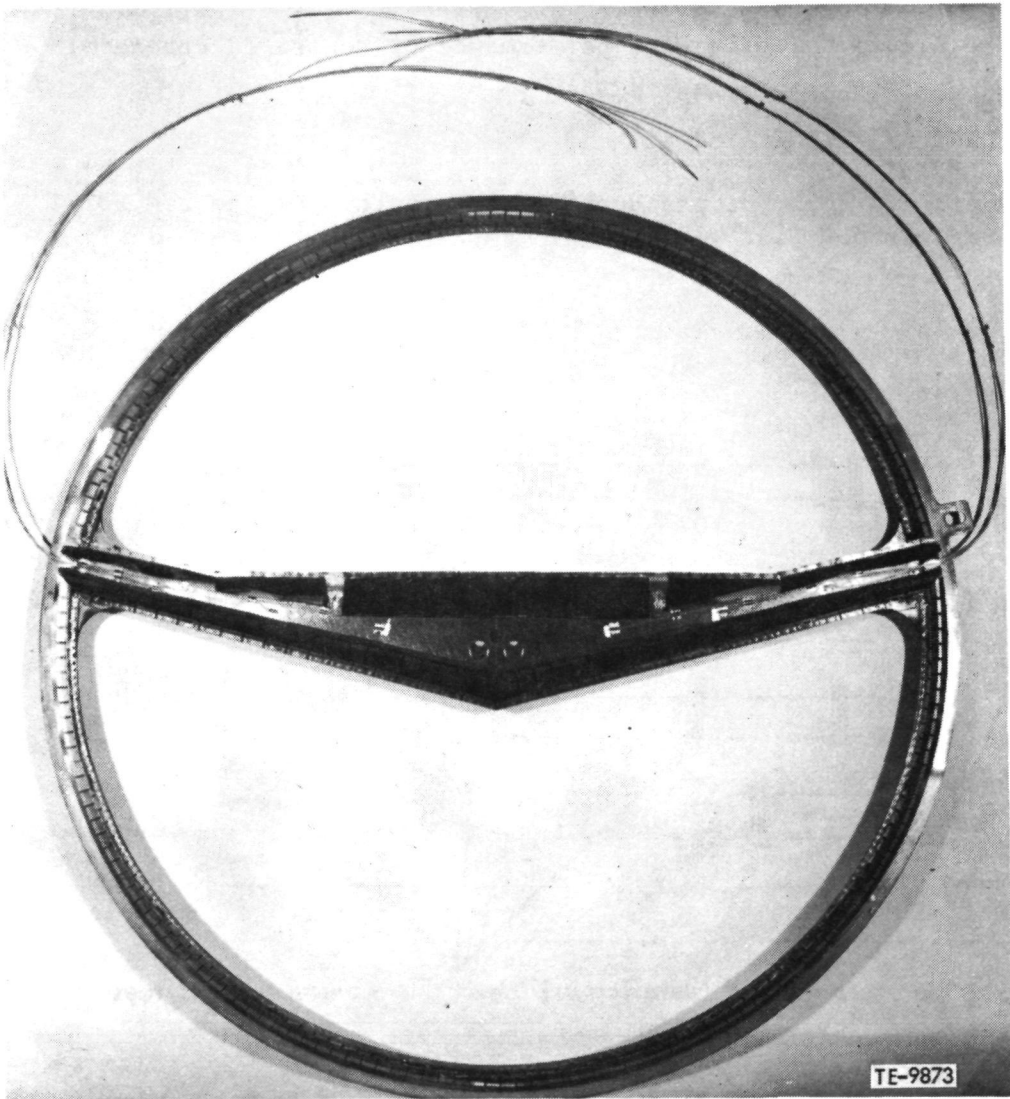
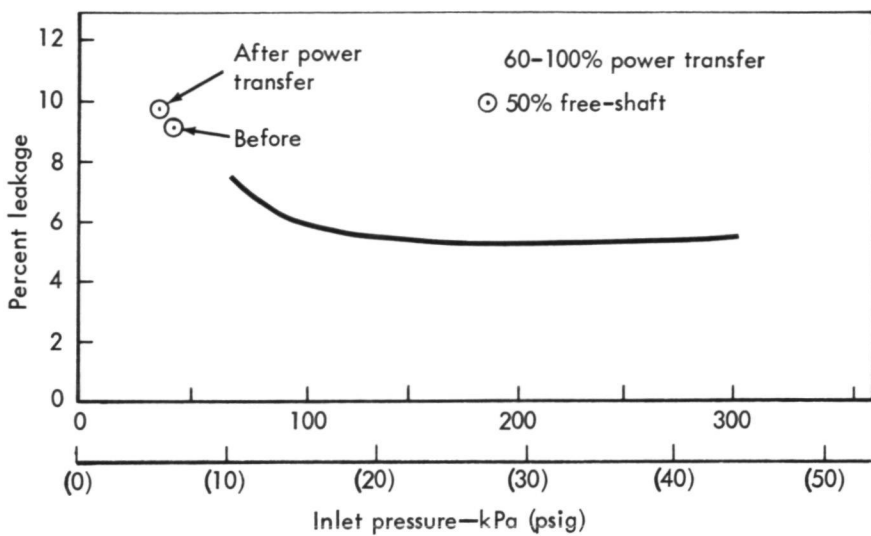


Figure 106. Crossarm inboard seal.

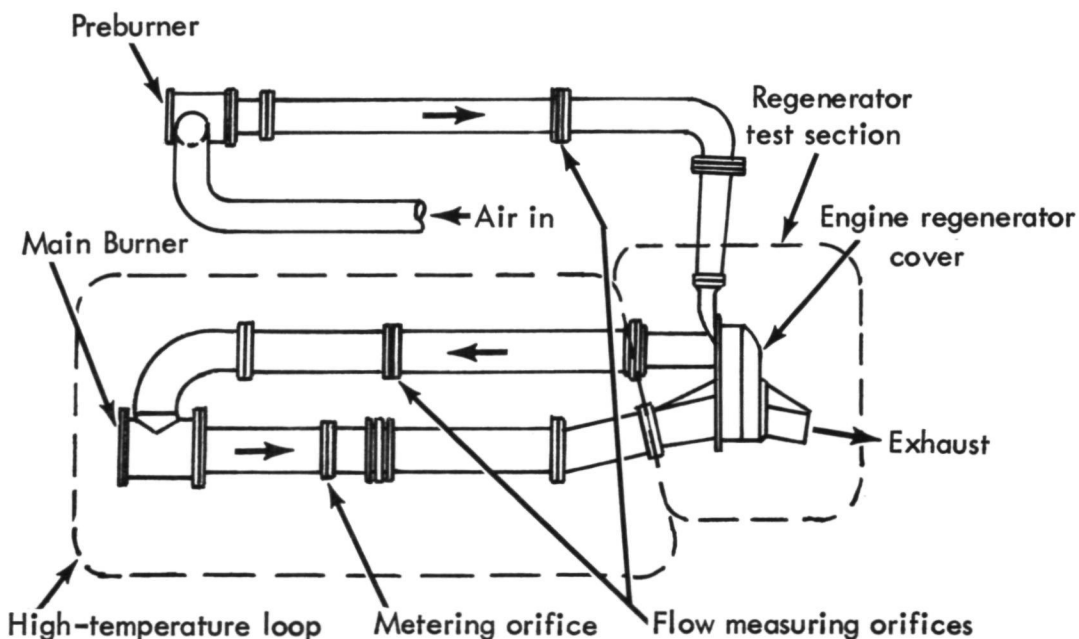


TE-9874

Figure 107. Leakage performance of resprayed crossarm.

HIGH-TEMPERATURE REGENERATOR RIG

Figure 108 is a diagram of the ducting arrangement for the new 982°C (1800°F) regenerator rig.



TE-7741

Figure 108. 982°C (1800°F) regenerator test rig ducting arrangement.

The high-temperature loop is completed, and fabrication of a new test section has started. A heat transfer analysis showed that either water or air cooling through a single channel in the crossarm of the test section would maintain tolerable temperature levels and gradients for operation at 982°C (1800°F). Water cooling was selected as more effective and lower in cost. Installation of the rig in a test cell and initial checkout are planned for February 1980.

LEAF RIG TESTING

A leaf rig test was completed in an effort to determine the effect of block crossarm distortion on the performance of the leaf of the inboard seal. An inboard seal with a straight crossarm leaf was used, and the rig was configured to simulate three different conditions that could exist with a flat-sided engine block: (1) the block crossarm flat as with a newly machined block, (2) a 0.076-cm (0.030 in.) high mound at the center of the block as has resulted from distortion on the engine, and (3) a 0.152-cm (0.060 in.) high mound which might occur at some combination of extended-length high-temperature testing. The mound was added to the center of the plexiglas rig cover, using auto body filler shaped to block measurements. Seal rim leaf heights (distance from seal platform to block) of 0.337 cm (0.133 in.), 0.373 cm (0.147 in.), 0.502 cm (0.198 in.) and 0.582 cm (0.229 in.) were used at each of the three cross-arm mount configurations. Rim leaf height is a variable in this test because as the block distortion increases, it must be accommodated by shimming the engine regenerator covers which, in turn, increases rim leaf height.

The results of this testing are plotted in Figure 109. The results at 0.337 cm (0.133 in.) leaf height are not shown since they are essentially the same as those at 0.373 cm (0.147 in.). As can be seen from the data, the block distortion itself is not as big an influence on leakage as the changes in leaf height which must be made to accommodate it. The X on the 0.373-cm (0.147 in.), zero distortion curve is at 100% power transfer pressure, and when a corresponding airflow of 0.0061 kg/s (0.0135 lb/sec) is corrected to 100% engine conditions, this represents approximately 0.6% regenerator leakage.

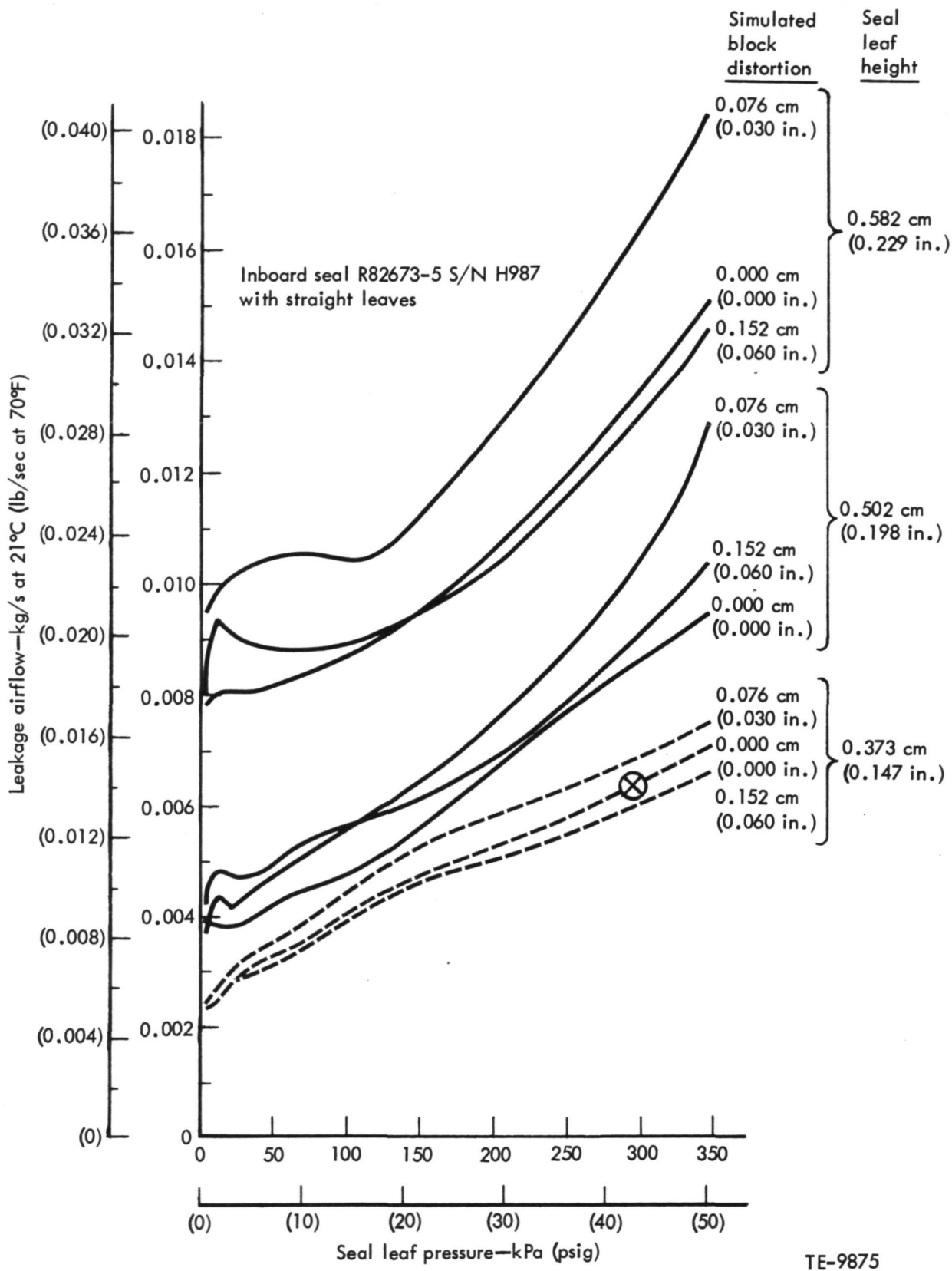


Figure 109. Leaf rig test of effect of simulated block crossarm distortion at three leaf heights.

VI. GENERAL ENGINE DESIGN AND DEVELOPMENT

INTRODUCTION

The nonceramic component activities that took place during this reporting period involved the evaluation of peak engine block temperatures in preparation for testing of the 2070°F engine configuration, the development of a 2070°F combustor, and the development of an engine electronic control system based on microprocessor/digital technology. The following are the major accomplishments and findings during this report period:

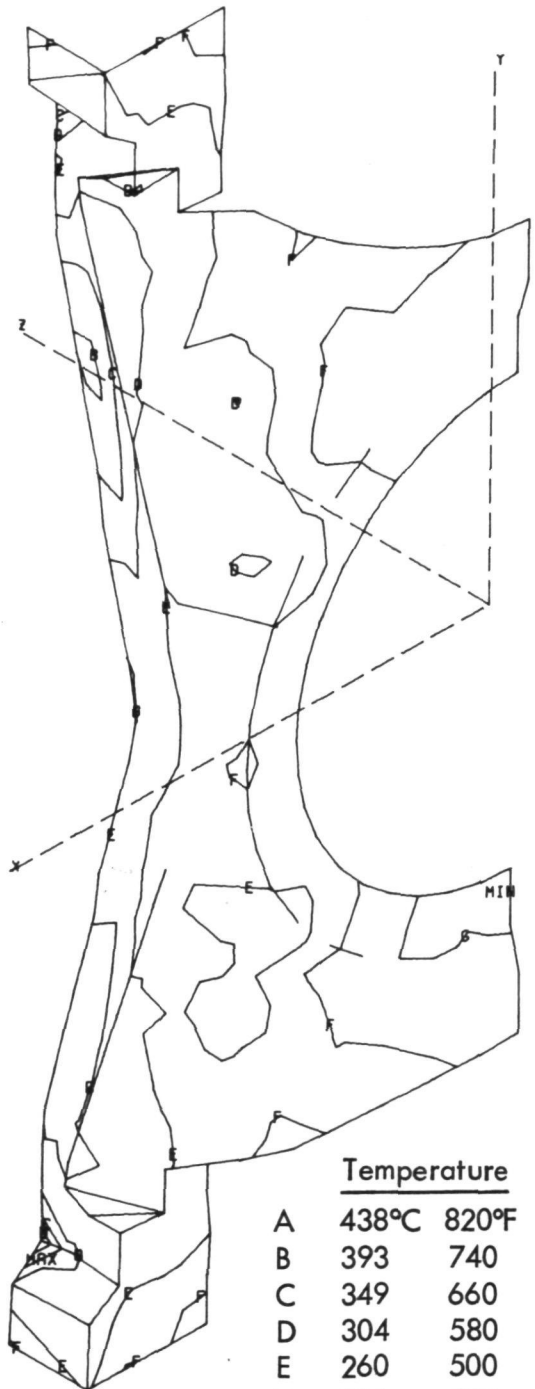
- o Development of a scheme to cool the engine block crossarm using ambient air
- o Fabrication of a 2070°F combustor
- o Completion of thermal paint and performance evaluation on the burner rig
- o Fabrication and vendor testing of a prototype microprocessor or engine control
- o Fabrication of support equipment and portable test case for interrogation of the control fault memory

ENGINE DESIGN MODIFICATIONS

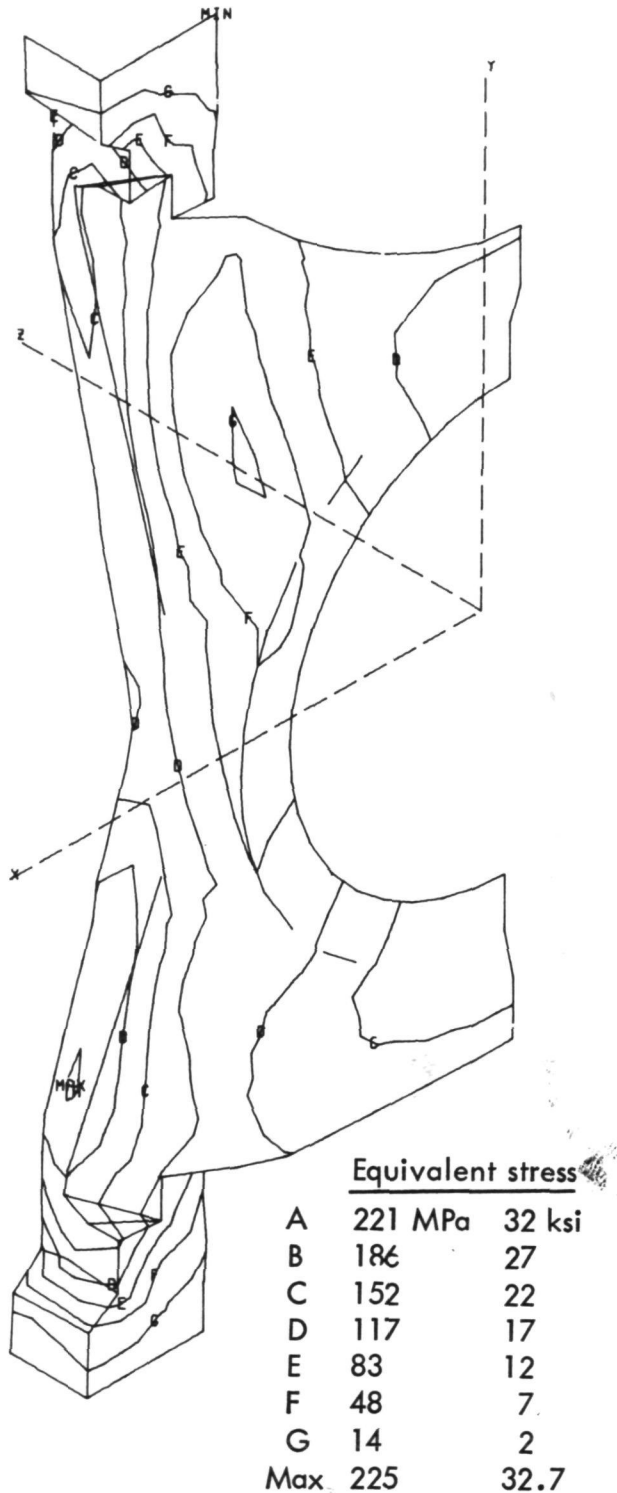
A series of design approaches have been evaluated to reduce the peak engine block temperature during operation at the maximum gas temperature conditions encountered in the CATE engines. During this six-month period, an investigation into the most promising of the approaches was conducted.

The peak block temperature occurs in the block crossarm which connects the bulkheads that separate high-pressure burner inlet air from the turbine exhaust. The crossarm is presently cooled by an internal cooling air circuit which uses compressor discharge air. Cooling the crossarm region by blowing ambient air instead of compressor discharge air through the block bulkhead cavity has been proposed and analyzed. Heat transfer analysis indicates that a reasonable amount of ambient air (0.014 kg/s (0.03 lb/sec)) blown through the existing cavity will reduce the peak crossarm temperature to the design goal of 482°C (900°F) at the maximum turbine exhaust temperature of 982°C (1800°F).

Figures 110 and 111 show the finite element analysis results for two different levels of ambient airflow through the crossarm cooling air cavity. The scheme analyzed consists of ambient air introduced through existing core plugs at the top of the block, flowing through the block crossarm cooling air cavity, and discharging through two core plugs at the bottom of the block. As can be seen, the peak crossarm temperature occurs near the middle of the lower half of the crossarm seal surface. In evaluating blower requirements, the 0.014-kg/s (0.03 lb/sec) ambient airflow through this modified cooling circuit is calculated to result in less than a 38-mm (1.5 in.) H₂O total pressure loss and, therefore, does not present a problem in terms of blower capacity. However, it is estimated that the scheme will increase engine heat rejection by 3.9 kW (220 Btu/min) and cause a 0.5% increase in engine SFC.



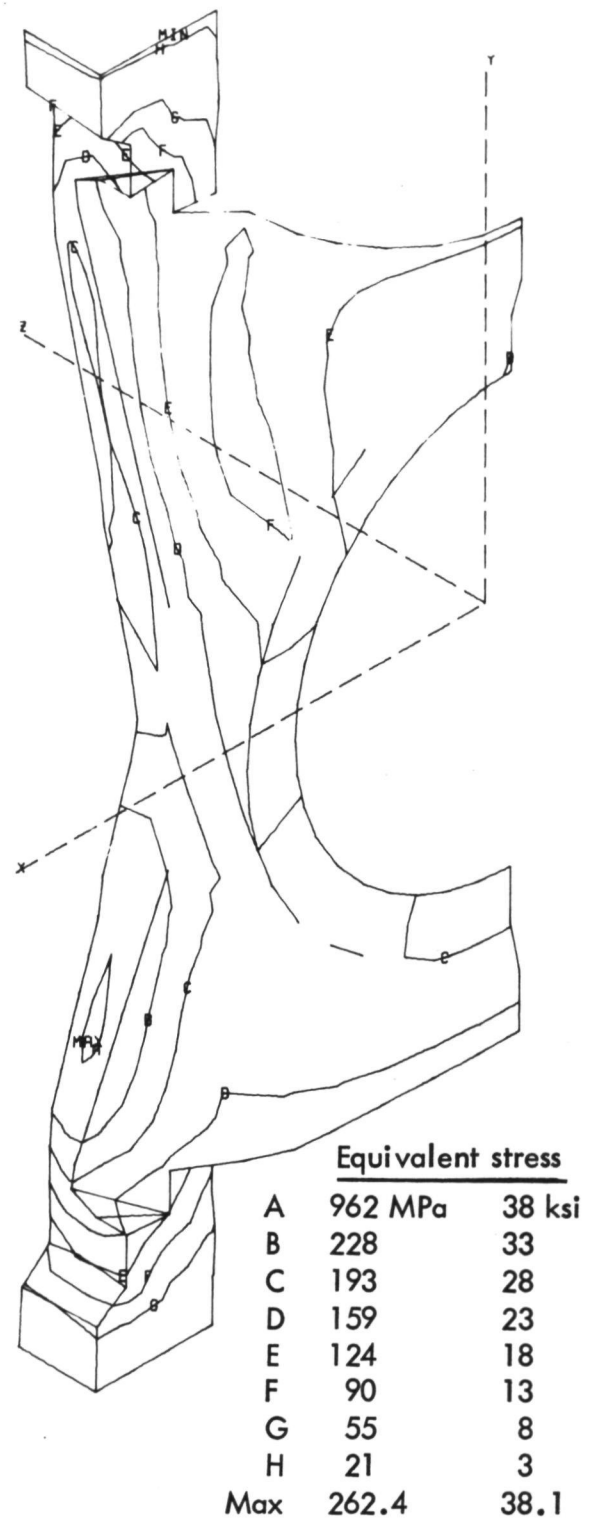
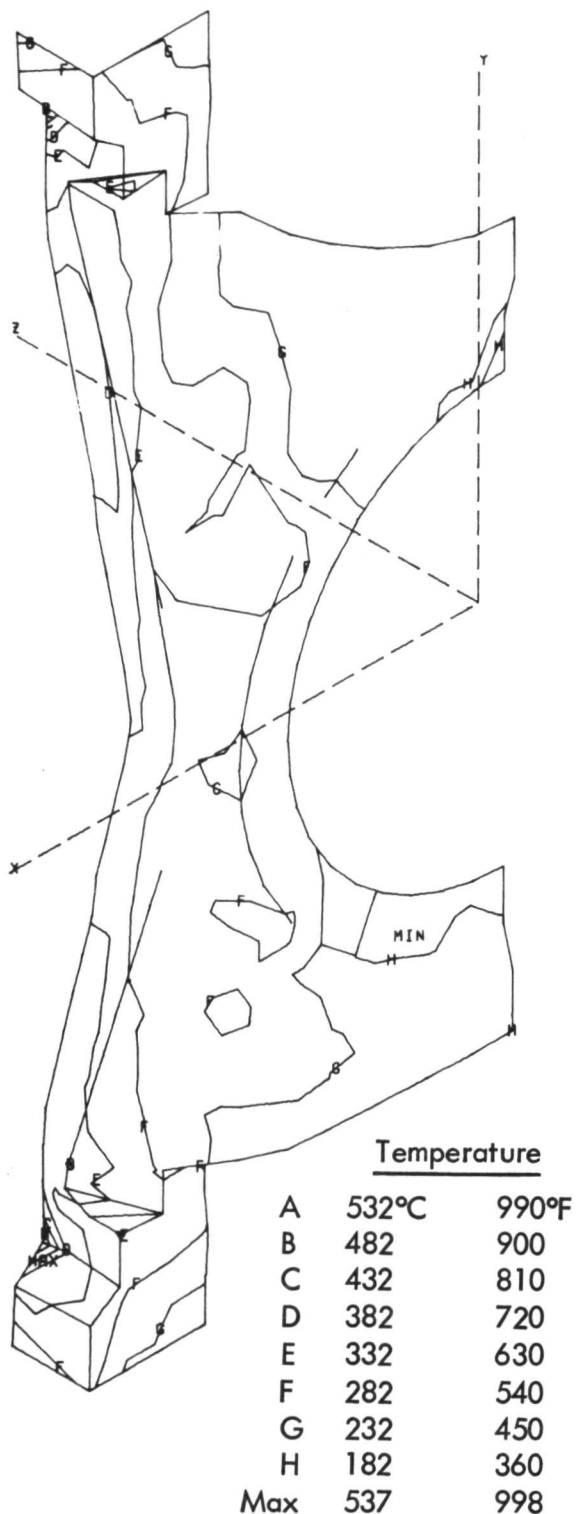
Temperature		
A	438°C	820°F
B	393	740
C	349	660
D	304	580
E	260	500
F	216	420
G	171	340
Max	442	828



Equivalent stress		
A	221 MPa	32 ksi
B	186	27
C	152	22
D	117	17
E	83	12
F	48	7
G	14	2
Max	225	32.7

TE-9851

Figure 110. Block crossarm and rear bulkhead with 0.018-kg/s (0.04 lb/sec) ambient air cooling at 982°C (1800°F) T₆.



TE-9852

Figure 111. Block crossarm and rear bulkhead with 0.009-kg/s (0.02 lb/sec) ambient air cooling at 982°C (1800°F) T6.

Plans call for evaluating this scheme by test because it can be accomplished with a minimum of modifications to the existing block. Compressor discharge air can be plumbed externally to the outer turbine cooling circuit, bypassing the crossarm cooling circuit. The crossarm cooling air cavity can then be vented to atmospheric pressure through the bottom two existing core plugs and supplied with blown ambient air through the top two core plug openings. Measurement of crossarm temperature versus airflow at various engine temperature levels is planned.

2070°F COMBUSTOR

A redesign of the IGT 404 combustor was required for the 2070°F CATE engine. The design, fabrication, and initial test phases have been successfully completed. Further combustor evaluations await the availability of the new higher-temperature test equipment heater which will enable the simulation of the actual combustor inlet design conditions of the 2070°F CATE engine cycle.

The combustor fabrication and test evaluation phases were carried out during the past six months. Two combustors were involved in the evaluation:

- o A prototype combustor made of Inco 601 material but otherwise incorporating the increased cooling air and other aerodynamic features was used principally to obtain starting and durability experience on the 1900°F CATE engine.
- o A 2070°F engine combustor made of Haynes 188 material and having final aerodynamic design features underwent a complete evaluation on the combustor rig, limited only to the 1310°F inlet air capability of the current test facility. (Design inlet air temperatures for the 2070°F CATE engine are 1357°F at 100% N_g and 1540°F at 80% N_g .)

Durability test time of the increased-cooling-air prototype combustor in the 1900°F CATE engine C-2 has now exceeded 1100 hours. The combustor has exhibited no durability or other operational problems during this period. Additional testing of this engine is planned.

The 2070°F engine combustor has now completed thermal paint and performance evaluations on the burner test rig. A total of 63.4 hours (airflow time) was utilized in this evaluation. Complete performance mapping included determinations of pressure drop, ambient starting, high- and low-speed efficiency, lean burning limits, and a thermal paint evaluation at 1900°F and 2070°F combustor outlet gas temperatures. The results of the burner rig test evaluation indicated that the performance of this combustor design was excellent and should present no problems when operating in the 2070°F engines.

The performance measured on the burner test rig is shown in Figures 112 through 116. The following are among the highlights of these exhibits:

- o Pressure drop value of 2.0% is below design goal of 2.2%.
- o Lean blowout limit of 3.72-kg/h (8.2 lb/hr) fuel flow rate is well below design goal of 4.54 kg/h (10 lb/hr).

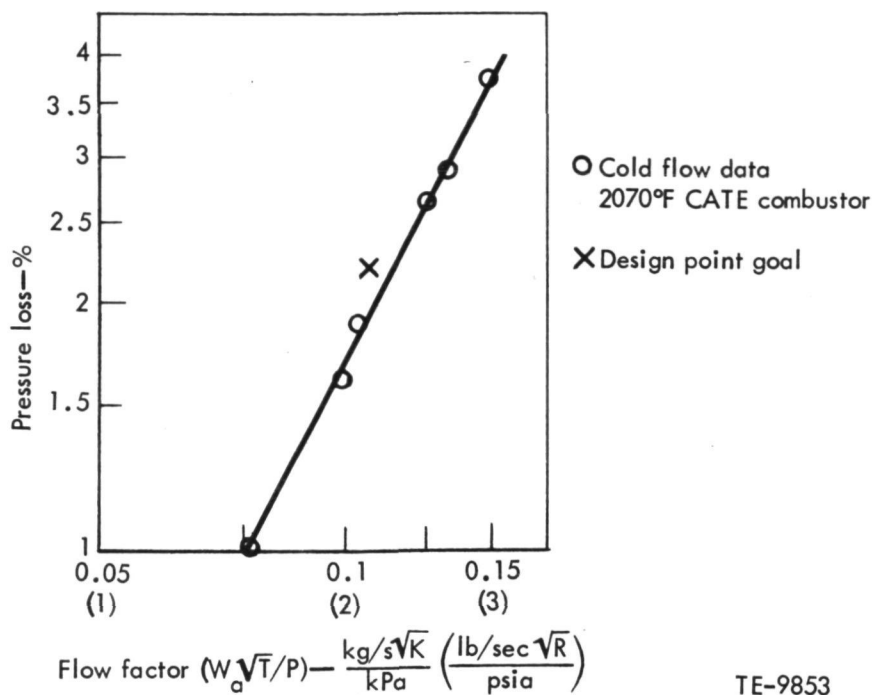


Figure 112. Combustor pressure loss.

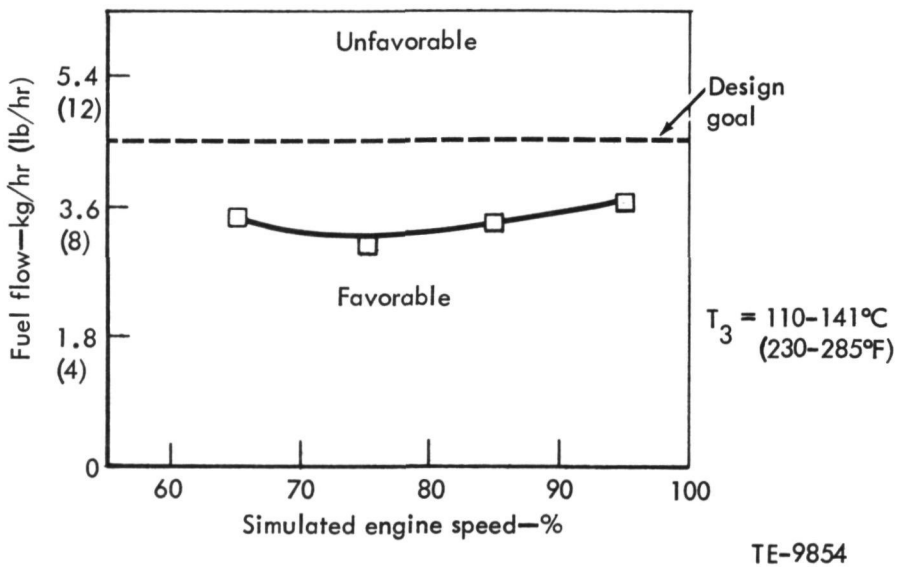
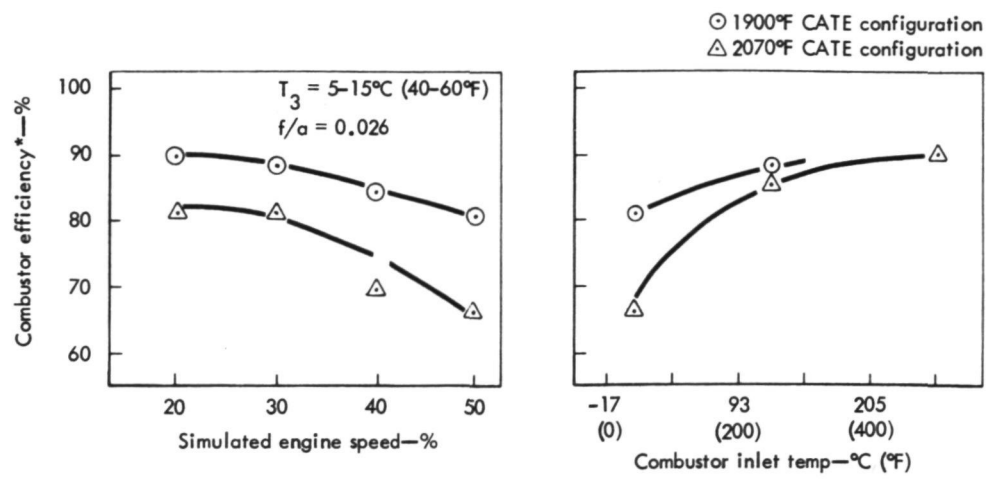


Figure 113. Lean burn limit.

- Efficiency in the starting "pullaway" range was slightly lower for the 2070°F combustor than values for the 1900°F combustor design because of the increased cooling air requirement, but no starting problems would be anticipated as a result of the minor efficiency decrease.



*Based on measured temperature rise

TE-9855

Figure 114. Low-speed combustion efficiency.

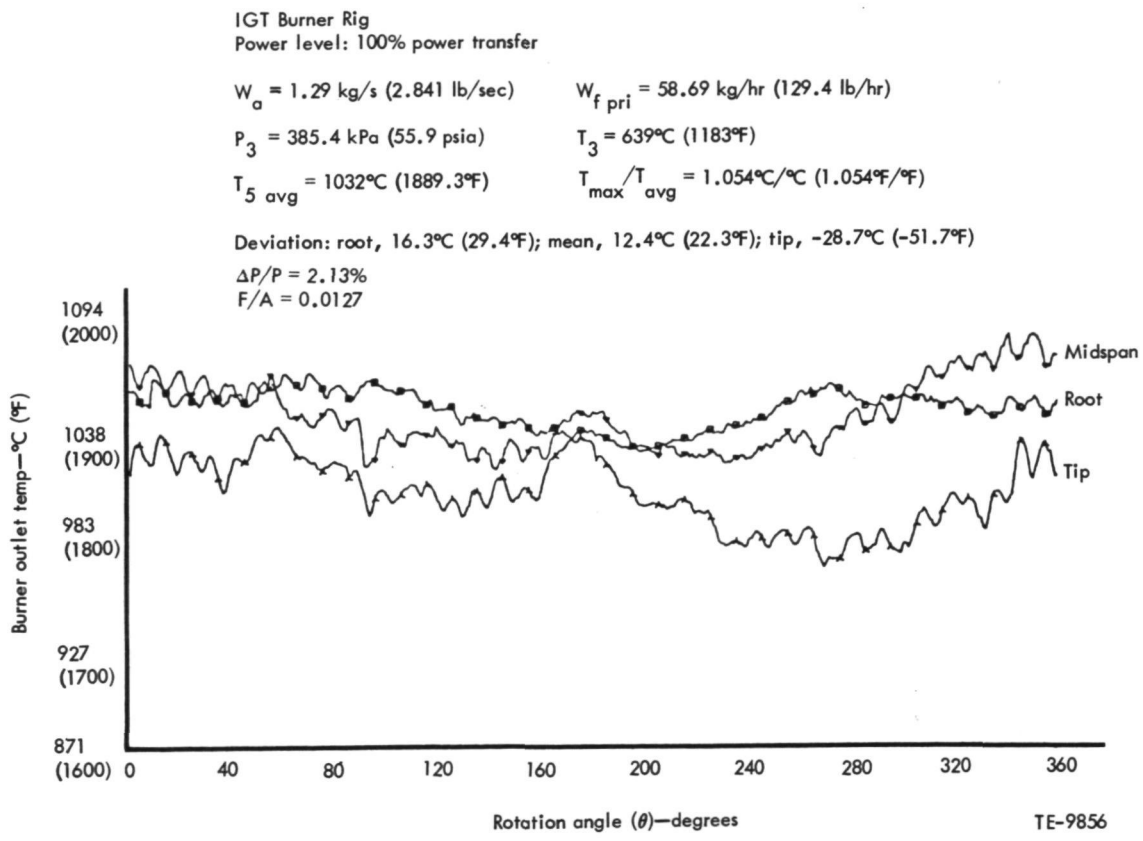


Figure 115. Combustor exit temperature traverse.

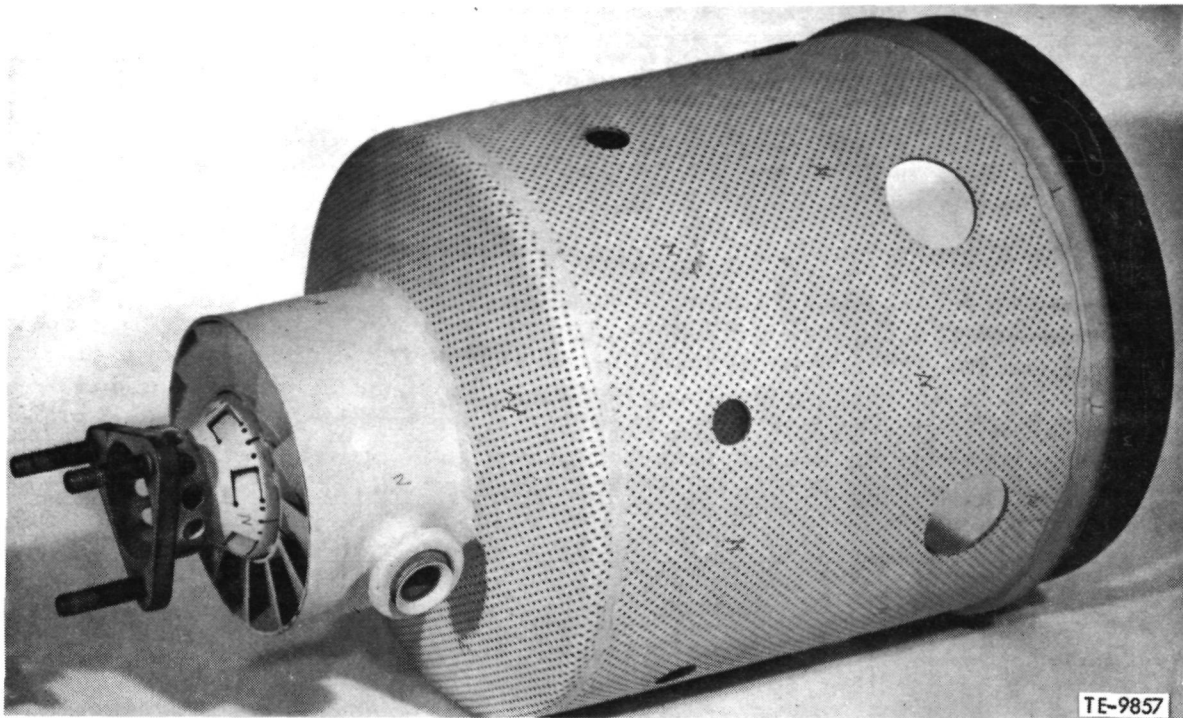


Figure 116. Thermal paint results at 1132°C (2070°F) BOT.

- o Gas temperature profile was uniform as exhibited by the T_{max}/T_{avg} value of 1.06 °F/°F or less at all operating conditions. The radial temperature gradient showed the slightly cooler tip which is typical of all IGT prechamber combustor configurations.
- o The SAE smoke number measured at maximum power condition was 5, which is well below an estimated visible limit of about 40.

All combustor and fuel nozzle surfaces were free of carbon deposits following the test. Metal temperatures were less than 860°C (1590°F) as determined by indications from temperature-indicating paints on the outer and inner surfaces of the combustor when tested at maximum heat flux of 80% power transfer condition.

CONTROLS

The C-1 and C-2 engines have been using analog electronic control, with closed-loop control of combustor exit gas temperature (T_4) as one of the prime functions. The increases in cycle temperature planned for the upcoming engine configurations exceed the capabilities of practical temperature sensors for the T_4 environment. As the result of analytical and design studies and special engine testing, power turbine exit gas temperature (T_6) was selected for control in the future CATE engines. The design and development of such a control was initiated, with the design to be based on microprocessor/digital technology.

One prototype microprocessor engine control was fabricated and tested at Woodward Governor Company during the report period. Support equipment, including a (1) portable test case which is used to interrogate the control fault memory

and (2) an engine simulator which enables closed-loop bench testing of the control functions, was also built and developed. By year end the prototype control was judged to be adequate for first engine testing at DDA beginning January 1980.

Four meetings were held during the period to review the software logic as documented on the Woodward Governor Company flow diagram and in the DDA design specification.

All software has been written, and about 75% of the available 8K PROM memory has been used. The remaining 2K of memory is very adequate for further software development. About two-thirds of the logic--for start-monitor, gasifier speed (N_1) governing, and power turbine exit (T_6) accel control--is debugged. The unit has demonstrated that its programmable-type digital logic will provide invaluable flexibility for change during the development of the CATE engines without sacrificing control hardware integrity.

Figure 117 is a photograph of the control assembly with cover removed. The unit has six removable circuit boards as shown and three chassis boards which are not visible in the picture. Field adjustments and the test connector are located on the back side, opposite the engine and application connectors shown. The design allows for one additional circuit board which can be used to add input or output functions if required during engine development.

A new T_6 thermocouple system was built and tested in engine C-1 during the report period, including special fast-response thermocouples which are used to judge the dynamic performance of the control.

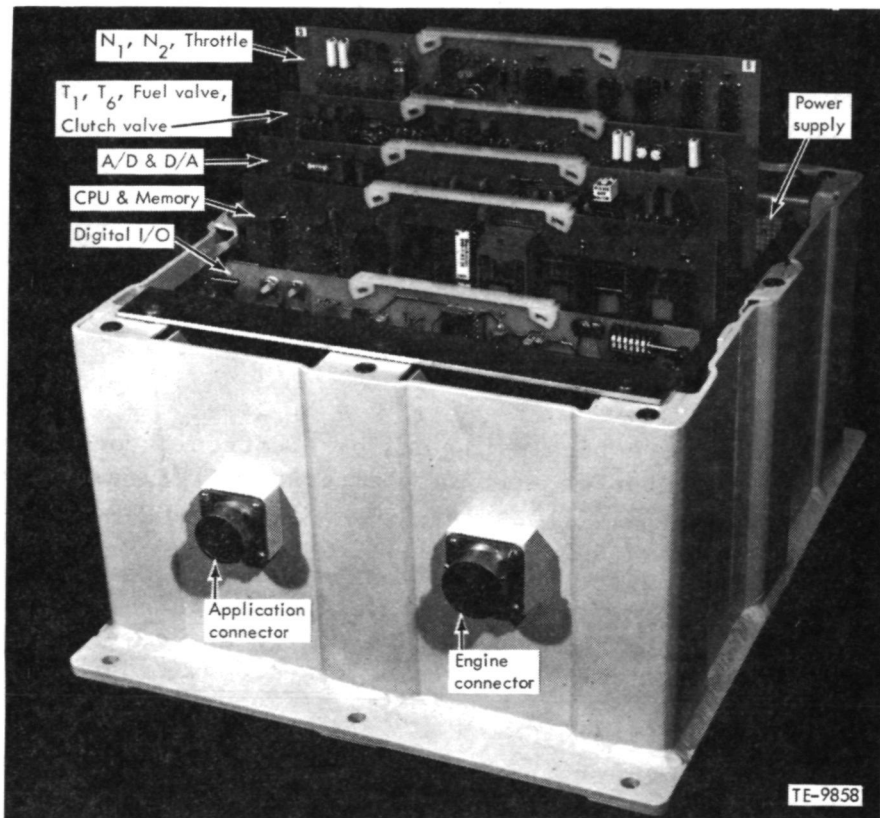


Figure 117. T₆ microprocessor engine control.

VII. ASSOCIATED ACTIVITIES - PAPERS AND EXHIBITS

During this reporting period, DDA participated in one exhibit and presented two papers.

In July 1979, Mr. H.E. Helms presented a paper entitled "Ceramic Applications in Turbine Engines" at the Sixth AMMRC Materials Technology Conference, Orcas Island, Washington.

In July 1979, Dr. P.W. Heitman presented a paper entitled "Characterization of Ceramic Component Materials" at the Sixth AMMRC Materials Technology Conference, Orcas Island, Washington. This paper discussed NDE inspection techniques and sintered characterization of SiC and Si_3N_4 as applied to the gasifier turbine tip shroud.

In October 1979, DDA participated in the Fall DOE/NASA Automotive Technology Development Contractors Coordination Meeting at Dearborn, Michigan, with a paper and an exhibit. The paper entitled "Ceramic Applications in Turbine Engines Progress Report" was presented by Mr. Franklin A. Rockwood; it focused on the progress made on the 2070°F engine configuration ceramic components to be introduced, abradability testing, ceramic material strength characteristics, and engine test results.

A new exhibit was introduced (Figure 118) which shows the various programs the GT404-4 is affecting with ceramic components and introduction of the 2070°F ceramic engine hardware.



Figure 118. Exhibit of various GT 404 projects that utilize ceramic components.

ACKNOWLEDGMENTS

The CATE program management acknowledges the efforts of the following personnel in contributing to the preparation of this report:

- | | |
|----------------|--|
| L. Davis | - Regenerator Seal Design |
| D. Decker | - Ceramic Turbine Inlet Plenum and High-Temperature Block Design |
| R. Fox | - Ceramic Regenerator Material Evaluation |
| M. French | - Ceramic Regenerator Design |
| Dr. P. Heitman | - Ceramic Materials Development and Characterization |
| P. Jablonski | - Ceramic Turbine Vane and Tip Shroud Design |
| D. Talcott | - Ceramic Machining Process Development |
| R. Furstnau | - Engine Electronic Control System |
| S. Thrasher | - Engine and Rig Testing |
| J. Wertz | - Ceramic Turbine Blade Design |
| E. Young | - 2070°F High-Temperature Combustor Design |
| R. Sullivan | - 2070°F High-Temperature Combustor Design |

PRECEDING PAGE BLANK NOT FILMED